
Dynamic patterns of biological systems

From transport to species diversity

Tobias Reichenbach



München 2008

Dynamic patterns of biological systems

From transport to species diversity

Tobias Reichenbach

Dissertation
an der Fakultät für Physik
der Ludwig-Maximilians-Universität
München

vorgelegt von
Tobias Reichenbach
aus Berlin

München, den 01. Februar 2008

Erstgutachter: Prof. Dr. Erwin Frey
Zweitgutachter: Prof. Dr. Karl Sigmund
Tag der mündlichen Prüfung: 17. 04. 2008

Contents

Zusammenfassung	ix
Abstract	xi
1 Pattern formation in biology	1
1.1 Sub- and multicellular patterns	2
1.2 Ecosystems and species diversity	7
2 Intracellular transport on parallel lanes	11
2.1 Active intracellular transport performed by molecular motors	11
2.2 Collective phenomena and theoretical model systems	15
2.3 Driven transport on multiple parallel lanes	18
2.4 Connection to classical non-equilibrium spin transport	20
2.5 Spontaneous density separation and polarization	23
2.6 Conclusion and Outlook	28
T. Reichenbach, T. Franosch, and E. Frey, <i>Phys. Rev. Lett.</i> 97 , 050603 (2006) .	31
T. Reichenbach, E. Frey, and T. Franosch, <i>New J. Phys.</i> 9 , 159 (2007)	35
T. Reichenbach, T. Franosch, and E. Frey, submitted (2008)	61
3 Dynamics of populations in cyclic competition	71
3.1 Biodiversity and evolutionary dynamics	71
3.2 Rock-Paper-Scissors dynamics as a motif of species interactions	74
3.3 Species coexistence and noise	76
3.4 The influence of locality and mobility on biodiversity	83
3.5 Pattern formation	86
3.6 Conclusion and Outlook	90
T. Reichenbach, M. Mobilia, and E. Frey, <i>Phys. Rev. E</i> 74 , 051907 (2006)	93
T. Reichenbach, M. Mobilia, and E. Frey, <i>Nature</i> 448 , 1046-1049 (2007)	105
T. Reichenbach, M. Mobilia, and E. Frey, <i>Phys. Rev. Lett</i> 99 , 238105 (2007)	115
T. Reichenbach, M. Mobilia, and E. Frey, submitted (2008)	119
Bibliography	139
Danksagung	153

List of Figures

1.1	Patterns of intracellular transport.	2
1.2	Spindle formation during cell division	3
1.3	Spatial protein signalling in single cells	5
1.4	Multicellular patterns in <i>Dictyostelium</i> aggregation	6
1.5	Laboratory and field patterns of ecosystems	8
1.6	Vegetation clusters in the Kalahari	10
2.1	The mechanism of active intracellular transport	12
2.2	Axonal transport	14
2.3	The totally asymmetric exclusion process (TASEP)	16
2.4	Driven transport on two parallel lanes	19
2.5	Spin transport	22
2.6	Spontaneous density separation resp. polarization	24
2.7	Phase diagrams	27
3.1	Frequency-dependent selection and cyclic dominance	73
3.2	Schematic state space of three competing species	77
3.3	Coexistence versus extinction in a cyclic population model	80
3.4	Mobility's impact on biodiversity	85
3.5	Rotating spiral patterns	89

Zusammenfassung

Die Ausbildung komplexer räumlicher Muster macht Differenzierung, beispielsweise in verschiedene funktionale Bestandteile, und damit Leben erst möglich. Oft sind solche Muster dynamisch, also zeitlich veränderlich. Tatsächlich bedeutet die Aufrechterhaltung von funktionaler Differenzierung, dass der zu erwartenden Entropiezunahme durch einen aktiven Prozess entgegengewirkt wird, was nur durch Arbeit und damit Energiekonsum möglich ist. Durch diese ständig verrichtete Arbeit bewegen sich lebendige Organismen, physikalisch gesehen, fern von einem thermodynamischen Gleichgewicht. Die dabei und dazu entstehenden raum-zeitlichen Muster haben besondere physikalisch-mathematische Eigenschaften. Ihre Untersuchung ist von herausragender Bedeutung für ein qualitatives und quantitatives Verständnis von Leben.

In der vorliegenden Arbeit werden zwei Prozesse von Musterbildung, zu zwei verschiedenen biologischen Phänomenen gehörend, untersucht. Bei beiden liegt unser Fokus auf dem Verständnis der fundamentalen physikalisch-mathematischen Prinzipien, die den jeweiligen Prozessen zugrunde liegen. Dazu entwickeln wir analytisch behandelbare Modelle, von denen wir erwarten, dass sie die prinzipielle Dynamik des biologischen Systems darstellen. Ihre Analyse liefert fruchtbare Einblicke in die Mechanismen von biologischer Musterbildung, im Wechselspiel von deterministischer Dynamik und unvermeidbaren stochastischen Einflüssen, fern vom thermodynamischen Gleichgewicht.

Eukaryotische Zellen haben einen aktiven Mechanismus für Teilchentransport entwickelt. Auf Bahnen, nämlich Proteinfilamenten, die sich durch die Zelle ziehen, “laufen” molekulare Motoren und transportieren Makromoleküle von einem Ort innerhalb der Zelle zu einem anderen. Notwendig ist dieser ausgefeilte Prozess durch die relative Grösse eukaryotischer Zellen, in denen passive Diffusion der Makromoleküle oft zu langsam wäre.

Der erste Teil dieser Arbeit beschäftigt sich mit kollektiven Phänomenen, die durch die Wechselwirkung einer großen Anzahl molekularer Motoren entstehen können. Staueffekte durch Behinderung der Motoren untereinander, bei hoher Dichte, sind möglich und wurden tatsächlich, nach theoretischer Vorhersage, experimentell *in vitro* beobachtet. Wir untersuchen den Einfluss von gelegentlichen “Spurwechseln” von Motoren, welche sich auf verschiedenen parallelen Bahnen eines molekularen Filaments bewegen. Neuartige Stauphänomene entstehen, in denen Regionen niedriger Motorendichte auf andere mit hoher Dichte stoßen und stationäre Muster verursachen. Wir zeigen, wie die zugrundeliegende Dynamik auch kollektive Phänomene in klassischem Spin-Transport, wie zum Beispiel Elektronentransport durch eine Kette von Quantenpunkten, beschreiben kann.

Der zweite Teil dieser Arbeit handelt von Ökologie. Eine enorme Vielfalt verschiedener Tier- und Pflanzenarten bevölkert die Erde, ein Reichtum, der wichtig für die Lebensfähigkeit eines jeden Ökosystems ist. Konzeptuelle Erklärungen dieser Vielfalt stossen jedoch überraschend schnell auf Schwierigkeiten. Warum setzt sich bei zwei konkurrierenden Spezies nicht langfristig eine allein durch, sei es aufgrund besserer Anpasstheit oder durch zufällige Ereignisse?

In unserer Arbeit weisen wir zunächst darauf hin, dass stochastische Effekte, bei genügend langen Wartezeiten, letztlich immer zum Aussterben von Arten führen. Wir schlagen deshalb eine Klassifizierung von stabiler und instabiler Koexistenz vor, die das Verhältnis der typischen Aussterbezeit zu den ökologisch relevanten Zeitskalen berücksichtigt. Im folgenden wenden wir diese Klassifizierung auf Stabilitätsuntersuchungen von Ökosystemen an. Ausgehend von Laborexperimenten zur Koexistenz verschiedener Stämme von *E.coli* Bakterien untersuchen wir den Einfluss von zyklischer Dynamik, wie sie zum Beispiel aus dem Kinderspiel "Stein-Schere-Papier" bekannt ist, im Zusammenspiel mit raum-zeitlicher Strukturbildung. Wie im Experiment beobachtet, können Bakterien miteinander koexistieren, wenn eine geringe Mobilität die Abgrenzung der verschiedenen Stämme voneinander, und damit die Ausbildung von Mustern, ermöglicht. Theoretisch zeigen wir, dass zunehmende Beweglichkeit der Bakterien zu relativ geometrischen Strukturen, nämlich ineinander verschlungenen Spiralen, führt. Wenn die Mobilität einen kritischen Wert überschreitet, wird diese Musterbildung unmöglich, was zum Aussterben von zwei der drei Stämmen führt. Experimentelle Untersuchungen zu diesem von uns vorhergesagten Einfluss der Mobilität der Bakterien sind derzeit im Labor von Prof. J. Rädler an der Ludwigs-Maximilians-Universität München in Vorbereitung.

Kapitel 1 gibt eine Einführung in biologische Musterbildung und stellt insbesondere verschiedene Beispiele von funktionalen Strukturen vor. Zwei solche Musterbildungsprozesse werden in den beiden nachfolgenden Kapiteln behandelt. Stauphänomene in intrazellulärem Transport bilden das Thema des 2. Kapitels, wo wir auch Anwendungen des theoretischen Modells auf Verkehrsflüsse und klassischen Spintransport erklären. Im 3. Kapitel werden konzeptionelle Mechanismen, welche die Koexistenz verschiedener konkurrierender Arten erlauben, untersucht und insbesondere raum-zeitliche Muster sowie der Einfluss von Mobilität beschrieben.

Abstract

The formation of complex spatial patterns enables differentiation, for example into different functional parts, and therefore constitutes a necessity of life. Often, such patterns are dynamic, i.e. temporally changing. Indeed, maintaining functional differentiation means to work against entropy increase by an active process, enabled by energy consume. Due to this constantly performed work, from a physical point of view, living organisms operate far from thermal equilibrium. The spatio-temporal patterns emerging in this way possess special physical and mathematical properties. Their investigation is of outstanding importance for a qualitative as well as quantitative understanding of life.

In this Thesis, two processes of pattern formation, belonging to two distinct biological phenomena, are investigated. In both cases, our focus lies on the understanding of the fundamental physical and mathematical principles underlying the respective process. For this purpose, we develop models that are analytically accessible and which we expect to capture the principal dynamics of the biological system. Their analysis allows for fruitful insights into the mechanisms of biological pattern formation, at the interplay of deterministic dynamics and unavoidable stochastic influences, far from thermal equilibrium.

Eukaryotic cells have developed an active mechanism for particle transport. Molecular motors “walk” on tracks, namely proteinfilaments, that span through the cell and thereby transport macromolecules from one place in the cell to another. This elaborate process is necessary due to the relatively large size of eukaryotic cells, which typically makes passive diffusion of molecules too slow.

The first part of this Thesis investigates collective phenomena, as can emerge by the interplay of a large number of molecular motors. Jams may arise from hindrance of the motors at high densities. Indeed, after theoretical prediction, such jams have been observed experimentally *in vitro*. We are investigating the influence of occasional “lane-changes” of motors, which move on one out of several parallel lanes on a protofilament. Novel jamming phenomena arise, with spatial regions of low motor density running into regions of high density and causing stationary patterns. We show that the underlying dynamics may also describe collective phenomena in classical spin transport, for example in electron transport through a chain of quantum dots.

The second part of this Thesis deals with ecology. An enormous diversity of different animal and plant species populates the earth, a richness that is of high importance for the viability of all ecological systems. However, conceptual explanations of this diversity

rapidly face difficulties. If two species compete, why does not one outcompete the other, by better adaptation or random effects, and remain as the only survivor in the long run? In our work, firstly, we point out that, upon long enough waiting time, random effects eventually always lead to species extinction. Therefore, we propose a classification of stable and unstable coexistence that considers the relation between the typical extinction time and the ecologically relevant time-scales. In the following, we apply this classification to investigations on the stability of ecological systems. Motivated from laboratory experiments on the coexistence of different bacterial strains of *E. coli*, we investigate the influence of cyclic dynamics, as is known from the children's game "rock-paper-scissors", and its interplay with spatio-temporal pattern formation. As has been observed in the experiment, bacteria can coexist if a low mobility enables the segregation of the different strains and thereby the formation of patterns. We show theoretically that increasing mobility of bacteria leads to relatively geometrical structures, namely entangled spirals. When mobility exceeds a threshold value, this pattern formation is no longer possible and two of the three strains extinct. Experiments aimed at an investigation of this influence of bacterial mobility predicted by ourselves are currently in preparation at the chair of Prof. J. Rädler at the Ludwigs-Maximilians-University Munich.

Chapter 1 provides an introduction to biological pattern formation; in particular, it presents different examples of functional structures. Two of these pattern-forming processes are treated in the two following chapters. Jamming phenomena arising in intracellular transport are investigated in Chapter 2; there, we also explain applications of the theoretical model to traffic and classical spin-transport. In Chapter 3, conceptual mechanisms for the coexistence of different competing species are investigated. In particular, we describe spatio-temporal patterns and the influence of mobility.

1 Pattern formation in biology

Functional differentiation through the formation of complex patterns is a necessity for life. At all scales of living organisms, from single cells to multicellular aggregations and interacting animals or plants, the building blocks self-organize into highly-evolved, functional structures. As an intriguing example, eukaryotic cells are in part organized by smaller interior compartments, the organelles [1]. Among these, the nucleus encapsulates the genetic information encoded in the DNA, translation and folding of new proteins takes place in the endoplasmatic reticulum, and mitochondria are responsible for energy production. Dynamic patterns, i.e. spatial structures which change on time-scales being short compared to the lifetime of the cell, emerge as well and are of high importance. During replication of bacteria, oscillating patterns of signalling proteins define the position of cell division, while a complex interplay between molecular motors and microtubules carries out chromosome segregation in eukaryotic cells. On the multicellular level, rotating spiralling patterns organize *Dictyostelium* mounds during cellular aggregation, in this way shaping the fruiting body. On the scale of whole ecosystems, spatial segregation of individuals is presumed to be a key promoter of species diversity.

The processes of life occur far from thermal equilibrium. Approaching equilibrium would, similarly to the possible heat death of the universe [2], result in a decrease of the organisms internal structure and thereby a loss in its ability of performing basic tasks. Consequently, to maintain a high level of differentiation, all living organisms actively work against entropy increase, enabled by constant energy consume. The dynamic patterns organizing internal differentiation of living organisms as well as multi-individual patterns therefore typically operate far from equilibrium, hence, they are *dynamic* and *active*.

In the following, we present selected examples of dynamic pattern formation processes on different time and length scales. Starting from self-arrangement of microtubules and molecular motors as well as spatio-temporally oscillating protein concentrations within single cells, we turn to the multicellular aggregation and patterning of *Dictyostelium*, and finally describe evidences for the self-formation of complex structures in large-scale ecosystems. This brief introductory tour through the fascinating field of complex, functional organization of spatio-temporal patterns is neither meant as a complete overview nor a representative choice, but rather as a “random walk” between selected topics. Although we believe the presented processes to be insightful and beautiful examples of the emergence and functioning of biological structures, we are well aware that many more, in no respect less interesting, phenomena exist. To the latter, one must count the fascinating patterns

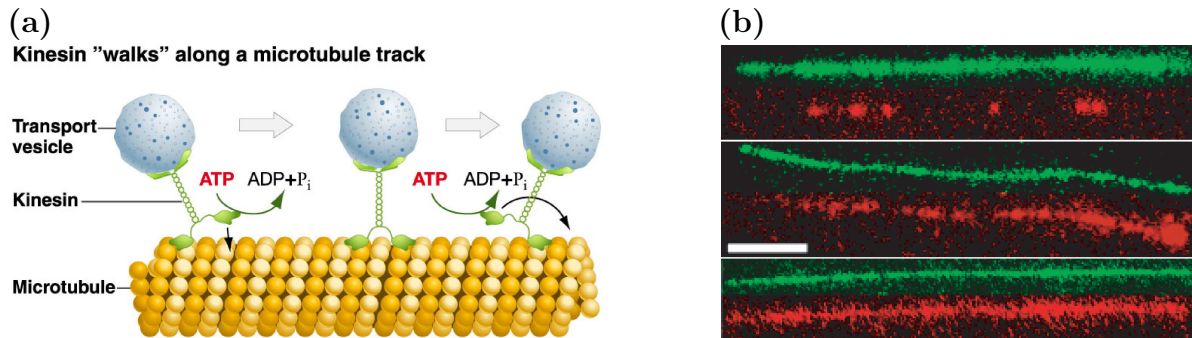


Figure 1.1: Patterns of intracellular transport. (a), We show a schematic picture of a motor protein, kinesin, “walking” on a microtubulus. The latter consists of α - and β -subunits, shown in dark resp. light yellow, which define the microtubulus’ polarity. Kinesin uses the polar structure to move unidirectionally, therefore providing fast transport of cargo particles. Its directed motion is enabled by hydrolysis of adenosine triphosphate (ATP). (b), A large number of molecular motors on the same microtubulus can cause collective phenomena such as traffic jams [11]. The picture has been reproduced from [12]. The authors of this study have experimentally investigated high-traffic effects. Fluorescently labeled kinesins (KIF1A) (red) were introduced to a microtubulus (green). Varying the kinesin concentration from low (top) over medium (middle) to high (bottom) values, different patterns of traffic organize. In particular, for medium density of kinesin, an intriguing comet-like pattern forms.

emerging during embryonal development [3], which determine the position of developing organs and the shape of the organism. Similarly, in the neuroscience of the brain [4, 5, 6], the development of the highly complex cortical network seems to be a dynamic, activity dependent process of neuronal self-organization. In the cardiac tissue, spiral wave propagation [7, 8] is believed to be responsible for heart fibrillation. Maybe the most visible biological patterns are found on the coat of animals, such as the line drawings of zebra coats or the jaguars’ spots [9, 10].

1.1 Sub- and multicellular patterns

Eukaryotic cells are shaped by the cytoskeleton, a dynamic structure of molecular filaments cross-linked by molecular motors. As one out of many functions, it enables intracellular transport, which is subject of Chapter 2. The “molecular tracks” on which such transport occurs are microtubules, see Fig. 1.1 (a). These filaments are part of the cell’s cytoskeleton and prove structural stability; moreover, they form the cilia and flagella of eukaryotic cells. Their various functions are reflected by their highly interesting mechanical properties, e.g. a length-dependent persistence length [13]. Microtubules are hollow cylinders, with a diameter of about 25 nanometer, while their length is subject to dynamic processes,

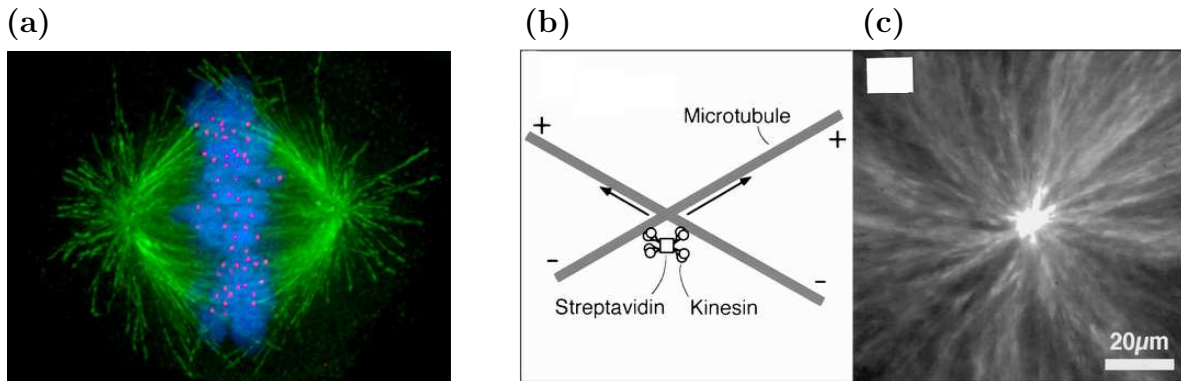


Figure 1.2: Spindle formation during cell division. **(a)**, The mitotic spindle *in vivo*, reproduced from [20]. Microtubules (green) are crosslinked by molecular motors, and bind to the chromosomes (blue) mediated by kinetochores (red). During cell division the spindle pulls the chromosomes apart into the emerging daughter cells. **(b)**, The dynamic crosslink of different microtubules by molecular motors is shown schematically. **(c)**, *In vitro* experiments of tubulin-motor-solutions yield formation of aster-like structures, similar to the mitotic spindle. The picture has been taken from [21].

polymerization and depolymerization, and can vary between several micrometers to possibly millimeters in axons of nerve cells. The basic structural units are α - and β -dimers, which pairwise aggregate into tubulin heterodimers, and then form the microtubulus. Due to the composition of heterodimers, which are polar (they are formed of two distinct subunits), the microtubules also possess a polarity. Commonly, one refers to the end where the α -dimer is exposed as the (-) end, while the other one (with the β -dimer exposed) is the (+) end. Due to polarity, microtubules are well-suited lanes for intracellular transport. Namely, molecular motors, such as kinesins and dyneins, “walk” unidirectionally on the microtubules and carry cargo particles to the required destination, c.f. Fig. 1.1 (a). These motor proteins employ the microtubules’ polarity to ensure unidirectional movement: most kinesins move towards the positive end, while dyneins “walk” in the opposite way, to the (-) end. In this situation, theoretical studies [14, 15, 16, 11, 17, 18, 19] have revealed a rich variety of one-dimensional patterns of low and high motor densities that can arise along a microtubulus induced by mutually obstructive effects. In particular, phenomena reminiscent of traffic jams may occur at distinct spatial positions. At a high enough density of molecular motors, they hinder each others motion, in part by obstruction of the cargo, in part by on-site exclusion of the motors themselves. Obstruction leads to jams when the mean free path on the microtubulus becomes comparable to the step size of the motors. Experimental studies have given evidence of the occurrence of such patterns *in vitro*, see Refs. [12, 22]. High densities of molecular motors lead to jams, while at medium densities an especially interesting comet-like structure, where jams and “unhindered traffic” alternate in a spatio-temporally dependent way, emerges. These processes are dynamic: although the patterns may appear as stationary in time, they are organized by a steady

flux of motors particles. *In vivo*, the typical densities of motor proteins on a microtubulus typically seems to be much lower than required for traffic phenomena. However, the *in vitro* studies reveal information on the motor interactions that may be useful in further understanding of these high-performing molecular engines. In Chapter 2 of this Thesis, we study jamming phenomena of molecular motors on parallel lanes, as encountered on a microtubulus. There, we describe in more detail the origin as well as the characteristic form of these one-dimensional patterns.

Segregation of chromosomes during mitotic or meiotic cell division is mastered by a complex interplay of microtubules and motors. The latter form a spindle apparatus that links to the centromeres of the chromosomes via a protein structure referred to as kinetochores, see Fig. 1.2 (a). The spindle then pulls the chromosomes apart into the two emerging daughter cells. The high importance of precise chromosomal segregation in cell division for the viability of organisms poses major challenges to the accurate functioning of the spindle formation and pulling processes. Although major investigations are currently devoted to the understanding of the spindle's self-formation and pulling, these issues are far from being understood. Main challenges are posed by the many constituents and parallel processes of cells *in vivo*. Principal insights have therefore been gained by *in vitro* studies of the spatio-temporal structures emerging from the interplay of microtubules and molecular motors, isolated from other cellular ingredients [23, 21, 24]. These experiments have shown that microtubules, dynamically cross-linked by motor proteins such as kinesin, c.f. Fig. 1.2 (b), are capable of self-organizing into complex structures reminiscent of the mitotic spindle. In particular, asters, see Fig. 1.2 (c), and vortices self-arrange when starting from a homogeneous solution of tubulin and motors. Theoretical investigations are devoted to the understanding of the basic principles driving these highly dynamic processes [24, 25, 26]. Successful identification of such underlying principles may be applicable to other types of intracellular, filamental pattern formation, such as cell polarization through the formation of polar caps [27], see Fig. 1.3 (b). There, proteins interact with molecular motors and microtubules and can induce spontaneously self-forming "caps" of increased protein concentration.

Another beautiful example of cellular pattern formation far from equilibrium are the spatio-temporal oscillations of Min-proteins in the bacterium *E.coli* [28]. In prokaryotic cells, bacteria and archaea, the genetic material is not contained in a nucleus, as in eukaryotic cells, but moves freely in the cell. During division, the cell elongates, and the duplicated chromosomes segregate into the two emerging half spaces. To successfully divide into two daughter cells, with each having identical genetic material, the cell must accurately determine its middle, where division takes place in the form of a contracting Z -ring. If the site of division is unprecise, some chromosomes might end up in the "wrong" daughter cell, leaving the other one with insufficient genetic material. Using *E.coli* as a model system for bacterial division, Min proteins oscillating between the two poles of the elongated bacterium have been found to determine the division site, see [28, 30] for recent reviews. Two time-series of microscopic pictures of *E.coli* short before division are shown in Fig. 1.3 (a),

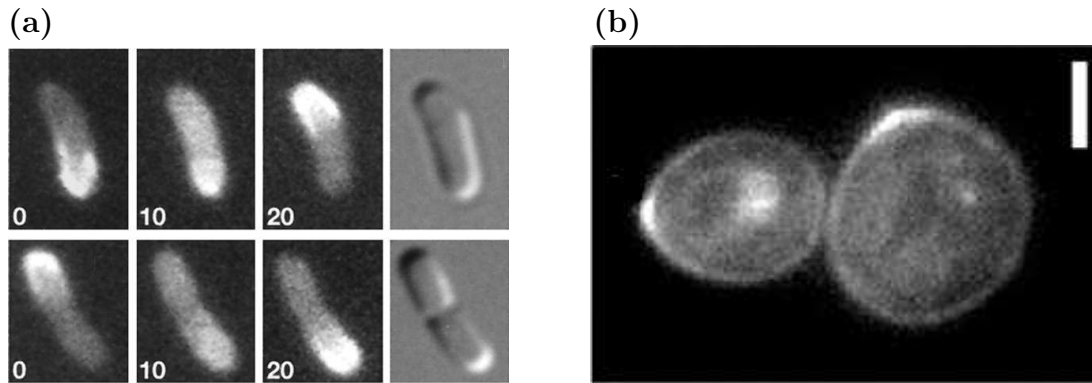


Figure 1.3: Spatial protein signalling in single cells. **(a)**, The spatial distribution of fluorescently labelled Min-D proteins in two cells of *E. coli* is shown for different times (given in seconds). Pole-to-pole oscillations emerge, which signal the bacterium its middle, an information that is crucial for its correct division during replication. The figures have been modified from [29]. **(b)**, Cell polarization in yeast is mediated by spatially-dependent concentrations of the protein Cdc42. In this picture, two cells spontaneously, i.e. in the absence of external spatial cues, develop a polarization in the form of Cdc42 caps, visible due to fluorescent labelling of the protein. The picture has been modified from [27]; the scale bar denotes $3\mu\text{m}$.

where Min-D proteins were fluorescently labeled. In the course of time (given in seconds), one clearly observes pole-to-pole oscillations of Min-D. In this way, the cell obtains precise and up-to-date information about its middle. Recent quantitative measurements of these dynamic patterns have fruitfully interacted with theoretical analysis [31, 32, 33, 34] to shed light on the dynamics and interactions of the different participating Min-proteins. Modelling in terms of reaction-diffusion equations yields a valuable description of the biological system, whereas stochastic fluctuations stemming from the low number of involved proteins seems to be of lower importance [32]. One of the main unresolved issues is the shape of the protein patterns when the cell actually divides. Namely, when the Z-ring, responsible for cell division, has formed and starts to contract, the Min-protein oscillations are expected to change qualitatively or break down. However, observations of such division events are extremely difficult.

Patterns do not only arise within single cells, but also on the multicellular level, as e.g. in *Dictyostelium* colonies. Being a group of cellular slime moulds, *Dictyostelium* appears in the form of individual amoebae when enough food is available. However, when environmental conditions are harsh (starvation), these individuals can aggregate into multicellular assemblies, called slugs, or form a fruiting body with a stalk supporting one or more balls of spores. Complex multicellular patterns organize these developments, as we explain in the following. The life-cycle of *Dictyostelium* is depicted in Fig. 1.4 (a). Under environmental stress, one cell starts to produce a signalling molecule (cAMP). Nearby cells move to the signal and produce cAMP themselves, resulting in the aggregation of the colony.

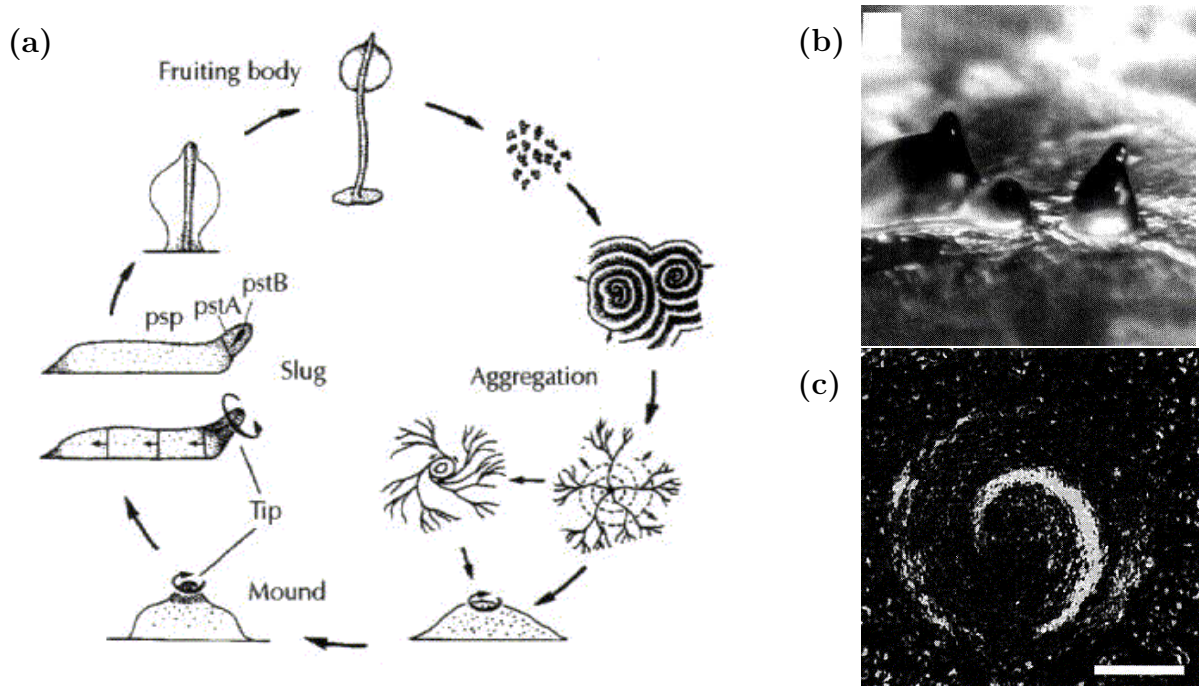


Figure 1.4: Multicellular patterns in *Dictyostelium* aggregation. (a), Life-cycle of the slime mould *Dictyostelium*. Under favorable environmental conditions (good availability of food), *Dictyostelium* exists as single amoebae. However, if food is lacking, the individual cells aggregate into a slug or further into a fruiting body. Aggregation of these multicellular objects is organized by the travelling (spiral) waves of the signalling molecule cAMP, resulting in waves of chemotactically moving cells. (b), Side view of three typical slug mounds. (c), Wave propagation of cells during mound formation; rotating spirals emerge. All three pictures have been taken from [35].

Thousands of individual cells aggregate, organized by rotating spiralling patterns of the signalling molecule cAMP. The cells chemotactically follow the cAMP signal, yielding waves of rotating cells. During mound formation, depicted in Fig. 1.4 (b) and (c), cells start to differentiate into two distinct types, prestalk and prespore cells (giving rise to the stalk resp. the spores in the fruiting body, see below). Interestingly, the organization of the mound has been found to also occur via spiralling cAMP waves, connected to waves of moving cells. The observed patterns, concentric ring waves or single- resp. multi-armed spirals, depend on the specific strain of *Dictyostelium* under investigation [35]. The slug is able to migrate and, upon encountering a better environment, it disintegrates again into individual amoebae. However, if no food-rich region is found, a fruiting body forms out of the slug. It consists of stalk cells, which die and form the “backbone” of the fruiting body. The latter carries spores, which are active cells protected by resistant cell walls. They can survive long, unfavorable environmental conditions and, upon improving environment, become new amoebae.

Aggregation of *Dictyostelium* is a social phenomenon: the individual cells cooperate, pro-

ducing the signalling molecule cAMP, to form a common, multicellular entity that is better designed to cope with starvation conditions than the solitary amoebae. Furthermore, during the formation of the fruiting body, the cells that die to build the stalk sacrifice themselves for the benefit of the survival of the colony. Only the spore cells can give rise to further offspring. In this context, similar to human social behavior, it is a nontrivial question how this high level of cooperation is maintained, and how the system protects itself from the invasion of “cheater” mutants. Indeed, imagine a mutation of *Dictyostelium* that refuses to form stalk. As such “cheater” cells would always be placed in the spores, they could more efficiently spread their genes, and thus overtake the population. However, in a colony of only cheaters, fruiting bodies could no longer form, resulting in a lower “fitness” of such colonies. Recent investigations have shown that a high genetic relatedness of *Dictyostelium* aggregates may play a key role in maintaining altruistic behavior [36]. Indeed, high genetic relatedness has been found in different fruiting bodies, and, in agreement with standard kin-selection theory introduced by Haldane and Hamilton [37, 38], represents a mechanism to segregate cooperative cells from “cheaters”. As cheater cells alone cannot form a social aggregate, they have a fitness disadvantage and are only rarely found. An open question is how the high genetic relatedness is achieved. While *Dictyostelium pupureum* preferably forms fruiting bodies with kin under laboratory conditions, this does not seem to be true for *Dictyostelium discoideum*. As a speculation, spatial segregation into clonal patches in its natural environment could be an alternative mechanism for achieving high genetic relatedness of the multicellular aggregates [36].

1.2 Ecosystems and species diversity

Ecosystems are formed by all living organisms coexisting in a certain area, as well as the physical properties of the environment. The enormous number of coexisting species found in the earth’s ecosystems constitutes a major challenge for a theoretical description. Indeed, in a simple model of two interacting species sharing the same resources, one should be fitter than the other, therefore outcompeting it and remaining the only survivor after some time. In theoretical biology, this argumentation is known as competitive exclusion principle, [39], Gause’s Law [40], or as the paradox of the plankton [41]. The latter term has become common as species coexistence seems most puzzling when considering different species of plankton, which apparently all live from a very small number of resources, namely sun light and minerals dissolved in water. Spatial segregation of different competing plankton species has been proposed as a mechanism to resolve the apparent paradox [42]. Similarly, in other contexts, formation of spatial patterns subject to the species’ dynamics has been widely investigated theoretically as a possible promoter of biodiversity. Experimental observations are much rarer, but seem to point in a similar direction [43, 44]. In Chapter 3 of this Thesis, inspired by laboratory experiments and in a specific setting, we theoretically investigate pattern formation and its influence on species coexistence. A more detailed introduction and review of theoretical and experimental results is provided there. Here, we continue

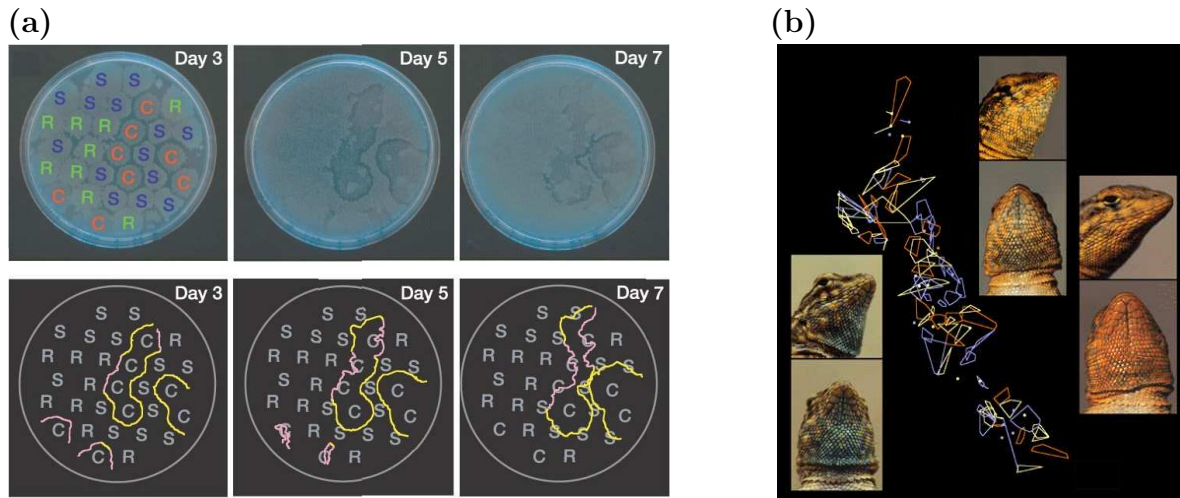


Figure 1.5: Laboratory and field patterns of ecosystems. **(a)**, Three strains of *E.coli* co-evolve on a Petri-dish by self-arranging into spatial patterns. The competition of the three strains is cyclic (of the rock-paper-scissors type, see text) and therefore non-equilibrium in nature. Consequently, the patterns are dynamic and change over time. The picture has been modified from [43]. **(b)**, Three types of mating strategies of lizards in California also display an example of the rock-paper-scissors dynamics. Blue-throated males (left), yellow-throated ones (middle) and orange-throated males (right) differ in the way they defend territories for mating, see text. Spatial patterns emerge where yellow-throated males tend to cluster around territories of orange-throated ones and smaller territories of blue-throated males coexist. A sketch of the wandering of different male lizards is shown in this picture, revealing the individual territories. The picture has been reproduced from [45].

with the presentation of three examples of observed patterns in natural ecosystems, the first one is particularly important for the studies in Chapter 3.

Three strains of *E.coli* that cyclically compete each other have been studied under laboratory conditions in Ref. [43]. Namely, the authors have considered the dynamics of a poison producing strain, a resistant strain and a sensitive one. They display a cyclic competition, similar to the childrens' game rock-paper-scissors: The poison producing strain kills the sensitive one, while the sensitive strain outgrows the resistant (resistance bears a certain cost), and the resistant bacteria grow faster than the poisonous ones (the latter are resistant *and* produce poison, which is yet an extra cost). When placed on a Petri-dish, all three strains coexist, arranging in time-dependent spatial clusters dominated by one strain. In Fig. 1.5, snapshots of these patterns monitored over several days are shown. Sharp boundaries between different domains emerge, and all three strains coevolve at comparable frequencies. The patterns are *dynamic*: Due to the nonequilibrium character of the species' cyclic interactions, clusters dominated by one bacterial strain cyclically invade each other, resulting in an endless hunt of the three species on the Petri-dish. The situation changes considerably when putting the bacteria in a flask with additional stirring.

Then, only the resistant strain survives, while the two other ones have been observed to die out after a certain transient time. These laboratory experiments thus provide intriguing experimental evidence for the importance of spatial patterns for the maintenance of biodiversity.

Similar rock-paper-scissors dynamics have been observed in lizard populations in the inner Coast Range of California [44]. Namely, males can follow three different mating strategies. The authors of this study have followed the territory use and patterns of these three strategies. Interestingly, these different types of mating behaviors are connected to throat-color polymorphisms, enabling a rather straight-forward identification of males following a certain strategy. Males with orange throats are very aggressive and defend large territories, while males with blue throats are less aggressive and guard smaller territories. “Sneaker” males, visually characterized by yellow stripes on their throats resembling females, do not defend territories. By evaluating the frequency of the three different strategies over several years, oscillations connected to cyclic dominance have been found. The field data presented in Ref. [44] prove that “sneaker” (yellow-throated) males can invade the very aggressive (orange-throated) ones, while those beat the less aggressive, blue-throated males. However, the latter, guarding only a smaller territory, successfully defend it against sneaker males. The whole dynamics is therefore described by the rock-paper-scissors game. All three mating strategies coexist in a stable manner, with certain oscillations in the frequencies. The interactions of the different male mating strategies inherently incorporate spatial patterns, namely the territories that orange-throated and blue-throated males defend. Field data show that the yellow, sneaker males tend to cluster around the territories of the aggressive, orange-throated ones, probably as they are more successful in invading those than the ones defended by the blue, less aggressive males. Analysis and theoretical description of these highly non-trivial spatio-temporal structures and in particular their influence on the stable coexistence of all three types of mating behavior constitute main challenges in future research.

Vegetation patterns may arise in ecosystems due to local interactions of plants. As an example, analysis of satellite images of the Kalahari vegetation has shown clustering of trees that is reminiscent of a self-organized critical state [46]. The authors of this study have looked at different places in the Kalahari Transect in southern Africa that differ in rainfall gradient and therefore in overall density of trees. Common to all areas is the homogeneous sand formation that underlies them. Spatial vegetation patterns therefore can not stem from inhomogeneities of the ground, but are inherently caused by plant interactions. At all locations, from high level of rainfall with a high tree density to places with low rainfall and sparse vegetation, trees have been found to form spatial cluster, see the satellite images in Fig. 1.6. Moreover, when plotting the number of tree clusters of certain size versus the cluster size, power laws emerge, indicating a critical behavior. This finding suggests these vegetation patterns to constitute examples of self-organized critical states, see [47] for a recent review on criticality in spatial ecosystems. Particularly puzzling in these observations is that the self-organized critical state occurs over a range

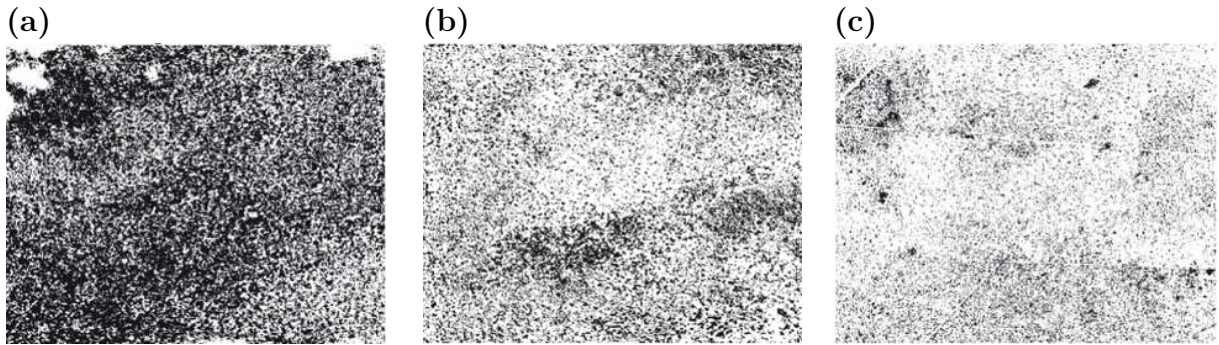


Figure 1.6: Vegetation clusters in the Kalahari. Satellite images from different places in the Kalahari Transect in southern Africa are shown, black dots indicate trees. **(a)** is taken at a location with high rainfall and a corresponding high tree density, while **(b)** corresponds to medium rainfall and **(c)** to low one, with only sparse vegetation. In all cases, trees tend to form clusters, and the distribution of these clusters obeys a power law, indicating a critical state, see text. Positive feedback of existing trees on the growth of nearby ones, mainly due to water keeping properties, seems to be the fundamental mechanism organizing the critical state. All pictures have been taken from [46].

of external conditions, namely at very different levels of rainfall. Positive feedback of trees on the growth of nearby ones seems to be the mechanism organizing the critical state [46]. The main driver of such positive influence is probably water availability: trees are capable of keeping water for a long time after rainfall, which constitutes a water source for trees growing nearby. Moreover, seed dispersal and nutrient availability is increased near existing trees, favoring new growth there. As pointed out by the authors of Ref. [46], this positive local feedback alone would probably either lead to deserts or fully grown forests. However, the (low) rainfall present in the Kalahari occurs, of course, globally, i.e. independent of the vegetation structure. Together with positive local feedback of trees, it can yield self-organized critical states, as has been shown in computer simulations [46].

Common to all these examples, ranging from subcellular patterns to large-scale ecosystems, is the apparent direct biological relevance for the functioning of the respective system. A qualitative and quantitative understanding of the basic principles underlying these structures is therefore of high interest and importance. However, despite a lot of progress in recent years, many basic issues remain unclear and require as well as allow for much future work on fundamental aspects of biological pattern formation. In our work, firstly, we have focussed on intracellular transport. The corresponding models as well as investigations and results are presented in the following Chapter 2. Secondly, the subsequent Chapter 3 contains considerations on the role of spatio-temporal pattern formation on maintaining biodiversity. Our investigations therein are motivated from the laboratory experiments on colicinogenic bacteria as have been introduced above.

2 Intracellular transport on parallel lanes

Active particle transport is a non-equilibrium phenomenon encountered within single cells [1, 48], information processing (spintronic) devices [49], or vehicular highway traffic [50, 51]. Often, such transport occurs on multiple parallel lanes resp. in the presence of internal states (such as spin states of an electron). In this Chapter, we study a generic model describing such scenarios. We are interested in collective phenomena arising from many interacting particles independent of the microscopic details of particles' active motion. We find collectively caused traffic jams which lead to one-dimensional patterns similar to the comet-like structures presented in Chapter 1, Fig. 1.1 (b). These effects can be rationalized using a suitable analytical approach.

In Sec. 2.1, we present an introduction to the origin and the mechanisms of biological transport within eukaryotic cells. A general account on theoretical model systems, aimed at a description of the emerging collective effects independent of the precise transport mechanisms, is provided in Sec. 2.2; there, the fundamental *totally asymmetric exclusion process* (TASEP) is also briefly reviewed. We then introduce a paradigmatic model for multi-lane traffic in Sec. 2.3 and explain its intimate relation to driven spin transport, Sec. 2.4. As generic behavior, the model exhibits a *spontaneous density separation* resp. a *spontaneous polarization*, which we explore in Sec. 2.5. There, we also describe the analytical approach, employing an, apparently exact, mean-field approximation in a mesoscopic limit of large systems. We conclude with a summary and an outlook. Our relevant articles present the phenomenology as well as analytical calculations in more detail. They have appeared in *Physical Review Letters* as well as the *New Journal of Physics* and are reprinted at the end of this Chapter, including a recently submitted manuscript.

2.1 Active intracellular transport performed by molecular motors

Eukaryotic cells typically range in size between $2\mu m$ and $100\mu m$, and thereby are about 10 - 1000 times bigger than prokaryotic ones. Within these large cell volumes, they possess a variety of internal components with specialized functions. For instance, the genetic code

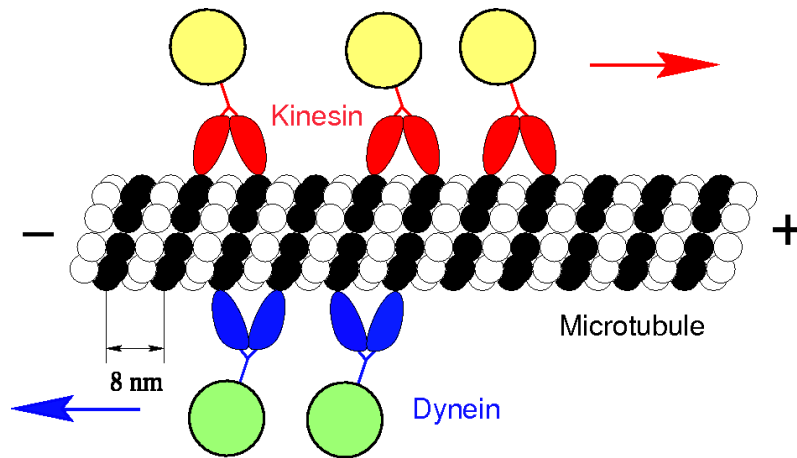


Figure 2.1: The mechanism of active intracellular transport. Molecular motors, for example kinesin and dynein, move unidirectionally along a microtubulus. A Brownian ratchet mechanism driven by ATP-hydrolysis underlies the directed “hand-over-hand” motion of the motor dimers, see text. The molecular motors carry cargo particles like macromolecules or vesicles, in this way providing efficient, directed transport. Kinesins usually move to the microtubulus’ (+) end (anterograde transport), while dyneins do the opposite (retrograde transport). The picture has been taken from Ref. [55].

(DNA) is contained in the nucleus, mitochondria produce energy, the endoplasmatic reticulum folds and expresses new proteins, chloroplasts in plant cells carry out photosynthesis, and the cytoskeleton composed of filaments such as microtubules organizes the interior structure as well as the overall shape of the cell. This high degree of intracellular specialization requires efficient mechanisms for transportation. For instance, newly expressed proteins must be delivered to their required destination, and minerals such as calcium and phosphate be brought from the cell’s boundary to the interior. For transportation, these molecules are wrapped by coats to form *vesicles*, i.e. easily handable cargo objects.

Transportation in cells is hindered by the dense packing of the cells’ interiors with biological macromolecules, a situation commonly referred to as molecular crowding [52, 53]. The high-volume occupation of the intracellular environment gives rise to large heterogeneities and therefore to anomalous transport properties such as subdiffusion [53, 54]. Namely, diffusing molecules or vesicles are often kept in local compartments formed by the surrounding macromolecules, and only occasionally “tunnel” to a neighboring compartment. This effect of hindering the diffusive motion is the more pronounced the larger the diffusing objects are. While small molecules such as gases and glucose are relatively unhindered, diffusion of large particles, such as macromolecules or vesicles, is considerably slowed down.

Due to the above described large size of eukaryotic cells as compared to prokaryotic ones, as well as the diffusion-limiting molecular crowding, random diffusion of large synthesized molecules or intracellular components like vesicles is not efficient enough as a transport

mechanism (while it usually suffices in prokaryotic cells). Nature has therefore invented *active transport mechanisms*. In the Introduction of this Thesis, we have already provided a first impression of their functioning. There, we have described how microtubules, being one-dimensional filaments inside the cells, serve as oriented tracks on which molecular motors walk, transporting cargo particles to their destination [48, 56]. Microtubules are hollow fibres, consisting of typically 13 parallel filaments. Composed of α - and β - subunits, they possess a polarity, usually denoted as the $(-)$ and the $(+)$ end. Molecular motors, such as kinesin and dynein, “walk” on these filaments, as illustrated in Fig. 2.1. They are dimers (molecule pairs) and in this way resemble a structure with two feet. “Walking” occurs through sequential movement of the motor domains (“feet”) to the front. Two basic mechanisms for this motion have been proposed. The first one is referred to as “hand over hand”, where at each step the last foot moves to the front, passing the other foot. The second possibility is the “inchworm” mechanism, where one foot always stays at the front, and the second one is trailed behind. Although there has been a long controversy about which of both mechanisms applies to motor proteins such as kinesin, recent experiments have given evidence for the first one [57]. The unidirectionality of the motion along the microtubules is enabled by a Brownian ratchet mechanism, see Ref. [58] for a recent review, and powered by adenosine triphosphate (ATP): at each motor’s step, one ATP molecule is hydrolyzed. More concretely, a foot decouples from the molecular track, randomly moves around and, upon being at a position in front of the other foot, rebinds to the microtubulus [59]. ATP hydrolysis changes the local conformation of the microtubulus and thereby provides the information for the foot where to reattach (namely in front of the other one). The precise mechanisms are still a matter of investigations, for example, recent results have shown a large influence of ATP concentration on the time the motor spends in one-head-bound resp. two-heads-bound configurations [60]. Independent of such details, what matters for our studies is solely the fact that the active movement of motor proteins transports attached cargos, for example large synthesized molecules or vesicles, to their destination in the cell. Concerning the direction of motor’s motion, kinesins usually walk towards the positive end of the microtubulus. This situation is called *anterograde transport*. Usually, this refers to motion (and transport) from the inner parts of the cell to the periphery. The other direction, to the $(-)$ end of the microtubule, is taken by dyneins, they perform *retrograde transport*.

Transport by molecular motors in axons provides an intriguing example of the necessity and efficiency of the above described transport mechanism. Axons are nerve fibers that conduct electrical impulses away from the neuron’s cell body, see Fig. 2.2. Their typical length can be several millimeters, or even longer. The longest axon in the human body runs from the base of the spindle to the big toes of the feet, which yields an overall length of about $1m$. On these *macroscopic* scales, efficient transport of organelles, such as mitochondria, or vesicles constitutes a considerable challenge. Indeed, as an example, the axon itself does not produce proteins and therefore is in constant need of proteins manufactured in the cell body and transported to the axon. In this situation, molecular motors as described above serve as reliable engines for fast axonal flow. As depicted in

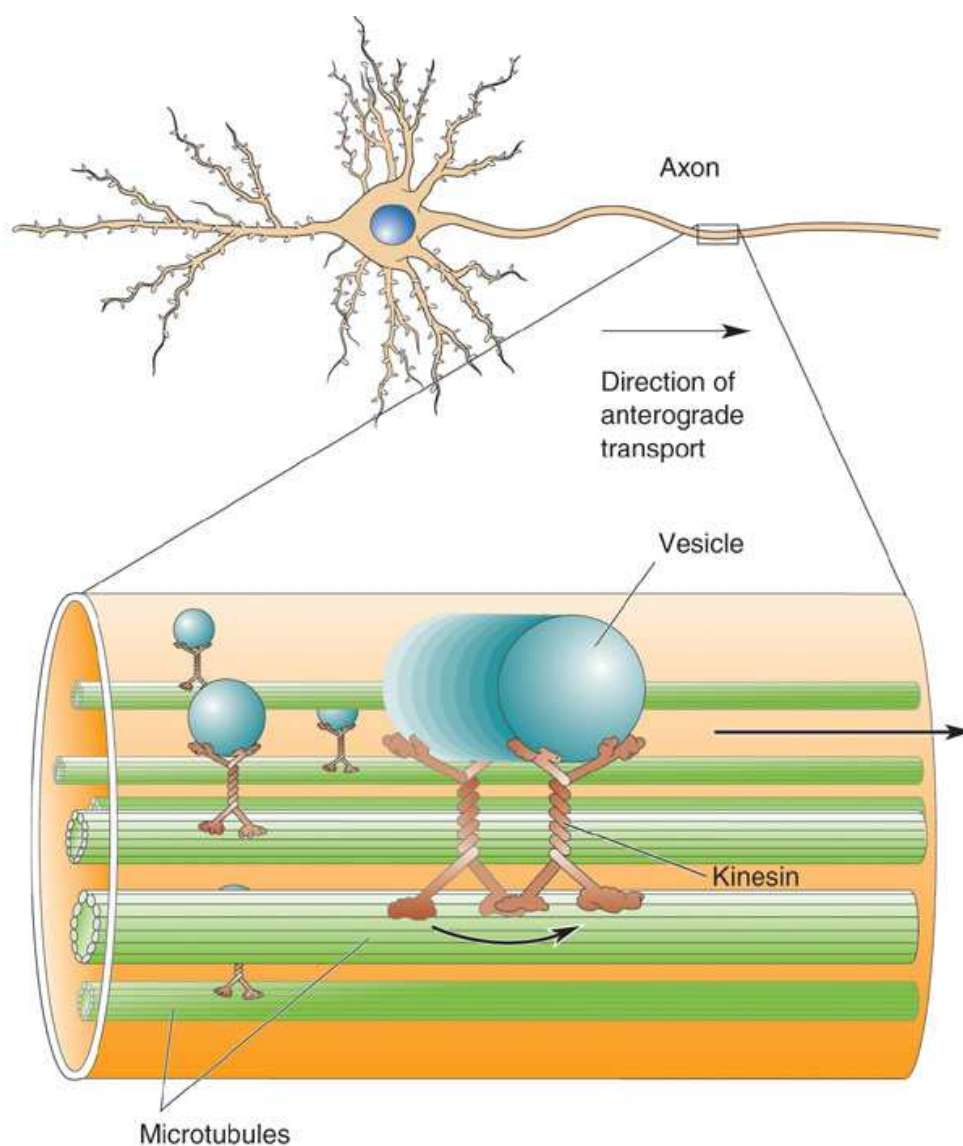


Figure 2.2: Axonal transport. Nerve cells possess fibers, the axons, that connect the cell body to other locations of the organism. Their lengths are macroscopic, ranging from millimeters up to as much as 1 meter. Molecular motors moving on microtubule tracks serve as efficient transport engines that, for example, provide the axon with proteins which are produced in the cell body. In the picture, kinesin, carrying a vesicle and walking along one out of many parallel microtubules is depicted. It moves to the positive end of the microtubulus, therefore providing axonal transport away from the cell body. The other direction, retrograde transport, also occurs and is typically performed by dynein. The picture has been taken from [61].

Fig. 2.2, many parallel microtubule cables extend along the axon. On them, motor proteins carrying cargo particles perform active transport. Concerning the speed, one differentiates *fast* axonal transport of vesicular cargos, at a velocity of about 50-400 *mm/day*, and *slow* axonal transport (of proteins). The latter operates at a speed of some millimeter per day, due to “stop-and go” effects [62, 63].

2.2 Collective phenomena and theoretical model systems

Interaction of a large number of molecular motors encountered on microtubules, as described above, can give rise to collective phenomena. As an example, in the axonal transport described at the end of the previous section, a large number of motor proteins has been found to move along the molecular filaments in a highly coordinated fashion [62, 63]. The easiest motor interaction one can imagine that could reproduce such behavior is *simple on-site exclusion*. This means that the molecular motors block each other when moving along the track: one motor cannot be overtaken by another one. Another example where such interaction is relevant is the translation of mRNA into the production of proteins. In this process, a ribosome moves unidirectionally along the mRNA and, with help of tRNA, synthesizes proteins [1]. A large number of ribosomes simultaneously operating on the same mRNA could give rise to traffic effects such as jams, as the ribosomes cannot overtake each other. Additional interactions of ribosomes or heterogeneities of the mRNA (“slow codons”) yield complex traffic scenarios [64, 65].

From the perspective of statistical physics, these systems are highly interesting due to their *nonequilibrium nature*. Indeed, the unidirectional motion of motor proteins along microtubules as well as ribosomes on mRNA implies that these systems operate far from thermal equilibrium. Detailed balance is broken, as particles only move forward, not backward. A constant flow of particles consequently characterizes these systems, which even in a possible steady state does not vanish. The development of generally applicable methods for the characterization of such nonequilibrium systems constitutes one of the main challenges of contemporary statistical physics. In contrast to equilibrium physics, where for example the Boltzmann-Gibbs ensemble provides a general concept, such universal approaches are still lacking. While it seems unclear whether they may be developed in future work or simply do not exist, at least not in such a comprehensive form as in the equilibrium situation, important branches of nowadays research aim at the investigations of specific simple models. In this respect, *driven diffusive systems* [66], as constituted by the above biological examples and reviewed in more detail below, form an especially interesting class of nonequilibrium behavior.

Pioneering work on theoretical models describing collective effects has been performed by C.T. MacDonald in 1968 [67]. Inspired by the physics of mRNA translation into proteins, as sketched above, he invented a simple model system, the *Totally Asymmetric Exclusion*

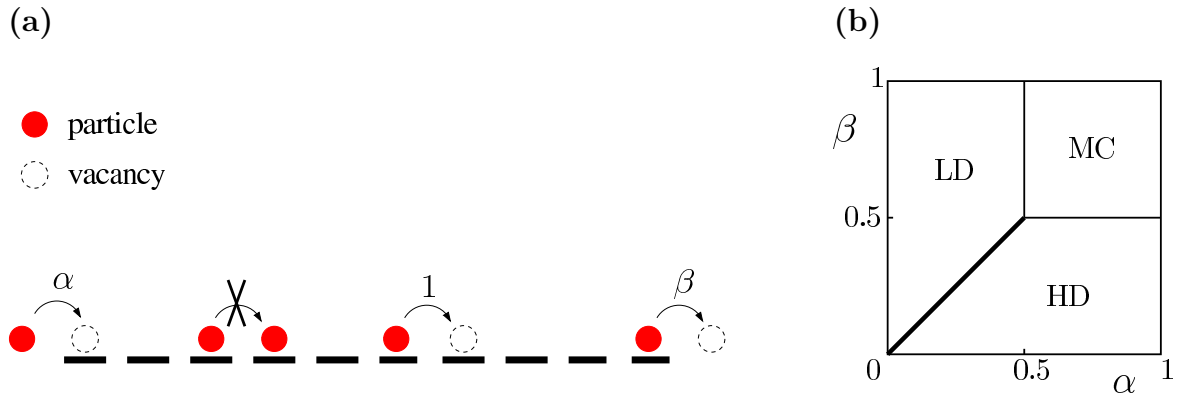


Figure 2.3: The totally asymmetric exclusion process (TASEP). **(a)**, Illustration of the non-equilibrium stochastic dynamics. On a one-dimensional lattice, particles move unidirectionally to the right, if the neighboring site is empty. Particles interact via on-site exclusion. Here, we show a TASEP with open boundaries. At the left, particles enter the lattice at rate α , and leave at the right boundary at an exit rate β . In bulk, the hopping rate is usually set to unity, fixing the timescale. **(b)**, State diagram of the TASEP. Depending on the entering and exiting rates, α and β , the system is either determined by the left boundary (low-density phase, LD), by the right boundary (high-density, HD), or by the bulk dynamics (maximal current phase, MC). Which of the three cases applies depends on whether entering, exiting or bulk process dominantly limit the particle current, see text. Continuous (thin lines) as well as discontinuous (bold line) transitions occur. These boundary-induced state transitions of the TASEP are a characteristic signature of its non-equilibrium behavior.

Process (TASEP). Since its proposition and first investigation in the 1960's, this model has turned into a paradigm for phase transitions and critical behavior far from equilibrium. A large amount of later work on driven diffusive systems has built on this model, and also the studies presented in this chapter may be viewed as a certain generalization. In the following, we therefore present a didactic introduction to the TASEP and its behavior.

Consider a one-dimensional lattice with open boundaries as depicted in Fig. 2.3 (a). Particles enter on the left side, at a given rate α . Within the lattice, they attempt to hop forward (to the neighboring site at the right) at an intrinsic rate which is usually set to unity, fixing the timescale. Hopping is only allowed under the constraint of site exclusion, each site may at most be occupied by one particle. Having reached the rightmost site of the lattice, particles leave it at another rate β . All these events are Poisson processes, occurring stochastically and being completely characterized by the intrinsic rate. Such stochastic dynamics underlies diverse situations, from ribosomes moving along mRNA to molecular motors “walking” along molecular tracks. In all these cases, motion of particles is characterized by unidirectionality (yielding non-equilibrium behavior), discrete steps, and intrinsic stochasticity. Although the precise mechanisms of such type of movement are extremely involved and largely differ from case to case, the above described TASEP dynamics captures non-trivial basic features and therefore represents a fundamental model univer-

sally describing driven diffusive systems. Its insightful non-equilibrium behavior, described in the following, possesses a broad range of applicability. Moreover, due to the existence of exact methods for its treatment, it constitutes a paradigmatic system for the investigation as well as the development of theoretical methods in the theory of non-equilibrium systems.

The TASEP evolves to a non-equilibrium steady state, characterized by a constant, non-vanishing flow of particles. The latter depends sensitively on the boundary conditions, meaning the entrance rate α as well as the exiting rate β . The latter feature stems from its nonequilibrium character; on the contrary, equilibrium systems are dominated by bulk effects and boundaries do not influence equilibrium states. In the TASEP, the particle current, and thereby the system's behavior, is either determined by the entrance processes, the flow in bulk, or the exit. Each of these puts limits to the possible current, and the lowest one determines the ensuing steady state.

Interestingly, a simple mean-field approach already yields the correct behavior of the system. Let ρ be the average density of particles at a given site in bulk. In principle, it could depend on the position in bulk. However, essentially due to particle conservation in bulk, it turns out that, apart from boundary effects, a spatially homogeneous density emerges. The latter gives rise to a particle current j , which is connected to the density ρ as follows. In a mean-field approach, correlations in the occupation numbers of neighboring sites are neglected. Then, the hopping probability from one site to a neighboring one is given by the probability that the left one is occupied and the other one is empty. Therefore,

$$j = \rho(1 - \rho), \quad (2.1)$$

is the mean-field current-density relation. Despite the simplicity of the above argumentation, exact methods such as recursion relations [68], a matrix formulation [69] or the Bethe ansatz [70, 71] have revealed the accuracy of this fundamental relation (within the continuum limit of a large number of lattice sites).

The current density-relation, Eq. (2.1), predicts a maximal current $j = 1/4$ emerging at a medium bulk density of $\rho = 1/2$. Indeed, low densities induce low currents due to the rare occurrence of particles which, on the other hand, can move relatively unhindered. At high densities, many particles are available, however, site exclusion induces large obstruction effects, and the current is also low. At medium densities, particle hindrance is moderate, as well as particle availability, and the current adopts its maximal value. The latter constitutes the limit that the bulk dynamics imposes on the current: Even if the boundary conditions would allow for larger flux, these would be reduced to the bulk's carrying capacity of $j = 1/4$.

The limitations on the particle current posed by the boundaries may also be evaluated in a mean-field manner. At the first site, a particle enters at a probability α , provided the site is empty, which occurs at a frequency of $1 - \rho$. Therefore, the current which could result from the left boundary condition reads $\alpha(1 - \rho)$. In the same way, the right boundary restricts the current to a maximal value of $(1 - \beta)\rho$. Now, given these expressions for the current at the boundaries as well as in bulk, one can read off the system's state diagram, depending on

the entering and exiting rates α and β . The latter is depicted in Fig. 2.3 (b). For entrance and exit rate both exceeding the value $1/2$, the system is limited by the bulk dynamics, and the maximal current emerges. This phase, arising for $\alpha, \beta \geq 1/2$, is therefore commonly referred to as *maximal current phase* (MC). In the other cases, one of the boundaries, namely the one with the lower rate, determine the system's state, as it poses the limiting restriction to the current. An entrance rate lower than the exit rate, $\alpha < \beta$, leads to a low density of particles, corresponding to the value of the entering rate: in bulk, $\rho = \alpha$. This *low density phase* (LD) contrasts with the *high density phase* (HD), which arises in the opposite case, namely when $\alpha > \beta$. In this situation, the right boundary limits the particle current, as only few particles can leave the track. A “traffic jam”, meaning a high particle density, arises, with a value determined by the exiting rate, $\rho = 1 - \beta$. The resulting state diagram is shown in Fig. 2.3 (b). Although the rates α and β can be arbitrarily large, the system's behavior does not depend on their precise value if they are larger than one. In the latter situation, the system would essentially behave as for a rate of value 1. The phase transitions arise in the continuum limit of large system sizes. Only then, the different phases become sharp; for finite systems, boundary layers and domain walls blur the transitions. Continuous as well as discontinuous transitions arise. The discontinuous one, separating the LD from the HD phase, is connected to the appearance of *delocalized domain walls*. Namely, a domain wall forms, spatially separating a low-density from a high-density region. Its position is not fixed but performs a random walk. As already mentioned above, the emergence of such boundary-induced phase transitions in driven diffusive systems like the TASEP, first pointed out in Ref. [72], is a manifestation of non-equilibrium behavior, and very different from what one encounters in equilibrium statistical mechanics.

Generally, the phenomenology of non-equilibrium processes is much richer than the one of equilibrium systems. In addition to the boundary induced phase transitions described above, driven diffusive systems obey a variety of unexpected, non-equilibrium phenomena. Among these are spontaneous symmetry breaking [73, 74], the emergence of phase separation accompanied by localized and delocalized domain walls [15, 75, 16], complex nucleation processes [76, 77], and density separation connected to the emergence of multicritical points in the state diagram [18, 19, 78]. The latter, arising in exclusion processes with internal states (corresponding, for example, to multiple parallel lanes), has been found and studied as part of this Thesis. In the following, we present an introduction into the models' definition as well as its main phenomenology. More elaborate investigations, theoretical methods and discussions have been published in *Physical Review Letters* and the *New Journal of Physics*. These articles are reprinted at the end of this Chapter.

2.3 Driven transport on multiple parallel lanes

Microtubules, the molecular tracks for motor proteins in intracellular transport, consist of typically 13 parallel filaments, which may be viewed as separate lanes. Experimentally,

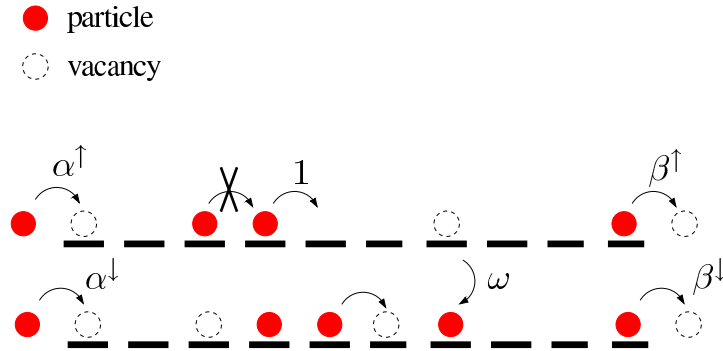


Figure 2.4: Driven transport on two parallel lanes. Particles enter the upper (lower) lane at rate α^\uparrow (α^\downarrow), and leave at the right at rates β^\uparrow (β^\downarrow). In bulk, they hop to the right (at unit rate) or change lanes at a low rate ω . All processes are constrained by hard-core on-site exclusion. The lanes’ weak coupling, stemming from the low lane change rate, induces involved behavior of the system’s non-equilibrium stationary state, see text.

molecular motors moving on them have been found to stay on one lane. However, the statistics of possible rare deviations, meaning occasional lane changes, is not known. Due to the intrinsic stochasticity of the motor’s steps as well as fluctuations in the cellular environment, it seems natural to assume the occurrence of rare “missteps”, where the motor, while stepping forward, also changes its lane. While experiments to investigate the abundance of such missteps seem too challenging to be undertaken nowadays, the implications for intracellular transport along microtubules are of genuine interest.

In this Thesis, we develop a paradigmatic model for driven transport on multiple parallel lanes. In the remainder of this Section, we introduce its dynamics, present unexpected effects arising from a small probability of particle lane changes, and discuss the system’s behavior in general terms.

Transport on multiple parallel lanes does not only occur within cells. Highway traffic [50, 51] often runs on several tracks, with vehicles moving parallel or antiparallel. The formation of traffic jams is crucially influenced by the different possible geometries of the underlying track [79]. Of course, in realistic models for highway traffic, several additional factors play important roles, such as different velocities of vehicles [80] or the existence of bottlenecks for the traffic flow [81, 82]. In our work, we ignore such additional complications and focus solely on the effects of multiple lanes with a (small) rate at which particles change between the lanes. Incorporating bottleneck effects or the existence of slow and fast moving particles represents an interesting issue and could motivate further studies.

The system’s dynamics, a driven exclusion process on parallel tracks, is depicted in Fig. 2.4. For simplicity, we consider two parallel lanes, each consisting of a large number of discrete lattice sites. The dynamics may be seen as a multiple-track generalization of the TASEP which has been introduced above. Particles enter the upper (lower) lane at rates α^\uparrow resp.

α^\downarrow , if the corresponding first site is empty. In bulk, they hop one site to the right, provided the neighboring site is unoccupied. The rates for these processes are set to one, and thereby fix the timescale. At a certain (low) rate ω , particles may change the lane, meaning they jump to the neighboring site on the other track if exclusion allows for it. Below, we explain the meaning of a “low” rate for this process. Exiting occurs at the right-most lattice site, at rates β^\uparrow (β^\downarrow) on the upper resp. the lower lane. As in the TASEP, all processes are only allowed under the constraint of hard core on-site exclusion, which represents the only interaction of the particles. The two lanes are *weakly coupled* due to the lane change processes occurring at the low rate ω . In the following, we show how this weak coupling gives rise to a number of intriguing effects. Note that, in contrast to weak coupling, a vanishing lane change rate results in two uncoupled TASEPs, while a very high rate, meaning a *strong coupling*, induces behavior that is qualitatively the one of a one-lane TASEP [83]. The scenario of weak coupling is therefore the most interesting one. Moreover, it seems most relevant in intracellular transport where motors probably switch between different lanes on a microtubulus only very rarely.

Previous work on multiple lane exclusion processes has focussed on different regimes or types of interactions than the one introduced above. One branch of studies has dealt with indirect coupling of two lanes, see e.g. Refs. [74, 84]. There, the hopping rate of a particle in bulk depends on the occupation of the neighboring sites of the other lane. As an example, particles on adjacent sites on the two lanes can obstruct each other. Such effects are known from vehicular traffic [50, 51] and also plausible in the context of intracellular transport. There, molecular motors carrying large cargo particles are likely to obstruct each other when moving close to each other on parallel lanes. Recently, together with Anna Melbinger, Thomas Franosch and Erwin Frey, we have started to investigate the consequences of such obstruction on the transport properties [85, 86]. Here, we disregard such interactions and solely focus on direct coupling due to particles changing between the lanes. Such models have recently been investigated in the situation of large lane change rates [83, 87, 88]. Qualitatively behaving as a one-lane TASEP, on a quantitative level, deviations occur which can be treated by calculating correlations between the channels. Asymmetric lane change rates induce novel effects, and domain walls occur that perform coupled random walks. The situation of low, but non-vanishing lane change rate has first been considered by ourselves. The relevant articles have appeared in *Physical Review Letters* and the *New Journal of Physics*; they are reprinted at the end of this Chapter. Recently, a study of particles moving in opposite directions on two weakly coupled lanes has been published [89].

2.4 Connection to classical non-equilibrium spin transport

Transport on two parallel lanes, as introduced above, possesses an intimate relation to classical, non-equilibrium spin transport. Indeed, the different lanes introduced above and

illustrated in Fig. 2.4 can, more generally, be viewed as “internal states” that the particles possess. In this interpretation, shown schematically in Fig. 2.5 (a), particles move on only one lane, but now possess an internal state. In this more general terminology, the property to reside on the upper lane (resp. the lower lane) translates into an internal state being “up” resp. “down”. The previous particle interaction in form of hard-core on-site exclusion now becomes Pauli’s exclusion principle: Two particles may occupy the same lattice site, if and only if they differ in their internal state. Upon viewing the internal states as actual spin states, a classical transport model for particles possessing spin results. Such a model may, for example, describe hopping transport of electrons through a chain of quantum dots.

Concerning experimental realizations of such a model, currently, state-of-the-art experiments involve double or triple quantum dots [90, 91]. Realizations of chains with a large number of coupled quantum dots could be challenging future projects. From the theoretical perspective, transport through a few coupled quantum dots already poses major challenges [92], mostly stemming from quantum phenomena such as phase coherence. The latter can, for example, give rise to the celebrated Kondo effect [93]. In this respect, the consideration of a classical spin transport model, as proposed above, constitutes a promising approach for the (qualitative) investigation of traffic effects in a large number of coupled quantum dots. A theoretical investigation of such a situation might be impossible if quantum effects were taken into account.

Spintronic devices aim to exploit the spin of electrons for information processing and transfer. A famous discovery in this field, the giant magnetoresistance found by Peter Grünberg [94] and Albert Fert [95], has been rewarded the Nobel prize in 2007. There, the flow of electrical current through thin alternating ferromagnetic and nonmagnetic metal layers is controlled by an applied magnetic field, which interacts with the electrons’ spins. Discovered in the late 1980’s, nowadays, it is commonly used in hard disk drives of computers, and constitutes a fascinating application of spintronics. The Datta-Das spin field-effect transistor, depicted in Fig. 2.5 (b) is another example of such devices, and related to the spin transport model described above. At the source, electrons at a prescribed spin state enter an essentially one-dimensional channel. Along this gate, a magnetic field can be applied, resulting in spin precession of the electrons. At the drain, electrons may be extracted depending on their spin state. Varying the magnetic field, the electrons’ spin at the drain and therefore the number of electrons leaving the drain, the current, can be controlled. This system possesses close similarities to the transport model shown in Fig. 2.5 (a), where also in-and outgoing particle currents are controlled by the entering and exiting rates as well as the spin flip rate in bulk (corresponding to spin precession caused by an external magnetic field). As a major probable difference, hard-core exclusion governs the behavior of the spin transport model in Fig. 2.5 (a), while it is an unresolved issue whether this type of particle interactions matters in the Datta-Das spin field-effect transistor.

Hard-core exclusion is a simplifying assumption for the much more involved interaction of electrons. More realistically, the latter repulse each other by electrostatic forces. Such

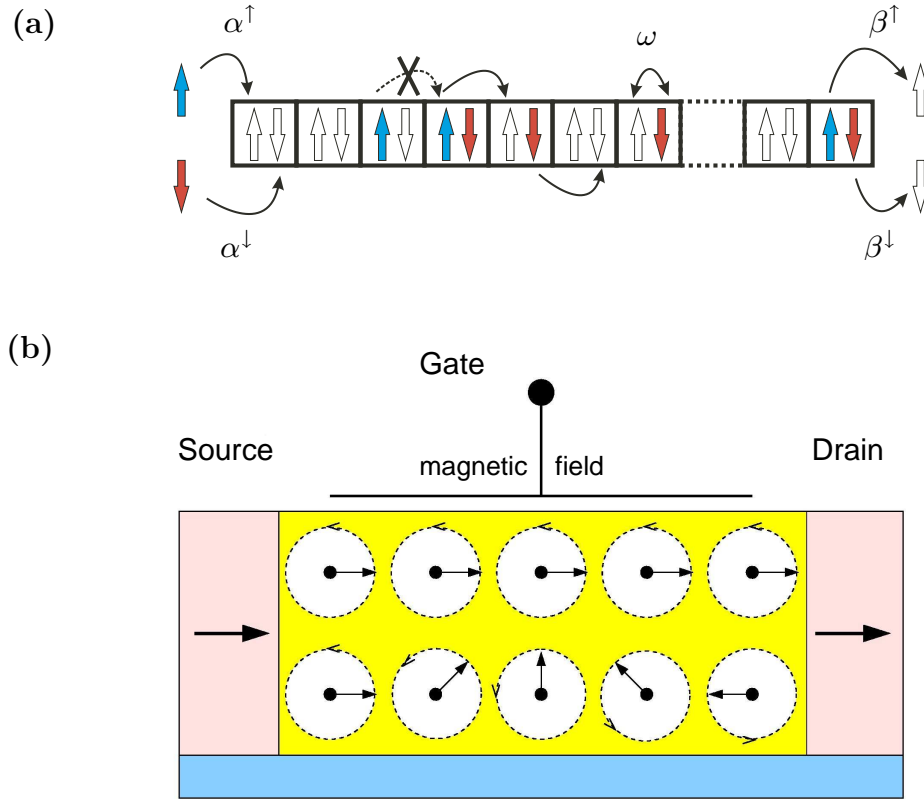


Figure 2.5: Spin transport. **(a)**, A model for classical non-equilibrium spin transport. This model is the same as the one for transport on two parallel lanes as depicted in Fig. 2.4; the two lanes now translate into two distinct spin states, see text. Particles with spin-up (spin-down) enter at the left at rates α^\uparrow (α^\downarrow). In bulk, they move unidirectionally to the right or flip their spin at a small rate ω , always respecting Pauli's exclusion principle. They leave the system at the right at rates β^\uparrow resp. β^\downarrow . The picture has been reproduced from [19]. **(b)**, The Datta-Das spin-field effect transistor possesses similarities to this model. There, electrons at a certain spin state enter at the left, the source, and move through the system. A magnetic field controls spin precession and thereby the spin state which electrons possess when arriving at the drain. Depending on this spin state, they may be extracted, giving rise to a drain current. The picture has been modified from [49].

Coulomb interactions has not been taken into account in the simple model presented above and depicted in Fig. 2.5 (a). It implies that, for example, two electrons with different spins can occupy the same lattice site, but with a lower probability than single occupation, due to electrostatic repulsion. Interestingly, when considering the two-lane interpretation of the model, see Fig. 2.4, such repulsion translates into obstruction of particles that occupy neighboring places on different lanes. Above, we have described that such interaction is to be expected in intracellular transport as well as vehicular traffic. Consequently, a model incorporating electrostatic repulsion (in the spin transport interpretation) resp. particle obstruction (in the two-lane picture) considers an additional aspect that is meaningful and important within both interpretations. Together with Anna Melbinger, Thomas Franosch and Erwin Frey we have developed and investigated such a model [85, 86]. The latter may be viewed as a non-equilibrium, classical version of the Hubbard model (see Ref. [96] for a recent introduction). Our studies have revealed a complex, highly non-trivial influence of electrostatic repulsion when the latter adopts medium values. In contrast, low and high values of repulsion render the system describable in terms of standard exclusion processes.

2.5 Spontaneous density separation and polarization

Traffic on multiple parallel lanes with low inter-lane particle hopping, as illustrated in Fig. 2.4, yields insightful collective phenomena. Among the most important one is a spontaneous density separation between the two lanes, arising at some spatial position which can be tuned by varying the entering and exiting rates, $\alpha^{\uparrow,\downarrow}$ and $\beta^{\uparrow,\downarrow}$. This spontaneous density separation is mediated by a domain wall, separating a low-density (LD) from a high-density (HD) region, which emerges at some specific position on one lane, c.f. Fig. 2.6. In the spin transport interpretation, see Fig. 2.5, this density separation translates into a spontaneous polarization.

In Refs. [18, 19, 78] we have investigated this phenomenon as well as others in much detail; these articles are reprinted at the end of this Chapter. In this section, we want to describe the spontaneous density separation and present the main theoretical concepts as well as implications.

Weak coupling of the two lanes, via a low inter-lane hopping rate, arises within a proper *mesoscopic limit*. Such a scaling has already successfully been employed when studying intracellular transport with motor attachment/detachment [15, 16]. We consider the asymptotic limit of a large number L of lattice sites on each lane, and scale the lane-change rate ω according to $\omega = \Omega/L$ with a fixed *global lane-change rate* Ω . Consequently, in the asymptotic limit $L \rightarrow \infty$, the local lane-change rate ω approaches zero, $\omega \rightarrow 0$. This mesoscopic limit describes the situation where the particles traversing the system change between the lanes only a few times (if at all) in total. Such a scenario is to be expected for the motion of motor proteins along microtubules: Typically, they stay on one lane,

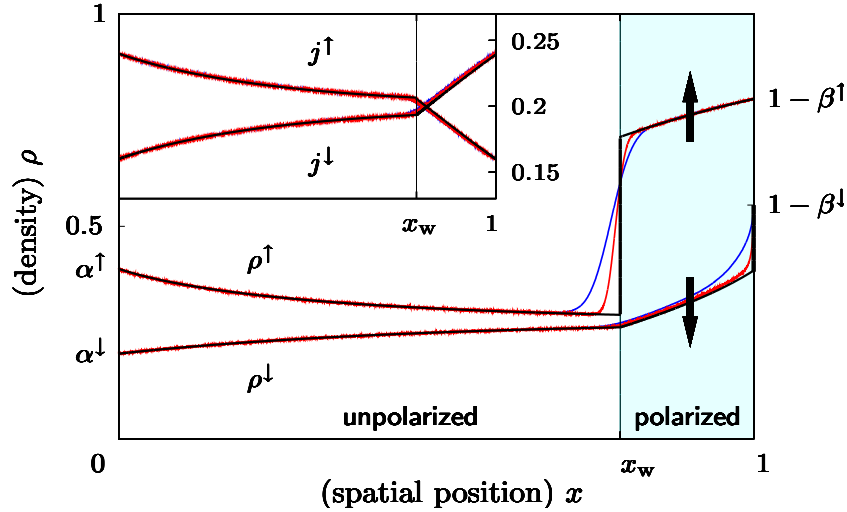


Figure 2.6: Spontaneous density separation resp. polarization. The spatial density profiles in the steady state for typical parameter values ($\alpha^\uparrow = 0.4, \alpha^\downarrow = 0.2, \beta^\uparrow = 0.2, \beta^\downarrow = 0.45$, and $\Omega = 0.5$) are shown. While the density on the lower lane resides at low values along the whole track (up to a boundary layer at the right), a discontinuity appears along the upper lane: a domain wall arises at a position x_w and separates a low-density region (LD) from a high-density (HD) one. This may be viewed as a spontaneous density separation (resp. a spontaneous polarization phenomenon when considering the spin-transport interpretation of the model), see text. The density's discontinuity at the position of the domain wall emerges in the mesoscopic limit of large system sizes, $L \rightarrow \infty$. We show simulation results from $L = 2000$ (blue) and $L = 10000$ sites (red), together with analytical curves (in black). The theoretical estimates are excellently reproduced by the stochastic simulations; the only deviations occur near the density discontinuities, and decrease for increasing system size. The picture has been reproduced from [18].

and lane switches seem to be extremely rare. Considering spin transport, the global rate Ω describes the total number of spin flips that an electron undergoes while traversing the system. As an example, regarding the Datta-Das spin field-effect transistor (see 2.5 (b)), such a global spin-flip rate stems from an external magnetic field and can be controlled by tuning the latter. Again, the assumption of a finite global spin-flip rate Ω (with an associated small local spin-flip rate ω) is meaningful.

The mesoscopic scaling of the lane-change rate ω , introduced above, induces spatially varying density profiles in the emerging non-equilibrium steady state. To see this, as well as for an analytical description, we use a mean-field approach as has already been proven useful in the analysis of TASEP, see Sec. 2.2. Let $\rho_i^{\uparrow(\downarrow)}$ denote the average density of particles on the upper (resp. the lower) lane. Its time evolution depends on the configuration of the neighboring lattice sites. As an example, the particle number of site i decreases at rate 1 if site i is occupied and site $i + 1$ empty, as then the particle may hop one step forward, leaving site i empty. In a mean-field approach, we neglect correlations between the occupation numbers of neighboring sites. For example, in this approximation, the probability that site

i is occupied and site $i + 1$ empty (both on the upper lane) simply reads $\rho_i^\uparrow(1 - \rho_{i+1}^\uparrow)$. This approach allows to write down self-consistent differential equations for the time-evolution of the densities $\rho^{\uparrow(\downarrow)}$, they are detailed in Ref. [19]. As an additional simplification, in the mesoscopic limit, we approximate the discrete values $\rho_i^\uparrow, \rho_i^\downarrow$ by continuous functions (continuous in the spatial position). Namely, setting the total length of the lattice to unity, the left boundary corresponds to a spatial position $x = 0$, and the right one to $x = 1$, while an intermediate lattice site i is located at $x = i/L$. Expansion in the lattice constant $1/L$ to first order yields partial differential equations for the densities' time-evolution, see Ref. [19], they read:

$$\begin{aligned} L\partial_t\rho^\uparrow(x,t) &= \partial_x \left\{ \rho^\uparrow(x,t) [1 - \rho^\uparrow(x,t)] \right\} + \Omega [\rho^\downarrow(x,t) - \rho^\uparrow(x,t)] , \\ L\partial_t\rho^\downarrow(x,t) &= \partial_x \left\{ \rho^\downarrow(x,t) [1 - \rho^\downarrow(x,t)] \right\} + \Omega [\rho^\uparrow(x,t) - \rho^\downarrow(x,t)] . \end{aligned} \quad (2.2)$$

The terms in the curly brackets denote the particle currents along one lane at location x :

$$\begin{aligned} j^\uparrow &= \rho^\uparrow[1 - \rho^\uparrow] , \\ j^\downarrow &= \rho^\downarrow[1 - \rho^\downarrow] . \end{aligned} \quad (2.3)$$

We have already encountered them in the TASEP, see Sec. 2.2. Lane-change events produce inter-lane currents, proportional to Ω :

$$\begin{aligned} j^{\uparrow\downarrow} &= \Omega\rho^\uparrow[1 - \rho^\downarrow] , \\ j^{\downarrow\uparrow} &= \Omega\rho^\downarrow[1 - \rho^\uparrow] . \end{aligned} \quad (2.4)$$

Their difference results in density changes, and is given by the second terms on the right-hand side of Eqs. (2.2). Altogether, these currents yield the time-evolution of the densities, as given by Eqs. (2.2).

In the stationary state, the left-hand side of Eqs. (2.2) vanishes, leaving one with ordinary differential equations for the spatial density variations. The latter may be solved, as described in Ref. [19]. To match the emerging solutions to the systems' behavior, we need boundary conditions for the Eqs. (2.2). They stem from entering and exiting processes, see Ref. [19] and yield, in principal, four boundary conditions. However, note that Eqs. (2.2) constitute two first-order differential equations, which are overdetermined by four boundary conditions. This overdeterminedness gives rise to density profiles that, at some spatial position, rapidly change from low to high values. At these distinct spatial positions, the density profiles are determined by higher orders in the lattice constant (while only the first order has been taken into account in Eqs. (2.2)). In the asymptotic limit of large system sizes, $L \rightarrow \infty$, they turn into *discontinuities*. If such a rapid spatial density change (giving rise to a discontinuity) occurs in bulk, we refer to the latter as a *domain wall*. In contrast, a sudden spatial density change at the boundary is usually called a *boundary layer*.

The appearance of these density discontinuities, domain walls and boundary layers, depends on the entering/exiting rates as well as the lane-change rate in an involved way. In

Ref. [19], we completely analyze this interplay, and provide phase diagrams for the system's behavior. Here, we want to exemplify a typical state of the system, which corresponds to a *spontaneous density separation or polarization*.

Exemplary density profiles emerging in the system's steady state are shown in Fig. 2.6. In the vicinity of the left boundary, both the density on the upper as well as on the lower lane are low, at comparable values. With increasing spatial position, due to lane changes, they approach each other. However, at a sharp position x_w , the density on the upper lane jumps to a large value, a domain wall forms in this density profile. Note that the particle currents on both lanes are continuous at this position, which is shown in the inset of Fig. 2.6. The latter stems from particle conservation in bulk and the only weak coupling of the two lanes. For positions to the right of the domain wall, a high density on the upper lane opposes a low density on the lower lane. One may view this phenomenon as a spontaneous density separation emerging at the position x_w of the domain wall. Considering the spin-transport interpretation, it corresponds to a polarization spontaneously arising at x_w . Namely, to the left of the domain wall position, both spin states have comparable densities, corresponding to low (or vanishing) polarization. To the right, the density difference jumps to a high value, such that the system is polarized in that region. Regarding solely the density on the lower lane, it remains in a low-density (LD) phase along the whole track, with a boundary layer emerging at the right. The density on the upper lane exhibits a low-density region (LD) coexisting with a high-density one (HD), separated by the localized domain wall. *Phase coexistence* emerges on this lane, similarly to the one observed in models for intracellular transport with attachment and detachment, see Refs. [15, 16]. In fact, there is an intimate relation between both models: in the present case, the possible lane changes of particles play a similar role as the bulk on/off-kinetics in the studies published in Refs. [15, 16].

The analytical results, derived in the mesoscopic limit from the solution of Eqs. (2.2) in the stationary state, agree perfectly with simulation results if system sizes are large, see Fig. 2.6. We attribute this apparent exactness to the absence of steady-state correlations, such that the mean-field approach yields exact results. Indeed, in Sec. 2.2 we have outlined how already in the TASEP, comparison of the mean-field approach to exact results has revealed the missing of spatial correlations. In the present two-lane (or two-state) model, the local coupling of the two lanes stemming from exchanges is only weak, and tends to zero in the mesoscopic limit. It therefore seems plausible that this additional coupling does not lead to correlations: possible correlations caused by lane changes are “washed out” by the large number of subsequent forward-hopping events. The apparent exactness of our analytical approach therefore stems from the lack of correlations in the steady state of the TASEP and the weak coupling of the two lanes.

The position and emergence of the domain wall can be controlled by the entering and exiting rates, $\alpha^{\uparrow,\downarrow}$ and $\beta^{\uparrow,\downarrow}$, as well as the global lane-change rate Ω . The analysis of this high-dimensional phase space is simplified by symmetries. Namely, as is also the case for the TASEP, the system obeys a *particle-hole symmetry*. Interchanging the notion of particles and holes, left and right, as well as $\alpha^{\uparrow,\downarrow} \leftrightarrow \beta^{\uparrow,\downarrow}$ leaves the dynamics invariant. In

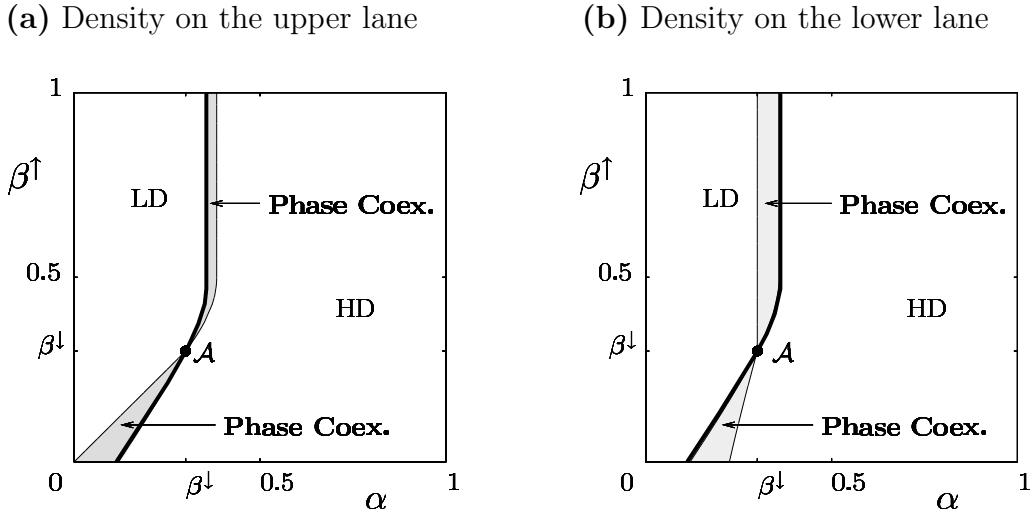


Figure 2.7: Phase diagrams. We show the phases of the densities separately for both lanes, in dependence of equal entrance rates $\alpha^\uparrow = \alpha^\downarrow = \alpha$ and β^\uparrow . The other parameters are kept fixed at $\beta^\downarrow = 0.3$ and $\Omega = 0.15$. Phase coexistence, implying spontaneous density separation resp. polarization, c.f. Fig. 2.6, arises in the grey shaded areas. The latter are localized around a discontinuous transition (bold line). Continuous transitions (thin lines) separate these regions from others with pure low-density (LD) or high-density (HD) phases on both lanes. These phase boundaries are analytical results. A multicritical point \mathcal{A} is localized at $\beta^\uparrow = \beta^\downarrow$ where the continuous and the discontinuous lines intersect. The picture has been modified from [18].

addition, a *lane symmetry* resp. *spin symmetry* is encountered. In our model, both lanes (spin states) are interchangeable, if we also transform $\alpha^\uparrow \leftrightarrow \alpha^\downarrow$ and $\beta^\uparrow \leftrightarrow \beta^\downarrow$.

Our approach allows to draw phase diagrams, showing the system's behavior depending on the parameters $\alpha^{\uparrow,\downarrow}$, $\beta^{\uparrow,\downarrow}$ and Ω . In Fig. 2.7, such phase diagrams are given for the case of equal entrance rates, $\alpha^\uparrow = \alpha^\downarrow = \alpha$ and a fixed lane-change rate of $\Omega = 0.15$. A discontinuous transition (bold line) as well as continuous transitions emerge, they intersect in a multicritical point \mathcal{A} . Hereby, the discontinuous transition can be traced back to current conservation in bulk. Indeed, the total current of particles on the upper and the lower lane does not spatially vary, as particles cannot enter or leave the system. The analysis of the system, see [19], shows that either the left or the right boundary (or bulk processes) poses the major limitations on the current and therefore determines its value. Both scenarios are separated by a discontinuous transition. There, similar to the situation in TASEP, fluctuating domain walls form in the density profiles of *both* lanes and induce interesting critical behavior, see Ref. [78]. The continuous transitions denote regions in phase space where a localized domain wall in the density profile of one lane leaves the system through the left or the right boundary, mediating between phase coexistence and pure low-density (LD) or high-density (HD) phases. As is the case for the discontinuous transition, their location can be found analytically within the approach using the differential equations (2.2) sketched

above, see Ref. [19] for the complete details. The apparent exactness of the analytically derived density profiles (in the asymptotic limit of large system sizes) implies the exactness of the theoretically predicted phase diagrams.

A phenomenon of domain wall delocalization emerges in this system. Namely, there exist regions in phase space where two phases with localized domain walls are separated by a discontinuous transition [19]. At the latter, the domain wall jumps from a certain position in bulk to another. This discontinuous change of position is accompanied by a delocalization of the domain wall, when approaching the transition, and a re-localization at the other position. In Ref. [78] we have investigated this delocalization in detail. As main result, we have found that the width of the localized domain wall diverges when approaching the discontinuous transition; more precisely, the width is proportional to the inverse square root of the distance to the transition. On the other hand, large system sizes induce small fluctuations of the domain wall and thereby a small width. As has already been observed for other systems exhibiting a localized domain wall, its width decreases with increasing system size, proportional to its inverse square root.

2.6 Conclusion and Outlook

Collective phenomena arise in a large variety of traffic-like scenarios [97]. Intracellular transport performed by molecular motors constitutes one of the biologically most important examples [11, 55]. However, active one-dimensional traffic also governs the motion of ribosomes along mRNA [67], the paths of ants on pheromone trails [98], non-equilibrium spintronic devices [49] and vehicular highway traffic [50, 51]. These examples demonstrate the large range of these phenomena, from biological contexts to information processing devices, and from nanostructures to macroscopic objects. The identification of universal principles governing the emergence of such collective effects, independent from the precise realization of the particle's active motion, constitutes one of the main challenges in the modern science of complex systems. Although some insights have been gained in recent years, many issues are yet unresolved and render this field highly attractive for future studies. The arising of self-organized patterns, like asters formed by the dynamic interplay of molecular motors and microtubules [21, 24, 26] building the mitotic spindle, see Chapter 1, denotes an example of such an issue where future progress could largely and fruitfully enhance our general understanding of traffic phenomena far from equilibrium.

In our work, we have developed and investigated a paradigmatic model describing transport on multiple parallel lanes. The latter has been designed to describe universal properties of multi-lane traffic, ranging from intracellular transport, see Section 2.1, to highway traffic as well as non-equilibrium spin transport when viewing the different lanes as distinct spin states, as detailed in Section 2.4. As main results, we have uncovered a spontaneous density separation, arising at a specific spatial position in the system by the formation of a

localized domain wall. Interestingly, in the spin-transport interpretation, this domain wall induces a spontaneous polarization phenomenon. The latter has potential relevance in the development of future spintronic devices. We have carefully studied how this effect can be tuned upon varying the system's parameters. Indeed, we have developed an analytical approach that, by comparison to data from stochastic simulations, has been seen to exactly describe the system's steady state. Consequently, we could derive phase diagrams which, in the asymptotic limit of large systems, fully describe the collective behavior. Discontinuous transitions emerge, where domain wall delocalization occurs. Taking finite-size fluctuations into account, we have calculated the asymptotic divergence of the domain wall's width when approaching the transition.

Naturally, in this simplified model we have ignored certain aspects of intracellular traffic resp. classical, non-equilibrium spin transport. As an example, molecular motors as well as electrons interact with each other in a way that is more complex than the simple hard-core exclusion that we have employed. Motor proteins carry large cargo particles leading to obstruction effects even if motors are spatially separate (but close to each other). Similarly, electrons are negatively charged and Coulomb force induces repulsion when they come close. Such a Coulomb force is distinct from hard-core exclusion, it builds up continuously when approaching another equally charged particle. Together with Anna Melbinger, Thomas Franosch and Erwin Frey, we have investigated the effects of such additional obstruction/repulsion, emerging when particles are close [85, 86]. Novel effects arise, such as "particle surfing" with accompanying density separation or the emergence of an unusual domain wall connecting a high-density region to its left to a low density region to its right. While certain analytical understanding, for example by intimately relating the current-density relation to the system's phase behavior, has been achieved, these kind of particle interactions pose major challenges as they violate the mean-field approximation. Novel theoretical methods for the investigations of the emerging correlated states need to be developed.

Exclusion Processes with Internal States

Tobias Reichenbach, Thomas Franosch, and Erwin Frey

Arnold Sommerfeld Center for Theoretical Physics (ASC) and Center for NanoScience (CeNS), Department of Physics, Ludwig-Maximilians-Universität München, Theresienstrasse 37, D-80333 München, Germany

(Received 8 May 2006; published 2 August 2006)

We introduce driven exclusion processes with internal states that serve as generic transport models in various contexts, ranging from molecular or vehicular traffic on parallel lanes to spintronics. The ensuing nonequilibrium steady states are controllable by boundary as well as bulk rates. A striking polarization phenomenon accompanied by domain wall motion and delocalization is discovered within a mesoscopic scaling. We quantify this observation within an analytic description providing exact phase diagrams. Our results are confirmed by stochastic simulations.

DOI: [10.1103/PhysRevLett.97.050603](https://doi.org/10.1103/PhysRevLett.97.050603)

PACS numbers: 05.70.Ln, 05.40.-a, 05.60.-k, 72.25.-b

Understanding the physical principles governing non-equilibrium transport in one-dimensional (1D) systems has been the subject of recent interest in both biological physics [1,2] and mesoscopic quantum systems [3]. Though there are fundamental differences due to quantum coherence effects, there is a variety of common themes. One of them is the control of a nonequilibrium steady state through particle injection and extraction at the boundaries and coupling to some external field in bulk. For example, a generic spintronic scheme [3] consists of sources and drains for spin injection and extraction where the spin orientation is controlled by a tunable effective magnetic field. The analog in nonequilibrium statistical mechanics is the asymmetric simple exclusion process with open boundaries [4]. In its simplest version, particles interacting only with hard-core repulsion move unidirectionally from the left to the right boundary, which are acting as sources and drains, respectively. These particles may either correspond to molecular engines like mRNA or kinesin moving actively along molecular tracks [5] or to macromolecules driven through nanoscale pores or channels [6] by some external field. Already this simplest conceivable model for collective transport exhibits phase transitions between different nonequilibrium steady states controlled by the entrance and exit rates at the boundaries [7]. It has recently been noted that a minimal model for intracellular transport has to account for the fact that molecular motors may enter or leave the track not only at the boundaries but also in bulk [8,9]. Then, the bulk reservoir of particles acts as a gate, which can induce phase separation [9] in a mesoscopic limit where the residence time of the particles is of the same order as the transit time.

In this Letter, we introduce a generalization of the (totally) asymmetric simple exclusion process (TASEP) in which particles possess some discrete internal states. For illustration, we restrict the discussion to two states which are referred to as spin-up (\uparrow) and spin-down (\downarrow); see Fig. 1. Inspired by Pauli's exclusion principle, we allow multiple occupancy of sites only if particles are in different internal states. The resulting dynamics underlies surpris-

ingly diverse situations. The internal states may correspond to distinct states of a molecular engine which are allowed to simultaneously occupy the same site of a molecular track and mutually inhibit each others motion. In the context of molecular [10] or vehicular [11] traffic, transport on several parallel lanes may be described by attributing internal states to vehicles (molecular motors) moving on a single lane. Even further, considering hopping transport in chains of quantum dots [12] with applied voltage, the states are directly identified with the spin of the electron. In this situation, the model specified in more detail below maps to a quasiclassical version of a nonequilibrium Ising spin chain with nearest neighbor hopping and spin flips, where particles still respect Pauli's exclusion principle but phase coherence is lost.

Motivated by this broad range of possible applications, we consider the following 1D lattice model with L sites and open boundaries illustrated in Fig. 1. At the left, particles with spin-up (\uparrow) are injected at rate α^\uparrow (α^\downarrow), respecting Pauli's exclusion principle; i.e., each site might at most be occupied by one spin-up and one spin-down state. Within bulk, particles hop unidirectionally to the right at rate r and may flip their spin orientation with rate ω , again under the constraint of Pauli's exclusion principle. Finally, the rates $\beta^{\uparrow\downarrow}$ control spin extraction at the right boundary. When interpreting our model as two-lane traffic [11], the states correspond to lanes such that

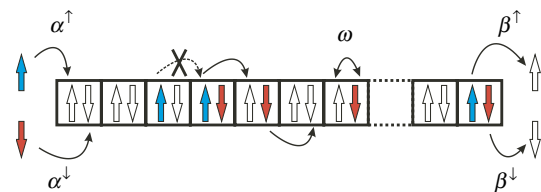


FIG. 1 (color online). Illustration of an exclusion model with two internal states. Particles in states \uparrow (\downarrow) enter with rates α^\uparrow (α^\downarrow), move unidirectionally to the right within the lattice, may flip at rate ω , and leave the system at rates β^\uparrow (β^\downarrow), always respecting Pauli's exclusion principle.

each site might at most be occupied once, and spin flip translates to switching between lanes.

The quantities of interest are the state-resolved density $\rho^{\uparrow\downarrow}(x)$ and current profiles $j^{\uparrow\downarrow}(x)$ in the nonequilibrium steady state as functions of the spatial position x , emerging from the interplay between external driving, coupling between the internal states (spin flips), and the exclusion principle. We identify a cooperative transition between a homogeneous state, where the density profiles of both internal states exhibit no significant spatial dependence, to a “polarized” state, where the density profile of one state changes abruptly along the track. The latter implies that the polarization $\rho^{\uparrow}(x) - \rho^{\downarrow}(x)$ switches from a “low” to a “high” value at a well-defined position x_w ; i.e., a domain wall forms. We find that this position can be tuned by changing the rates of spin injection (source) and extraction (drain) as well as the spin flip rate (gate). For the transition from a polarized to an unpolarized state, two scenarios emerge. Either the domain wall leaves the system continuously through the left or right boundary or it exhibits a delocalization transition. There are thus two genuinely distinct modes of switching the polarized state of the system on and off.

The system’s dynamics is governed by boundary (α, β) and bulk (r, ω) rates, where from now on we fix the time scale by setting the hopping rate to unity, $r = 1$. Obviously, if the spin flip rate ω is fast, i.e., comparable with the hopping rate, the spin degrees of freedom can be considered as relaxed such that the system’s behavior is qualitatively the same as for TASEP without internal states [13]. However, if the typical number of spin flips that a particle performs while traversing the system becomes comparable to the entrance and exit rates, one expects the interplay between these processes to yield interesting collective effects. In order to highlight this dynamic regime, we introduce the gross spin flip rate $\Omega = L\omega$, which we choose to be of the same order as the boundary rates. A proper mesoscopic limit [9] is defined by keeping Ω fixed as the number of lattice sites L tends to infinity.

Much of the system’s behavior can already be inferred on the basis of symmetries and current conservation. Consider the motion of holes with a given internal state, i.e., the absence of a particle with opposite spin. These holes move from right to left and flip their spin state at the same rate ω . The dynamics exhibits a particle-hole symmetry: changing the notion of particles and holes with simultaneous interchange of “left” and “right” as well as $\alpha^{\uparrow\downarrow} \leftrightarrow \beta^{\downarrow\uparrow}$ leaves the system’s dynamics invariant. In addition, there is a spin symmetry as seen by interchanging the spin states and the injection and extraction rates, $\alpha^{\uparrow} \leftrightarrow \alpha^{\downarrow}$ and $\beta^{\uparrow} \leftrightarrow \beta^{\downarrow}$. Let us now study the spin and particle currents passing through site i , denoted by $j_i^{\uparrow\downarrow}$ and $J_i = j_i^{\uparrow} + j_i^{\downarrow}$, respectively. Since particles are not allowed to leave or enter the system, except for the boundaries, the particle current J_i is strictly conserved and thus spatially

constant, $J = J_i$. Unlike the particle current, the spin currents are not conserved individually. Because of spin flip processes, there is a leakage current from one spin state to the other. Since spin flips typically occur on time scales comparable to the time a particle needs to traverse the system (mesoscopic limit), this leakage current is only weak, and consequently both spin currents exhibit a slowly varying spatial dependence.

Similar to TASEP, the particle current is limited either by the left or right boundary or the capacity of the bulk. The latter restricts the current to values below a maximal value of $1/2$. For the left boundary, the current cannot exceed $J_{\text{IN}} = \alpha^{\uparrow}(1 - \alpha^{\uparrow}) + \alpha^{\downarrow}(1 - \alpha^{\downarrow})$, while the right boundary constrains it to a value not larger than $J_{\text{EX}} = \beta^{\uparrow}(1 - \beta^{\uparrow}) + \beta^{\downarrow}(1 - \beta^{\downarrow})$. If the current is below the maximal current, it is determined by the smaller of the boundary currents: $J = \min(J_{\text{IN}}, J_{\text{EX}})$ [15]. Depending on which of both cases applies, we discern two complementary regions in the five-dimensional parameter space spanned by $\alpha^{\uparrow\downarrow}$, $\beta^{\uparrow\downarrow}$, and Ω . We refer to the region where the total current is given by J_{IN} as the injection dominated region (IN), while the case $J = J_{\text{EX}}$ corresponds to the extraction dominated region (EX). Note that both regions are connected by particle-hole symmetry. Since this symmetry is discrete, we expect discontinuous phase transitions upon crossing the border from the injection to the extraction dominated region, i.e., the IN-EX boundary. At this boundary the system exhibits phase coexistence, which similar to TASEP [17] manifests itself in a delocalized domain wall between a low density (LD) and a high density (HD) state of both spin states. Thus, based on mere symmetry arguments, we conclude that across the IN-EX boundary a delocalization transition appears. The simultaneous formation of a domain wall in the density profiles of both spin states exclusively occurs at the IN-EX boundary. This restriction also originates in the conserved particle current, as can be seen by the following argument: For the presence of a domain wall in the spin-up density profile, the spin-up current in the vicinity of the left boundary is determined by the entrance rate, $j_{i=1}^{\uparrow} = \alpha^{\uparrow}(1 - \alpha^{\uparrow})$, while at the right boundary the exit rate specifies its value to $j_{i=L}^{\uparrow} = \beta^{\uparrow}(1 - \beta^{\uparrow})$. If a domain wall simultaneously forms in the spin-down density profile, analogous relations hold for its current. By conservation of the particle current, $J = j_i^{\uparrow} + j_i^{\downarrow}$, we encounter the constraint

$$\alpha^{\uparrow}(1 - \alpha^{\uparrow}) + \alpha^{\downarrow}(1 - \alpha^{\downarrow}) = \beta^{\uparrow}(1 - \beta^{\uparrow}) + \beta^{\downarrow}(1 - \beta^{\downarrow}), \quad (1)$$

which determines the IN-EX boundary.

Even more intriguing phase behavior emerges away from the phase boundary between the injection and extraction dominated regions. In particular, we find a broad parameter regime where a localized domain wall forms in the density profile of one spin state, whereas the profile of the other spin state remains almost flat. The generic

situation, as obtained from stochastic simulations and mean-field (MF) calculations (discussed below), is exemplified in Fig. 2 for the IN region. Both spin states enter at comparable rates, and their respective densities approach each other due to spin flips as the spins traverse the system until they reach the point x_w . There, the density of spin-up jumps to a high value (HD), while the one of spin-down remains at a low level (LD). We encounter a spontaneous polarization effect: in the vicinity of the right boundary, the densities of spin-up and -down largely differ, although they did not when entering the system. We will refer to the parameter range where this spin polarization effect occurs in the IN region as the LD-HD_{IN} phase. Employing spin symmetry to Fig. 2 yields a domain wall appearing in the density profile of the spin-down state, while one concludes from particle-hole symmetry that there is also a corresponding LD-HD_{EX} phase in the EX region. Varying the entrance and exit rates, one can smoothly tune the domain wall position as long as the IN-EX boundary is not crossed. If x_w passes the point $x_w = 1$ in the situation of Fig. 2, the density of spin-up changes from the LD-HD_{IN} phase to the LD phase. On the other hand, $x_w = 0$ marks the transition between the LD-HD_{EX} and the HD phase. Regarding the domain wall position x_w as an order parameter, these transitions are continuous.

The formation of a localized domain wall can be understood from the continuity of the spin currents (Fig. 2), which in turn arises from the only weak leakage current in the mesoscopic limit [9]. Say the domain wall forms in the spin-up state. Then we have to match the currents adjacent to the left (l) and right (r) of this wall, which in the limit of large system size are given by $j_{l/r}^\uparrow(x) = \rho_{l/r}^\uparrow(x) \times [1 - \rho_{l/r}^\uparrow(x)]$. Both currents should coincide at the position

of the domain wall, $j_l^\uparrow(x_w) = j_r^\uparrow(x_w)$, while the density shows a discontinuity. Together, we arrive at the condition $\rho_r^\uparrow(x_w) = 1 - \rho_l^\uparrow(x_w)$ for the domain wall position x_w . The spatial dependence of the density implies that a suitable position x_w indeed exists within a certain parameter region.

Let us now underpin the so far general discussion by a quantitative analytical description. Consider therefore the average density $\rho_i^{\uparrow,\downarrow}$ at site i for spin-up and -down states. The dynamical rules yield equations for their time evolution, which upon factorizing two-point correlations reduce to a closed set of difference equations; such MF approximations have been fruitfully applied within related contexts [9,18,19]. In a continuum limit, the difference equations turn into differential equations, which to leading order in the lattice constant $1/L$ take the form

$$(2\rho^\uparrow - 1)\partial_x \rho^\uparrow + \Omega\rho^\downarrow - \Omega\rho^\uparrow = 0, \quad (2a)$$

$$(2\rho^\downarrow - 1)\partial_x \rho^\downarrow + \Omega\rho^\uparrow - \Omega\rho^\downarrow = 0. \quad (2b)$$

Together with appropriate boundary conditions arising from the entrance and exit processes, they allow a straightforward analytic solution, the details of which will be presented in a forthcoming publication [16]. We have compared the analytic solution to extensive stochastic simulations through careful finite-size scaling analysis. Upon increasing the system size L , the densities converge to the analytical prediction, as exemplified in Fig. 2. The observed exactness of the analytical density profiles in the limit of large systems originates, on the one hand, in the exact mean-field current-density relation in the TASEP [4]. On the other hand, the coupling of the two internal states in our model locally tends to zero when the system size L is increased, such that correlations between them are washed out. The situation is somewhat analogous to TASEP combined with Langmuir kinetics [9].

The analytical approach therefore allows one to obtain the exact phase diagrams of the system. In particular, we may determine the regions where phase separation and thus the polarization phenomenon occur. In general, a large variety of different phases appears with discontinuous as well as continuous transitions between them. As anticipated by our symmetry arguments, a discontinuous transition accompanied by a domain wall delocalization occurs across the border between the injection and extraction dominated regions, which is given by Eq. (1). Continuous transitions appear inside the IN as well as the EX region, when the domain wall leaves the system at one of its boundaries: $x_w = 0$ and $x_w = 1$. The locations in phase space where these special domain wall positions occur, the phase boundaries, can be obtained from the analytical solution of the density profiles, as the latter reveals the position x_w ; details will be presented elsewhere [16].

For illustration, we focus on the special case of equal entrance rates, $\alpha^\uparrow = \alpha^\downarrow \equiv \alpha$, which already exhibits the main features of the possible nonequilibrium steady states. In particular, when a domain wall occurs in the density

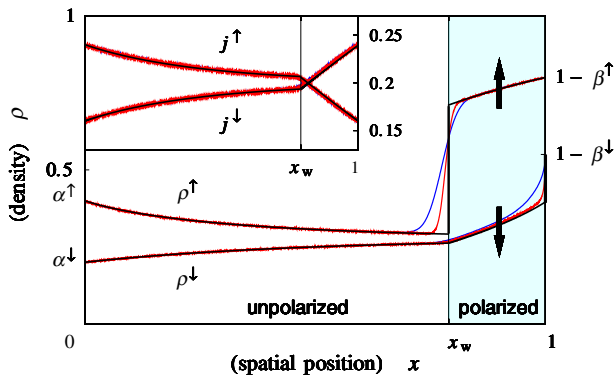


FIG. 2 (color online). The polarization phenomenon appearing in the IN region ($\alpha^\uparrow = 0.4$, $\alpha^\downarrow = 0.2$, $\beta^\uparrow = 0.2$, $\beta^\downarrow = 0.45$, and $\Omega = 0.5$). A domain wall forms in the density profile of spin-up states, while spin-down stays in a LD phase. The spin currents, shown in the inset, are both continuous. Solid lines correspond to the analytical solution, while dashed lines indicate results from stochastic simulations on lattices with $L = 2000$ (blue or dark gray) and $L = 10000$ (red or light gray).

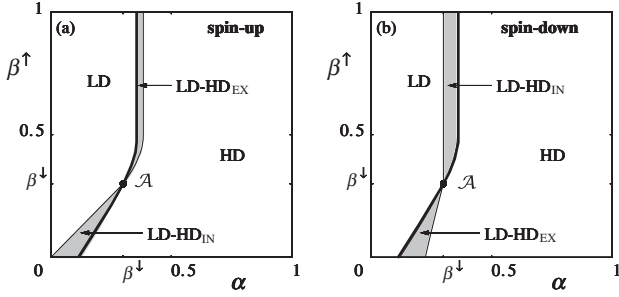


FIG. 3. Phase diagram for equal injection rates $\alpha^\uparrow = \alpha^\downarrow \equiv \alpha$. Phases for spin-up and -down are shown in panels (a) and (b), respectively, as a function of α and β^\downarrow for fixed values $\beta^\uparrow = 0.3$ and $\Omega = 0.15$. Phase separation (shaded areas) arises in the IN as well as the EX region. The delocalization-transition line (thick line) is identical in (a) and (b). Thin lines correspond to continuous transitions.

profile of one of the spin states within the IN region, it lucidly shows the polarization phenomenon: both spins have equal densities in the vicinity of the left boundary, but strongly differ at the right one. The phase diagram for the spin-up and spin-down states, resulting from the analytical solution, is presented in Fig. 3. In the two-lane interpretation of the model, the states refer to the upper and lower lane. For both internal states the same first order line marks the transition between the IN and EX region. The polarized state (shaded area), where a domain wall appears either in the spin-up or -down state, intervenes between the LD and HD phases. There are continuous transitions from pure (LD, HD) to coexistence phases as the domain wall enters or exits the system at the boundary. The lines marking these transitions intersect the IN-EX boundary in a multicritical point \mathcal{A} , where all boundary rates equalize, $\alpha = \beta^\uparrow = \beta^\downarrow$.

Consider now a horizontal path through the phase diagram below the multicritical point \mathcal{A} . For small values of the injection rate α the system is in the injection dominated region, and both spin states (lanes) are in a homogeneous LD state. Then, upon crossing the phase boundary for the spin-up state, the system switches to a polarized state, similar to Fig. 2, such that a domain wall appears in the density profile of the spin-up state (upper lane), entering continuously from the right boundary; for the same parameter range the spin-down state stays in a homogeneous LD state. Approaching the IN-EX boundary this domain wall delocalizes, and upon crossing relocalizes again, but now as a domain wall in the spin-down state (lower lane). As the spin-up state has turned to a HD phase, we encounter polarization near the left boundary. Crossing the IN-EX boundary, the system thus switches its polarization from

the right boundary to the left one. A further increase of the injection rate finally shifts the position of the domain wall to the left boundary such that the system remains in a HD phase for both spin states (lanes). For a path through the phase diagram above \mathcal{A} , similar arguments hold.

Two of the lines that mark continuous transitions are readily obtained. The transition from the LD to the LD-HD_{IN} phase is determined by $x_w = 1$; since $\rho^\uparrow(x) = \rho^\downarrow(x) = \alpha$ for $x < x_w$, it is located along the diagonal, $\alpha = \beta^\downarrow$, for the spin-up state and parallel to the vertical axis, $\alpha = \beta^\downarrow$, for the spin-down state. We emphasize that these phase boundaries in the injection dominated regime do not depend on the magnitude of the gross spin flip rate Ω ; i.e., qualitatively tuning the system's state is possible only upon changing the injection or extraction rates. The lines corresponding to continuous transition in the EX region are more involved [16]. Its most notable feature is that the width of the polarized phase decreases with increasing spin flip rate Ω , until it finally vanishes in the limit $\Omega \rightarrow \infty$.

The authors are grateful for insightful discussions with Felix von Oppen and Ulrich Schollwöck.

-
- [1] N. Hirokawa, *Science* **279**, 519 (1998).
 - [2] A. Rustom *et al.*, *Science* **303**, 1007 (2004).
 - [3] Žutić, J. Fabian, and S. D. Sarma, *Rev. Mod. Phys.* **76**, 323 (2004).
 - [4] B. Derrida, *Phys. Rep.* **301**, 65 (1998).
 - [5] J. Howard, *Mechanics of Motor Proteins and the Cytoskeleton* (Sinauer Associates, Sunderland, MA, 2001).
 - [6] T. Chou and D. Lohse, *Phys. Rev. Lett.* **82**, 3552 (1999).
 - [7] J. Krug, *Phys. Rev. Lett.* **67**, 1882 (1991).
 - [8] R. Lipowsky, S. Klumpp, and T. M. Nieuwenhuizen, *Phys. Rev. Lett.* **87**, 108101 (2001).
 - [9] A. Parmeggiani, T. Franosch, and E. Frey, *Phys. Rev. Lett.* **90**, 086601 (2003); *Phys. Rev. E* **70**, 046101 (2004).
 - [10] H. Hinsch, R. Kouyos, and E. Frey, "Traffic and Granular Flow" (to be published).
 - [11] D. Helbing, *Rev. Mod. Phys.* **73**, 1067 (2001).
 - [12] C. K. Hahn *et al.*, *Appl. Phys. Lett.* **73**, 2479 (1998).
 - [13] The physics in this limit has previously been discussed in terms of a two-lane model [14].
 - [14] E. Pronina and A. B. Kolomeisky, *J. Phys. A* **37**, 9907 (2004).
 - [15] Strictly speaking, this holds only for rates smaller than 1/2. Larger rates effectively act as 1/2 [16].
 - [16] T. Reichenbach, T. Franosch, and E. Frey (to be published).
 - [17] C. MacDonald, J. Gibbs, and A. Pipkin, *Biopolymers* **6**, 1 (1968).
 - [18] B. Derrida, E. Domany, and D. Mukamel, *J. Stat. Phys.* **69**, 667 (1992).
 - [19] M. R. Evans *et al.*, *Phys. Rev. Lett.* **74**, 208 (1995).

Traffic jams induced by rare switching events in two-lane transport

Tobias Reichenbach¹, Erwin Frey and Thomas Franosch

Arnold Sommerfeld Center for Theoretical Physics (ASC)
and Center for NanoScience (CeNS), Department of Physics,
Ludwig-Maximilians-Universität München, Theresienstrasse 37,
D-80333, München, Germany
E-mail: tobias.reichenbach@physik.lmu.de

New Journal of Physics **9** (2007) 159

Received 6 February 2007

Published 4 June 2007

Online at <http://www.njp.org/>

doi:10.1088/1367-2630/9/6/159

Abstract. We investigate a model for driven exclusion processes where internal states are assigned to the particles. The latter account for diverse situations, ranging from spin states in spintronics to parallel lanes in intracellular or vehicular traffic. Introducing a coupling between the internal states by allowing particles to switch from one to another induces an intriguing polarization phenomenon. In a mesoscopic scaling, a rich stationary regime for the density profiles is discovered, with localized domain walls in the density profile of one of the internal states being feasible. We derive the shape of the density profiles as well as resulting phase diagrams analytically by a mean-field approximation and a continuum limit. Continuous as well as discontinuous lines of phase transition emerge, their intersections induce multi-critical behaviour.

¹ Author to whom any correspondence should be addressed.

Contents

1. Introduction	2
2. The model	4
2.1. Dynamical rules	4
2.2. Two-lane interpretation	5
2.3. Symmetries	6
3. Mean-field equations, currents and the continuum limit	6
3.1. Mean field approximation and currents	6
3.2. Mesoscopic scaling and the continuum limit	8
4. Partition of the parameter space and the generic density behaviour	10
4.1. Effective rates	10
4.2. IN, EX, and MC region	11
4.3. The generic state of the densities	12
4.4. Phases and phase boundaries	13
5. Stochastic simulations	15
6. Two-dimensional phase diagrams	15
6.1. Equal injection rates	15
6.2. The general case	18
7. Conclusions	22
Acknowledgments	23
Appendix A. The densities in the first order approximation and the critical value Ω_C	23
References	26

1. Introduction

Non-equilibrium critical phenomena arise in a broad variety of systems, including non-equilibrium growth models [1], percolation-like processes [2], kinetic Ising models [3], diffusion limited chemical reactions [4], and driven diffusive systems [5]. The latter provide models for transport processes ranging from biological systems, like the motion of ribosomes along a m -RNA chain [6] or processive motors walking along cytoskeletal filaments [7, 8], to vehicular traffic [9, 10]. In this work, we focus on the steady-state properties of such one-dimensional transport models, for which the totally asymmetric simple exclusion process (TASEP) has emerged as a paradigm (for reviews see e.g. [11]–[13]). There, particles move unidirectionally from left to right on a one-dimensional lattice, interacting through on-site exclusion. The entrance/exit rates at the open left/right boundary control the system’s behaviour; tuning them, one encounters different non-equilibrium phases for the particle densities [14].

Intense theoretical research has been devoted to the classification of such non-equilibrium phenomena. For example, within the context of reaction–diffusion systems, there is strong evidence that phase transitions from an active to an absorbing state can be characterized in terms of only a few universality classes, the most important being the one of directed percolation (DP) [15]. To search for novel critical behaviour, fruitful results have been obtained by coupling two reaction–diffusion systems [16, 17], each undergoing the active to absorbing phase transition. Due to the coupling, the system exhibits a multi-critical point with unusual critical behaviour.

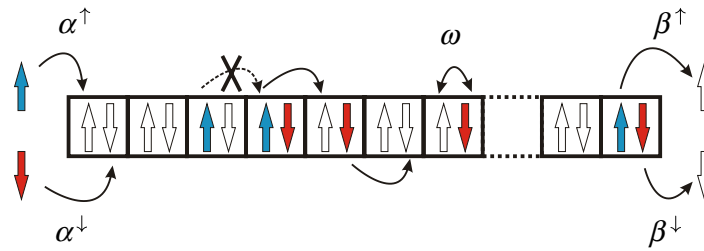


Figure 1. Illustration of an exclusion model with two internal states, adopting the language of spin transport. Particles in states \uparrow (\downarrow) enter with rates α^\uparrow (α^\downarrow), move unidirectionally to the right within the lattice, may flip at rate ω and leave the system at rates β^\uparrow (β^\downarrow), always respecting Pauli's exclusion principle.

We want to stress that already in equilibrium physics seminal insights have been gained by coupling identical systems. For instance, spin-ladders incorporate several Heisenberg spin chains [18]. There, quantum effects lead to a sensitive dependence on the chain number: for even ones a finite energy gap between the ground state and the lowest excitation emerges whereas gapless excitations dominate the low-temperature behaviour if the number of spin chains is odd.

In this work, we generalize the TASEP in a way that particles possess two internal states; we have recently published a short account of this work in [19]. Allowing particles to occasionally switch from one internal state to the other induces a coupling between the latter; indeed, the model may alternatively be regarded as two coupled TASEPs. When independent, each of them separately undergoes boundary-induced phase transitions [14]. The coupling is expected to induce novel phenomena, which are the subject of the present work.

Exclusion is introduced by allowing multiple occupancy of lattice sites only if particles are in different internal states. Viewing the latter as spin-1/2 states, i.e. spin-up (\uparrow) and spin-down (\downarrow), this directly translates into Pauli's exclusion principle; see figure 1. Indeed, the exclusion process presented in this work may serve as a model for semiclassical transport in mesoscopic quantum systems [20], like hopping transport in chains of quantum dots in the presence of an applied field [21]. Our model incorporates the quantum nature of the particles through Pauli's exclusion principle, though phase coherence is ignored. A surprising analogy to a simple spintronics scheme, the Datta–Das spin field-effect transistor [20], holds. There, electrons move unidirectionally through a ferromagnetic metal or a semiconductor. The polarization of the electrons is controllable by a source for spin injection, a drain for spin extraction as well as a gate in the form of a tunable magnetic field that controls the strength of spin precession. In our model, this is mimicked by considering the spin-flip rate as a control parameter.

The model is potentially relevant within biological contexts, as well. In intracellular traffic [7, 22], molecular motors walking on parallel filaments may detach from one lane and attach on another, resulting in an effective switching between the lanes. In our model, identifying the two internal states with different lanes, one recovers a transport model on two lanes with simple site exclusion. In the same way, the system presented in this work serves as a highly simplified cartoon model of multi-lane highway traffic taking lane switching into account [9, 10].

Significant insight into multi-lane traffic has been achieved (see [9, 10] and references therein). In particular, novel phases have been discovered in the case of indirect coupling, i.e. the velocity of the particles depends on the configuration on the neighbouring lane [23]–[25]. Recently, models have been presented that allow particles to switch between lanes, and the

transport properties have in part been rationalized in terms of an effective single lane TASEP [26]–[28]. There, the case of strong coupling has been investigated: the time-scale of lane switching events is the same as of forward hopping. In our model, we explicitly want to ensure a competition between the boundary processes and the switching between the internal states. We therefore employ a mesoscopic scaling, i.e. we consider the case where the switching events are rare as compared to forward hopping. This is the situation encountered in intracellular traffic [7] where motors nearly exclusively remain on one lane and switch only very rarely. In the context of spin transport, it corresponds to the case where forward hopping occurs much faster than spin precession (weak external magnetic field).

The outline of the present paper is the following. In section 2, we introduce the model in the context of spin transport as well as two-lane traffic. Symmetries and currents are discussed, which play a key role in the following analysis. Section 3 describes in detail the mean-field approximation and the differential equations for the densities obtained therefrom through a continuum limit. The mesoscopic scaling is motivated and introduced, the details of the analytic solution for the spatial density profiles being condensed in appendix A. We obtain the generic form of the density profiles in section 4, and compare our analytic results to stochastic simulations. We find that they agree excellently, suggesting the exactness of our analytic approach in the limit of large systems. As our main result, we encounter the polarization phenomenon, where the density profiles in the stationary non-equilibrium state exhibit localized ‘shocks’. Namely, the density of one spin state changes abruptly from low-density (LD) to high-density (HD). The origin of this phenomenon is rationalized in terms of singularities in coupled differential equations. We partition the full parameter space into three distinct regions, and observe a delocalization transition. The methods to calculate the phase boundaries analytically are developed simultaneously. Section 5 presents details on the stochastic simulations which we have carried out to corroborate our analytic approach. The central result of this work is then addressed in section 6, where two-dimensional analytic phase diagrams are investigated. Our analytic approach identifies the phases where the polarization phenomenon occurs, as well as the continuous and discontinuous transitions that separate the phases. The nature of the transitions is explained by the injection/extraction limited current which is conserved along the track. As a second remarkable feature of the model, we uncover multi-critical points, i.e. points where two lines of phase boundaries intersect or the nature of a phase transition changes from discontinuous to a continuous one. Although multi-critical points are well-known in equilibrium statistical mechanics, a fundamental description for such a behaviour for systems driven far from equilibrium still constitutes a major challenge. A brief summary and outlook concludes this work.

2. The model

In this section, we describe our model in terms of spin transport as well as two-lane traffic. Though we will preferentially use the language of spins in the subsequent sections, the two-lane interpretation is of no lesser interest, and straightforwardly obtained. Furthermore, we introduce two symmetries which are manifest on the level of the dynamical rules.

2.1. Dynamical rules

We consider hopping transport on a one-dimensional lattice, composed of L sites, with open boundaries, see figure 1. Particles possess internal states, which we restrict to two different

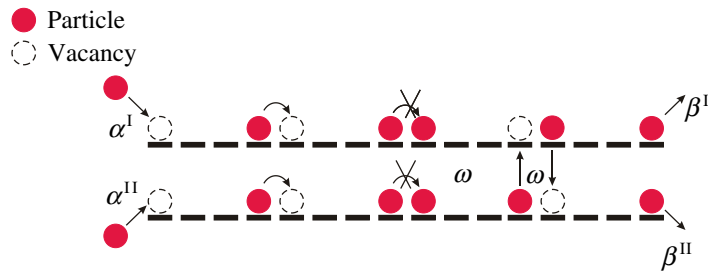


Figure 2. Illustration of the two-lane interpretation. We label the upper lane as lane I and the lower one as lane II. They possess individual entering rates, α^I resp. α^{II} as well as exiting rates, β^I resp. β^{II} .

kinds; adopting a spin notation, they are referred to as spin-up (\uparrow) and spin-down (\downarrow). They enter at the left boundary at rates α^\uparrow resp. α^\downarrow , and move unidirectionally from left to the right through the lattice. The time-scale is fixed by putting the rate for these hopping events to unity. Within the bulk, particles may also flip their spin state, from spin-up to spin-down and back, at rate ω . Finally, having reached the right boundary, particles may exit the system at rates β^\uparrow resp. β^\downarrow , depending on their spin state. We allow all of these processes only under the constraint of Pauli's exclusion principle, meaning that every lattice site may at most be occupied by one particle of a given state. Spin-up and spin-down thus may simultaneously occupy the same site, however two particles with identical spin polarization cannot share a lattice site. In summary, our dynamical rules are the following:

- i. at site $i = 1$ (left boundary), particles with spin-up (spin-down) may enter at rate α^\uparrow (α^\downarrow),
- ii. at site $i = L$ (right boundary), particles with spin-up (spin-down) leave the lattice at rate β^\uparrow (β^\downarrow),
- iii. particles may hop at unit rate from site $i - 1$ to the neighbouring site i for $i \in \{2, \dots, L\}$, i.e. within bulk,
- iv. within bulk, particles can flip their spin state with rate ω , i.e. spin-up turns into spin-down and vice versa,

always respecting Pauli's exclusion principle. Processes (i)–(iii) constitute the TASEP for the two different states separately, while rule (iv) induces a coupling between them. Indeed, when the spin-flip rate ω vanishes, we recover the trivial situation of two independent TASEPs, while we will show that a proper treatment of ω through a mesoscopic scaling induces nontrivial effects.

2.2. Two-lane interpretation

Having introduced our model in the language of semi-classical spin transport, where Pauli's exclusion principle is respected while phase coherence completely ignored, we now want to show that it also describes transport with site exclusion on two parallel lanes. As schematically drawn in figure 2, we consider two parallel lanes, each consisting of L sites, labelled as upper lane (I) and lower lane (II). They are identified with the internal states of the particles considered before: a particle with spin-up (spin-down) now corresponds to a particle on lane I (lane II). The processes (i) and (ii) describe entering of particles at lane I (II) at rate $\alpha^I \equiv \alpha^\uparrow$ ($\alpha^{II} \equiv \alpha^\downarrow$)

and exiting of lane I (II) at rate $\beta^I \equiv \beta^\uparrow$ ($\beta^{II} \equiv \beta^\downarrow$). Due to (iii), particles hop unidirectionally to the right on each individual lane; at rate ω , they may switch from lane I to II and back. Pauli's exclusion principle translates into simple site exclusion: all the above processes are allowed under the constraint of admitting at most one particle per site. Again, we clearly observe that it is process (iv) that couples two TASEPs, namely the ones on each individual lane, to each other.

2.3. Symmetries

Already on the level of the dynamical rules (i)–(iv) presented above, two symmetries are manifest that will prove helpful in the analysis of the system's behaviour. We refer to the absence of particles with certain state as holes with the opposite respective state². Considering their motion, we observe that the dynamics of the holes is governed by the identical rules (i)–(iv), with 'left' and 'right' interchanged, i.e. with a discrete transformation of sites $i \leftrightarrow L - i$ as well as rates $\alpha^{\uparrow,\downarrow} \leftrightarrow \beta^{\downarrow,\uparrow}$. The system thus exhibits a *particle–hole symmetry*. Even more intuitively, the two states behave qualitatively identical. Indeed, the system remains invariant upon changing spin-up to spin-down states and vice versa with a simultaneous interchange of $\alpha^\uparrow \leftrightarrow \alpha^\downarrow$ and $\beta^\uparrow \leftrightarrow \beta^\downarrow$, constituting a *spin symmetry* (in terms of the two-lane interpretation, it translates into a *lane symmetry*).

When analysing the system's behaviour in the five-dimensional phase space, constituted of the entrance and exit rates $\alpha^{\uparrow,\downarrow}$, $\beta^{\uparrow,\downarrow}$ and ω , these symmetries allow to connect different regions in phase space, and along the way to simplify the discussion.

3. Mean-field equations, currents and the continuum limit

In this section, we shall make use of the dynamical rules introduced above to set up a quantitative description for the densities and currents in the system. Within a mean-field approximation, their time evolution is expressed through one-point functions only, namely the average occupations of a lattice site. Such mean-field approximations have been successfully applied to a variety of driven diffusive systems, see e.g. [12]. We focus on the properties of the non-equilibrium steady state, which results from boundary processes (entering and exiting events) as well as bulk ones (hopping and spin-flip events). Both types of processes compete if their time-scales are comparable; we ensure this condition by introducing a *mesoscopic scaling* for the spin flip rate ω . Our focus is on the limit of large system sizes L , which is expected to single out distinct phases. To solve the resulting equations for the densities and currents, a continuum limit is then justified, and it suffices to consider the leading order in the small parameter, namely the ratio of the lattice constant to system size. Such a mesoscopic scaling has been already successfully used in [29, 30] in the context of TASEP coupled to Langmuir dynamics.

3.1. Mean field approximation and currents

Let $n_i^\uparrow(t)$ resp. $n_i^\downarrow(t)$ be the fluctuating occupation number of site i for spin-up resp. spin-down state, i.e. $n_i^{\uparrow,\downarrow}(t) = 1$ if this site is occupied at time t by a particle with the specified spin state and $n_i^{\uparrow,\downarrow}(t) = 0$ otherwise. Performing ensemble averages, the expected occupation, denoted by $\rho_i^\uparrow(t)$

² The convention to flip the spin simultaneously is natural in the language of solid-state physics. In the context of two-lane traffic, it appears more natural to consider vacancies moving on the *same* lane in the reverse direction.

and $\rho_i^\downarrow(t)$, is obtained. Within a mean-field approximation, higher order correlations between the occupation numbers are neglected, i.e. we impose the factorization approximation

$$\langle n_i^r(t)n_j^s(t) \rangle = \rho_i^r(t)\rho_j^s(t); \quad r, s \in \{\uparrow, \downarrow\}. \quad (1)$$

Equations of motion for the densities can be obtained via *balance equations*. The time-change of the density at a certain site is related to appropriate currents. The spatially varying *spin current* $j_i^\uparrow(t)$ quantifies the rate at which particles of spin state \uparrow at site $i-1$ hop to the neighbouring site i . Within the mean-field approximation, equation (1), the current is expressed in terms of densities as

$$j_i^\uparrow(t) = \rho_{i-1}^\uparrow(t)[1 - \rho_i^\downarrow(t)], \quad i \in \{2, \dots, L\}, \quad (2)$$

and similarly for the current $j_i^\downarrow(t)$. The sum yields the total *particle current* $J_i(t) \equiv j_i^\uparrow(t) + j_i^\downarrow(t)$. Due to the spin-flip process (iv), there also exists a *leakage current* $j_i^{\uparrow\downarrow}(t)$ from spin-up state to spin-down state. Within mean-field

$$j_i^{\uparrow\downarrow}(t) = \omega\rho_i^\uparrow(t)[1 - \rho_i^\downarrow(t)], \quad (3)$$

and similarly for the leakage current $j_i^{\downarrow\uparrow}(t)$ from spin-down to spin-up state. Now, for $i \in \{2, \dots, L-1\}$ we can use balance equations to obtain the time evolution of the densities,

$$\frac{d}{dt}\rho_i^\uparrow(t) = j_i^\uparrow(t) - j_{i+1}^\uparrow(t) + j_i^{\downarrow\uparrow}(t) - j_i^{\uparrow\downarrow}(t). \quad (4)$$

This constitutes an exact relation. Together with the mean field approximation for the currents, equations (2) and (3), one obtains a set of closed equations for the local densities

$$\frac{d}{dt}\rho_i^\uparrow(t) = \rho_{i-1}^\uparrow(t)[1 - \rho_i^\uparrow(t)] - \rho_i^\uparrow(t)[1 - \rho_{i+1}^\uparrow(t)] + \omega\rho_i^\downarrow(t) - \omega\rho_i^\uparrow(t). \quad (5)$$

At the boundaries of the track, the corresponding expressions involve also the entrance and exit events, which are again treated in the spirit of a mean-field approach

$$\frac{d}{dt}\rho_1^\uparrow(t) = \alpha^\uparrow[1 - \rho_1^\uparrow(t)] - \rho_1^\uparrow(t)[1 - \rho_2^\uparrow(t)] + \omega\rho_1^\downarrow(t) - \omega\rho_1^\uparrow(t), \quad (6)$$

$$\frac{d}{dt}\rho_L^\uparrow(t) = \rho_{L-1}^\uparrow(t)[1 - \rho_L^\uparrow(t)] - \beta^\uparrow\rho_L^\uparrow(t) + \omega\rho_L^\downarrow(t) - \omega\rho_L^\uparrow(t). \quad (7)$$

Due to the spin symmetry, i.e. interchanging \uparrow and \downarrow , an analogous set of equations holds for the time evolution of the density of particles with spin-down state.

In the stationary state, the densities $\rho_i^{\uparrow(\downarrow)}(t)$ do not depend on time t , such that the time derivatives in equations (5)–(7) vanish. Therefrom, we immediately derive the spatial conservation of the particle current: indeed, summing equation (4) with the corresponding equation for the density of spin-down states yields

$$J_i = J_{i+1}, \quad i \in \{2, \dots, L-1\}, \quad (8)$$

such that the particle current does not depend on the spatial position i . Note that this does not apply to the individual spin currents, they *do* have a spatial dependence arising from the leakage currents.

In a qualitative discussion, let us now anticipate the effects that arise from the non-conserved individual spin currents as well as from the conserved particle current. The latter has its analogy in TASEP, where the particle current is spatially conserved as well. It leads to two distinct regions in the parameter space: one where the current is determined by the left boundary, and the other where it is controlled by the right one. Both regions are connected by the discrete particle–hole symmetry. Thus, in general, discontinuous phase transitions arise when crossing the border from one region to the other. In our model, we will find similar behaviour: the particle current is either determined by the left or by the right boundary. Again, both regions are connected by the discrete particle–hole symmetry, such that we expect discontinuous phase transitions at the border between both. Except for a small, particular region in the parameter space, this behaviour is captured quantitatively by the mean-field approach and the subsequent analysis, which is further corroborated by stochastic simulations. The phenomena linked to the particular region will be presented elsewhere [31].

On the other hand, the non-conserved spin currents may be compared to the current in TASEP coupled to Langmuir kinetics, see [29, 30]. Due to attachment and detachment processes, the in-lane current is only weakly conserved, allowing for a novel phenomenon, namely phase separation into a LD and a HD region separated by a localized domain wall. The transitions to this phase are continuous considering the domain wall position x_w as the order parameter. In our model, an analogous but even more intriguing phase will appear as well, with continuous transitions being possible.

3.2. Mesoscopic scaling and the continuum limit

3.2.1. Mesoscopic scaling. Phases and corresponding phase transitions are expected to emerge in the limit of large system size, $L \rightarrow \infty$, which therefore constitutes the focus of this work. We expect interesting phase behaviour to arise from the coupling of spin-up and spin-down states via spin-flip events, in addition to the entrance and exit processes. Clearly, if spin-flips occur on a fast time-scale, comparable to the hopping events, the spin degree of freedom is relaxed, such that the system’s behaviour is effectively the one of a TASEP. Previous work on related two-lane models [27, 26] focused on the physics in that situation. In this work, we want to highlight the dynamical regime where coupling through spin-flips is present, however not sufficiently strong to relax the system’s internal degree of freedom. In other words, we consider physical situations where spin-flips occur on the same time-scale as the entrance/exit processes. Defining the *gross* spin-flip rate $\Omega = \omega L$ yields a measure of how often a particle flips its spin state while traversing the system. To ensure competition between spin-flips with boundary processes, a *mesoscopic scaling* of the rate ω is employed by keeping Ω fixed, of the same order as the entrance/exit rates, when the number of lattice sites becomes large $L \rightarrow \infty$.

3.2.2. Continuum limit and first order approximation. The total length of the lattice will be fixed to unity and one may define consistently the lattice constant $\epsilon = 1/L$. In the limit of large systems $\epsilon \rightarrow 0$, a *continuum limit* is anticipated. We introduce continuous functions $\rho^\uparrow(x)$ resp. $\rho^\downarrow(x)$ through $\rho^\uparrow(x_i) = \rho_i^\uparrow$ resp. $\rho^\downarrow(x_i) = \rho_i^\downarrow$ at the discrete points $x_i = i\epsilon$. Expanding these to

first order in the lattice constant,

$$\rho^{\uparrow(\downarrow)}(x_{i\pm 1}) = \rho^{\uparrow(\downarrow)}(x_i \pm \epsilon) = \rho^{\uparrow(\downarrow)}(x_i) \pm \epsilon \partial_x \rho^{\uparrow(\downarrow)}(x_i), \quad (9)$$

the difference equations (5)–(7) turn into differential equations. Observing that $\omega = \epsilon\Omega$ is already of order ϵ , we find that the zeroth order of equation (5) vanishes, and the first order in ϵ yields

$$[2\rho^\uparrow(x) - 1]\partial_x \rho^\uparrow(x) + \Omega\rho^\downarrow(x) - \Omega\rho^\uparrow(x) = 0. \quad (10)$$

Similarly, the same manipulations for ρ^\downarrow yield

$$[2\rho^\downarrow(x) - 1]\partial_x \rho^\downarrow(x) + \Omega\rho^\uparrow(x) - \Omega\rho^\downarrow(x) = 0. \quad (11)$$

The expansion of equations (6) and (7) in powers of ϵ , yields in zeroth order

$$\begin{aligned} \rho^\uparrow(0) &= \alpha^\uparrow, & \rho^\uparrow(1) &= 1 - \beta^\uparrow, \\ \rho^\downarrow(0) &= \alpha^\downarrow, & \rho^\downarrow(1) &= 1 - \beta^\downarrow, \end{aligned} \quad (12)$$

which impose *boundary conditions*. Since two boundary conditions are enough to specify a solution of the coupled first-order differential equations, the system is apparently over-determined. Of course, the full analytic solution, i.e. where all orders in ϵ are incorporated, will be only *piecewise* given by the first-order approximation, equations (10)–(12). Between these branches, the solution will depend on higher-orders of ϵ , therefore, these intermediate regions scale with order ϵ and higher. They vanish in the limit of large systems, $\epsilon \rightarrow 0$, yielding *domain walls* or *boundary layers*.

Let us explain the latter terms. At the position of a domain wall, situated in bulk, the density changes its value discontinuously, from one of a LD region to one of a HD. Boundary layers are pinned to the boundaries of the system. There as well, the density changes discontinuously: from a value that is given by the corresponding boundary condition to that of a LD or HD region which is imposed by the opposite boundary.

3.2.3. Symmetries and currents revisited. In the following, we reflect important properties of the system, symmetries and currents, on the level of the first-order approximation, equations (10)–(12). The explicit solution of the latter can be found in appendix A.

The particle–hole symmetry, already inferred from the dynamical rules, now takes the form

$$\rho^{\uparrow(\downarrow)}(x) \leftrightarrow 1 - \rho^{\uparrow(\downarrow)}(1 - x), \quad \alpha^{\uparrow(\downarrow)} \leftrightarrow \beta^{\uparrow(\downarrow)}. \quad (13)$$

Interchanging \uparrow and \downarrow in the densities as well as the in and outgoing rates yields the spin symmetry,

$$\rho^\uparrow(x) \leftrightarrow \rho^\downarrow(x), \quad \alpha^\uparrow \leftrightarrow \alpha^\downarrow, \quad \beta^\uparrow \leftrightarrow \beta^\downarrow. \quad (14)$$

The individual spin currents as well as the particle current have been anticipated to provide further understanding of the system's behaviour. In the continuum limit the zeroth order of the spin currents is found to be $j^{\uparrow(\downarrow)}(x) = \rho^{\uparrow(\downarrow)}(x)[1 - \rho^{\uparrow(\downarrow)}(x)]$, such that equations (10), (11) may

be written in the form

$$\partial_x j^\uparrow = \Omega[\rho^\downarrow - \rho^\uparrow], \quad \partial_x j^\downarrow = \Omega[\rho^\uparrow - \rho^\downarrow]. \quad (15)$$

The terms on the right-hand side, arising from the spin-flip process (iv), are seen to violate the spatial conservation of the spin currents. However, due to the mesoscopic scaling of the spin flip rate ω , the leakage currents between the spin states are only weak, see equation (3), locally tending to zero when $\epsilon \rightarrow 0$, such that the spin currents vary *continuously* in space. This finding imposes a condition for the transition from one branch of first-order solution to another, as described above: such a transition is only allowed when the corresponding spin currents are continuous at the transition point, thus singling out distinct positions for a possible transition.

Finally, summing the two equations in equation (15) yields the spatial conservation of the particle current: $\partial_x J = 0$.

4. Partition of the parameter space and the generic density behaviour

The parameter space of our model, spanned by the five rates $\alpha^{\uparrow,\downarrow}$, $\beta^{\uparrow,\downarrow}$, and Ω , is of high dimensionality. However, in this section, we show that it can be decomposed into only three basic distinct regions: the maximal-current (MC) region as well as the injection-limited (IN) and the extraction-limited one (EX). While trivial phase behaviour occurs in the MC region, our focus is on the IN and EX region (connected by particle–hole symmetry), where a striking polarization phenomenon occurs. The generic phase behaviour in these regions is derived, exhibiting this effect.

4.1. Effective rates

The entrance and exit rates as well as the carrying capacity of the bulk impose restrictions on the particle current. For example, the capacity of the bulk limits the individual spin currents $j^{\uparrow(\downarrow)}$ to maximal values of $1/4$. The latter occurs at a density of $1/2$, as seen from the previous result $j^{\uparrow(\downarrow)} = \rho^{\uparrow(\downarrow)}[1 - \rho^{\uparrow(\downarrow)}]$. To illustrate the influence of the injection and extraction rates, we first consider an ‘open’ right boundary i.e. $\beta^\uparrow = \beta^\downarrow = 1$. Particles then leave the system unhindered, such that only the entrance rates may limit the particle current. Provided one of these rates, say α^\uparrow , exceeds the value $1/2$, the current of the corresponding state (\uparrow) is limited by the capacity of the bulk to a value of $1/4$ in the vicinity of the left boundary. A boundary layer thus forms in the density profile of spin-up state at the left boundary, connecting the value of the injection rate α^\uparrow to the value $1/2$. Up to this boundary layer, the density profile $\rho^\uparrow(x)$ is identical to the one where α^\uparrow takes a value of $1/2$, cf figure 3. Similar reasoning holds for the extraction rates $\beta^{\uparrow(\downarrow)}$. They as well behave effectively as $1/2$ when exceeding this value. To treat these findings properly, we introduce the *effective rates*

$$\alpha_{\text{eff}}^{\uparrow(\downarrow)} = \min\left[\alpha^{\uparrow(\downarrow)}, \frac{1}{2}\right], \quad (16a)$$

$$\beta_{\text{eff}}^{\uparrow(\downarrow)} = \min\left[\beta^{\uparrow(\downarrow)}, \frac{1}{2}\right]. \quad (16b)$$

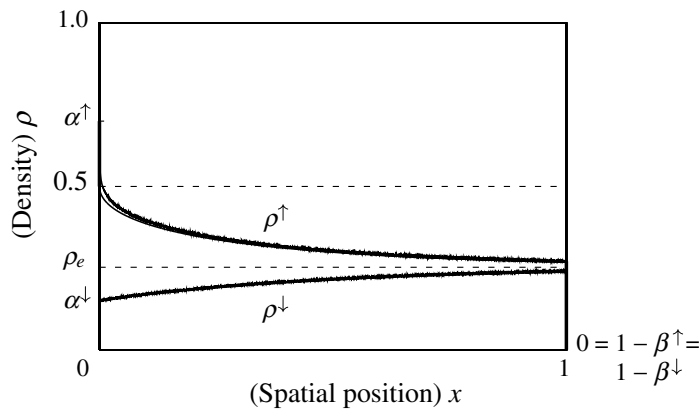


Figure 3. Illustration of the effective rates. The right boundary is ‘open’, such that only the capacity of the bulk and the entrance rates limit the spin currents. The injection rate $\alpha^\uparrow > \frac{1}{2}$ effectively acts as $\frac{1}{2}$. The analytic predictions correspond to the solid lines, the results from stochastic simulations for $L = 10\,000$ are indicated by the wiggly line. With increasing spatial position, the densities approach a common value ρ_e . The parameters used are $\alpha^\uparrow = 0.7$, $\alpha^\downarrow = 0.15$ and $\Omega = 0.5$.

The system’s bulk behaviour will only depend on them, and, in particular, remain unaffected when a rate is varied at values exceeding $1/2$.

4.2. IN, EX, and MC region

Equipped with these results, in the case of an ‘open’ right boundary, the spin currents in the vicinity of the left boundary are given by $j^\uparrow = \alpha_{\text{eff}}^\uparrow(1 - \alpha_{\text{eff}}^\uparrow)$ resp. $j^\downarrow = \alpha_{\text{eff}}^\downarrow(1 - \alpha_{\text{eff}}^\downarrow)$, resulting in a particle current J_{IN} imposed by the injection rates: $J_{\text{IN}} = \alpha_{\text{eff}}^\uparrow(1 - \alpha_{\text{eff}}^\uparrow) + \alpha_{\text{eff}}^\downarrow(1 - \alpha_{\text{eff}}^\downarrow)$. The analogous relations, with the injection and extraction rates interchanged, hold for the case of an ‘open’ left boundary, $\alpha^\uparrow = \alpha^\downarrow = 1$. The particle current is then controlled by the right boundary: $J_{\text{EX}} = \beta_{\text{eff}}^\uparrow(1 - \beta_{\text{eff}}^\uparrow) + \beta_{\text{eff}}^\downarrow(1 - \beta_{\text{eff}}^\downarrow)$. In general, depending on which imposes the stronger restriction, either the left or the right boundary limits the particle current: $J \leq \min(J_{\text{IN}}, J_{\text{EX}})$. Indeed, $J = \min(J_{\text{IN}}, J_{\text{EX}})$ holds except for an anomalous situation, where the current is lower than this value³. Depending on which of both cases applies, two complementary regions in phase space are distinguished: $J_{\text{IN}} < J_{\text{EX}}$ is termed *IN region*, while $J_{\text{IN}} > J_{\text{EX}}$ defines the *EX region*. Since they are connected by discrete particle–hole symmetry, we expect *discontinuous phase transitions* across the border between both, to be referred as *IN–EX boundary*.

Right at the IN–EX boundary, the system exhibits coexistence of LD and HD phases, separated by domain walls. Interestingly, this phase coexistence emerges on *both* lanes (states), which may be seen as follows. Recall that a domain wall concatenates a region of low and another of HD. However, while the densities exhibit a discontinuity, the spin currents must be continuous. In other words, the spin currents, and therefore the particle currents, imposed by the left and right boundary must match each other. This yields the condition $J_{\text{IN}} = J_{\text{EX}}$, which is nothing but the relation describing the IN–EX boundary. Actually, what we have shown with this argument is that domain walls on both lanes (states) are *at most* feasible at the IN–EX boundary. However,

³ This situation arises in a certain neighbourhood of the multi-critical points \mathcal{B} , discussed in section 6.

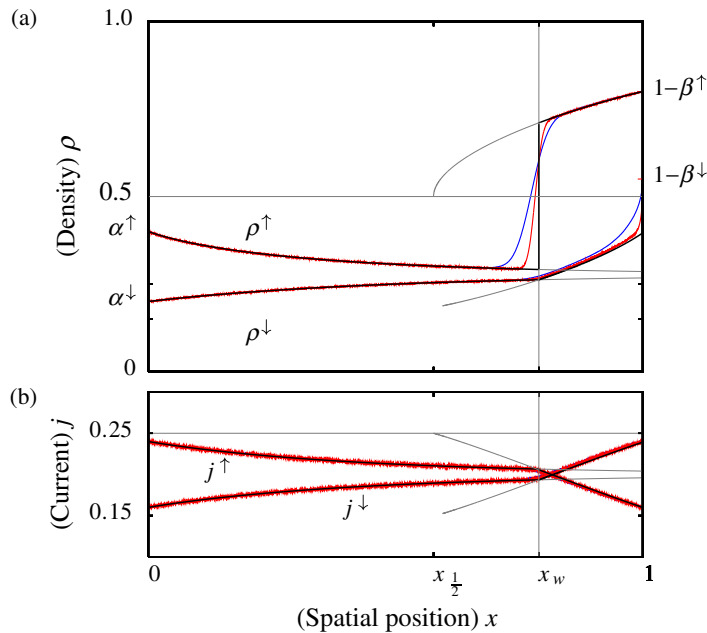


Figure 4. The densities (a) and currents (b) in the IN region: generic state, exhibiting the polarization phenomenon. Results from stochastic simulations are shown as blue ($L = 2000$) resp. red ($L = 10\,000$) lines. They piecewise obey the first-order approximations (black), grey lines indicate continuations of the latter into regions where the densities are no longer given by them. The parameters are $\alpha^\uparrow = 0.4$, $\alpha^\downarrow = 0.2$, $\beta^\uparrow = 0.2$, $\beta^\downarrow = 0.45$, and $\Omega = 0.5$.

it turns out that there, they do indeed form, and are delocalized. We refer to our forthcoming publication [31] for a detailed discussion of this phenomenon. Away from the IN–EX boundary, it follows that at most on one lane (state) a domain wall may appear.

When both entrance rates α^\uparrow , α^\downarrow as well as both exit rates β^\uparrow , β^\downarrow exceed the value $1/2$, the particle current is limited by neither boundary, but only through the carrying capacity of the bulk, restricting it to twice the maximal value $1/4$ of the individual spin currents: $J = 1/2$. The latter situation therefore constitutes the *maximal current region*.

4.3. The generic state of the densities

As we have seen in the previous section, particularly simple density profiles emerge in the MC region. There, up to boundary layers, the density profiles remain constant at a value $1/2$ for each spin state. Another special region in parameter space is the IN–EX boundary, characterized by the simultaneous presence of domain walls in both spin states, as we discuss elsewhere [31].

Away from these regions, the generic situation for the density profiles is illustrated in figure 4. Here, we have considered parameters belonging to the IN region; the behaviour in the EX region follows from particle–hole symmetry. A domain wall emerges for one spin state and a boundary layer for the other one. For specificity, we consider a domain wall for the spin-up state, the other situation is obtained from spin symmetry. The density profiles $\rho_1^{\uparrow(\downarrow)}$ close to the left boundary are given by the solution of the first-order differential equations (10) and (11), obeying the left boundary conditions $\rho_1^\uparrow(x=0) = \alpha_{\text{eff}}^\uparrow$ and $\rho_1^\downarrow(x=0) = \alpha_{\text{eff}}^\downarrow$. For the density profiles $\rho_1^{\uparrow(\downarrow)}$ in

the vicinity of the right boundary, we use the fact that the current in bulk is determined by the injection rates, $J = J_{\text{IN}}$ (which defines the IN region). Therefore, the densities satisfy right boundary conditions which are given by $\rho_r^\uparrow(x = 1) = 1 - \beta_{\text{eff}}^\uparrow$; and $\rho_r^\downarrow(x = 1)$ is found from the conservation of the particle current:

$$J = \alpha_{\text{eff}}^\uparrow(1 - \alpha_{\text{eff}}^\uparrow) + \alpha_{\text{eff}}^\downarrow(1 - \alpha_{\text{eff}}^\downarrow) = \beta_{\text{eff}}^\uparrow(1 - \beta_{\text{eff}}^\uparrow) + \rho_r^\downarrow(x = 1)[1 - \rho_r^\downarrow(x = 1)]. \quad (17)$$

At some point x_w in bulk, the left and right solutions have to be concatenated by a domain wall for spin-up. To determine the position x_w of this domain wall, we use the *continuity* of the spin currents; see figure 4(b)⁴. This continuity condition singles out a distinct spatial position for the domain wall: denote by $\rho_l^\uparrow(x_w)$ the value of the density to the left of x_w , and $\rho_r^\uparrow(x_w)$ the value to the right. From $j^\uparrow = \rho^\uparrow(1 - \rho^\uparrow)$ together with $\rho_l^\uparrow(x_w) \neq \rho_r^\uparrow(x_w)$, we arrive at the condition

$$\rho_l^\uparrow(x_w) = 1 - \rho_r^\uparrow(x_w) \quad (18)$$

for the domain wall position⁵. From the conservation of the particle current J , it follows that the density ρ^\downarrow is continuous at the position x_w .

When considering the internal states as actual spins, the appearance of a domain wall in the density profile of one of the spin states results in a *spontaneous polarization phenomenon*. Indeed, while both the density of spin-up and spin-down remain at comparable low values in the vicinity of the left boundary, this situation changes upon crossing the point x_w . There, the density of spin-up jumps to a high value, while the density of spin-down remains at a low value, resulting in a polarization in this region.

Comparing the generic phase behaviour to the one of TASEP, we observe that the IN region can be seen as the analogue to the LD region there: within both, a LD phase accompanied by a boundary layer at the right boundary arises. Following these lines, the EX region has its analogue in the HD region, while the MC region is straightforwardly generalized from the one of TASEP. Furthermore, the delocalization transition across the IN–EX boundary is similar to the appearance of a delocalized domain wall at the coexistence line in TASEP.

4.4. Phases and phase boundaries

In the generic situation of figure 4, the density of spin-down is in a homogeneous LD state, while for spin-up, a LD and a HD region coexist. We refer to the latter as the LD–HD_{IN} phase, as the phase separation arises within the IN region, to be contrasted from a LD–HD_{EX} phase which may arise within the EX region. Clearly, the LD–HD_{IN} phase is only present if the position x_w of the domain wall lies within bulk. Tuning the system's parameter, it may leave the system through the left or right boundary, resulting in a homogeneous phase. Indeed, $x_w = 1$ marks the transition between the LD–HD_{IN} phase and the pure LD state, while at $x_w = 0$ the density changes from the LD–HD_{IN} to a homogeneous HD state. Regarding the domain wall position x_w as an order parameter, these transitions are continuous. Implicit analytic expressions for these

⁴ Indeed, though they are not spatially conserved, the mesoscopic scaling of the spin-flip rate ω was seen to cause a only slowly varying spatial dependence; in the continuum limit, the spin currents are continuous.

⁵ For TASEP-like transport the particle–hole symmetry restricts the density jump to this mirror relation. More general current–density relations are feasible [32, 33], but are not expected to change the picture qualitatively.

phase boundaries, derived in the following, are obtained from the first-order approximation, equations (10) and (11).

Spin symmetry yields the analogous situation with a domain wall appearing in the density profile of spin-down, while particle–hole symmetry maps it to the EX region, where a pure HD phase arises for one of the spins. Discontinuous transitions accompanied by delocalized domain walls appear at the submanifold of the IN–EX boundary (see [31] for a detailed discussion).

The phase boundaries may be computed from the condition $x_w = 0$ and $x_w = 1$ in the situation of figure 4. Consider first the case of $x_w = 0$. There, the density profiles are fully given by the first-order approximation $\rho_r^{\uparrow(\downarrow)}$ satisfying the boundary conditions at the right. The condition (18) translates to

$$\rho_r^{\uparrow}(x=0) = 1 - \rho_r^{\downarrow}(x=0) = 1 - \alpha_{\text{eff}}^{\uparrow} \quad (19)$$

which yields an additional constraint on the system's parameters. This defines the hyper-surface in the IN region where $x_w = 0$ occurs, and thus the phase boundary between the LD–HD_{IN} and the pure HD phase.

Similarly, if $x_w = 1$, the densities follow the left solution $\rho_l^{\uparrow(\downarrow)}(x)$, determined by the left boundary conditions, within the whole system. From equation (18) we obtain

$$\rho_l^{\uparrow}(x=1) = 1 - \rho_l^{\downarrow}(x=1) = \beta_{\text{eff}}^{\uparrow}. \quad (20)$$

Again, the latter is a constraint on the parameters and defines the hyper-surface in the IN region where $x_w = 1$ is found, being the phase boundary between the LD–HD_{IN} and the homogeneous LD phase.

The conditions (19) and (20) yield implicit equations for the phase boundaries. The phase diagram is thus determined up to solving algebraic equations, which may be achieved numerically. Further insight concerning the phase boundaries is possible and may be obtained analytically, which we discuss next.

Firstly, we note that in the case of equal injection rates, $\alpha^{\uparrow} = \alpha^{\downarrow}$, the density profiles in the vicinity of the left boundary are constant. If in addition $\alpha^{\uparrow} = \alpha^{\downarrow} = \beta^{\uparrow} < 1/2$, we observe from equation (20) that a domain wall at $x_w = 1$ emerges. Therefore, this set of parameters always lies on the phase boundary $x_w = 1$, independent of the value of Ω .

Secondly, we investigate the phase boundary determined by $x_w = 0$. Comparing with figure 4, we observe that the first-order approximation ρ_r^{\uparrow} for the density of spin-up may reach the value $\frac{1}{2}$ at a point which is denoted by $x_{1/2}$: $\rho_r^{\uparrow}(x_{1/2}) = \frac{1}{2}$. This point corresponds to a branching point of the first-order solution. Increasing Ω , the value of $x_{1/2}$ increases as well. The domain wall in the density of spin-up can only emerge at a value $x_w \geq x_{1/2}$. At most, $x_w = x_{1/2}$, in which case a domain wall with infinitesimal small height arises. For the phase boundary specified by $x_w = 0$, this implies that it only exists as long as $x_{1/2} \leq 0$. The case $x_w = x_{1/2} = 0$ corresponds to a domain wall of infinitesimal height, which is only feasible if $\alpha_{\text{eff}}^{\uparrow} = \frac{1}{2}$. Now, for given rates $\alpha_{\text{eff}}^{\uparrow} = \frac{1}{2}$, α^{\downarrow} , β^{\uparrow} , the condition $x_{1/2} = 0$ yields a critical rate $\Omega^*(\alpha^{\downarrow}, \beta^{\uparrow})$, depending on the rates α^{\downarrow} , β^{\uparrow} . The situation $x_w = 0$ can only emerge for rates $\Omega \leq \Omega^*(\alpha^{\downarrow}, \beta^{\uparrow})$. Varying the rates α^{\uparrow} , α^{\downarrow} and β^{\uparrow} , the critical rate $\Omega^*(\alpha^{\downarrow}, \beta^{\uparrow})$ changes as well. In appendix A, we show that its largest value occurs at $\alpha^{\downarrow} = \beta^{\uparrow} = 0$. They yield the rate $\Omega_C \equiv \Omega^*(\alpha^{\downarrow} = \beta^{\uparrow} = 0)$, which is calculated to be

$$\Omega_C = 1 + \frac{1}{4}\sqrt{2} \ln(3 - 2\sqrt{2}) \approx 0.38. \quad (21)$$

The critical $\Omega^*(\alpha^\downarrow, \beta^\uparrow)$ are lying in the interval between 0 and Ω_C : $\Omega^*(\alpha^\downarrow, \beta^\uparrow) \in [0, \Omega_C]$, and all values in this interval in fact occur. The rate Ω_C defines a *scale* in the spin-flip rate Ω : For $\Omega \leq \Omega_C$, the phase boundary determined by $x_w = 0$ exists, while disappearing for $\Omega > \Omega_C$.

Thirdly, we study the form of the phase boundaries for large Ω , meaning $\Omega \gg \Omega_C$. In this case, the phase boundary specified by $x_w = 0$ is no longer present. Furthermore, it turns out that in this situation, the densities close to the left boundary quickly approximate a common value ρ_e . The latter is found from conservation of the particle current: $2\rho_e(1 - \rho_e) = J$. We now consider the implications for the phase boundary determined by $x_w = 1$. With $\rho_1^\uparrow(x = 1) = \rho_e$, equation (20) turns into $\rho_e = \beta_{\text{eff}}^\uparrow$, yielding

$$2\beta_{\text{eff}}^\uparrow(1 - \beta_{\text{eff}}^\uparrow) = \alpha_{\text{eff}}^\uparrow(1 - \alpha_{\text{eff}}^\uparrow) + \alpha_{\text{eff}}^\downarrow(1 - \alpha_{\text{eff}}^\downarrow). \quad (22)$$

This condition specifies the phase boundary $x_w = 1$, asymptotically for large Ω . It constitutes a simple quadratic equation in the in and outgoing rates, independent of β^\downarrow , and contains the set $\alpha^\uparrow = \alpha_{\text{eff}}^\downarrow = \beta^\uparrow$.

5. Stochastic simulations

To confirm our analytic findings from the previous section, we have performed stochastic simulations. The dynamical rules (i)–(iv) described in section 2.1 were implemented using random sequential updating. In our simulations, we have performed averages over typically 10^5 time steps, with $10 \times L$ steps of updating between successive ones. Finite size scaling singles out the analytic solution in the limit of large system sizes, as exemplified in figures 3 and 4.

For all simulations, we have checked that the analytic predictions are recovered upon approaching the mesoscopic limit. We attribute the apparent exactness of our analytic approach in part to the exact current density relation in the steady state of the TASEP [34]. The additional coupling of the two TASEPs in our model is only weak: the local exchange between the two states vanishes in the limit of large system sizes. Correlations between them are washed out, and mean-field is recovered.

The observed exactness of the analytic density profiles within the mesoscopic limit implies that our analytic approach yields exact phase diagrams as well. The latter are the subject of the subsequent section.

6. Two-dimensional phase diagrams

In this section, we discuss the phase behaviour on two-dimensional cuts in the whole five-dimensional parameter space. Already the simplified situation of equal injection rates, $\alpha^\uparrow = \alpha^\downarrow$, yields interesting behaviour. There as well as in the general case, we investigate the role of the spin-flip rate Ω by discussing the situation of small and large values of Ω .

6.1. Equal injection rates

For simplicity, we start our discussion of the phase diagram with equal injection rates, $\alpha^\uparrow = \alpha^\downarrow$. Then, the spin polarization phenomenon, depicted in figure 4, becomes even more striking. Starting from equal densities at the left boundary, and hence zero polarization, spin polarization suddenly switches on at the domain wall position x_w . The particular location of x_w is not triggered by a cue on the track, but tuned through the model parameters.

The phase transitions from LD to the LD–HD_{IN} arising in the IN region take a remarkably simple form. Their location is found from $x_w = 1$, and is determined by equation (20) (if phase coexistence arises for spin-up). Since $\rho^\uparrow(x) = \rho^\downarrow(x) = \alpha = \text{constant}$ for $x < x_w$, equation (20) turns into $\alpha = \beta^\uparrow$. The latter transition line intersects the IN–EX boundary, given by $J_{\text{IN}} = J_{\text{EX}}$, at $\beta^\uparrow = \beta^\downarrow = \alpha$, i.e. at the point where all entrance and exit rates coincide. At this *multi-critical point* \mathcal{A} , a continuous line intersects a discontinuous one. The same transition in the density of spin-down state is, from similar arguments, located at $\alpha = \beta^\downarrow$, and also coincides with the IN–EX boundary in \mathcal{A} . Neither the multi-critical point \mathcal{A} nor these phase boundaries depend on the magnitude of the gross spin flip rate Ω . Therefore, qualitatively tuning the system’s state is possible only upon changing the injection or extraction rates. The other phase transitions within the IN region, namely from the HD to the LD–HD_{IN} phase, are more involved. The analytic solution given by (A.12) and (A.13) has to be considered together with the condition (19) for the transition. However, at the end of section 4.4, we have found that these transitions (determined by $x_w = 0$) disappear for sufficiently large $\Omega > \Omega_C$.

6.1.1. Large values of Ω . In the situation of large $\Omega > \Omega_C$, phase transitions arising from $x_w = 0$ in the IN region or from the analogue in the EX region do not emerge, as discussed at the end of section 4.4. We have drawn resulting phase diagrams in figure 5, showing the phase of spin-up (spin-down) in the left (right) panels, depending on α and β^\uparrow . Along the IN–EX boundary, being the same line (shown as bold) in the left and right panels, a delocalization transition occurs. At the multi-critical point \mathcal{A} , it is intersected by continuous lines emerging within the IN resp. the EX region. When $\beta^\downarrow > 1/2$, a MC phase emerges in the upper right quadrant, see figures 5(c)–(d).

To illustrate the system’s phase behaviour, let us consider what happens along a horizontal line in the phase diagrams (a) and (b), at a value $\beta^\uparrow > \beta^\downarrow$. At such a line, for small values of α , both spin states are in LD phases. Upon crossing a certain value of α , a domain wall enters at $x_w = 1$ in the spin-down density profile. Then, spin-down exhibits phase coexistence (LD–HD_{IN}), while spin-up remains in a LD phase. Further increasing α , the bold line is reached, where delocalized domain walls arise in both spin states. For larger values of α , a localized domain wall emerges for spin-up (implying a LD–HD_{EX} phase), and a pure HD phase for spin-down. If α is further increased, the domain wall in the spin-up density profile leaves the system through the left boundary (at $x_w = 0$), and pure HD phases remain for both spin states.

While we have found the transitions within the IN region by simple expressions in the previous subsection, the ones emerging in the EX region are more complex and involve the full analytic solutions (A.12) and (A.13). Their most notable feature is that the width of the corresponding coexistence phase decreases with increasing spin-flip rate Ω , until it finally vanishes in the limit $\Omega \rightarrow \infty$. This may be seen by considering the analogue of equation (22) in the EX region, which describes the phase boundary as it is asymptotically approached when $\Omega \rightarrow \infty$:

$$2\alpha_{\text{eff}}(1 - \alpha_{\text{eff}}) = \beta_{\text{eff}}^\uparrow(1 - \beta_{\text{eff}}^\uparrow) + \beta_{\text{eff}}^\downarrow(1 - \beta_{\text{eff}}^\downarrow), \quad (23)$$

it coincides with the IN–EX boundary.

6.1.2. Small values of Ω . As discussed at the end of section 4.4, when $\Omega < \Omega_C$, the appearance of additional phase transitions becomes possible. For example, within the IN region, the situation $x_w = 0$ may emerge. It describes the transition from the HD to the LD–HD_{IN} phase; the analogue

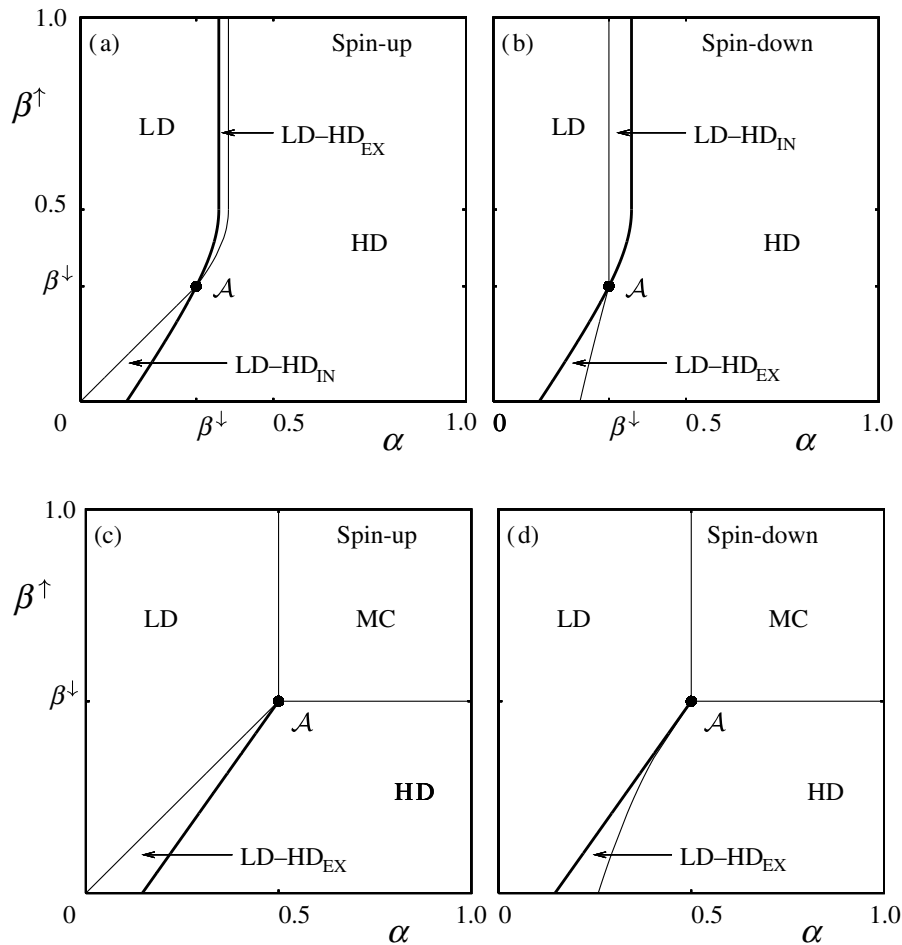


Figure 5. Phase diagrams in the situation of equal entrance rates $\alpha^\uparrow = \alpha^\downarrow \equiv \alpha$ and large Ω . The phases of the densities of spin-up (spin-down) state are shown in (a) resp. (b) for a value $\beta^\downarrow = 0.3$. At a multi-critical point \mathcal{A} , continuous lines (thin) intersect with a discontinuous line (bold), the IN–EX boundary. If $\beta^\downarrow \geq \frac{1}{2}$, the MC phase appears for spin-up, see (c), as well for spin-down, drawn in (d). In the first situation, the switching rate is $\Omega = 0.15$, while $\Omega = 0.2$ in the second.

occurs in the EX region. In figure 6, we show resulting phase diagrams for the spin-up (left panel) and spin-down (right panel), resp. The additional transition lines intersect the IN–EX boundary (bold) at additional multi-critical points \mathcal{B}_{IN} and \mathcal{B}_{EX} . Also, they partly substitute the IN–EX boundary as a phase boundary: across some parts of the latter, phase transitions do not arise. This behaviour reflects the *decoupling* of the two states for decreasing spin-flip rate Ω . Indeed, for $\Omega \rightarrow 0$, the states become more and more decoupled, such that the IN–EX boundary, involving the combined entrance and exit rates of both states, loses its significance.

6.1.3. Multi-critical points. Although the shapes of most of the transition lines appearing in the phase diagrams shown in figure 6 are quite involved, they also exhibit simple behaviour. *Pairwise*, namely one line from a transition in spin-up and another from a related transition in spin-down states, they intersect the IN–EX boundary in the same multi-critical point. This

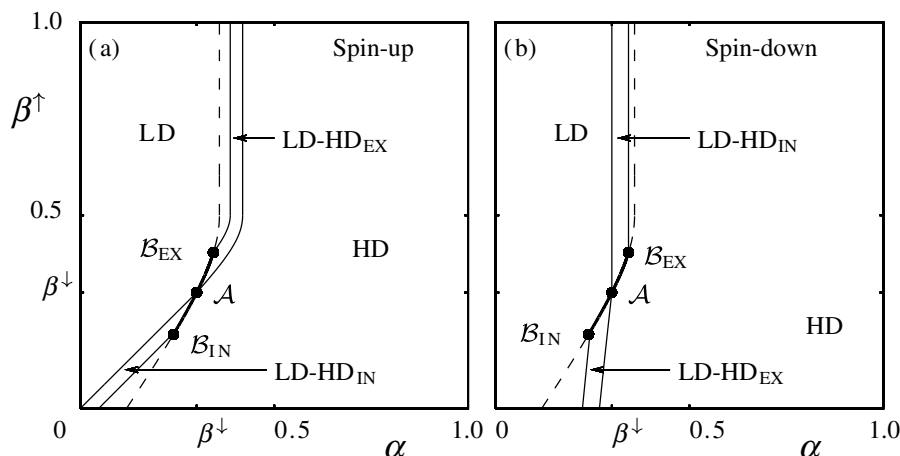


Figure 6. Phase diagrams in the situation of figures 5(a) and (b), but with Ω decreased to a small value, $\Omega = 0.05$. Additional phase transitions emerge in the IN as well as the EX region, accompanied by multi-critical points \mathcal{B}_{IN} and \mathcal{B}_{EX} . Caused by them, phase transitions do no longer appear across some parts of the IN–EX boundary, which is there shown as dashed line.

intriguing phenomenon may be understood by considering the multi-critical points: e.g. at \mathcal{A} , the transition line from the LD to the LD–HD_{IN} phase in the density profile of spin-up intersects the IN–EX boundary, which implies that there we have a domain wall in the density profile of spin-up at the position $x_w = 1$. However, being on the IN–EX boundary, the condition $J_{\text{IN}} = J_{\text{EX}}$ implies that in this situation a domain wall forms as well in the density of spin-down states, also located at $x_w = 1$. Consequently, \mathcal{A} also marks the point where the transition line specified by $x_w = 1$ for spin-down states intersects the IN–EX boundary. Due to the special situation of equal entrance rates, one more pair of lines intersects in this point. Similarly, at \mathcal{B}_{IN} , the transition line from the HD to LD–HD_{IN} phase in the density profile of spin-up intersects the IN–EX boundary, such that a domain wall forms in the density of spin-up at $x_w = 0$. Again, as $J_{\text{IN}} = J_{\text{EX}}$ holds on the IN–EX boundary, this implies the formation of a domain wall in the density of spin-down at $x_w = 1$, corresponding to the transition from the LD to the LD–HD_{EX} phase for spin-down in the EX region.

6.2. The general case

Having focused on the physically particularly enlightening case of equal entering rates in the previous subsection, we now turn to the general case. To illustrate our findings, we show phase diagrams depending on the injection and extraction rates for spin-up states, α^\uparrow and β^\uparrow . Similar behaviour as for equal entrance rates is observed. The multi-critical point \mathcal{A} now splits up into two distinct points \mathcal{A}_{IN} and \mathcal{A}_{EX} .

6.2.1. Large values of Ω : asymptotic results. Again, large Ω prohibit the emergence of the phase transition from the HD to the LD–HD_{IN} phase in the IN region as well as from the LD to the LD–HD_{EX} phase within the EX region, see end of section 4.4. In this paragraph, we consider phase diagrams which are approached asymptotically when $\Omega \rightarrow \infty$. Convergence is fast in Ω , and the asymptotic phase boundaries yield an excellent approximation already for $\Omega \gtrsim 2\Omega_C$.

The transition from LD to the LD–HD_{IN} phase in the IN region asymptotically takes the form of equation (22), and the one from HD to the LD–HD_{EX} phase in the EX region is obtained by particle–hole symmetry. All phase boundaries, including the IN–EX boundary, are thus given by simple quadratic expressions.

Phase diagrams with different topologies that can emerge are exhibited in figures 7 and 8. As in the previous subsection, we show the phases of spin-up (spin-down) states on the left (right) panels. The phase boundaries between the LD and the LD–HD_{IN} phase in the IN region for spin-up as well as spin-down both intersect the IN–EX boundary in a multi-critical point \mathcal{A}_{IN} , being located at $\beta^\uparrow = \beta^\downarrow$. Similarly, the lines of continuous transitions within the EX region both coincide with the IN–EX boundary in a multi-critical point \mathcal{A}_{EX} , which is situated at $\alpha^\uparrow = \alpha^\downarrow$. Note that the phase transitions emerging in the density profile of spin-down within the IN region do not depend on β^\uparrow , thus being horizontal lines in the phase diagrams. Within the EX region they are independent of α^\uparrow , yielding vertical lines.

For $\alpha^\downarrow, \beta^\downarrow < 1/2$, figure 7 shows different topologies of phase diagrams, which only depend on which of the multi-critical points $\mathcal{A}_{IN}, \mathcal{A}_{EX}$ is present. If both appear, see figure 7(a) and (b), the LD–HD_{IN} and the LD–HD_{EX} phase for spin-up are adjacent to each other, separated by the IN–EX boundary. Although in both phases localized domain walls emerge, their position changes discontinuously upon crossing the delocalization transition. For example, starting within the LD–HD_{IN} phase, the domain wall delocalizes when approaching the IN–EX boundary, and, having crossed it, relocalizes again, but at a different position.

When $\alpha^\downarrow = \beta^\downarrow < 1/2$, a subtlety emerges, see figures 8(a) and (b). If both $\alpha^\uparrow \geq 1/2$ and $\beta^\uparrow \geq 1/2$, i.e. in the upper right quadrant of the phase diagrams, these rates effectively act as $1/2$, and the condition $J_{IN} = J_{EX}$ for the IN–EX boundary is fulfilled *in this whole region*. Therefore, delocalized domain walls form on both lanes within this region, as is confirmed by our stochastic simulations [31].

The MC phase emerges when all rates exceed or equal the value $1/2$, corresponding to the upper left quadrant of the phase diagrams in figures 8(c) and (d).

6.2.2. Small values of Ω . When $\Omega < \Omega_C$, the transitions from LD to LD–HD_{IN} within the IN region as well as the analogue in the EX region are possible. As in the case of equal entering rates, the corresponding transition lines pairwise intersect the IN–EX boundary in multi-critical points \mathcal{B}_{IN} and \mathcal{B}_{EX} . As all transitions between phases of the spin-down density within the IN region are independent of β^\uparrow , the corresponding lines are simply horizontal; and within the EX region, their independence of α^\uparrow implies that they yield vertical lines. The phase diagram for the density of spin-down is thus easily found from the IN–EX boundary given by $J_{IN} = J_{EX}$ together with the locations of the multi-critical points $\mathcal{A}_{IN}, \mathcal{A}_{EX}, \mathcal{B}_{IN}$ and \mathcal{B}_{EX} . The latter follow from the intersection of phase transition lines for the density of spin-up, involving the whole analytic solution (A.12) and (A.13), with the IN–EX boundary.

In figure 9 two interesting topologies that may arise are exemplified. Induced by the presence of the multi-critical point \mathcal{B}_{IN} , phase transitions do not occur across all the IN–EX boundary, which is then only shown as dashed line. In figures 9(a) and (b), the points \mathcal{A}_{EX} and \mathcal{B}_{IN} are present. The LD–HD_{IN} phase for spin-up intervenes the LD and the HD phase; the LD–HD_{EX} phase for spin-up is also present, though very tiny. In the phase diagram of spin-down, the LD–HD_{IN} phase intervenes the LD and the HD phase accompanied by continuous as well as discontinuous transitions. Again, the presence of the multi-critical points induces the topology;

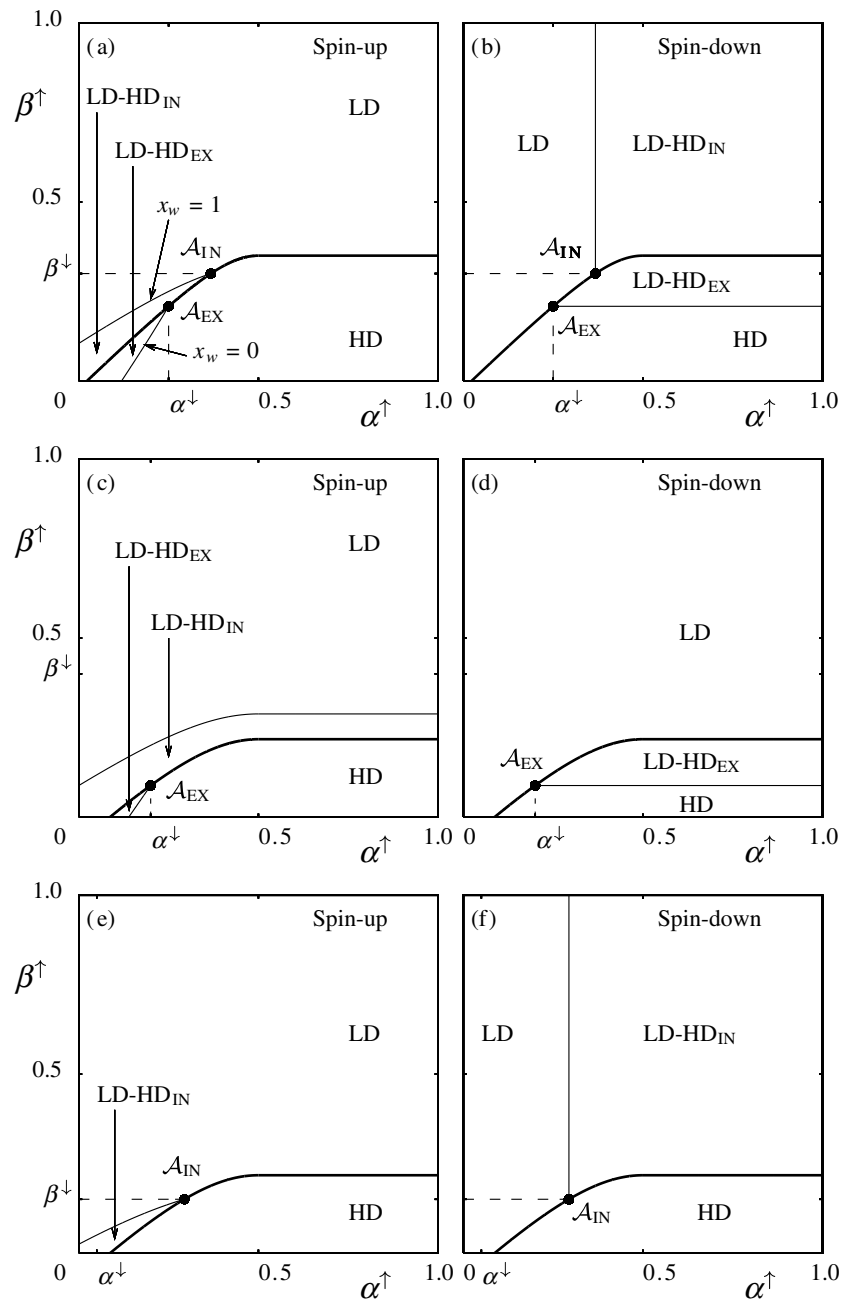


Figure 7. Phase diagrams in the general situation: asymptotic results for large Ω . Lines of continuous transitions (thin) within the IN resp. EX region intersect the delocalization transition line (bold) in multi-critical points \mathcal{A}_{IN} resp. \mathcal{A}_{EX} . Both of these points appear in (a) and (b) ($\alpha^\downarrow = 0.25$, $\beta^\downarrow = 0.3$) while only \mathcal{A}_{EX} is present in (c) and (d) ($\alpha^\downarrow = 0.2$, $\beta^\downarrow = 0.4$) and \mathcal{A}_{IN} alone in (e) and (f) ($\alpha^\downarrow = 0.05$, $\beta^\downarrow = 0.15$), yielding different topologies.

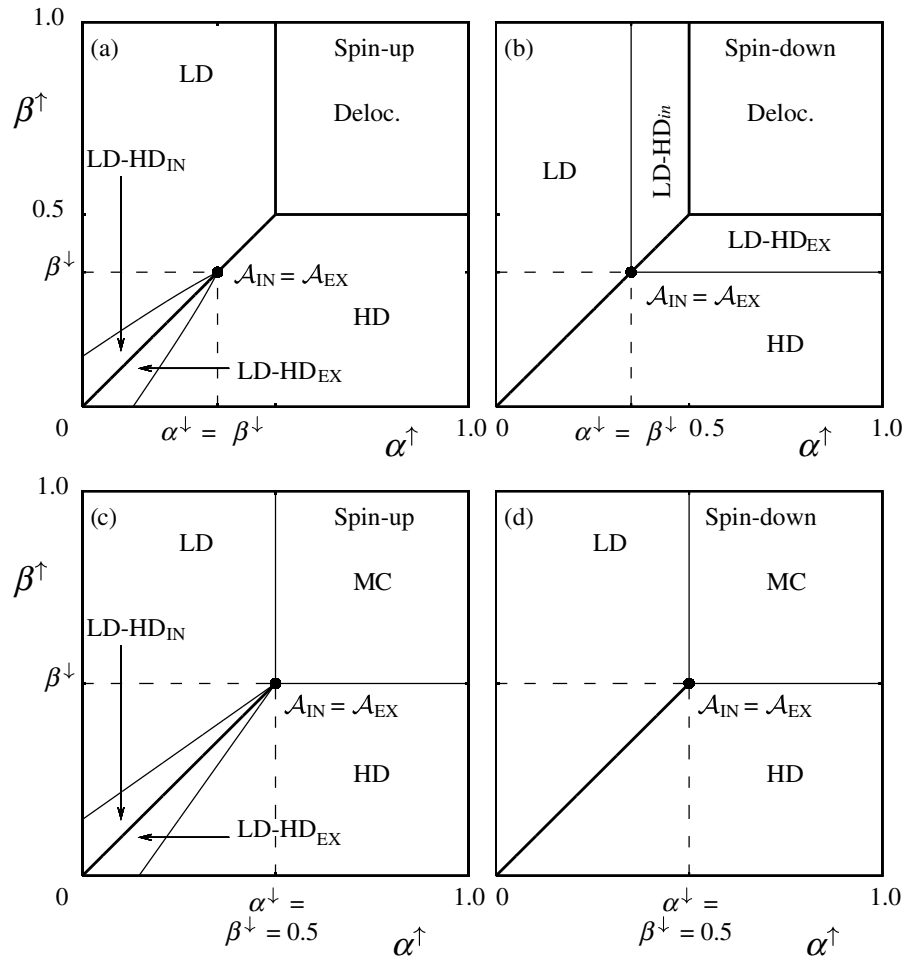


Figure 8. Delocalization as well as MC. When $\alpha^\downarrow = \beta^\downarrow < 1/2$ and $\alpha^\uparrow, \beta^\uparrow \geq 1/2$ (upper right quadrant in (a) and (b)), delocalized domain walls form in the density profiles of both spin states. If instead $\alpha^\downarrow, \beta^\downarrow \geq 1/2$, the MC phase emerges, see (c) and (d).

e.g. in figures 9(c) and (d), only \mathcal{B}_{IN} appears. For the discussion of the possible topologies, we encounter the restriction that \mathcal{A}_{IN} and \mathcal{B}_{IN} cannot occur together, as well as \mathcal{A}_{EX} and \mathcal{B}_{EX} exclude each other (otherwise, the lines determined by $x_w = 0$ and $x_w = 1$ would cross).

We now discuss the influence of the spin-flip rate Ω on the continuous transition lines for spin-up. In section 4.4 the manifold defined by $\alpha^\uparrow = \beta^\uparrow = \alpha_{\text{eff}}^\downarrow$ was found to be a sub-manifold of the phase boundary specified by $x_w = 1$ in the IN region. Independent of Ω , the point $\alpha^\uparrow = \beta^\uparrow = \alpha_{\text{eff}}^\downarrow$, denoted by \mathcal{N}_{IN} , thus lies on the boundary between the LD and the LD-HD_{IN} phase (determined by $x_w = 1$). For large Ω , this boundary approaches the one given by equation (22).

Regarding the transition from the HD to the LD-HD_{IN} within the IN region (determined by $x_w = 0$), section 4.4 revealed that for increasing Ω it leaves the IN region at a critical transfer rate $\Omega^*(\alpha^\downarrow, \beta^\uparrow)$. In the limit $\Omega \rightarrow 0$, the densities $\rho^\uparrow(x)$ and $\rho^\downarrow(x)$ approach constant values, and both the curve $x_w = 1$ as $x_w = 0$ for spin-up in the IN region approach the line $\beta^\uparrow = \alpha^\uparrow$ for

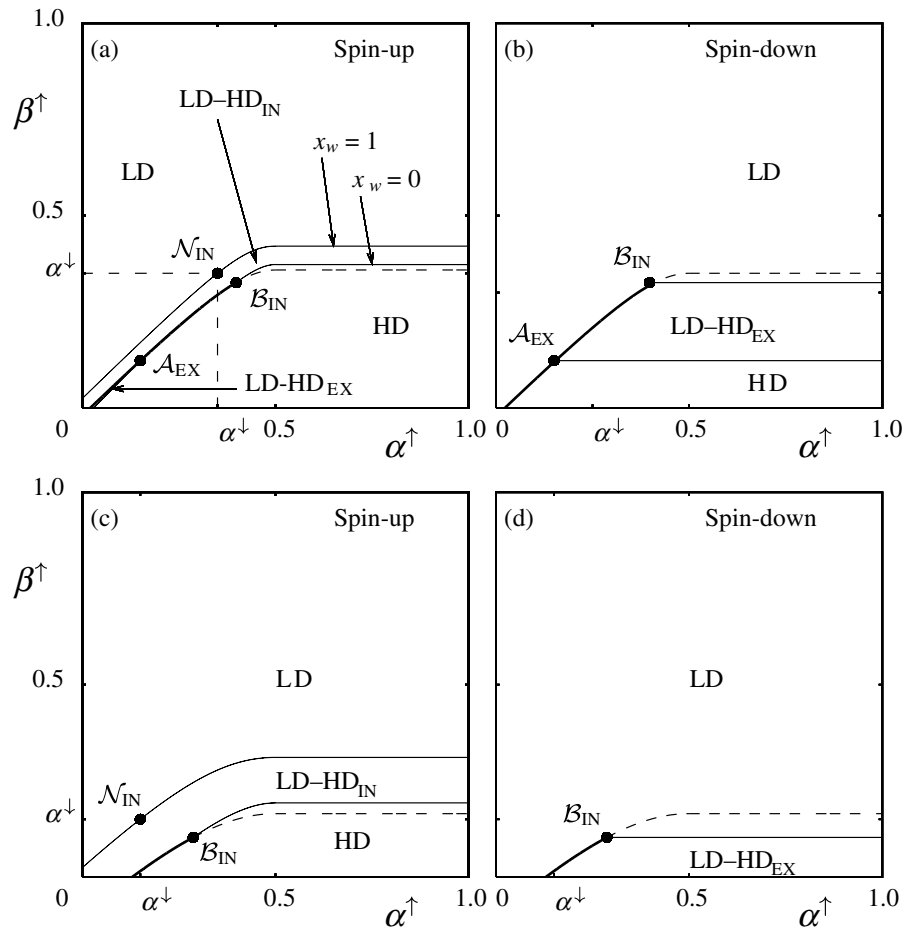


Figure 9. Phase diagrams in the general case and small values of Ω . The nodal point \mathcal{N}_{IN} remains unchanged when Ω is varied. The appearance of the multi-critical point \mathcal{B}_{IN} is accompanied by the non-occurrence of phase transitions across parts of the IN–EX boundary, then shown as dashed line. The multi-critical point \mathcal{A}_{EX} emerges in (a) and (b), but not in the situation of (c) and (d). Parameters are $\Omega = 0.08$, $\alpha^\downarrow = 0.35$, $\beta^\downarrow = 0.45$ in (a) and (b) and $\Omega = 0.2$, $\alpha^\downarrow = 0.15$, $\beta^\downarrow = 0.4$ in (c) and (d).

$\alpha^\uparrow \leq \frac{1}{2}$. The phase in the upper right quadrant in the phase diagram converges to the MC phase, such that in this limit, the case of two uncoupled TASEPs is recovered.

7. Conclusions

We have presented a detailed study of an exclusion process with internal states recently introduced in [19]. The TASEP has been generalized by assigning two internal states to the particles. Pauli's exclusion principle allows double occupation only for particles in different internal states. Occasional switches from one internal state to the other induce a coupling between the transport processes of the separate states. Such a dynamics encompasses diverse situations, ranging from vehicular traffic on multiple lanes to molecular motors walking on intracellular tracks and future spintronics devices.

We have elaborated on the properties of the emerging non-equilibrium steady state focusing on density and current profiles. In a mesoscopic scaling of the switching rate between the internal states, nontrivial phenomena emerge. A localized domain wall in the density profile of one of the internal states induces a spontaneous polarization effect when viewing the internal states as spins. We provide an explanation based on the weakly conserved currents of the individual states and the current-density relations. A quantitative analytic description within a mean-field approximation and a continuum limit has been developed and solutions for the density and current profiles have been presented. A comparison with stochastic simulations revealed that our analytic approach becomes exact in the limit of large system sizes. We have attributed this remarkable finding to the exact current-density relation in the TASEP, supplemented by the locally weak coupling of the two TASEPs appearing in our model: $\omega \rightarrow 0$ in the limit of large system sizes. Local correlations between the two internal states are thus obliterated, as particles hop forward on a much faster time-scale than they switch their internal state.

Furthermore, the parameter regions that allow for the formation of a localized domain wall have been considered. Analytic phase diagrams for various scenarios, in particular the case of equal entrance rates, have been derived. The phase diagrams have been found to exhibit a rich structure, with continuous as well as discontinuous non-equilibrium phase transitions. The discontinuous one originates in the conserved particle current, which is either limited by injection or extraction of particles. At the discontinuous transition between both regimes, delocalized domain walls emerge in the density profiles of *both* internal states. Multi-critical points appear at the intersections of different transition lines organizing the topology of the phase diagrams. Two classes of multi-critical points are identified, one of them arises only for sufficiently small gross spin-flip rate $\Omega < \Omega_C$. The value Ω_C , calculated analytically, provides a natural scale for the rate Ω .

It would be of interest to see which of the described phenomena qualitatively remain when generalizing the model to include more than two internal states. Indeed, within the context of molecular motors walking on microtubuli [7], between 12 and 14 parallel lanes are relevant. Also, the internal states might differ in the sense of different switching rates from one to another [28] and the built-in asymmetry may result in different phases. In the context of intracellular transport it appears worthwhile to investigate the consequences of a coupling to a bulk reservoir, cf [29, 30, 35]; in particular, to study the interplay of domain wall formation induced by attachment and detachment processes as well as rare switching events.

Acknowledgments

We are grateful for helpful discussions with Felix von Oppen, Ulrich Schollwöck, Paolo Pierobon and Mauro Mobilia. Financial support of the German Excellence Initiative via the program ‘Nanosystems Initiative Munich (NIM)’ is gratefully acknowledged.

Appendix A. The densities in the first order approximation and the critical value Ω_C

In this appendix, we give details on the derivation of the analytic solution of the mean-field approximation in the continuum limit to first-order in ϵ , i.e. the system of differential equations (10) and (11).

Summing them we find

$$\partial_x[2\rho^\uparrow(x_i) - 1]^2 + \partial_x[2\rho^\downarrow(x_i) - 1]^2 = 0, \quad (\text{A.1})$$

such that

$$[2\rho^\uparrow(x_i) - 1]^2 + [2\rho^\downarrow(x_i) - 1]^2 = J, \quad (\text{A.2})$$

constitutes a first integral. Remember that

$$j^{\text{tot}} = \rho^\uparrow(x_i)[1 - \rho^\uparrow(x_i)] + \rho^\downarrow(x_i)[1 - \rho^\downarrow(x_i)],$$

such that J is given by the total current:

$$J = 2 - 4j^{\text{tot}}. \quad (\text{A.3})$$

This equation suggests the following parameterization:

$$\cos \theta = J^{-1/2}(2\rho^\uparrow - 1), \quad \sin \theta = J^{-1/2}(2\rho^\downarrow - 1). \quad (\text{A.4})$$

The derivative reads

$$\frac{\sqrt{J}}{2} \cos \theta \frac{d\theta}{dx} = \frac{d\rho^\uparrow}{dx}, \quad (\text{A.5})$$

which leads to the differential equation

$$\sqrt{J} \sin \theta \cos \theta \frac{d\theta}{dx} = \Omega(\sin \theta - \cos \theta). \quad (\text{A.6})$$

This may be solved by a separation of variables:

$$\frac{\Omega}{\sqrt{J}} x = \int_{\theta(0)}^{\theta(x)} \frac{\sin \theta \cos \theta}{\sin \theta - \cos \theta} d\theta. \quad (\text{A.7})$$

To perform the integral, the substitution $y = \tan \theta/2$ is useful. We obtain the inverse function $x = x(\theta)$:

$$x(\theta) = \frac{\sqrt{J}}{\Omega} G(y) \Big|_{y=\tan(\theta/2)} + I. \quad (\text{A.8})$$

Here we defined the function $G(y)$ by

$$G(y) = \left\{ \frac{1+y}{1+y^2} + \frac{\sqrt{2}}{4} \ln \left| \frac{\sqrt{2} - (1+y)}{\sqrt{2} + 1+y} \right| \right\}, \quad (\text{A.9})$$

and I is an constant of integration.

To obtain the inverse functions $x(\rho^\uparrow)$ and $x(\rho^\downarrow)$, we have to express $\tan \frac{\theta}{2}$ by ρ^\uparrow resp. ρ^\downarrow . Recognize that $\tan \frac{\theta}{2}$ can be positive or negative. We therefore define

$$s^\downarrow = \begin{cases} -1 & \text{if } \rho^\downarrow < \frac{1}{2} \\ +1 & \text{if } \rho^\downarrow > \frac{1}{2} \end{cases}, \quad (\text{A.10})$$

and analogously s^\uparrow with \uparrow and \downarrow interchanged. Now

$$\tan \frac{\theta}{2} = s^\downarrow \sqrt{\frac{1 - J^{-1/2}(2\rho^\uparrow - 1)}{1 + J^{-1/2}(2\rho^\uparrow - 1)}}. \quad (\text{A.11})$$

The inverse functions $x(\rho^\uparrow)$ and $x(\rho^\downarrow)$ thus read:

$$x(\rho^\uparrow) = \frac{\sqrt{J}}{\Omega} G(y) \Big|_{y=s^\downarrow \sqrt{\frac{1-J^{-1/2}(2\rho^\uparrow-1)}{1+J^{-1/2}(2\rho^\uparrow-1)}}} + I, \quad (\text{A.12})$$

$$x(\rho^\downarrow) = \frac{\sqrt{J}}{\Omega} G(y) \Big|_{y=s^\uparrow \sqrt{\frac{1-J^{-1/2}(2\rho^\downarrow-1)}{1+J^{-1/2}(2\rho^\downarrow-1)}}} + I. \quad (\text{A.13})$$

The constants of integration I and $J = 2 - 4j^{\text{tot}}$ are determined by matching the boundary conditions. The inverse functions of equations (A.12) and (A.13) constitute the solution to equations (10) and (11), within the first-order approximation to the mean-field equations for the densities in the continuum limit.

Next, we derive the result on Ω_C given at the end of section 4.4. Therefore, consider figure 4. We are interested in the point $x_{1/2}$, and thus in the right branch of the spin-up density profile. As the spin-down density is in the LD phase, i.e. it is smaller than $\frac{1}{2}$, we have $s^\downarrow = -1$ in the above solution for ρ^\uparrow . Thus, $y \leq 0$ in equation (A.12). At the branching point of the analytic solution, i.e. the point $x_{1/2}$, we have the density $\frac{1}{2}$, such that there $y = -1$, implying $G(y) = 0$. Now, if this branching point lies on the right boundary, $x_{1/2} = 0$, as it does for the critical Ω^* , this yields $I = 0$ in equation (A.12). On the other hand, the right branch satisfies the boundary condition on the right: $\rho^\uparrow(x = 1) = 1 - \beta^\uparrow$. Upon substitution into equation (A.12), we obtain

$$1 = x(1 - \beta^\uparrow) = \frac{\sqrt{J}}{\Omega^*} G(y) \Big|_{y = -\sqrt{\frac{1-J^{-1/2}(1-2\beta^\uparrow)}{1+J^{-1/2}(1-2\beta^\uparrow)}}}. \quad (\text{A.14})$$

which for given $\alpha^\downarrow, \beta^\uparrow$ is an equation for $\Omega^*(\alpha^\downarrow, \beta^\uparrow)$. In particular, $\Omega^*(\alpha^\downarrow, \beta^\uparrow)$ is monotonically increasing in G . Investigating $G(y)$, it turns out that $G(y)$ is in turn increasing in y . Since y is bounded from above by $y = 0$, the maximal value for $G(y)$ is provided by $G(y = 0) = 1 + \frac{1}{4}\sqrt{2} \ln(3 - 2\sqrt{2})$. Next, we note that $\Omega^*(\alpha^\downarrow, \beta^\uparrow)$ is an increasing function of \sqrt{J} . With the constraint that $\alpha_{\text{eff}}^\uparrow = \frac{1}{2}$, which is necessary for $x_{1/2} = 0$, the largest \sqrt{J} arises for $\alpha^\downarrow = 0$, i.e. $\sqrt{J} = 1$. Combining both results, the maximal value for the critical rates $\Omega^*(\alpha^\downarrow, \beta^\uparrow)$ occurs for $\alpha^\downarrow = 0$ and $y = 0$. Both conditions together yield

$$\Omega_C = 1 + \frac{1}{4}\sqrt{2} \ln(3 - 2\sqrt{2}). \quad (\text{A.15})$$

Finally, we note that $\alpha^\downarrow = 0$ and $y = 0$ implies $\beta^\uparrow = 0$, such that Ω_C arises if $\alpha^\downarrow = 0$ and $\beta^\uparrow = 0$.

References

- [1] Barabasi A and Stanley H 1995 *Fractal Concepts in Surface Growth* (Cambridge: Cambridge University Press)
- [2] Deutscher G, Zallan R and Adler J (ed) 1983 *Percolation Structures and Processes (Annals of the Israel Physical Society vol 5)* (Bristol: Adam Hilger)
- [3] Droz M, Rácz Z and Schmidt J 1989 *Phys. Rev. A* **39** 2141
- [4] Mattis D C and Glasser M L 1998 *Rev. Mod. Phys.* **70** 979
- [5] Schmittmann B and Zia R 1995 *Phase Transitions and Critical Phenomena* vol 17, ed C Domb and J Lebowitz (London: Academic)
- [6] MacDonald C, Gibbs J and Pipkin A 1968 *Biopolymers* **6** 1
- [7] Howard J 2001 *Mechanics of Motor Proteins and the Cytoskeleton* (Sunderland: Sinauer)
- [8] Hirokawa N 1998 *Science* **279** 519
- [9] Helbing D 2001 *Rev. Mod. Phys.* **73** 1067
- [10] Chowdhury D, Santen L and Schadschneider A 2000 *Phys. Rep.* **329** 199
- [11] Derrida B and Evans M 1997 *Nonequilibrium Statistical Mechanics in One Dimension* ed V Privman (Cambridge: Cambridge University Press) pp 277–304
- [12] Mukamel D 2000 *Soft and Fragile Matter* ed M Cates and M Evans (Bristol: Institute of Physics Publishing) pp 237–58
- [13] Schütz G 2001 *Phase Transitions and Critical Phenomena* vol 19, ed C Domb and J Lebowitz (San Diego: Academic) pp 3–251
- [14] Krug J 1991 *Phys. Rev. Lett.* **67** 1882
- [15] Odor G 2004 *Rev. Mod. Phys.* **76** 663
- [16] Täuber U C, Howard M J and Hinrichsen H 1998 *Phys. Rev. Lett.* **80** 2165
- [17] Noh J D and Park H 2005 *Phys. Rev. Lett.* **94** 145702
- [18] Dagotto E and Rice T M 1996 *Science* **271** 618
- [19] Reichenbach T, Franosch T and Frey E 2006 *Phys. Rev. Lett.* **97** 050603
- [20] Zutic I, Fabian J and Sarma S D 2004 *Rev. Mod. Phys.* **76** 323
- [21] Hahn C K, Park Y J, Kim E K and Min S 1998 *Appl. Phys. Lett.* **73** 2479
- [22] Hinsch H, Kouyos R and Frey E 2006 *Traffic and Granular Flow '05* ed A Schadschneider, T Pöschel, R Kühne, M Schreckenberg and D E Wolf (Berlin: Springer)
- [23] Popkov V and Peschel I 2001 *Phys. Rev. E* **64** 026126
- [24] Popkov V and Schütz G M 2003 *J. Stat. Phys.* **112** 523
- [25] Popkov V 2004 *J. Phys. A: Math. Gen.* **37** 1545
- [26] Pronina E and Kolomeisky A B 2004 *J. Phys. A: Math. Gen.* **37** 9907
- [27] Mitsudo T and Hayakawa H 2005 *J. Phys. A: Math. Gen.* **38** 3087
- [28] Pronina E and Kolomeisky A B 2006 *Physica A* **372** 12
- [29] Parmeggiani A, Franosch T and Frey E 2003 *Phys. Rev. Lett.* **90** 086601
- [30] Parmeggiani A, Franosch T and Frey E 2004 *Phys. Rev. E* **70** 046101
- [31] Reichenbach T, Franosch T and Frey E in preparation
- [32] Shaw L B, Zia R K P and Lee K H 2003 *Phys. Rev. E* **68** 021910
- [33] Pierobon P, Franosch T and Frey E 2006 *Phys. Rev. E* **74** 031920
- [34] Derrida B 1998 *Phys. Rep.* **301** 65
- [35] Klumpp S and Lipowsky R 2003 *J. Stat. Phys.* **113** 233

Domain wall delocalization, dynamics and fluctuations in an exclusion process with two internal states

Tobias Reichenbach, Thomas Franosch, and Erwin Frey

Arnold Sommerfeld Center for Theoretical Physics (ASC) and Center for NanoScience (CeNS), Department of Physics, Ludwig-Maximilians-Universität München, Theresienstrasse 37, D-80333 München, Germany

Received: date / Revised version: date

Abstract. We investigate the delocalization transition appearing in an exclusion process with two internal states resp. on two parallel lanes. At the transition, delocalized domain walls form in the density profiles of both internal states, in agreement with a mean-field approach. Remarkably, the topology of the system's phase diagram allows for the delocalization of a (localized) domain wall when approaching the transition. We quantify the domain wall's delocalization close to the transition by analytic results obtained within the framework of the domain wall picture. Power-law dependences of the domain wall width on the distance to the delocalization transition as well as on the system size are uncovered, they agree with numerical results.

PACS. 0 5.40.-a, 05.60.-k, 64.60.-i, 72.25.-b

1 Introduction

Driven one-dimensional transport phenomena [1] currently receive much attention as they constitute a challenging class of non-equilibrium dynamical systems. In such systems, collective effects induce unexpected phenomena, including e.g. boundary-induced phase transitions [2] or pattern formation [3]. Possible applications are found in a large variety of contexts, ranging from biology (e.g. the motion of ribosomes along mRNA [4] or molecular motors on intracellular filaments [5,6,7,8,9,10,11]) to electron hopping transport with applied voltage [12,13] and vehicular highway traffic [14,15].

As unifying descriptions of such non-equilibrium systems are still lacking, much effort is devoted to the understanding of particular models and the identification of universal properties as well as analytic methods. In this context, the Totally Asymmetric Exclusion Process (TASEP) has emerged as a paradigm (see e.g. [16,17] for a review). There, particles move unidirectionally from left to right through a one-dimensional lattice. The injection resp. extraction rates at the left resp. right boundaries serve as control parameters; tuning them, different phases of the stationary-state density are observed. Although being exactly solvable [18,19,20], a mean-field (MF) approach already yields the exact phase diagram, originating in an exact MF current-density relation [18]. Beyond MF, fluctuations have been successfully taken into account in the framework of the domain wall picture [21,22]. There, one considers a domain wall separating a low-density (LD) region from a high-density (HD) one. The domain wall's dy-

namics yields information about the phase behavior and boundary effects arising in finite systems.

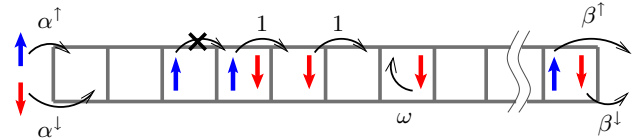


Fig. 1. (Color online) Illustration of an exclusion model with two internal states, denoted as spin-up (\uparrow) and spin-down (\downarrow). Particles are injected at the left boundary at rates $\alpha^\uparrow, \alpha^\downarrow$, and extracted at the right at rates $\beta^\uparrow, \beta^\downarrow$. Within bulk, particles move unidirectionally to the right, or flip their state (at rate ω), always obeying Pauli's exclusion principle.

Recently, we have proposed a generalization of TASEP where particles possess two weakly coupled internal states [13,23]. As an example, these internal states may correspond to different parallel lanes in vehicular traffic on highways [14]. Concerning intracellular transport, microtubules consists of typically 12-14 parallel lanes, and molecular motors progressing on them may (though rarely) switch between these lanes. Our work provides a minimal model that takes such lane changes into account. Also, the internal states may describe spin states of electrons, e.g., when performing hopping transport through a chain of quantum dots [12], suggesting possible application of our model to spintronics devices.

In the subsequent paper, we adopt the language of spins for the internal states. The system's dynamics, de-

scribed in the following, is depicted in Fig. 1. Particles with spin-up (down) state enter at the left boundary at rate α^\uparrow (α^\downarrow), under the constraint of Pauli's exclusion principle. The latter means that each lattice site may at most be occupied by one particle of a given state, such that particles with spin-up and spin-down may share one site, but no two spin-up or spin-down particles are allowed. (In the context of multi-lane traffic, this translates into simple site exclusion.) Within the lattice, particles hop to the neighboring right lattice site at constant rate (which we set to unity), again respecting Pauli's exclusion principle. Spin flip events may occur, we denote the respective rate by ω . Finally, particles are extracted at the right boundary at rate β^\uparrow (β^\downarrow), depending on their spin state.

In [13, 23] we have taken advantage of a MF approach in a continuum limit, see e.g. [24] for a review, to describe the emerging non-equilibrium stationary density profiles. Comparison to data from stochastic simulations has, through finite size scaling, uncovered an apparent exactness of the analytic results in the limit of large system sizes. We have traced back this exactness to the weak coupling of the two internal states, see below, as well as the exactness of the MF approach for TASEP [16]. As it implies the exactness of the analytically derived phase diagrams (see Fig. 2 for a two-dimensional cut), we have full knowledge of the system's phase behavior. The latter exhibits a rich variety of phases, in particular, a localized domain wall, separating a low-density (LD) from a high-density (HD) region, may emerge in the density profile of one spin state. We refer to this situation as a coexistence of LD and HD, abbreviated as LD-HD. Continuous as well as discontinuous transitions between the different phases appear and induce multicritical points (e.g. \mathcal{A}_{IN} and \mathcal{A}_{EX} in Fig. 2). Hereby, as we already announced in [13, 23], domain wall delocalization appears at the discontinuous transition. Namely, as an example, consider the red (grey) line in Fig. 2. It crosses a discontinuous transition, which separates two LD-HD phases. In both, localized domain walls emerge, but at different positions in bulk. Upon crossing the delocalization transition along the red line, the domain wall delocalizes, and then localizes again at a different position. The aim of this article is the investigation of the domain wall's delocalization process when approaching the discontinuous transition.

In this paper, we present detailed investigations on the delocalization transition. Starting from MF considerations, we show that at the transition line delocalized domain walls appear in the density profiles of both spin states. More precise, the MF approach predicts a one-parameter family of solutions with domain walls for spin-up and spin-down, which we conclude to perform coupled random walks. Further on, including fluctuations via the domain wall picture allows to quantify the delocalization of a localized domain wall when approaching the delocalization transition, e.g. along the path depicted in red (or grey) in Fig. 2.

The outline of this paper is the following. In the next section we review the MF approach (see our previous article [23] for a detailed discussion), and present the solu-

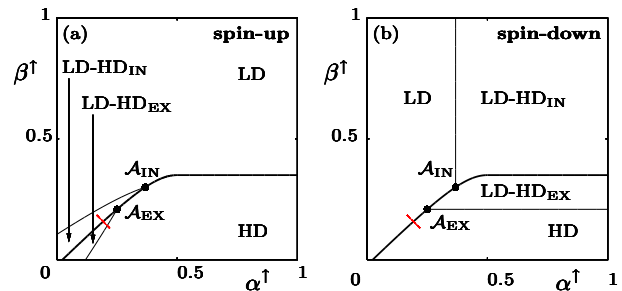


Fig. 2. Phase diagrams for the density of spin-up (a) and spin-down (b): two-dimensional cuts for fixed values of $\alpha^\downarrow = 0.25$, $\beta^\downarrow = 0.3$ and in the asymptotic limit of large Ω . Hereby, $\Omega = \omega/L$ is the gross spin flip rate. Lines of continuous transitions (thin) intersect the delocalization transition line (bold) in multicritical points \mathcal{A}_{IN} and \mathcal{A}_{EX} . The scope of this paper is to elucidate the system's behavior at the delocalization transition as well as when approaching the latter along the path shown in red (or grey).

tion for the density profiles at the delocalization transition line. The solution turns out to be not unique, but is a one-parameter family, indicating the delocalization. Our stochastic simulations are described in Section 3. Section 4 goes beyond MF by taking fluctuations into account. Within the domain wall picture, we investigate the delocalization of a domain wall when approaching the delocalization transition. As a result, we find power law dependences for the width of the domain wall distribution on the system size and the distance to the delocalization transition line. Our conclusions are presented in Sec. 5.

2 Predictions from the mean-field approach

We are interested in the stationary density profiles which emerge in the system's non-equilibrium steady state. Therefore, denote the occupation number of site i for spin-up resp. spin-down state by n_i^\uparrow resp. n_i^\downarrow , i.e. $n_i^{\uparrow(\downarrow)} \in \{0, 1\}$, depending on whether this site is occupied by a particle with corresponding spin state or not. Performing sample averages, we obtain the average occupation, $\rho_i^{\uparrow(\downarrow)} \equiv \langle n_i^{\uparrow(\downarrow)} \rangle$. In the mean-field (MF) approximation, higher order correlations between the occupation numbers are neglected, i.e. we assume

$$\langle n_i^r n_j^s \rangle = \rho_i^r \rho_j^s; \quad r, s \in \{\uparrow, \downarrow\}. \quad (1)$$

The dynamical rules of the system lead to equations for the densities in the stationary state; see Ref. [23] for a detailed discussion. Further on, in a continuum limit, the total length of the lattice is set to unity and the limit of number of lattice sites $L \rightarrow \infty$ is considered. Hereby, the densities $\rho_i^{\uparrow(\downarrow)}$ approximate smooth functions $\rho^{\uparrow(\downarrow)}(x)$ with $x \in [0, 1]$; for the latter, we eventually obtain two coupled differential equations:

$$\partial_x j^\uparrow = \Omega[\rho^\downarrow - \rho^\uparrow], \quad \partial_x j^\downarrow = \Omega[\rho^\uparrow - \rho^\downarrow]. \quad (2)$$

Here, we have defined currents for the individual spin states: $j^{\uparrow(\downarrow)}(x) = \rho^{\uparrow(\downarrow)}(x)[1 - \rho^{\uparrow(\downarrow)}(x)]$. Also, the gross spin flip rate $\Omega = \omega L$ was introduced; in a mesoscopic scaling, we keep this rate fixed when performing the limit $L \rightarrow \infty$, see Refs. [25,26]. In this way, competition between the bulk processes (spin flips) and the boundary processes (particle injection and extraction) emerges. This weak coupling is opposed to strong coupling, where ω is kept constant when considering large systems, which leads to different effects [27,28,29]. A closed analytic form for the solution to Eqs. (2) is feasible and has been presented in [23].

The injection and extraction processes lead to boundary conditions for Eqs. (2):

$$\begin{aligned} \rho^{\uparrow}(0) &= \alpha_{\text{eff}}^{\uparrow}, \\ \rho^{\downarrow}(0) &= \alpha_{\text{eff}}^{\downarrow}, \\ \rho^{\uparrow}(1) &= 1 - \beta_{\text{eff}}^{\uparrow}, \\ \rho^{\downarrow}(1) &= 1 - \beta_{\text{eff}}^{\downarrow}, \end{aligned} \quad (3)$$

where we have introduced effective rates $\alpha_{\text{eff}}^{\uparrow(\downarrow)}, \beta_{\text{eff}}^{\uparrow(\downarrow)}$ according to

$$\begin{aligned} \alpha_{\text{eff}}^{\uparrow(\downarrow)} &= \min\left[\alpha^{\uparrow(\downarrow)}, \frac{1}{2}\right], \\ \beta_{\text{eff}}^{\uparrow(\downarrow)} &= \min\left[\beta^{\uparrow(\downarrow)}, \frac{1}{2}\right]. \end{aligned} \quad (4)$$

They reflect the fact that bulk processes limit the individual spin currents to maximal values of $1/4$, corresponding to densities of $1/2$. Injection or extraction rates exceeding this value cannot lead to larger currents, but effectively act as $1/2$ (see [23]).

The boundary conditions (3) apparently overdetermine the system of two differential equations (2). Indeed, two types of singularities may occur where the densities exhibit discontinuities: boundary layers (discontinuity at the boundary) and domain walls (discontinuity in bulk). An analytic description of the domain wall positions is feasible from the observation that the spin currents $j^{\uparrow(\downarrow)}(x) = \rho^{\uparrow(\downarrow)}(x)[1 - \rho^{\uparrow(\downarrow)}(x)]$ at these positions must be continuous. The only solution to this condition is that a density $\rho^{\uparrow(\downarrow)}$ changes to the new value $1 - \rho^{\uparrow(\downarrow)}$ at the position of the discontinuity.

As particles cannot leave the system in bulk, the particle current $J = j^{\uparrow} + j^{\downarrow}$ is spatially conserved. In case that no boundary layer occurs at the left, i.e. the densities do not have any discontinuities there, it is given from (3) by the value $J_{\text{IN}} = \alpha_{\text{eff}}^{\uparrow}(1 - \alpha_{\text{eff}}^{\downarrow}) + \alpha_{\text{eff}}^{\downarrow}(1 - \alpha_{\text{eff}}^{\uparrow})$. In this case, the system is dominated by injection processes; we refer to the region in parameter space, where this behavior occurs, as the IN-region. On the other hand, also extraction can determine the system's behavior, the particle current is then given by $J_{\text{EX}} = \beta_{\text{eff}}^{\uparrow}(1 - \beta_{\text{eff}}^{\downarrow}) + \beta_{\text{eff}}^{\downarrow}(1 - \beta_{\text{eff}}^{\uparrow})$, occurring in the EX-region.

The *delocalization transition* occurs at $J_{\text{IN}} = J_{\text{EX}}$. There, the system is in a superposition of the injection dominated and the extraction dominated behavior. In this

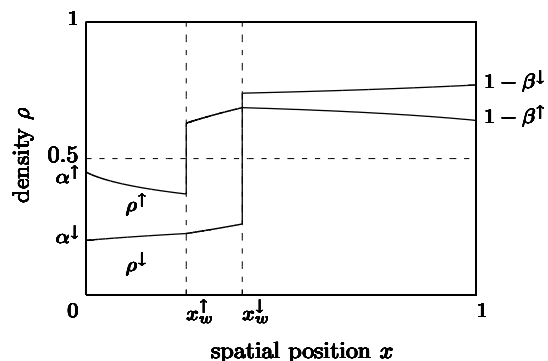


Fig. 3. Domain walls in the densities of both spin states at the delocalization transition: results from the MF approach. The positions of the domain walls are only determined up to one degree of freedom: choosing the position x_w^{\uparrow} for the domain wall of spin-up yields the position x_w^{\downarrow} for spin-down and vice versa. The densities found in stochastic simulations are the average over this one-parameter family of solutions. Parameters are $\alpha^{\uparrow} = 0.45$, $\alpha^{\downarrow} = 0.2$, $\beta^{\uparrow} = 0.36$, $\beta^{\downarrow} = 0.23$ and $\Omega = 0.3$.

situation, delocalized domain walls appear in the density profiles of *both* spin states. Indeed, only when $J_{\text{IN}} = J_{\text{EX}}$, density profiles satisfying the boundary conditions at the left boundary as well as at the right one are feasible. Instead of discontinuities at the boundaries, they exhibit discontinuities within bulk: domain walls. In the following, we want to present the MF picture for the density behavior at the delocalization transition and show that a one-parameter family of solutions emerges within the MF approach.

2.1 The one-parameter family of analytic solutions

The generic picture of the MF analytic solution at the delocalization transition is presented in Fig. 3. As the equation $J_{\text{IN}} = J_{\text{EX}}$ is fulfilled, the density profiles can match the left as well as the right boundary conditions. This implies that, in bulk, domain walls arise at positions x_w^{\uparrow} and x_w^{\downarrow} in spin-up resp. spin-down state; we have chosen $x_w^{\uparrow} < x_w^{\downarrow}$, the other case is obtained by the symmetry of the two spin states. In the vicinity of the left boundary, the densities are given by the analytic solution $\rho_l^{\uparrow,\downarrow}$ obeying the left boundary conditions $\rho_l^{\uparrow}(x=0) = \alpha_{\text{eff}}^{\uparrow}$, $\rho_l^{\downarrow}(x=0) = \alpha_{\text{eff}}^{\downarrow}$. At the point x_w^{\uparrow} , the density of spin-up jumps from the value $\rho_l^{\uparrow}(x_w^{\uparrow})$ to the value $1 - \rho_l^{\uparrow}(x_w^{\uparrow})$, while the density of spin-down is continuous. To the right of x_w^{\uparrow} , the densities follow a different branch of analytic solution, we name it $\rho_m^{\uparrow,\downarrow}$ as the intermediate branch. It is determined by the boundary conditions $\rho_m^{\uparrow}(x_w^{\uparrow}) = 1 - \rho_l^{\uparrow}(x_w^{\uparrow})$ and $\rho_m^{\downarrow}(x_w^{\uparrow}) = \rho_l^{\downarrow}(x_w^{\uparrow})$. At the point x_w^{\downarrow} , the density of spin-down changes discontinuously from a value $\rho_m^{\downarrow}(x_w^{\downarrow})$ to a value $1 - \rho_m^{\downarrow}(x_w^{\downarrow})$, while the density of spin-up remains continuous. To the right of x_w^{\downarrow} , the densities obey the analytic solution $\rho_r^{\uparrow,\downarrow}$ satisfying the boundary conditions at the right: $\rho_r^{\uparrow}(x=1) = 1 - \beta_{\text{eff}}^{\uparrow}$, $\rho_r^{\downarrow}(x=1) = 1 - \beta_{\text{eff}}^{\downarrow}$.

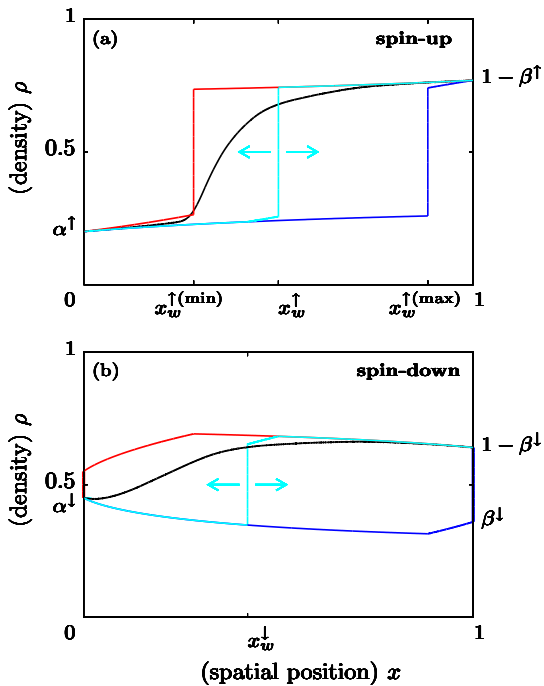


Fig. 4. (Color online) Analytic versus numerical results for the density profiles at the delocalization transition. The analytic approach predicts a one-parameter family of solutions, we show the one with the minimal domain wall positions (red or grey) and with the maximal one (blue or dark grey) as well as an intermediate (light blue or light grey). Stochastic simulations yield an average over these solutions, resulting in densities interpolating between the extrema (black). Parameters are the same as in Fig. 3.

Now, for the situation to be feasible, we have additional conditions coming from considering the continuity of the spin currents at the point x_w^\downarrow , namely $\rho_r^\uparrow(x_w^\downarrow) = \rho_m^\uparrow(x_w^\downarrow)$ and $\rho_r^\downarrow(x_w^\downarrow) = 1 - \rho_m^\downarrow(x_w^\downarrow)$. As the particle current is conserved, these two conditions are not independent: the validity of one implies the validity of the other. Only one condition thus exists for two variables, the latter being the positions of the domain walls x_w^\uparrow and x_w^\downarrow . Our considerations therefore leave us with a one-parameter family of solutions; as parameter, we can e.g. take one of the domain wall positions, x_w^\uparrow or x_w^\downarrow .

2.2 Spatial boundaries for the domain walls

In the course of time, the system takes all states specified by the one-parameter family of solutions. Averaged over sufficiently long times, the densities represent the average over the latter, resulting in a smoothing of the density profiles. In Fig. 4, we show how the results may look like. We observe that certain spatial boundaries ($x_w^{\uparrow(\min)}$ and $x_w^{\uparrow(\max)}$ in the above picture) exist. They define the bulk region where the domain walls may appear. The description of these boundaries is the scope of this subsection.

The boundaries for the residence regions of the domain walls originate in the constraint that the domain wall positions must lie between 0 and 1. Indeed, let us consider the minimal positions $x_w^{\uparrow(\min)}$, $x_w^{\downarrow(\min)}$ which are feasible for the domain walls in the spin-up and spin-down state. We had found in Subsec. 2 that fixing the domain wall position in the density profile of one of the states determines the position of the other domain wall. The situation $x_w^{\downarrow(\min)} = x_w^{\uparrow(\min)} = 0$ can thus only emerge if $x_w^{\downarrow(\min)} = 0$ induces $x_w^{\uparrow(\min)} = 0$ (corresponding to the multicritical point \mathcal{A}_{IN} , see the detailed discussion in Ref. [23]). In general, only one of these minimal domain wall positions is at 0, and induces a minimal position for the other one which is larger than 0. Analogously, in general, a maximal domain wall position of 1 only occurs for one of the spin states, and induces a domain wall position smaller than 1 for the other. The exceptional case $x_w^{\downarrow(\max)} = x_w^{\uparrow(\max)} = 1$ occurs at the multicritical point \mathcal{A}_{EX} , as the latter lies at the transition from a coexistence phase to a HD phase, for both spin states, see Ref. [23]

Which situation occurs, may be read off from the phase diagrams by considering the phases in the vicinity of the delocalization transition. As an example, we consider a point on the delocalization transition line in Fig. 2 (a), (b), at the intersection with the path shown in red. In its vicinity, in the EX-region, the density of spin-down is in a pure HD-phase, such that a domain wall at position $x_w^\downarrow = 0$ forms there when approaching the delocalization transition. The density of spin-up exhibits a localized shock at a position $0 < x_w^\uparrow < 1$. We thus observe $x_w^{\downarrow(\min)} = 0$ and $0 < x_w^{\uparrow(\min)} < 1$. Similarly, considering the IN-region in the vicinity of this point yields the maximal feasible domain wall positions there: $x_w^{\downarrow(\max)} = 1$ and $0 < x_w^{\uparrow(\max)} < 1$.

The analytic solutions to the density profiles in the situation of $x_w^{\uparrow(\min)}$, $x_w^{\downarrow(\min)}$ (red) as well as for $x_w^{\uparrow(\max)}$, $x_w^{\downarrow(\max)}$ (blue) are shown in Fig. 4. The intermediate solution (light blue) varies between these two extrema. In the system, averaged over sufficiently long time, this results in smoothed density profiles. In Fig. 4 we show the results from stochastic simulations as black lines, agreeing with our analytic considerations.

3 Stochastic simulation methods

To validate our analytic calculations, we have carried out extensive stochastic simulations. An efficient simulation method originally due to Gillespie [30, 31] was implemented. There, in each time step, a random number determines whether particle injection, particle extraction, a spin flip event or a particle hopping forward may occur in the next time step. The time interval to the next process is chosen from an exponential waiting time distribution.

Simulations in the neighborhood of the delocalization transition need long waiting times until the densities reach stationary profiles, due to the random walks performed by the domain walls. We carried out simulations with up to

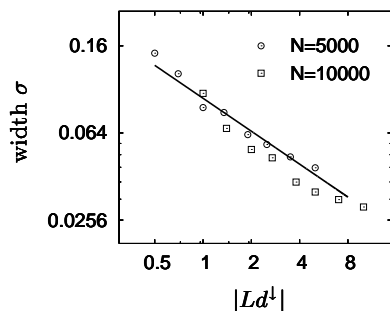


Fig. 5. The width σ of the domain wall distribution in the spin-up density profile for the case of a localized domain wall there, at a small distance d^\downarrow to the delocalization transition. Numerical results are shown in a double logarithmic scale, depending on $|Ld^\downarrow|$. The data are obtained from system sizes of $L = 5000$ (open circles) and $L = 10000$ (open boxes), with d^\downarrow varied between 1×10^{-4} and 1×10^{-3} . The solid line indicates the slope $-\frac{1}{2}$. Approximately, we recover $\sigma \sim |Ld^\downarrow|^{-1/2}$.

10^8 time windows, each consisting of $10 \times L$ steps of updating. An example of resulting density profiles is given in Fig. 4 for a point on the delocalization transition line, the densities are observed to interpolate between two extremal analytic solutions.

In the subsequent section, we investigate the scaling of the width σ of the domain wall when approaching the delocalization transition. For the numerical data, we have computed the stationary density profiles for system sizes of $L = 5000$ and $L = 1000$ at different distances to the delocalization transition. The width σ was obtained by fitting the densities profiles in the vicinity of the domain wall with the function $A \cdot \text{erf}[(x - b)/\sigma] + C + Dx$, with parameters A, b, C, D, σ . The first term describes a Gaussian distribution of the domain wall, while the latter two terms account for the background density profile (to linear order in x). The results are shown in Fig. 5 and agree well with the analytic predictions. We attribute deviations to the fact that for large σ the above fitting becomes less accurate as the domain wall distribution deviates from a gaussian.

4 Beyond mean-field: Approaching the delocalization transition

In the previous Sections, we have described how delocalized domain walls in the density profiles of both states appear at the delocalization transition. Here, we investigate the emergence of delocalization when approaching the delocalization line by applying the domain wall picture. Including fluctuations, the latter allows us to calculate the width of the domain wall distribution for finite system sizes L . It diverges as one approaches the delocalization line, yielding delocalized domain walls.

4.1 The domain wall picture

The domain wall picture [21] allows to include fluctuations, such as the particle-number fluctuations in the TASEP [22], helping in understanding its dynamics [32], and thus go beyond the MF approximation. In this approach, we start with the assumption that sharp and localized domain walls appear in the density profiles of both states. Injection and extraction of particles as well as spin-flips induce dynamics for them, they perform random walks. Our focus is on the emerging stationary state. As the latter arises in a non-equilibrium system, it need not obey detailed balance. Writing down the master equation for the random walk, we are able to calculate the fluctuations of the domain wall positions around the stationary values, yielding the width of the domain walls or boundary layers which form in finite systems.

The dynamics induced by entering and exiting particles or spin-flips is the following. If the total number of particles of given internal state in the system is increased by one, the domain wall in the density profile of this state moves a certain value to the left. In the other case, if the number of particles of given state is decreased by one, the domain wall of this state moves to the right.

Denote Δ_\uparrow resp. Δ_\downarrow the height of the domain wall in the density profile of the spin-up resp. spin-down states. They are functions of the domain wall positions: $\Delta_\uparrow = \Delta_\uparrow(x_w^\uparrow, x_w^\downarrow)$, $\Delta_\downarrow = \Delta_\downarrow(x_w^\uparrow, x_w^\downarrow)$. Increasing the number of spin-up particles by one shifts the position x_w^\uparrow by the value $\delta x_w^\uparrow = -L^{-1}\Delta_\uparrow^{-1}$, and decreasing its number results in a shift $\delta x_w^\uparrow = L^{-1}\Delta_\uparrow^{-1}$. The changes δx_w^\downarrow result analogously from particles with spin-down entering and exiting.

4.2 Fokker-Planck equation and the generic form of the domain wall distribution

In our model, six processes alter the particle number of one or both internal states:

- (i) A particle with spin-up entering at the left boundary
- (ii) A particle with spin-up leaving at the right boundary
- (iii) A particle with spin-down entering at the left boundary
- (iv) A particle with spin-down leaving at the right boundary
- (v) A particle with spin-up flipping to spin-down in bulk
- (vi) A particle with spin-down flipping to spin-up in bulk

Their probabilities and resulting changes δx_w^\uparrow , δx_w^\downarrow are listed in Tab. 1.

To shorten our expressions, we introduce the vectors $\underline{x}_w = (x_w^\uparrow, x_w^\downarrow)$ and $\delta \underline{x}_w = (\delta x_w^\uparrow, \delta x_w^\downarrow)$. Defining $P(\underline{x}_w, t)$ as the probability density of finding the domain wall positions x_w^\uparrow , x_w^\downarrow at time t , the processes (i)-(vi) allow us to

Process	Probability \mathcal{W}	δx_w^\uparrow	δx_w^\downarrow
(i)	$\alpha_{\text{eff}}^\uparrow(1 - \alpha_{\text{eff}}^\uparrow)$	$-L^{-1}\Delta_\uparrow^{-1}$	0
(ii)	$\beta_{\text{eff}}^\downarrow(1 - \beta_{\text{eff}}^\downarrow)$	$L^{-1}\Delta_\downarrow^{-1}$	0
(iii)	$\alpha_{\text{eff}}^\downarrow(1 - \alpha_{\text{eff}}^\downarrow)$	0	$-L^{-1}\Delta_\downarrow^{-1}$
(iv)	$\beta_{\text{eff}}^\uparrow(1 - \beta_{\text{eff}}^\uparrow)$	0	$L^{-1}\Delta_\uparrow^{-1}$
(v)	$\Omega \int_0^1 \rho^\uparrow(x)[1 - \rho^\downarrow(x)]dx$	$L^{-1}\Delta_\uparrow^{-1}$	$-L^{-1}\Delta_\downarrow^{-1}$
(vi)	$\Omega \int_0^1 \rho^\downarrow(x)[1 - \rho^\uparrow(x)]dx$	$-L^{-1}\Delta_\uparrow^{-1}$	$L^{-1}\Delta_\downarrow^{-1}$

Table 1. Six processes lead to changes in the domain wall positions. This table lists their probabilities and resulting changes δx_w^\uparrow , δx_w^\downarrow .

write down the master equation

$$\partial_t P(\underline{x}_w, t) = \sum_{\delta \underline{x}_w} \left\{ P(\underline{x}_w + \delta \underline{x}_w, t) \mathcal{W}(\underline{x}_w + \delta \underline{x}_w \rightarrow \underline{x}_w) - P(\underline{x}_w, t) \mathcal{W}(\underline{x}_w \rightarrow \underline{x}_w + \delta \underline{x}_w) \right\}. \quad (5)$$

The transition probabilities $\mathcal{W}(\underline{x}_w \rightarrow \underline{x}_x + \delta \underline{x}_w)$ are the ones listed in Tab. 1.

For the expectation values of the changes δx_w^\uparrow , δx_w^\downarrow we obtain

$$\begin{aligned} \langle \delta x_w^\uparrow \rangle &= L^{-1} \Delta_\uparrow^{-1} \left\{ \beta_{\text{eff}}^\uparrow(1 - \beta_{\text{eff}}^\uparrow) - \alpha_{\text{eff}}^\uparrow(1 - \alpha_{\text{eff}}^\uparrow) \right. \\ &\quad \left. + \Omega \int_0^1 [\rho^\uparrow(x) - \rho^\downarrow(x)] dx \right\}, \\ \langle \delta x_w^\downarrow \rangle &= L^{-1} \Delta_\downarrow^{-1} \left\{ \beta_{\text{eff}}^\downarrow(1 - \beta_{\text{eff}}^\downarrow) - \alpha_{\text{eff}}^\downarrow(1 - \alpha_{\text{eff}}^\downarrow) \right. \\ &\quad \left. + \Omega \int_0^1 [\rho^\downarrow(x) - \rho^\uparrow(x)] dx \right\}, \end{aligned} \quad (6)$$

which, of course, depend on the densities ρ^\uparrow and ρ^\downarrow and thereby on the domain wall positions x_w^\uparrow , x_w^\downarrow . Investigating the fixed point of the random walk, i.e. the values \bar{x}_w^\uparrow , \bar{x}_w^\downarrow where $\langle \delta x_w^\uparrow \rangle = \langle \delta x_w^\downarrow \rangle = 0$, we find as a necessary condition $\alpha_{\text{eff}}^\uparrow(1 - \alpha_{\text{eff}}^\uparrow) + \alpha_{\text{eff}}^\downarrow(1 - \alpha_{\text{eff}}^\downarrow) = \beta_{\text{eff}}^\uparrow(1 - \beta_{\text{eff}}^\uparrow) + \beta_{\text{eff}}^\downarrow(1 - \beta_{\text{eff}}^\downarrow)$, or $J_{\text{IN}} = J_{\text{EX}}$, describing the delocalization transition. Thus, domain walls within the density profiles of *both* states are only feasible there; otherwise, at most one of the domain wall positions, say \bar{x}_w^\uparrow , can lie inside the bulk. The other one, say \bar{x}_w^\downarrow , is driven outside of the system and turns into a boundary layer. We then set $\bar{x}_w^\downarrow = 0$ or $\bar{x}_w^\downarrow = 1$, depending on whether a HD or a LD phase occurs. With this convention, the values \bar{x}_w^\uparrow , \bar{x}_w^\downarrow are given by the MF analytic solution.

We are interested in the fluctuations of the domain wall positions around the mean values \bar{x}_w^\uparrow , \bar{x}_w^\downarrow , and therefore define the quantities

$$\begin{aligned} y^\uparrow &= x_w^\uparrow - \bar{x}_w^\uparrow, \\ y^\downarrow &= x_w^\downarrow - \bar{x}_w^\downarrow, \end{aligned} \quad (7)$$

as the deviations. Again, they are arranged in a vector $\underline{y} = (y^\uparrow, y^\downarrow)$, and we have $\delta \underline{y} = \delta \underline{x}_w$.

Applying the Kramers-Moyal expansion [33] of the master equation (5) around the mean-field values to second order in the quantities y^\uparrow , y^\downarrow results in the Fokker-Planck equation

$$\partial_t P(\underline{y}, t) = -\partial_i [a_i(\underline{y}) P(\underline{y}, t)] + \frac{1}{2} \partial_i \partial_j [B_{ij}(\underline{y}) P(\underline{y}, t)]. \quad (8)$$

Here, the indices i, j stand for spin-up and spin-down. In the above equation, the summation convention implies summation over them. The partial derivative ∂_i is the short-hand notation of $\partial/\partial y^i$.

The quantities a_i and B_{ij} are, according to the Kramers-Moyal expansion:

$$\begin{aligned} a_i(\underline{y}) &= \sum_{\delta \underline{y}} \delta y^i \mathcal{W}(\underline{y} \rightarrow \underline{y} + \delta \underline{y}), \\ B_{ij}(\underline{y}) &= \sum_{\delta \underline{y}} \delta y^i \delta y^j \mathcal{W}(\underline{y} \rightarrow \underline{y} + \delta \underline{y}). \end{aligned} \quad (9)$$

For our case, they are given in App. A.

Now, we expand the Fokker-Planck equation around $\underline{y} = 0$, using the linear noise approximation of van Kampens Ω -expansion [34]. As $B_{ij}(\underline{y} = 0) \neq 0$, we consider approximately $B_{ij}(\underline{y}) \approx B_{ij}(\underline{y} = 0) \equiv B_{ij}$. On the other hand, $a_i(\underline{y} = 0) = 0$ is possible, and we include the first order:

$$a_i(\underline{y}) \approx a_i(\underline{y} = 0) + y^j \partial_j a_i(\underline{y})|_{\underline{y}=0}. \quad (10)$$

Defining $A_{ij} = \partial_j a_i(\underline{y})|_{\underline{y}=0}$ and $a_i \equiv a_i(\underline{y} = 0)$, the Fokker-Planck equation (8) turns into

$$\begin{aligned} \partial_t P(\underline{y}, t) &= -a^i \partial_i P(\underline{y}, t) - \partial_i [A_{ij} y^j P(\underline{y}, t)] \\ &\quad + \frac{1}{2} B_{ij} \partial_i \partial_j P(\underline{y}, t). \end{aligned} \quad (11)$$

The above expanded Fokker-Planck equation may be solved by the ansatz

$$P(\underline{y}, t) \sim \exp \left[-\frac{1}{2} (\Sigma^{-1})_{ij} y^i y^j + \xi_i^{-1} y^i \right], \quad (12)$$

which is the generic form of the domain wall resp. boundary layer distribution. When put into Eq. (11), it leads to a matrix equation for Σ :

$$\Sigma A^T + A \Sigma + B = 0, \quad (13)$$

the solution is given in App. A. ξ is then determined by

$$\xi_i^{-1} = -(\Sigma^{-1})_{ij} A_{jk}^{-1} a_k. \quad (14)$$

Here, we continue by discussing the physical meaning of Σ and ξ . First, assume that a domain wall emerges in the density profile of the spin-up states. Then, \bar{x}_w^\uparrow lies in bulk, and we have $a_\uparrow = 0$. According to Eq. (14), this implies $\xi_\uparrow^{-1} = 0$. The domain wall distribution in the spin-up density is therefore Gaussian and its width given by $(\Sigma_{\uparrow\uparrow})^{1/2}$.

Second, for a boundary layer forming in the density of spin-up states, it follows that $a_\uparrow \neq 0$ and therefore also

$\xi_{\uparrow}^{-1} \neq 0$. As for large enough systems fluctuations are small ($y^{\uparrow}, y^{\downarrow} \ll 1$), the contribution to the domain wall distribution coming from $\xi_{\uparrow}^{-1} y^{\uparrow}$ is the dominating one. The value ξ_{\uparrow} thus describes how far the boundary layer extends into bulk, we refer to it as the *localization length*.

4.3 Approaching the coexistence line

When the delocalization line is approached, we know from the MF analysis that domain walls delocalize. In the domain wall picture, this must result in a diverging width of the domain wall resp. boundary layer distributions. In this section, we want to show that this divergence indeed emerges within the above description. Also, we calculate the corresponding exponents and compare our findings to stochastic simulations.

We define the quantities

$$\begin{aligned} d^{\uparrow} &= \beta_{\text{eff}}^{\uparrow}(1 - \beta_{\text{eff}}^{\downarrow}) - \alpha_{\text{eff}}^{\uparrow}(1 - \alpha_{\text{eff}}^{\downarrow}) + \Omega \int_0^1 [\rho^{\uparrow} - \rho^{\downarrow}] dx, \\ d^{\downarrow} &= \beta_{\text{eff}}^{\downarrow}(1 - \beta_{\text{eff}}^{\uparrow}) - \alpha_{\text{eff}}^{\downarrow}(1 - \alpha_{\text{eff}}^{\uparrow}) + \Omega \int_0^1 [\rho^{\downarrow} - \rho^{\uparrow}] dx, \end{aligned} \quad (15)$$

as a measure of distance to the delocalization transition line, where $d^{\uparrow} = d^{\downarrow} = 0$ is encountered. Our aim is to calculate Σ and ξ for $d^{\uparrow}, d^{\downarrow} \rightarrow 0$, i.e. along a path that ends at the coexistence line.

Different paths are possible. Applying the two symmetries of the model, they fall into two classes. First, we may have a localized domain wall in the density of one of the internal states, and a pure LD or HD phase for the other one. In the second class, the densities of both states are in pure LD or HD phases.

Note that the second case is similar to the situation in TASEP. There as well we may approach the coexistence line on a path along which LD or HD is encountered; in this situation, the localization length ξ diverges. In our model, exactly the same behavior emerges: the localization lengths $\xi^{\uparrow}, \xi^{\downarrow}$, describing the boundary layers in the densities of spin-up resp. spin-down state, both diverge.

The first case, corresponding to the path shown in red in Fig. 2, does not possess an analogy to earlier studied ASEP models. Also off the delocalization transition line, we have a domain wall, which is localized. It allows us to study how its width diverges when approaching the IN-EX-boundary, i.e. how its delocalization arises.

We start our considerations with the first case. As a representative example, a situation with a localized domain wall in the spin-up density and a pure LD or HD phase for spin-down is studied. This case implies $d^{\uparrow} = 0$ and $d^{\downarrow} = \beta_{\text{eff}}^{\uparrow}(1 - \beta_{\text{eff}}^{\downarrow}) + \beta_{\text{eff}}^{\downarrow}(1 - \beta_{\text{eff}}^{\uparrow}) - \alpha_{\text{eff}}^{\uparrow}(1 - \alpha_{\text{eff}}^{\downarrow}) - \alpha_{\text{eff}}^{\downarrow}(1 - \alpha_{\text{eff}}^{\uparrow}) \neq 0$. Both $d^{\downarrow} < 0$ and $d^{\downarrow} > 0$ are possible. Our focus is on the width $\sigma = (\Sigma_{\uparrow\uparrow})^{1/2}$ of the domain wall distribution in the spin-up density. More specific, we aim at finding the scaling behavior of σ depending on the

system size L and the distance d^{\downarrow} . We expect that $\sigma \rightarrow 0$ for increasing system size $L \rightarrow \infty$ on the one hand, and that σ diverges for $d^{\downarrow} \rightarrow 0$ on the other hand.

In App. A, we solve the expanded Fokker-Planck equation (11). Considering the solution (26), we recognize that $\Sigma \sim (\det A)^{-1}$, and from (22) we infer $\det A \sim d^{\downarrow}$. Combining these two results, we arrive at $\sigma = (\Sigma_{\uparrow\uparrow})^{1/2} \sim |d^{\downarrow}|^{-1/2}$, such that σ diverges when the delocalization transition line is approached. The mathematical reason is that one eigenvalue of A goes to zero (such that $\det A \rightarrow 0$). Of course, the eigenvector to the vanishing eigenvalue corresponds to the direction along the one-parameter curve on which the mean-field values $\bar{x}_w^{\uparrow}, \bar{x}_w^{\downarrow}$ can reside when the delocalization transition line is reached. Thus, the divergence of the width of the domain wall distribution originates in the one degree of freedom which exists at the delocalization transition.

The dependence of σ on the system size L is also of interest. Remembering $A \sim L^{-1}$ and $B \sim L^{-2}$, and with help of Eq. (26), we arrive at $\sigma \sim L^{-1/2}$. Thus, with increasing L , the domain wall distribution gets sharper aligned to its mean value. Together with the previous result, we obtain the following scaling behavior for the width $\sigma = (\Sigma_{\uparrow\uparrow})^{1/2}$ of the domain wall distribution in the spin-up density:

$$\sigma \sim |Ld^{\downarrow}|^{-1/2}. \quad (16)$$

Comparing these results to stochastic simulations, see Fig. 5, we recover a good agreement.

In the second case, the densities of both states are in pure LD or HD phases, i.e. boundary layers occur in both density profiles. As discussed at the end of Subsec. 4.2, the latter implies $a_{\uparrow}, a_{\downarrow} \neq 0$, thus $\xi_{\uparrow}, \xi_{\downarrow} \neq 0$ and $\xi_{\uparrow}, \xi_{\downarrow}$ are found to be the localization lengths, describing how far the boundary layers extend into bulk. We are thus interested in their scaling behavior.

Both $d^{\uparrow}, d^{\downarrow}$ are different from 0; approaching the delocalization transition line translates into $d^{\uparrow}, d^{\downarrow} \rightarrow 0$. Our starting point is again the solution to the expanded Fokker-Planck equation (11) given in App. A. From Eq. (26) we infer that $\Sigma \sim (\det A)^{-1}$. Together with $a_i \sim d^i$ and Eq. (14), this implies for the localization lengths $\xi_i \sim (d^i)^{-1}$. For the scaling behavior in L , we observe $a_i \sim L^{-1}$ and find $\xi_i \sim L^{-1}$. Together, the scaling behavior is given by

$$\begin{aligned} \xi_{\uparrow} &\sim (Ld^{\uparrow})^{-1}, \\ \xi_{\downarrow} &\sim (Ld^{\downarrow})^{-1}. \end{aligned} \quad (17)$$

As discussed in the beginning of this subsection, the same scaling behavior emerges in TASEP for the localization length ξ of the boundary layer when approaching the coexistence line.

5 Summary

The appearance of a domain wall delocalization is a particular feature of the exclusion process with internal states introduced in Refs. [13, 23]. Indeed, in the simplest driven

exclusion process, the TASEP [2, 16], such a delocalization of a localized domain wall does not emerge. There, boundary layers characterize the different phases. A delocalized domain wall forms at the phase boundary between low- and high-density phases, while localized domain walls do not build up. Upon coupling to external reservoirs [25, 26], localized domain walls may appear in bulk, separating a low-density from a high-density region. Varying the system's parameters, their location changes continuously, and they may leave bulk through the left or the right boundary, causing continuous transitions to pure LD or HD phases. Domain wall delocalization, corresponding to a discontinuous transition, does not emerge.

The exclusion processes with internal states exhibits, in addition to continuous phase transitions similar to the ones described above, *discontinuous transitions*. In particular, in phase space, two regions with localized domain walls may be separated by such a discontinuous transition; there, the domain wall position jumps from a certain location in bulk to another. This jump is connected to a delocalization of the domain wall: Approaching the discontinuous transition, the domain wall delocalizes and, upon crossing the transition, re-localizes at the other position.

We have presented a detailed study of this delocalization phenomenon. First, we have investigated the system's behavior at the discontinuous transition. From mean-field considerations, delocalized domain walls have been identified which perform coupled random walks, resulting in smoothed density profiles that lack sharp shocks. Second, we have investigated the delocalization of a localized domain wall upon approaching the discontinuous transition. Using the domain wall picture, we have set up a quantitative description of the delocalization. Starting from coupled random walks of the domain walls, we have expanded the corresponding Master-equation in the Kramers-Moyal formalism, used the linear noise approximation by van Kampen and obtained an analytically solvable Fokker-Planck equation. The latter has revealed power-law dependences of the domain wall width σ on the distance d to the delocalization transition and the system size L : $\sigma \sim |Ld|^{-1/2}$. These findings have been validated by stochastic simulations.

As in similar driven diffusive systems where a localized domain wall appears [25, 26], the domain wall's width tends to zero with increasing system size, and is proportional to its inverse square root. However, in the present system, the domain wall can delocalize, namely upon approaching the discontinuous transition. There, the width diverges, being proportional to the inverse square root of the distance to the transition.

We believe that the above discussed domain wall delocalization represents a robust and generic phenomenon that may emerge in other driven diffusive system a well, such as weakly coupled antiparallel transport [35] or in models for intracellular transport on multiple lanes that take motors' internal states into account [36, 37]. Its identification in other non-equilibrium systems will shed further light on their universal phenomenology. Its observation in real systems, such as intracellular transport of kinesins

moving on the parallel protofilaments of a microtubulus, constitutes a challenge for future research.

Financial support of the German Excellence Initiative via the program "Nanosystems Initiative Munich" and the German Research Foundation via the SFB TR12 "Symmetries and Universalities in Mesoscopic Systems" is gratefully acknowledged. Tobias Reichenbach acknowledges funding by the Elite-Netzwerk Bayern.

A The Fokker-Planck equation and its solution

In this Appendix, we want to give more details concerning the technical parts of Sec. 4. The coefficients of the Fokker-Planck equation (8) are derived, and the solution to the resulting matrix equation (13) is given.

A.1 The coefficients of the Fokker-Planck equation

The Fokker-Planck equation for the distribution of the domain wall positions reads

$$\partial_t P(\underline{y}, t) = -\partial_i [a_i(\underline{y})P(\underline{y}, t)] + \frac{1}{2} B_{ij} \partial_i \partial_j P(\underline{y}, t). \quad (18)$$

The coefficients a_i and B_{ij} are given by Eqs. (9), we exemplify their calculation for a_\uparrow . According to (9), the latter is connected to the changes y^\uparrow , arising from the processes (i), (ii), (v) and (vi) (see Subsec. 4.2). The changes together with the respective rates are read off from Tab. 1. We obtain

$$\begin{aligned} a_\uparrow(\underline{y}) &= L^{-1} \Delta_\uparrow^{-1} \left[-\alpha_{\text{eff}}^\uparrow (1 - \alpha_{\text{eff}}^\uparrow) + \beta_{\text{eff}}^\uparrow (1 - \beta_{\text{eff}}^\uparrow) \right. \\ &\quad \left. + \Omega \int_0^1 \rho^\uparrow [1 - \rho^\downarrow] dx - \Omega \int_0^1 \rho^\downarrow [1 - \rho^\uparrow] dx \right] \\ &= L^{-1} \Delta_\uparrow^{-1} d^\uparrow, \end{aligned} \quad (19)$$

where we used the definitions (15) for the distances $d^{\uparrow, \downarrow}$ to the delocalization transition. The other coefficients are obtained along the same lines; together, they read

$$\begin{aligned} a_\uparrow(\underline{y}) &= L^{-1} \Delta_\uparrow^{-1} d^\uparrow, \\ a_\downarrow(\underline{y}) &= L^{-1} \Delta_\downarrow^{-1} d^\downarrow, \\ B_{\uparrow\uparrow}(\underline{y}) &= L^{-2} \Delta_\uparrow^{-2} \left\{ \alpha^\uparrow (1 - \alpha^\uparrow) + \beta^\uparrow (1 - \beta^\uparrow) + \Omega j^{\text{tot}} \right. \\ &\quad \left. + \Omega \int_0^1 [\rho^\uparrow(x) - \rho^\downarrow(x)]^2 dx \right\}, \\ B_{\uparrow\downarrow}(\underline{y}) &= -L^{-2} \Delta_\uparrow^{-1} \Delta_\downarrow^{-1} \left\{ \Omega j^{\text{tot}} \right. \\ &\quad \left. + \Omega \int_0^1 [\rho^\uparrow(x) - \rho^\downarrow(x)]^2 dx \right\}, \\ B_{\downarrow\downarrow}(\underline{y}) &= L^{-2} \Delta_\downarrow^{-2} \left\{ \alpha^\downarrow (1 - \alpha^\downarrow) + \beta^\downarrow (1 - \beta^\downarrow) + \Omega j^{\text{tot}} \right. \\ &\quad \left. + \Omega \int_0^1 [\rho^\uparrow(x) - \rho^\downarrow(x)]^2 dx \right\}. \end{aligned} \quad (20)$$

For the expanded Fokker-Planck equation (11), the matrix elements A_{ij} are given as the derivatives $A_{ij} = \partial_j a_i(\underline{y})|_{\underline{y}=0}$:

$$\begin{aligned} A_{\uparrow\uparrow} &= -L^{-1}\Delta_{\uparrow}^{-2}(\partial_{\uparrow}\Delta_{\uparrow})d^{\uparrow} - L^{-1}, \\ A_{\uparrow\downarrow} &= -L^{-1}\Delta_{\uparrow}^{-2}(\partial_{\downarrow}\Delta_{\uparrow})d^{\uparrow} + L^{-1}\Delta_{\uparrow}^{-1}\Delta_{\downarrow}, \\ A_{\downarrow\uparrow} &= -L^{-1}\Delta_{\downarrow}^{-2}(\partial_{\uparrow}\Delta_{\downarrow})d^{\downarrow} + L^{-1}\Delta_{\downarrow}^{-1}\Delta_{\uparrow}, \\ A_{\downarrow\downarrow} &= -L^{-1}\Delta_{\downarrow}^{-2}(\partial_{\downarrow}\Delta_{\downarrow})d^{\downarrow} - L^{-1}. \end{aligned} \quad (21)$$

The key point of the analysis is the observation that in the determinant of A ,

$$\begin{aligned} \det A &= L^{-2}\{\Delta_{\uparrow}^{-1}[\Delta_{\uparrow}^{-1}(\partial_{\uparrow}\Delta_{\uparrow}) + \Delta_{\downarrow}^{-1}(\partial_{\downarrow}\Delta_{\uparrow})]d^{\uparrow} \\ &+ \Delta_{\downarrow}^{-1}[\Delta_{\downarrow}^{-1}(\partial_{\downarrow}\Delta_{\downarrow}) + \Delta_{\uparrow}^{-1}(\partial_{\uparrow}\Delta_{\downarrow})]d^{\downarrow} \\ &+ \Delta_{\uparrow}^{-2}\Delta_{\downarrow}^{-2}[(\partial_{\uparrow}\Delta_{\uparrow})(\partial_{\downarrow}\Delta_{\downarrow}) - (\partial_{\downarrow}\Delta_{\uparrow})(\partial_{\uparrow}\Delta_{\downarrow})]d^{\uparrow}d^{\downarrow}\}, \end{aligned} \quad (22)$$

the terms independent of $d^{\uparrow}, d^{\downarrow}$ have canceled. Thus, for $d^{\uparrow}, d^{\downarrow} \rightarrow 0$, we encounter $\det A \rightarrow 0$. We show in the following that this causes the domain walls to delocalize when $d^{\uparrow}, d^{\downarrow} \rightarrow 0$.

A.2 Solution of the Fokker-Planck equation

For the solution of the expanded Fokker-Planck equation (11), we already anticipated the form

$$P(\underline{y}, t) \sim \exp\left[-\frac{1}{2}(\Sigma^{-1})_{ij}y^i y^j + \xi_i^{-1}y^i\right]. \quad (23)$$

To solve the resulting matrix equation

$$\Sigma A^T + A\Sigma + B = 0, \quad (24)$$

for Σ , we write it in vector form:

$$\begin{pmatrix} 2A_{\uparrow\uparrow} & 2A_{\uparrow\downarrow} & 0 \\ A_{\downarrow\uparrow} & A_{\uparrow\uparrow} + A_{\downarrow\downarrow} & A_{\uparrow\downarrow} \\ 0 & 2A_{\downarrow\uparrow} & 2A_{\downarrow\downarrow} \end{pmatrix} \begin{pmatrix} \Sigma_{\uparrow\uparrow} \\ \Sigma_{\uparrow\downarrow} \\ \Sigma_{\downarrow\downarrow} \end{pmatrix} + \begin{pmatrix} B_{\uparrow\uparrow} \\ B_{\uparrow\downarrow} \\ B_{\downarrow\downarrow} \end{pmatrix} = 0. \quad (25)$$

Note that B and Σ are symmetric. The above equation can be inverted to give

$$\begin{pmatrix} \Sigma_{\uparrow\uparrow} \\ \Sigma_{\uparrow\downarrow} \\ \Sigma_{\downarrow\downarrow} \end{pmatrix} = -\frac{1}{2(A_{\uparrow\uparrow} + A_{\downarrow\downarrow}) \det A} \times \begin{pmatrix} \det A + A_{\downarrow\downarrow}^2 & -2A_{\uparrow\downarrow}A_{\downarrow\downarrow} & A_{\uparrow\downarrow}^2 \\ -A_{\downarrow\uparrow}A_{\downarrow\downarrow} & 2A_{\uparrow\uparrow}A_{\downarrow\downarrow} & -A_{\uparrow\uparrow}A_{\uparrow\downarrow} \\ A_{\downarrow\uparrow}^2 & -2A_{\uparrow\uparrow}A_{\downarrow\uparrow} & \det A + A_{\uparrow\uparrow}^2 \end{pmatrix} \begin{pmatrix} B_{\uparrow\uparrow} \\ B_{\uparrow\downarrow} \\ B_{\downarrow\downarrow} \end{pmatrix}. \quad (26)$$

For the scaling behavior, we observe $\Sigma \sim \det A$. When the delocalization transition is approached, as $\det A \rightarrow 0$, also $\Sigma \rightarrow 0$. Thus Σ^{-1} , describing the widths of the domain walls, diverges; and the domain walls delocalize.

References

1. B. Schmittmann and R. K. P. Zia. In C. Domb and J. Lebowitz, editors, *Phase Transitions and Critical Phenomena*, volume 17. Academic Press, London, 1995.
2. J. Krug. Boundary-induced phase transitions in driven diffusive systems. *Phys. Rev. Lett.*, 67:1882, 1991.
3. I. T. Georgiev, B. Schmittmann, and R. K. P. Zia. Anomalous nucleation far from equilibrium. *Phys. Rev. Lett.*, 94:115701, 2005.
4. C. T. MacDonald, J. H. Gibbs, and A. C. Pipkin. Kinetics of biopolymerization on nucleic acid templates. *Biopolymers*, 6:1, 1968.
5. N. Hirokawa. Kinesin and dynein superfamily proteins and the mechanism of organelle transport. *Science*, 279:519–526, 1998.
6. J. Howard. *Mechanics of Motor Proteins and the Cytoskeleton*. Sinauer Press, Sunderland, Massachusetts, 2001.
7. R. Lipowsky, S. Klumpp, and T. M. Nieuwenhuizen. Random walks of cytoskeletal motors in open and closed compartments. *Phys. Rev. Lett.*, 87:108101, 2001.
8. K. Kruse and K. Sekimoto. Growth of fingerlike protrusions driven by molecular motors. *Phys. Rev. E*, 66:031904, 2002.
9. S. Klumpp and R. Lipowsky. Traffic of molecular motors through tube-like compartments. *J. Stat. Phys.*, 113:233, 2003.
10. G. A. Klein, K. Kruse, G. Cuniberti, and F. Jülicher. Filament depolymerization by motor molecules. *Phys. Rev. Lett.*, 94:108102, 2005.
11. H. Hirsch, R. Kouyos, and E. Frey. In A. Schadschneider, T. Pöschel, R. Kühne, M. Schreckenberg, and D. E. Wolf, editors, *Traffic and Granular Flow '05*. Springer, 2006.
12. I. Žutić, J. Fabian, and S. Das Sarma. Spintronics: Fundamentals and applications. *Rev. Mod. Phys.*, 76:323, 2004.
13. T. Reichenbach, T. Franosch, and E. Frey. Exclusion processes with internal states. *Phys. Rev. Lett.*, 97:050603, 2006.
14. D. Helbing. Traffic and related self-driven many-particle systems. *Rev. Mod. Phys.*, 73:1067, 2001.
15. D. Chowdhury, L. Santen, and A. Schadschneider. Statistical physics of vehicular traffic and some related systems. *Phys. Rep.*, 329:199, 2000.
16. B. Derrida. An exactly soluble non-equilibrium system: The asymmetric simple exclusion process. *Phys. Rep.*, 301:65–83, 1998.
17. G. Schütz. In C. Domb and J. Lebowitz, editors, *Phase Transitions and Critical Phenomena*, volume 19, pages 3–251. Academic Press, San Diego, 2001.
18. B. Derrida, E. Domany, and D. Mukamel. An exact solution of a one-dimensional asymmetric exclusion model with open boundaries. *J. Stat. Phys.*, 69:667, 1992.
19. G. M. Schütz and E. Domany. Phase transitions in an exactly soluble one-dimensional exclusion process. *J. Stat. Phys.*, 72:277–296, 1993.
20. B. Derrida, M. R. Evans, V. Hakim, and V. Pasquier. Exact solution of a 1D asymmetric exclusion model using a matrix formulation. *J. Phys. A: Math. Gen.*, 26:1493, 1993.
21. A. B. Kolomeisky, G. M. Schütz, E. B. Kolomeisky, and J. P. Straley. Phase diagram of one-dimensional driven lattice gases with open boundaries. *J. Phys. A: Math. Gen.*, 31(33):6911–6919, 1998.

22. L. Santen and C. Appert. The asymmetric exclusion process revisited: Fluctuations and dynamics in the domain wall picture. *J. Stat. Phys.*, 106:187, 2002.
23. T. Reichenbach, E. Frey, and T. Franosch. Traffic jams induced by rare switching events in two-lane transport. *New J. Phys.*, 9:159, 2007.
24. D. Mukamel. In M. Cates and M. Evans, editors, *Soft and Fragile Matter*, pages 237–258. Institute of Physics Publishing, Bristol, 2000.
25. A. Parmeggiani, T. Franosch, and E. Frey. Phase coexistence in driven one dimensional transport. *Phys. Rev. Lett.*, 90:086601, 2003.
26. A. Parmeggiani, T. Franosch, and E. Frey. The totally asymmetric simple exclusion process with Langmuir kinetics. *Phys. Rev. E*, 70:046101, 2004.
27. B. Schmittmann, J. Krometsch, and R. K. P. Zia. Will jams get worse when slow cars move over? *Europhys. Lett.*, 70:299–305, 2005.
28. E. Pronina and A. B. Kolomeisky. Two-channel totally asymmetric simple exclusion processes. *J. Phys. A: Math. Gen.*, 37:9907, 2004.
29. E. Pronina and A. B. Kolomeisky. Asymmetric coupling in two-channel simple exclusion processes. *Phys. A*, 372:12–21, 2006.
30. D. T. Gillespie. Stochastic simulations of chemical processes. *J. Comp. Phys.*, 22:403, 1976.
31. D. T. Gillespie. Exact simulations of coupled chemical reactions. *J. Phys. Chem.*, 81:2340–2361, 1977.
32. P. Pierobon, A. Parmeggiani, F. von Oppen, and E. Frey. Dynamic correlation functions and Boltzmann Langevin approach for driven one dimensional lattice gas. *Phys. Rev. E*, 72:036123, 2005.
33. U. Täuber. lecture note.
34. N.G. van Kampen. *Stochastic Processes in Physics and Chemistry*. North Holland Publishing Company, first edition, 1981.
35. R. Juhasz. Weakly coupled, antiparallel, totally asymmetric simple exclusion processes. *Phys. Rev. E*, 76:021117, 2007.
36. A. Basu and D. Chowdhury. Traffic of interacting ribosomes on mRNA during protein synthesis: effects of chemo-mechanics of individual ribosomes. *Phys. Rev. E*, 75:021902, 2007.
37. D. Chowdhury and J. Wang. Traffic of single-headed motor proteins KIF1A: effects of lane changing, 2007. arXiv.org:0712.4304.

3 Dynamics of populations in cyclic competition

Cyclic competition of species, as metaphorically described by the children’s game “rock-paper-scissors”, is an intriguing motif of species interactions. When individuals possess spatial degrees of freedom with locally restricted interactions, this type of competition may lead to preserved species coexistence. Non-equilibrium spatial patterns form and ensure biodiversity [43, 99, 100, 101]. We are interested in the impact of stochasticity as well as individuals’ mobility on the stability of diversity as well as the emerging patterns. We develop a suitable classification for the stability/instability of coexistence when population dynamics is stochastic. In this framework, and within a paradigmatic model for cyclically competing species, we demonstrate the existence of a sharp mobility threshold, such that diversity is maintained below, but jeopardized above that value. We show that entangled rotating spiral waves accompany biodiversity.

In Section 3.1, we introduce theoretical concepts of evolutionary dynamics and point out the “paradoxon” of biodiversity, while the rock-paper-scissors interaction motif is presented in Section 3.2. The influence of fluctuations on biodiversity is the subject of Section 3.3; there, we develop a suitable criterion for distinguishing stable from unstable coexistence. We apply the latter to a prototypical model for cyclic competition in Section 3.4 and identify a mobility threshold for biodiversity. Mobility’s influence on the self-organizing patterns is considered in Section 3.5, an entanglement of travelling spiral waves emerges in a suitable continuum limit. These findings are rationalized using stochastic partial differential equations (SPDE) as well as a complex Ginzburg-Landau equation (CGLE). In Section 3.6 we summarize our findings and present possible further directions of research. More detailed descriptions can be found in our publications, which have appeared in *Physical Review E*, *Nature*, *Physical Review Letters* as well as in a submitted manuscript. They are reprinted at the end of this Chapter.

3.1 Biodiversity and evolutionary dynamics

A huge biodiversity is present in the earth’s ecosystems. As a striking example, a 30-g soil sample from a Norwegian forest has been estimated to contain some 20,000 common bacterial species and about 500,000 rare ones [102, 103]. Generally, although biodiversity

seems to decrease from the equator to the poles [104, 105], all ecosystems of our planet, from the tropics [106, 107] to the oceans' deep sea [108, 109, 110, 111], are characterized by large numbers of different species which coexist and coevolve together. This diversity is essential for the viability of ecological systems and often fruitfully increases its productivity [112].

Conceptual explanations of this astonishing biodiversity constitute one of the most striking puzzles in modern theoretical ecology [112, 113]. Indeed, in a naive understanding of Darwinian evolution, two species that live on the same resources would compete until the fitter one (or a random one if evolution mainly operates in a neutral regime [114]) survives. This general argument, known in theoretical ecology as the *competitive exclusion principle*, was first formulated by Gause [40], and applies to the scenario where different species compete for the *same* resources. Segregation of species into ecological niches avoids this situation and constitutes one mechanism for maintaining a high diversity. However, the number of species populating ecosystems seems to considerably exceed the available ecological niches. Although both numbers, the one of the different species as of distinct niches, are, in most situations, very hard to measure, their mismatch becomes apparent when considering plankton. Indeed, a large number of different plankton species live on a very limited number of resources, mainly solar energy and minerals that are dissolved in water; this counterintuitive species diversity is therefore also referred to as *paradox of the plankton* [41, 42].

The investigation of basic mechanisms maintaining a species diversity that is higher than the available different resources is one of the goals of this Thesis. In this Chapter, we study two such ingredients that, if combined, allow for stable coexistence of various species. The first one concerns the type of species' interactions, and is the *rock-paper-scissors competition motif*, introduced in Section 3.2. The second one is spatial segregation of individuals with accompanying locally restricted interactions, see Section 3.4.

The evolutionary dynamics of interacting species poses considerable challenges for a theoretical description. They stem from the large amount of interacting species, each comprising a certain number of individuals. The precise type of competition is mostly only known approximatively, and spatial separation of individuals as well as age structure induce additional complications. A variety of approaches exists, which differ, for example, in the way how selection is modelled, or how stochastic and spatial effects are incorporated. Concerning selection, the first pioneering studies as well as a main branch of contemporary ones that aim at quantifying species evolution view populations as advancing in a constant fitness landscape, see, for example, Ref. [115]. In this framework, each individual possesses a certain fitness, which depends on the environment. Due to mutations and selection, the population composed of many individuals constantly increases its average fitness. However, in many biological situations, an individual's fitness depends on its interactions with others. In particular, it may alter if the composition of the population changes. As an example, consider a bacterium that produces a toxin and in this way can kill neighboring sensitive bacteria, see Fig. 3.1. In an environment of many surrounding sensitive bacteria, production of the toxin is a clear fitness advantage. However, over time, some sensitive

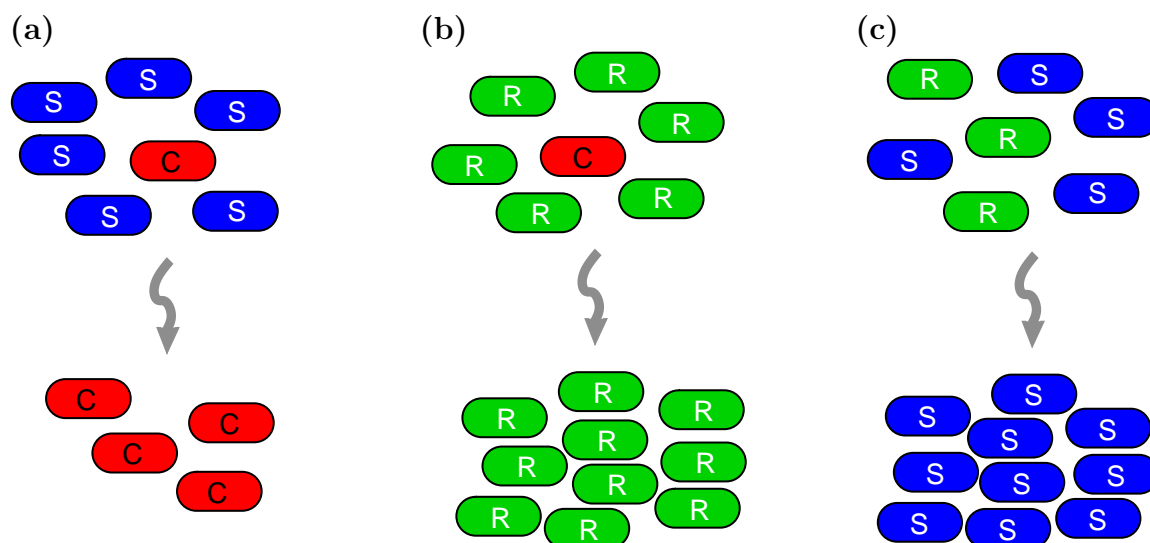


Figure 3.1: Frequency-dependent selection and cyclic dominance. We consider three types of bacteria. Strain C produces a colicin which is toxic and kills the sensitive strain S, but not the resistant bacteria R. These three strains have already been described in the Introduction, Chapter 1. **(a)**, A toxin-producing bacteria surrounded by sensitive ones clearly has a higher fitness, as it may kill its neighbors and then reproduce unopposed. **(b)**, Placed among resistant bacteria, producing the toxin causes some cost without associated benefit and therefore reduces the fitness of C to lower values than those of R. This example illustrates how the fitness of C, and therefore its evolutionary success, depends on the type of individuals in its neighborhood, a situation named *frequency dependent selection*. **(c)**, Interestingly, when comparing S and R alone, S has a growth advantage as the property of resistance bears some cost. Consequently, S, R and C display cyclic dominance, see text.

bacteria will develop resistance to the toxin. Compared to the latter, the toxin-producing bacterial strain is disadvantageous as the production bears some cost without providing benefit. Such a situation illustrates *frequency dependent selection* as an individual's fitness depends on the frequency of other species. *Evolutionary game theory* provides an advanced framework for the quantitative description of such scenarios, see Refs. [116, 117, 118, 119] for an introduction and reviews. There, the fitness of an individual is influenced by its interactions with others, its “partners in a game”, and in this way naturally incorporates dependences on the way in which the total population is composed of different subpopulations. However, we want to stress that frequency-dependent selection can also be obtained in other contexts than evolutionary game theory; as an example, the pioneering work of Lotka and Volterra [120, 121] on predator-prey models already describes the dependence on the reproductive success of prey resp. predators on the occurrence of the other species. Of course, although using a somewhat different language, these approaches are related: for example, the Lotka-Volterra equations describe oscillatory behavior similar to the one of the rock-paper-scissors dynamics widely studied in evolutionary game theory [116]. In

this paradigmatic game, three strategies, rock, paper, and scissors, cyclically dominate each other: rock crushes scissors, scissors cut paper, and paper wraps rock in turn. In our work, we consider three species exhibiting similar cyclic competition and observe density oscillations as are also characteristic for the Lotka-Volterra model.

From another point of view, theoretical approaches to evolutionary dynamics may be divided into *individual-based models* and *coarse-grained* ones. Individual-based approaches attempt to describe evolution via the consideration of single agents that interact. Stochastic effects stemming, for example, from the finite size of the population as well as possible spatial degrees of freedom are naturally accounted for in these models. However, they often rely on computer simulations. The often missing analytical tractability denotes one of their shortcomings and renders the generality of the derived results occasionally unclear. In contrast, coarse-grained models describe typically mean densities of different interacting species. In its simplest form, this is achieved via ordinary differential equations (ODE) for the time-evolution of the species' abundances. The celebrated *replicator equation* emerging from a few generic assumptions in game theory is a prominent example. Such ODE are typically nonlinear, which makes general bifurcation theory developed in mathematics [122, 123] applicable, but also frequently renders these problems hard to solve analytically. Again, one often has to rely on numerical solutions. However, the concepts of bifurcations considerably help in determining the universality of the emerging behavior. Incorporation of stochastic effects or spatial degrees of freedom into such coarse-grained descriptions represents non-trivial aspects. Concepts as the Fokker-Planck equation or corresponding stochastic differential equations (SDE) may account for internal noise, while diffusion terms are capable of taking spatial structure on which individuals move into account. We will present such approaches in Sections 3.3 and 3.4. Here, we conclude with remarking that the connection of the latter concepts to the individual-based models is subject of ongoing research. Indeed, in our work, we employ a certain limit in which an interacting particle model becomes describable by coarse-grained stochastic partial differential equations (SPDE).

3.2 Rock-Paper-Scissors dynamics as a motif of species interactions

The interaction networks of many different species coexisting in an ecosystem typically show complex behavior, see Ref. [124] for a review. In some way, this situation resembles the complex gene-regulation networks of single cells. There, considerable insight has been gained by the study of simple recurrent *motifs*, see Refs. [125, 126, 127]. The functional properties of the latter can be analyzed, and yield conclusions concerning the global functioning of the overall network. However, although such a reductionistic approach bears clear advantages, it seems probable that crucial functions of gene-regulation networks only emerge when considering larger entities, often referred to as *modules* [128]. An insightful

example is constituted by the genetic switch of the lambda phage [129], whose functional mechanisms probably cannot be explained by consideration of simple motifs. Such issues are subject of intense current research.

Here, following a reductionistic approach to complex species interaction networks, we focus on a single motif, the *rock-paper-scissors dynamics*. In this type of interaction, three species dominate each other in a cyclic manner: the first one outperforms the second one, which beats a third, and the third has a selection advantage compared to the first one, closing the cycle. The children's game "rock-paper-scissors" exhibits the same prototypical dynamics, and therefore lends its name to this type of competition.

The rock-paper-scissors dynamics denotes a non-hierarchical competition, as each of the three interacting species beats another one but is itself outperformed by the remaining. This characteristics might question its occurrence in real ecosystems, where interactions are mostly believed to be hierarchical. As an example, considering food webs, the directed network of which species feeds on which is typically hierarchical, and organized into different trophic levels. However, species interactions are much richer than what is captured by food webs. Indeed, selection in nature occurs only very rarely through "killing" of individuals by superior ones, but is nearly always mediated by *reproductive advantages* of one species. The latter are involved functions, depending, for example, on mating strategies, and can lead to cyclic dominance. We list some examples of the occurrence of rock-paper-scissors dynamics in nature in the following.

Cyclic dominance is exhibited by microbial communities of colicinogenic bacteria, as already presented in the Introduction, Chapter 1, as well as briefly described in Sec. 3.1 and Fig. 3.1. Consider three strains of *E.coli* where the C strain produces a colicin, which acts as a toxic on a sensitive strain S. The third strain R is resistant, which bears some cost: these bacteria reproduce slower than the sensitive strain S. However, resistance is advantageous when facing C bacteria: the latter are themselves resistant and occasionally produce the toxin, which is a growth disadvantage. Consequently, the three strains cyclically dominate each other: C kills S, S outgrows R, and R outgrows C in turn, see Fig. 3.1. Experimental investigations of the coexistence properties of these three strains have unraveled important influence of spatial patterns. Namely, B. Kerr et al. [43] have, in one setting, grown all three strains together on a Petri dish. As result, spatial clusters dominated by different strains formed, and all coexisted over several days. In the second setting, the bacteria were grown in a well-stirred flask, where spatial patterns could not form, causing rapid extinction of the sensitive as well as the colicin-producing strain and leaving the sensitive one as the only survivor. Consequently, the rock-paper-scissors interaction motif with additional spatial separation of individuals denotes one mechanism for the maintenance of stable bacterial coexistence. These experiments provide the motivation for the studies in this Chapter. From a theoretical viewpoint, we aim at an investigation of the influence of individuals' mobility which, depending on its strength, is expected to mediate between the Petri-dish and the flask environment. Indeed, we find that a critical mobility value sharply delineates a biodiverse scenario, where all three strains coexist (for

low mobilities), from a uniform one for higher mobilities, where only one strain remains.

The above described three strains of colicinogenic *E.coli* may be seen as a model system for bacteria occurring, for example, in soil. There, a large variety of different bacteria coexists, as described in Sec. 3.1. The small subset of *E.coli* still comprises many different strains. In particular, some bacteria are capable of producing a variety of toxins, while being resistant to these and/or others. Other bacteria are resistant without production of any colicins, or only sensitive. In fact, all combinations of colicin production, resistance and sensitivity on the different toxins occur; a diversity that is puzzling from a theoretical perspective. In this respect, laboratory experiments of only three strains and one toxin are meaningful for the identification of mechanisms for the maintenance of biodiversity in soil. Indeed, spatial segregation, which plays a crucial role in the experiments of B. Kerr [43], also seems to be relevant in maintaining bacterial diversity in soil [130].

Another prominent appearance of rock-paper-scissors dynamics is constituted by lizards species in the inner Coast Range of California [44, 131]. As an example, three different mating strategies, corresponding to color polymorphisms, exhibit cyclic dominance, as described in the Introduction, Chapter 1. The rock-paper-scissors interaction motif has also been identified in very different ecosystems, from coral reef invertebrates [132] to rodents in the high-Arctic tundra in Greenland [133].

3.3 Species coexistence and noise

As described above, cyclic dominance of different competing species, in combination with local interactions of individuals, promotes stable diversity. In this Section, we aim at an investigation of such population dynamics in the situation where individuals interact with all others in the ecosystem, that means when they are not spatially segregated. Such scenarios arise when individuals' mobility is high compared to the size of the ecosystem. For example, bacteria grown in flasks such as in the experiments of Ref. [43] or in chemostats are well-mixed in the above sense. The time-evolution of the population abundances is, firstly, governed by the way the different species compete, and, secondly, by intrinsic noise. The latter stems from the stochasticity of individuals' reproduction as well as competition events, together with the fact that individuals are discrete and population sizes are finite. Interestingly, when a large number of individuals interact, both effects - the type of species competition and noise - can be decoupled. Namely, the temporal evolution of the ecosystem may be described by stochastic differential equations (SDE), equivalent to a Fokker-Planck equation. The SDE consist of deterministic terms, resulting from the individuals' interactions, and noise terms, that account for fluctuations. In this Section, we review this approach, while technicalities may be found in the article on cyclic Lotka-Volterra models (Section III B therein), as well as in the comprehensive article on self-organization of mobile populations (Section 3.5 therein), which are reprinted at the end of this Chapter. We

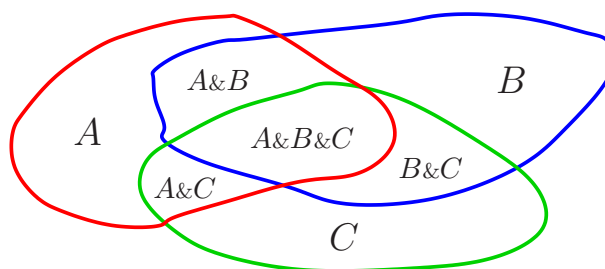


Figure 3.2: Schematic state space of three competing species, referred to as A , B , and C . There are absorbing states where only A , only B , or only C are present. In contrast, states where A and B coexist or where all three species are encountered are named *reactive*, as there reproduction and interaction events are possible. Eventually, the stochastic process reaches one of the absorbing states where the system is trapped and the temporal evolution ends. Consequently, biodiversity is always lost. However, the waiting time for extinction may exceed the ecologically relevant time-scales by orders of magnitude, see text, such that diversity is stable on meaningful time intervals.

argue that, under general conditions, noise unavoidably leads to species extinction. However, the typical time-scales on which extinction occurs may be very different, depending on the type of species competition. Investigating stochastic effects in a model for cyclic competition, we deduce a suitable classification of stability/instability of diversity when population dynamics is noisy.

As outlined above, reproduction of individuals as well as their interaction occurs on a random basis. As an example, although it is known that *E.coli* duplicates on average every 20 minutes under suitable conditions, single cells may considerably deviate from such a typical rate. *Stochastic processes* form the suitable theoretical framework for the description of such events [134, 135, 136]. In our case, all possible states of the system, described by the sizes of different coexisting species, form a discrete and finite state space. Transitions between different states occur on a stochastic basis, e.g. according to a certain probability distribution; they stem from reproduction or interaction events. Often, such transitions are modelled as *Poisson processes*, occurring at a characteristic rate. One may question the suitability of this representation as it may considerably deviate from reality in some cases, for example, the above mentioned bacterial growth occurs much more regularly than what one would infer from a Poisson process. However, when considering a large number of subsequent events, as occur in large natural systems, the central limit theorem guarantees that (under suitable conditions) the final, accumulated probability distribution will be gaussian, independent of the single ones. Therefore, modelling the reproduction or interaction events as Poissonian is as well suited as other processes as long as one focusses on many events in a large state space. In our work, we are always interested in the latter situation and use Poisson processes for describing the individuals' reproduction and interactions.

Extinction of species in nature is an irreversible process. Indeed, the revival of species that have gone extinct, due to mutation or recombination of related ones, is extremely improbable, as the genetic code possesses a huge degree of genetic variability. Models for ecosystems must therefore take the possibility of ultimate species extinction into account. More concretely, above, we have described how stochastic processes in a discrete and finite state space serve as a suitable framework for population dynamics that take effects of fluctuations into account. Now, within the state space, the set of states where one species has gone extinct must be *absorbing*, meaning that once the system has reached this set of states, it cannot leave it anymore, see Fig. 3.2 for a schematic illustration. The latter property reflects the irreversibility of extinction. Moreover, there exist single *absorbing states*, corresponding to the survival of only one species. The theory of stochastic processes guarantees that, in the course of temporal evolution, the system will end up in one of the absorbing states. Namely, this property always holds when a trajectory in phase space exists that connects the initial state to an absorbing state. Even if the probability for the realization of such a trajectory is extremely low, after long enough waiting time, it will occur. Therefore, ultimately, biodiversity is lost. However, as is described below, the waiting time until extinction occurs may be extremely long, and the ecological relevant time-scales much shorter. In this situation, it is justified to consider biodiversity as stable, despite the ultimate occurrence of extinction.

In the remainder of this Section, we consider an insightful model for three cyclically competing populations formulated in the language of stochastic processes. Based on its behavior, we develop a suitable and general definition of stable/unstable biodiversity in the presence of absorbing states.

Let A , B , and C denote three species that dominate each other according to the rock-paper-scissors dynamics introduced in Section 3.2. The interactions are modelled as the following reactions,



They occur as Poisson processes at rates k_A , k_B , and k_C , and model, e.g., a “killing” of a B individual by an A individual with successive reproduction of A . Cyclic dominance occurs as A can kill B , B preys on C , and C on A in turn. More realistically, one could decouple “killing” and reproduction, which will be considered in Section 3.4. Here, we continue with investigating the reactions (3.1) as they yield fruitful insight into the effects of noise.

A detailed study of the above introduced stochastic system has been published in *Physical Review E* and is reprinted at the end of this Chapter. Here, we describe and discuss the main findings. The stochastic system is formally described by a master equation, see the article in *Physical Review E* (Section III B therein), which involves all possible

transitions between the states that can emerge. We are interested in a large number N of interacting individuals, described by the asymptotic limit $N \rightarrow \infty$. Consequently, a large number of states with many associated transitions characterizes the system. An exact solution of the master equation is thereby probably rendered impossible. However, a systematic expansion in the inverse system size $1/N$ is feasible and yields an analytically tractable description of the system's behavior. In the article on cyclic Lotka-Volterra models (Section III B therein), we detail this Kramers-Moyal expansion in general terms, see also the presentation in [136]. The zeroth order in the inverse system size is given by deterministic rate equations for the time-evolution of the species' mean densities, while the first order gives stochastic effects. Neglecting higher orders in $1/N$, one obtains stochastic differential equations (SDE). In the general case of a number S of interacting species, with relative abundances $\mathbf{x} = (x_1, \dots, x_S)$, $x_i \in [0, 1]$, these SDE are of the form

$$\partial_t x_i = f_i(\mathbf{x}) + C_{ij}(\mathbf{x})\xi_j, \quad i \in \{1, \dots, S\}. \quad (3.2)$$

The nonlinear functions $f_i(\mathbf{x})$ describe the deterministic time-evolution of the mean species' abundances \mathbf{x} , while the second term takes fluctuations into account. Namely, the ξ_i denote white noise, $\langle \xi_i(t)\xi_j(t') \rangle = \delta_{ij}\delta(t-t')$. In Eq. (3.2), they are multiplied with a density-dependent factor $C_{ij}(\mathbf{x})$, which is proportional to the inverse square root of the system size $1/\sqrt{N}$. The resulting multiplicative noise is weak for large systems, it reflects the first order of the system-size expansion. The above SDE are understood in the sense of Ito calculus, see Ref. [134], and associated to a Fokker-Planck equation as described in the article on self-organization of mobile populations (Section 3.5 and Appendix D therein). Such SDE have recently been considered in the context of Evolutionary Game Theory [137, 138]; depending on the details of the stochastic process under consideration, the nonlinear deterministic part is given by the standard or the adjusted replicator equation. In our case, for the reactions (3.1), the stochastic differential equations read

$$\begin{aligned} \partial_t a &= a[k_C b - k_B(1-a-b)] + C_{AA}\xi_A + C_{AB}\xi_B, \\ \partial_t b &= b[k_A(1-a-b) - k_C a] + C_{BA}\xi_A + C_{BB}\xi_B. \end{aligned} \quad (3.3)$$

Hereby, a and b denote the abundances of species A and B relative to the total population size N ; the frequency c of species C follows as $c = 1 - a - b$ as the reactions (3.1) leave the total number N of individuals unchanged. As in the general case, the first terms on the right-hand-side of the above SDE are the deterministic parts, describing the time evolution of the expectation values of the densities a and b . The second and third terms encode density-dependent fluctuations, the matrix C is given by

$$C = \frac{1}{3\sqrt{2N}} \begin{pmatrix} -\sqrt{3} & 1 \\ \sqrt{3} & 1 \end{pmatrix}. \quad (3.4)$$

The two-dimensional phase space of the system with the deterministic trajectories, stemming from the SDE (3.3) in the case of vanishing noise, as well as one realization of a

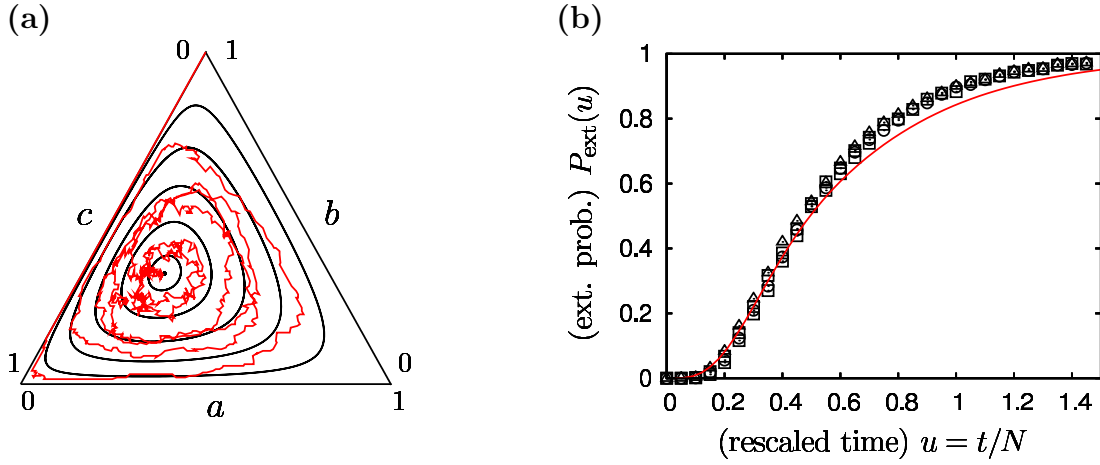


Figure 3.3: Coexistence versus extinction in a cyclic population model. We investigate a stochastic process describing three species A , B , and C , exhibiting cyclic dominance, see text. **(a)**, The phase space is the simplex S_3 , where the species' densities a , b , and c are constrained by $a + b + c = 1$. The deterministic dynamics yields neutrally stable, closed cycles (black), surrounding a neutrally stable internal fixed point. Due to fluctuations, a stochastic trajectory (red) can “jump” between these orbits, and eventually reaches the absorbing boundary with ultimate extinction of two species. In this picture, we have chosen $k_A = 1$, $k_B = 1.5$ and $k_C = 2$. **(b)**, The extinction probability depends only on the rescaled time, $u = t/N$, and increases from 0 to 1 upon increasing the waiting time u . In particular, the mean waiting time T is proportional to the system size N . Analytical calculations (red line) as well as stochastic simulations for different system sizes (triangles: $N = 100$, boxes: $N = 200$, circles: $N = 500$) confirm this behavior. Here, equal reaction rates $k_A = k_B = k_C = 1$ have been considered. Both pictures have been modified from [139].

stochastic trajectory are depicted in Fig. 3.3 (a). The system's deterministic behavior is characterized by an internal fixed point where all species coexist, as well as closed orbits surrounding it. A constant of motion, similar to the energy in classical mechanics, ensures the closing of these outer deterministic trajectories, which are therefore neutrally stable under perturbations. Consequently, stochastic fluctuations can accumulate unhindered, and, for example starting at the coexistence fixed point, the system follows a trajectory that, due to noise, in average spirals outwards, with random steps inward and outward. Eventually, the absorbing boundary where one species has died out is reached. Out of the two remaining ones, one is dominating the other and after some short time remains the only survivor. Consequently, although the deterministic picture predicts the (neutrally stable) coexistence of all three species, fluctuations invalidate this picture and unavoidably induce extinction of two.

Which of the three absorbing states is reached, that means whether A , B , or C survives, is subject to a random process. When all reaction rates are equal, meaning $k_A = k_B = k_C = 1$, all species clearly have an equal chance of surviving. Together with Maximilian Berr, Erwin

Frey and Martin Schottenloher, we have investigated how the survival probability of a given species changes upon choosing asymmetric rates, as is the case in Fig. 3.3 (a). Interestingly, in the asymptotic limit of large systems, $N \rightarrow \infty$ and for asymmetric rates, we have found that one distinct species, namely the one which, in a certain sense, is “closest” to the internal fixed point, is guaranteed to survive [140, 141]. The two others become extinct after a mean time proportional to the system size. Therefore, when all rates differ and when many individuals interact, despite the randomness of the stochastic process, one can precisely determine which species survives and which die out.

The mean time for extinction in this model is intimately connected to the neutral stability of the deterministic orbits. Indeed, fluctuations perpendicular to these orbits are neither enhanced nor suppressed by the deterministic dynamics, and therefore, considering the distance from the coexistence fixed point as the radius, the systems’ radial motion is governed by fluctuations alone. In the framework of the SDE (3.3) and the associated Fokker-Planck equation, this observation can be captured analytically. Using the theory of random walks [142], one can compute the mean first passage time T when the system has reached the absorbing boundary. The latter time is proportional to the strength of noise. Now, as the typical size of the fluctuations decreases with increasing system size N as $1/\sqrt{N}$, the analytic approach reveals that the mean extinction time T is proportional to N , $T \sim N$. This result reflects the fact that the deterministic dynamics does neither support nor hinder extinction, the latter is induced by noise alone.

We are now in the position to define a criterion for differentiating stable from unstable coexistence. Above, we have described how, under general conditions, fluctuations ultimately lead to species extinction in ecological systems due to the existence of absorbing states. A meaningful definition of “stability” and “instability” of species diversity therefore incorporates the time-scales needed for extinction and their dependence on the system size N . The neutrally stable coexistence lies as “critical situation” in-between stable and unstable one. Above, we have seen how it leads to a mean-extinction time T which increases proportional to the system size N . In contrast, in well-mixed models as the one considered above, stable coexistence leads to an exponential increase of T in N , while for an unstable one the dependence of T on N is logarithmic [143, 144, 145, 146]. In other words, deterministically stable coexistence opposes extinction and leads to a mean extinction time which is extremely long for large systems. In particular, coexistence is maintained on ecologically relevant time-scales which typically lie below. In contrast, extinction occurs fast if it is supported by the deterministic evolution.

Specifying the above considerations, we propose a quantitative classification of coexistence’s stability in the presence of absorbing states, which is presented in the following Box. Neutral stability is defined as the situation where T , denoting the mean extinction time, increases proportional to some power of N , which is more general than the $T \sim N$ behavior encountered in the model described above. The reason is that there exist situations where a $T \sim \sqrt{N}$ dependence separates stable from unstable coexistence, see Refs. [143, 144, 146]. The occurrence of other powers of α than 1 or 1/2 in scenarios lying

Box: Classification of coexistence's stability

Stability: If the mean extinction time T increases faster than any power of the system size N , meaning $T/N^\alpha \rightarrow \infty$ in the asymptotic limit $N \rightarrow \infty$ and for any value of $\alpha > 0$, we refer to coexistence as *stable*. In this situation, typically, T increases exponentially in N .

Instability: If the mean extinction time T increases slower than any power in the system size N , meaning $T/N^\alpha \rightarrow 0$ in the asymptotic limit $N \rightarrow \infty$ and for any value of $\alpha > 0$, we refer to coexistence as *unstable*. In this situation, typically, T increases logarithmically in N .

Neutral stability: Neutral stability lies inbetween stable and unstable coexistence. It emerges when the mean extinction time T increases proportional to some power $\alpha > 0$ of the system size N , meaning $T/N^\alpha \rightarrow \mathcal{O}(1)$ in the asymptotic limit $N \rightarrow \infty$ and for some value $\alpha > 0$.

between stable and unstable coexistence is probable and motivates the above definition. Stable resp. unstable diversity typically exhibit exponential resp. logarithmic dependence of the mean extinction time on the system size [143, 144, 145, 146].

The strength of the above classification lies in that it only involves quantities which are directly measurable (for example through computer simulations), namely the mean extinction time and the system size. Therefore, it is generally applicable to stochastic processes, e.g. incorporating additional internal population structure like individuals' age or sex, or where individual's interaction networks are more complex, such as lattices, scale-free-networks or fractal ones. In these situation, it is typically impossible to infer analytically, from the discussion of fixed points' stability, whether the deterministic population dynamics yields a stable or unstable coexistence. However, based on the scaling of extinction time T with system size N , differentiating stable from unstable diversity according to the above classification is feasible. In Section 3.4, we will follow this line of thought and fruitfully apply the above concept to the investigation of a rock-paper-scissors game on a two-dimensional lattice, where individuals' mobility is found to mediate between stable and unstable coexistence.

In recent articles, Alan Hastings has proposed that the state of ecological systems may be more appropriately viewed as persistent transient behavior than stable equilibria, see Refs. [147, 148]. Indeed, in the above discussion we have inferred that, in a strict sense, intrinsic stochasticity always renders coexistence of species unstable. However, a large species diversity populates the earth's ecosystems. Obviously, the relevant time-scales are given by the time at which new species form, due to mutation and selection, as well as by the time during which properties of the ecosystem change, for example by global changes

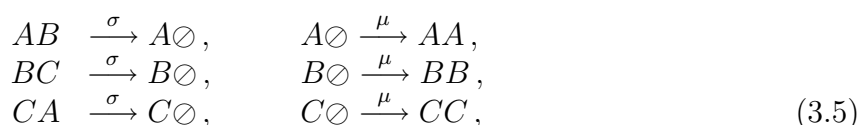
in temperature or the steadily evolving surface of the earth. Although these time-scales are long, as much as millions of years, they may be short in comparison to the time needed for random effects to induce species extinction. On these shorter, ecologically meaningful time-scales, the system can be in transient states which persist. The above classification presents a quantitative concept that translates these observations into mathematical relations.

3.4 The influence of locality and mobility on biodiversity

Mobility is ubiquitous in natural ecosystems, from bacteria that swim and tumble to animals migrating from place to place. Disregarding plants, which can form interesting patterns as described in the Introduction, Chapter 1, and Refs. [46, 149], modelling ecosystems in the form of individuals being motile on some spatial structure and interacting with others in a local neighborhood constitutes a generally applicable approach. We have developed such a model for cyclically competing species, and focussed on the effects of mobility on maintaining species diversity as well as its effects on pattern formation. Our findings on mobility's impact on biodiversity have been published in a *Letter to Nature*, which is reprinted at the end of this Chapter. Here, we present conceptual issues and the main findings. In the subsequent Section 3.5, self-organizing spiral patterns under the influence of mobility are investigated.

Mobility of individuals counteracts locality of interactions. Indeed, through motion, individuals explore a larger neighborhood and interact with many more than if they were static. Now, both experimentally, through the study of colicinogenic, static bacteria on Petri dishes [43] reviewed in Sections 1.2 and 3.1, as well as theoretically, see Refs. [150, 100, 151, 152, 153, 99, 154] and references therein, it has been shown that locally restricted interactions promote species diversity. Upon increasing individuals' mobility, locality is weakened, and biodiversity rendered less stable. In a paradigmatic model for three cyclic competing species, described below, we have quantified this behavior. In a suitable asymptotic limit of large systems, a critical value of mobility separates a biodiverse regime, emerging for mobilities lower than the threshold value, from a uniform regime where diversity is lost, for motilities exceeding the critical value.

As in Section 3.3 we model cyclic dominance of three species A , B , and C by stochastic reactions similar to Eqs. (3.1), although we now decouple selection ("killing") from reproduction. Therefore, selection occurs through reactions of the form $AB \rightarrow A\emptyset$, where \emptyset denotes an empty site, and reproduction by $A\emptyset \rightarrow AA$. As individuals can only reproduce on available empty sites, the population growth is limited by a finite carrying capacity. In total, the reactions read,



where σ denotes the selection and μ the reproduction rate. We consider the most symmetric (and therefore analytically tractable) situation where all three species possess equal μ and σ . Below, we demonstrate that the more general case of asymmetric rates may differ quantitatively, but not qualitatively; in other words, the qualitative behavior of the symmetric system is robust. In the absence of spatial degrees of freedom, the deterministic ODE for the time-development of the different densities have been studied by May and Leonard [155]. We therefore refer to the above reactions, Eqs. (3.5), as May-Leonard reactions.

In contrast to the well-mixed scenario considered in Section 3.3, individuals are now equipped with spatial degrees of freedom and mobility. For this purpose, individuals are arranged on a two-dimensional lattice, such that each site is either occupied by one individual or empty. We use periodic boundary conditions, although the qualitative results are independent of this property. On this lattice, individuals interact with their four nearest neighbors (von Neumann neighborhood), either through selection, reproduction, or exchange. The latter occurs at an exchange rate ϵ , by individuals at neighboring sites changing their locations, or by an individual hopping on an empty neighboring site. We set the linear length of the lattice, given by \sqrt{N} sites, as the unit of length. The mobility of individuals, stemming from random exchanges, is then given by $M = \epsilon/(2N)$, see Section 3.5. Indeed, \sqrt{M} denotes the diffusion length, being the typical length that an individual moves in one time unit, in relation to the linear lattice size.

Mobility competes with locality of interactions if both length scales, being the linear size of the system, set to unity, and the diffusion length, given by \sqrt{M} , are of comparable order. Consequently, a suitable limit of large system sizes, $N \rightarrow \infty$ keeps the diffusion length constant. Therefore, in this limit, the local exchange rate $\epsilon = 2NM$ tends to infinity. In Section 3.5 we show that in the so-defined continuum limit, the system's behavior is captured by stochastic partial differential equations (SPDE). Here, we employ it to derive a phase transition between a biodiverse state and a uniform state at a critical mobility value M_c .

Computer simulations show that low values of mobility induce coexistence which is stable on accessible time-scales, while high mobilities lead to rapid extinction of two species. These observations can be quantified employing the stability/instability concept presented at the end of Section 3.3. In principal, this implies to study the mean extinction time depending on the system size, which reveals the stability/instability of species coexistence. As we want to investigate the dependence of the stability/instability on another parameter, namely individuals' mobility, we choose a computationally more economic approach. We compute the extinction probability P_{ext} that, initially starting with randomly distributed individuals, two species have gone extinct after a waiting time t_W proportional to the system size, $t_W \sim N$. Finite-size scaling, that means computation of the mobility-dependent extinction probabilities for different system sizes N , then reveals the stability/instability of biodiversity. Namely, if the mean-extinction time T scales proportional to N , being the neutrally stable scenario, the extinction probability approaches a constant value between 0

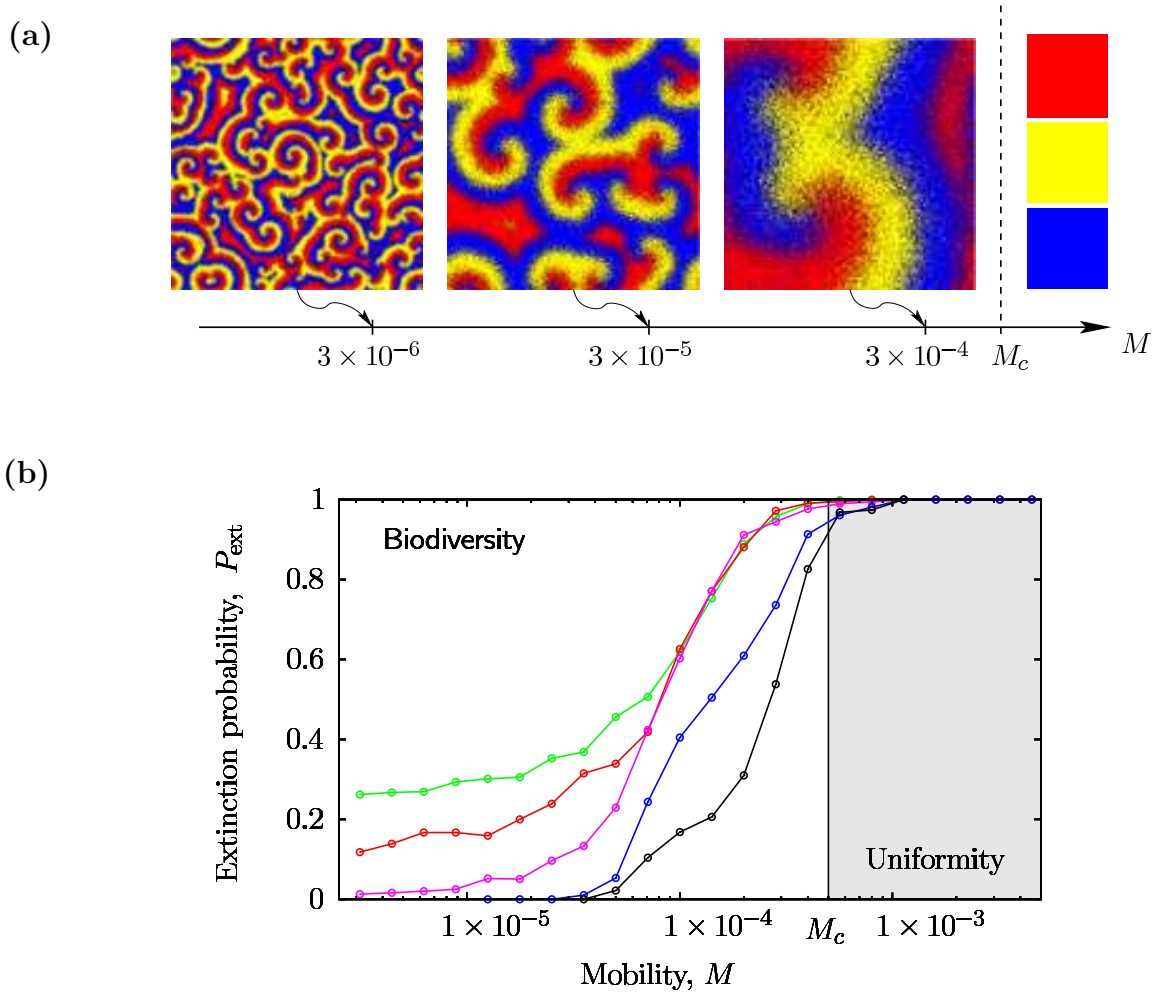


Figure 3.4: Mobility’s impact on biodiversity. We investigate a paradigmatic model for cyclically competing species, where individuals interact locally on a square lattice and are equipped with mobility, see text. (a), For low values of mobility, all three species coexist, self-organizing into entangled rotating spiral waves. We show snapshots for different values of individuals’ mobility M . Increasing M results into a “zooming” into the system; the spatial structures’ size is proportional to \sqrt{M} . At a critical value M_c , they outgrow the system, and only one species survives. In our model, the three species are symmetric, and they have an equal chance of prevailing. (b), Computing the extinction probability P_{ext} after a waiting time proportional to the system size reveals the stability/instability of species diversity, according to the definition presented at the end of Section 3.3, see text. In the asymptotic limit of large systems, a critical value of mobility M_c emerges that sharply separates a biodiverse regime, where P_{ext} tends to 0, from a uniform one, where two species rapidly become extinct and P_{ext} approaches 1. We consider system sizes ranging from $N = 20 \times 20$ (green) over $N = 30 \times 30$ (red), $N = 40 \times 40$ (purple), $N = 100 \times 100$ (blue) to $N = 200 \times 200$ (black). The figures have been reproduced from [156].

and 1 (excluding both values), when $N \rightarrow \infty$. In contrast, when the extinction probability tends to 0, this means that $T/N \rightarrow \infty$ and indicates stable diversity, while P_{ext} approaching 1 implies $T/N \rightarrow 0$ with instable coexistence. Note that here we have used a definition of stable/unstable coexistence as the one introduced at the end of Section 3.3, but with $\alpha = 1$ for computational convenience. However, we have checked that our results also fulfill the more general classification employing any arbitrary α . Indeed, when coexistence is stable, which arises for low mobility, the mean extinction time T increases exponentially in N , while for high mobility, it is logarithmic in N and coexistence is unstable.

The influence of mobility on the stability properties of species diversity is shown in Fig. 3.4. Hereby, we have considered equal values for reproduction and selection rates, which have been set to unity, $\mu = \sigma = 1$. Computing the extinction probability for different values of mobility and increasing system size, see Fig. 3.4 (a), a transition between stable and unstable coexistence sharpens at a critical mobility of $M_c \approx 4.5 \times 10^{-4}$. Below this value, P_{ext} approaches 0 when the system size is risen, implying stable diversity. In contrast, above the critical value, the extinction probability remains at a value of about 1, such that diversity is quickly lost in this regime. In our simulations, we have considered systems sizes ranging from $N = 20 \times 20$ up to $N = 200 \times 200$, and computed P_{ext} by averaging over typically 500 distinct runs. The obtained numerical data indicate that the transition becomes sharp at M_c , although accessing larger system sizes would be desirable to better determine the value of the critical mobility. However, that would require much higher computational effort.

Spatial patterns form when mobility is low and induce stable species coexistence. These spiralling, rotating structures are the subject of Section 3.5. When mobility is risen, the size of these patterns increases, as shown in Fig. 3.4 (b). At the critical value M_c , they “outgrow” the system, and leave uniform states where one species alone covers the entire lattice. In Section 3.5, we show that an increase of M results in a “zooming” into the system at a factor of \sqrt{M} . The latter behavior generally arises in interacting particle systems with mobile individuals such as the one considered above, as is revealed by stochastic partial differential equations (SPDE), see below.

3.5 Pattern formation

In the presence of individuals’ mobility, pattern formation of competing populations is fruitfully described by stochastic partial differential equations (SPDE). Specifically, within the above introduced continuum limit, where the mobility $M \sim \epsilon/N$ is kept fixed when $N \rightarrow \infty$, the stochastic dynamics is aptly captured by stochastic equations for the time evolution of the species densities. Generally, consider S species with densities $\mathbf{x}(\mathbf{r}, t) = (x_1(\mathbf{r}, t), \dots, x_S(\mathbf{r}, t))$ and, possibly differing, mobilities M_1, \dots, M_S . Their stochastic temporal development obeys SPDE of the form

$$\partial_t x_i(\mathbf{r}, t) = M_i \Delta x_i(\mathbf{r}, t) + f_i[\mathbf{x}(\mathbf{r}, t)] + C_{ij}[\mathbf{x}(\mathbf{r}, t)] \xi_j(\mathbf{r}, t), \quad i \in \{1, \dots, S\}. \quad (3.6)$$

Their derivation is sketched in the article on self-organization of mobile populations (Sections 3.4, 3.5 therein). The first term on the right-hand-side involves the Laplace operator Δ and takes diffusion, stemming from individuals' mobility, into account. The nonlinear functions f_i deterministically describe species interactions. As an example, in the context of Evolutionary Game Theory, they are given by the nonlinear terms in the replicator equation resp. the adjusted replicator equation, depending on which microscopic process (local update or Moran process) one considers, see Refs. [137, 138]. Note that these terms are the same as appear in the general SDE (3.2) which describe coevolution of different species in the absence of spatial degrees of freedom and with a large number of interacting individuals. The same holds for the noise terms, being the last ones on the right-hand-side of Eqs. (3.6); they agree with the noise terms of the general SDE (3.2), up to the fact that they now have a spatial dependence. Being Gaussian noise, their correlation is given by $\langle \xi_i(\mathbf{r}, t) \xi_j(\mathbf{r}', t') \rangle = \delta_{ij} \delta(\mathbf{r} - \mathbf{r}') \delta(t - t')$. The coefficients C_{ij} are density-dependent as well as proportional to the inverse square root of the system size. Consequently, the fluctuation terms in the above SPDE are small for large populations.

Firstly, the strength of connecting the stochastic system to the SPDE (3.6) lies in the simplicity and generality of the form of Eqs. (3.6). Their derivation uses generic arguments, and does not depend on, for example, the precise form of the lattice, which could be squared, hexagonal, or triangular, or the shape and size of individuals' neighborhood as long as it is local. Such details only reflect in constant prefactors of the diffusion terms, but do not yield changes in form. The other terms, the nonlinear deterministic functions f_i and the fluctuations, agree with the ones that emerge for well-mixed populations, as described by the SDE (3.2), and are independent of spatial degrees of freedom.

Secondly, the approach of mapping the interacting particle system to the SPDE (3.6) yields extremely insightful results, as it enables the application of bifurcation theory. Determining the bifurcations that the nonlinear functions f_i exhibit, see e.g. Ref. [122], defines universality classes for the emerging patterns. Namely, in the vicinity of bifurcations, the behavior is described by generic *normal forms*, see Ref [123], characterizing each bifurcation type. The resulting universality classes have already been widely studied in the physical and mathematical community, mostly by investigating deterministic partial differential equations, see e.g. Refs. [10, 157, 158, 159] for reviews as well as references therein. Although specific models for competing populations will not yield SPDE that are identical to the general equations studied there, their bifurcation behavior may coincide with an equation that has already been investigated. Consequently, the specific SPDE falls into that universality class, and generic results may be transferred.

As an intriguing example, cyclically competing species often yield deterministic behavior exhibiting a Hopf bifurcation. Deriving the normal form of the corresponding nonlinear functions f_i , and upon ignoring effects of noise, the SPDE describing cyclic competition belong to the universality class of the *complex Ginzburg-Landau equation* (CGLE), see Refs. [157, 158] for recent reviews. As a generic feature, in two spatial dimensions, travelling spiral waves result. Their wavelength, spreading velocity, and frequency can be calculated

analytically from the coefficients of the CGLE. The emerging spiral waves can exhibit a variety of instabilities, such as a core instability or an Eckhaus instability. The latter occurs when the spirals are unstable against long-wave perturbations; in this case, convectively unstable spirals may emerge. Such issues, in particular in connection to the influence of noise as well as initial conditions, are active areas of current research. This interest is to a large extent triggered by the occurrence and importance of spiral waves in a number of natural systems, as described below.

Travelling spiral waves are non-equilibrium phenomena stemming from oscillatory behavior and appear in various chemical and biological systems. The Belousov-Zhabotinskii-reaction [160, 161, 162] is a prominent chemical reaction where such patterns occur. A mix of potassium bromate, cerium(IV) sulfate, propanedioic acid and citric acid in dilute sulfuric acid, under the influence of external stimuli, exhibits spatio-temporally varying concentrations, the resulting changes in color visualize spiral patterns. Furthermore, spiral waves of calcium oscillations are of biological relevance in cell signalling [163, 164, 165]; in this context, fluctuations stemming from stochastic opening of calcium channels have considerable impact, see [165] for a recent review. Heart fibrillation is believed to be caused by the emergence of spiral waves in the cardiac tissue [166, 167]. In the Introduction, Chapter 1, we have described how *Dictyostelium* aggregation as well as the formation of its slug's mound is organized by spiral waves of the signalling molecule cAMP [168, 35]; such patterns also appear in myxobacteria organization [169].

Concerning population dynamics, rotating spiralling patterns have been observed in theoretical models for insect populations [100]. Cyclic competition as described by the rock-paper-scissors game has often been considered in the situation of static individuals. Experimentally, by investigation of colicinogenic *E.coli* on a Petri dish [43] as well as theoretically, see [101] for a recent review and Refs. [170, 171, 172, 173], static individuals under cyclic dominance in two spatial dimensions have been found to coexist in a stable manner and form mostly irregular patterns that are dominantly shaped by fluctuations and therefore pose major challenges in characterization.

Our approach of mobile individuals shows that, in the asymptotic limit of large populations and an accompanying high local exchange rate, surprisingly regular, geometric spiral waves form, see the snapshots in Fig. 3.5 (c), (d). This behavior reflects the accessibility of the interacting particle system by stochastic partial differential equations (3.6), in the continuum limit when $N \rightarrow \infty$. For small systems, much more irregular patterns appear, see Fig. 3.5 (b), due to the dominant influence of intrinsic noise. As stated above, the description of this situation is challenging. Methods such as generalized mean-field considerations, taking multi-site correlations into account, may be fruitfully applied [101]. We focus on the opposite case, when the system size is large and the SPDE (3.6) are applicable [156, 174, 175]. Comparison of the snapshots shown in Fig. 3.5 (c), (d) shows that both approaches indeed yield (statistically) identical results. The latter is quantitatively supported by the computation of spatio-temporal correlation functions which coincide, in particular, within both descriptions, the spirals' wavelength, spreading velocity, frequency

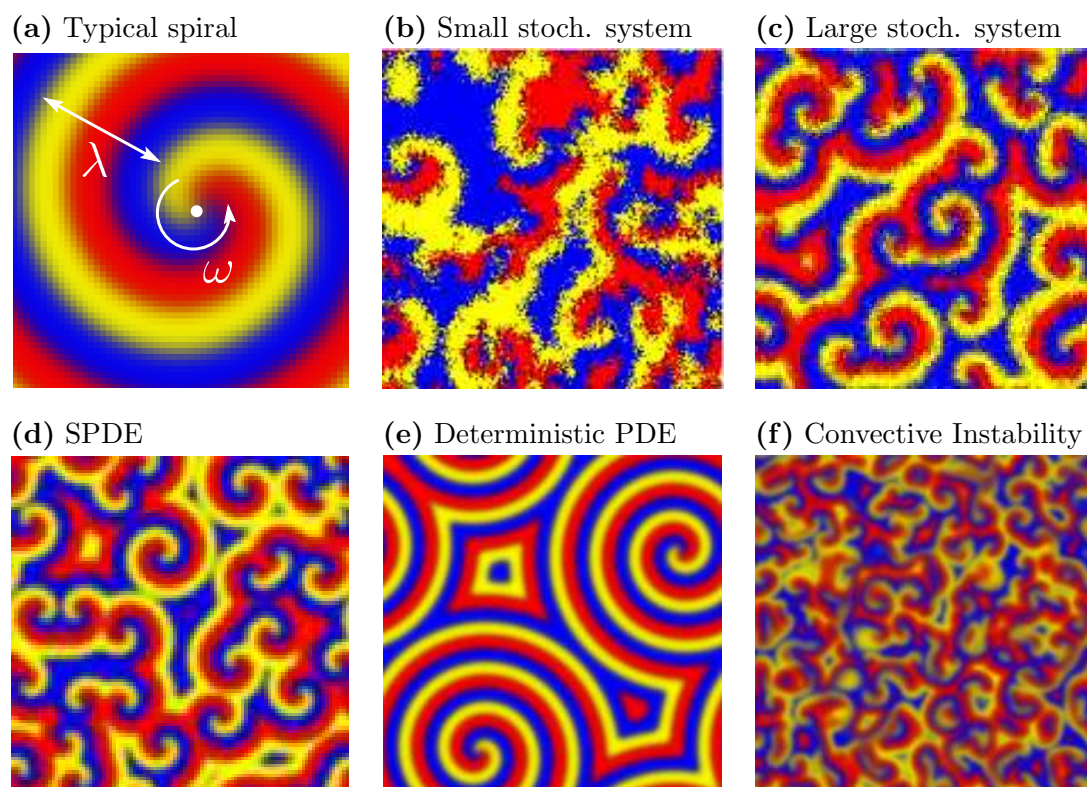


Figure 3.5: Rotating spiral patterns. (a), A typical spiral is characterized by its wavelength λ and frequency ω , yielding a certain spreading velocity. (b), For small system size, the patterns emerging in a stochastic model of cyclically dominating species, modelled by the May-Leonard reactions, Eqs. (3.5), are highly irregular, their shape is dominated by noise. For this snapshot, we have simulated the system with equal reproduction and selection rates, $\mu = \sigma = 1$, on a lattice of size $N = 200 \times 200$, with individuals global mobility being $M = 1 \times 10^{-5}$. Consequently, the local exchange rate is low, $\epsilon = 0.8$. (c), Lattice simulations for a larger system, $N = 500 \times 500$ with the same mobility and therefore a higher exchange rate, $\epsilon = 5$. The system is describable by the SPDE (3.6). An entanglement of regular, geometric spiral waves forms. (d), The numerical solution of the corresponding SPDE yields statistically identical patterns. (e), Ignoring the noise terms does not affect the spirals' wavelength and frequency, but the overall vortex density. The latter is, due to the absence of fluctuations, solely determined by initial spatial inhomogeneities, and may considerably deviate from the stochastic descriptions. (f), Upon including the reactions given by Eqs. (3.1), a convective instability may occur, yielding “blurred” spiral waves.

as well as the average vortex density agree.

Noise plays a subtle role in initially perturbing the system and inducing, under suitable initial conditions, an average density of about 0.5 spiral vortices per square wavelength. Neglecting fluctuation terms in the SPDE (3.6) results in deterministic reaction-diffusion equations. The numerical solution of the latter, see Fig. 3.5 (e), yields spiral waves with the

correct wavelength, velocity and frequency. However, the vortex density, and therefore the spirals' entanglement, depends crucially on initial spatial inhomogeneities. In particular, if no spatial inhomogeneities are present, spirals do not form, and the systems remains spatially uniform.

For large system sizes, within the continuum limit, the interacting particle systems are describable by the SPDE (3.6), and may consequently exhibit their different universal types of pattern formation. In the example of cyclically competing populations which we have considered, the nonlinear parts of the SPDE (3.6) fall into the universality class of the normal form of the Hopf bifurcation. Therefore, the driving mechanism of the self-organizing patterns is captured by a complex Ginzburg-Landau equation (CGLE). For the stochastic reactions which we have considered, we were able to analytically derive the CGLE. Comparison of its predictions for characteristic quantities of the spiral waves, namely wavelength, velocity and frequency, yields a good agreement with numerical results.

Above, we have mentioned various instabilities that the CGLE exhibits. It is tempting to search for such instabilities in suitable stochastic models for interacting, mobile individuals. For the May-Leonard reactions (3.5), the CGLE yields stable spiral waves, in agreement with the behavior of the stochastic system. If we complement the reactions (3.5) with the reactions (3.1) of the neutrally stable model considered in Section 3.3, a convective instability can arise [176]. The resulting patterns appear as “blurred” spiral waves as shown in Fig. 3.5 (e). Future studies may uncover the footprints of other types of instabilities in stochastic population models.

3.6 Conclusion and Outlook

Coexistence of different species in the earth's ecosystems is crucial for their viability. Theoretical explanations of the observed extremely high degree of species diversity pose major challenges. Indeed, under general, realistic assumptions, stochastic models for population dynamics unavoidably lead to the ultimate extinction of all but one species. However, ecosystems' behavior may better correspond to persistent transient states of noisy dynamics than to the latter's ultimate fate [148, 147]. We have argued that ecologically relevant time-scales are concededly long, but not necessarily long enough for the disappearance of such persistent transients.

As a main result, we have developed a classification of species stability/instability in the presence of fluctuations. This concept is based on ecologically relevant and accessible (by simulations) observables, namely the mean extinction time T and the number of interacting individuals N . In brief, typically, an exponential increase of T in N induces coexistence which remains stable on extremely long time-scales. In contrast, logarithmic dependence of T on N indicates unstable diversity. This classification has been derived from the

consideration of a model exhibiting neutrally stable coexistence; in this “critical” situation, the mean extinction time depends linearly on the system size.

This classification may be significantly relevant and useful in future studies of stochastic population dynamics. For instance, the influence of internal age structure or the type of topology of the individuals’ interaction network on the maintenance of biodiversity constitute highly important further questions. In our work, we have shown how the influence of individuals’ mobility on species diversity may be treated in the framework of the above classification. In the asymptotic limit of large systems, we have found a mobility threshold which separates maintained diversity from rapid extinction. Generally, such state transitions are accompanied by *critical phenomena*. Together with Jonas Cremer and Erwin Frey, we are currently studying universal scaling behavior and critical exponents of the mean extinction time depending on the system size, in the framework of well-mixed populations [144, 146]. Mean-field exponents emerge, a scenario that is expected to dramatically change when including spatial degrees of freedom.

Self-organization of mobile individuals has been shown to be governed by the dynamics of stochastic partial differential equations. Their universality classes, stemming from the bifurcation behavior, describe the types of patterns and instabilities that may appear in such stochastic population models with mobile individuals. We have investigated cyclically competing populations and observed the emergence of entangled spiral waves, as predicted by an underlying complex Ginzburg-Landau equation. Possible instabilities may be an interesting topic of further work. While we have focussed on the situation where all species are equally mobile, different values of motility appear in natural ecosystems and can, for example, cause Turing patterns [10, 177]. When mobility is low, irregular patterns emerge that cannot be described by stochastic partial differential equations. The development of further methods for their description and classification can trigger future studies and yield further insights into the dominant role of fluctuations. As an example, together with Anton Winkler and Erwin Frey, we are currently applying real-space renormalization group arguments to the investigation of such systems [178, 179].

Our methods and results may also be relevant for social sciences. Indeed, every society exhibits a large spectrum of different human behaviors. For instances, in many situations, people face the decision of cooperating with others, for the benefit of all that contribute, or following a cheater strategy and exploiting others. While not cooperating often seems the rational behavior in such public good games [180, 181], societies maintain a considerable, possibly varying, level of cooperation. Among the mechanisms that allow for the coexistence of cooperators and cheaters are local interactions of spatially distributed individuals [182] and cyclic dynamics of different strategies [183, 184]. Incorporating individuals’ mobility renders such systems describable by stochastic partial differential equations, and insights from our studies on species in cyclic competition may be used and transferred to these kind of problems.

The studies which we have presented are theoretical, in part analytical calculations and in

part computer simulations. However, we believe that our results may be fruitfully applied to real-life experiments. As an example, one may employ colicinogenic bacteria on Petri-dishes, extending the studies presented in [43]. Namely, in experiments stimulated by our studies, the bacteria may be rendered mobile using a liquid agar. In Ref. [156], we have estimated the order of the critical mobility in this case, and shown that it could be experimentally accessible. Demonstration of a mobility threshold for biodiversity using microbial communities on a Petri-dish would be a fascinating subject. Moreover, the theoretical predictions for mobility's impact on pattern formation constitute a current challenge for experimental investigation. Individuals' mobility should render the emerging patterns more regular and geometric. Last but not least, in the light of a recent publication on patterns of neutral bacterial growth [185], investigating bacterial communities' patterns of growth and coexistence would provide insight into the influence of selection.

Coexistence versus extinction in the stochastic cyclic Lotka-Volterra model

Tobias Reichenbach, Mauro Mobilia, and Erwin Frey

*Arnold Sommerfeld Center for Theoretical Physics and Center for NanoScience, Department of Physics,
Ludwig-Maximilians-Universität München, Theresienstrasse 37, D-80333 München, Germany*

(Received 8 June 2006; revised manuscript received 11 August 2006; published 10 November 2006)

Cyclic dominance of species has been identified as a potential mechanism to maintain biodiversity, see, e.g., B. Kerr, M. A. Riley, M. W. Feldman and B. J. M. Bohannan [Nature **418**, 171 (2002)] and B. Kirkup and M. A. Riley [Nature **428**, 412 (2004)]. Through analytical methods supported by numerical simulations, we address this issue by studying the properties of a paradigmatic non-spatial three-species stochastic system, namely, the “rock-paper-scissors” or cyclic Lotka-Volterra model. While the deterministic approach (rate equations) predicts the coexistence of the species resulting in regular (yet neutrally stable) oscillations of the population densities, we demonstrate that fluctuations arising in the system with a finite number of agents drastically alter this picture and are responsible for extinction: After long enough time, two of the three species die out. As main findings we provide analytic estimates and numerical computation of the extinction probability at a given time. We also discuss the implications of our results for a broad class of competing population systems.

DOI: [10.1103/PhysRevE.74.051907](https://doi.org/10.1103/PhysRevE.74.051907)

PACS number(s): 87.23.Cc, 05.40.-a, 02.50.Ey, 05.10.Gg

I. INTRODUCTION

Understanding biodiversity and coevolution is a central challenge in modern evolutionary and theoretical biology [1–3]. In this context, for some decades much effort has been devoted to mathematically model dynamics of competing populations through nonlinear, yet deterministic, set of rate equations such as the equations devised by Lotka and Volterra [4,5] or many of their variants [1–3]. This heuristic approach is often termed as population-level description. As a common feature, these deterministic models fail to account for stochastic effects (such as fluctuations and spatial correlations). However, to gain some more realistic and fundamental understanding on generic features of population dynamics and mechanisms leading to biodiversity, it is highly desirable to include internal stochastic noise in the description of agents’ kinetics by going beyond the classical deterministic picture. One of the main reasons is to account for discrete degrees of freedom and finite-size fluctuations [6,7]. In fact, the deterministic rate equations always (tacitly) assume the presence of infinitely many interacting agents, while in real systems there is a large, yet finite, number of individuals (recently, this issue has been addressed in Refs. [8,9]). As a consequence, the dynamics is intrinsically stochastic and the unavoidable finite-size fluctuations may have drastic effects and even completely invalidate the deterministic predictions.

Interestingly, both *in vitro* [10] and *in vivo* [11] experiments have recently been devoted to experimentally probe the influence of stochasticity on biodiversity: The authors of Refs. [10,11] have investigated the mechanism necessary to ensure coexistence in a community of three populations of *Escherichia coli* and have numerically modeled the dynamics of their experiments by the so-called “rock-paper-scissors” model, well known in the field of game theory [12,13]. This is a three-species cyclic generalization of the Lotka-Volterra model [14–16]. As a result, the authors of Ref. [10] reported that in a well-mixed (nonspatial) environ-

ment (i.e., when the experiments were carried out in a flask) two species went extinct after some finite time, while coexistence of the populations was never observed. Motivated by these experimental results, in this work we theoretically study the stochastic version of the cyclic Lotka-Volterra model and investigate in detail the effects of finite-size fluctuations on possible population extinction or coexistence.

For our investigation, as suggested by the flask experiment of Ref. [10], the stochastic dynamics of the cyclic Lotka-Volterra model is formulated in the natural language of urn models [17] and by adopting the so-called individual-based description [18]. In the latter, the explicit rules governing the interaction of a finite number of individuals with each other are embodied in a master equation. The fluctuations are then specifically accounted for by an appropriate Fokker-Planck equation derived from the master equation via the so-called van Kampen expansion [19]. This program allows us to quantitatively study the deviations of the stochastic dynamics of the cyclic Lotka-Volterra model with respect to the rate equation predictions and to address the question of the extinction probability, the computation of which is the main result of this work. From a more general perspective, we think that our findings have a broad relevance, both theoretical and practical, as they shed further light on how stochastic noise can dramatically affect the properties of the numerous nonlinear systems whose deterministic description, as in the case of the cyclic Lotka-Volterra model, predicts the existence of neutrally stable solutions, i.e., cycles in the phase portrait [20].

This paper is organized as follows. The cyclic Lotka-Volterra model is introduced in the next section and its deterministic rate equation treatment is presented. In Sec. III, we develop a quantitative analytical approach that accounts for stochasticity; a Fokker-Planck equation is derived from the underlying master equation within a van Kampen expansion. This allows us to compute the variances of the agents’ densities. We also study the time dependence properties of the system by carrying out a Fourier analysis from a set of Langevin equations. Section III D is devoted to the compu-

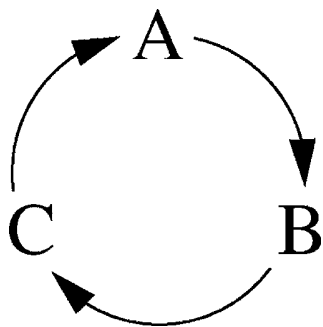


FIG. 1. Illustration of cyclic dominance of three states A , B , and C . The latter may correspond to the strategies in a rock-paper-scissors game [12] or to different bacterial species [10,11].

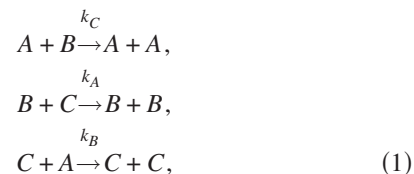
tation of the probability of having extinction of two species at a given time, which constitutes the main issue of this work. In the final section, we summarize our findings and present our conclusions.

II. THE CYCLIC POPULATION MODEL: INTRODUCTION AND ANALYSIS OF THE RATE EQUATIONS

A. The model

The cyclic Lotka-Volterra model under consideration here is a system where three states A , B , and C cyclically dominate each other: A invades B , B outperforms C , and C in turn dominates over A , schematically drawn in Fig. 1. These three states A , B , and C allow for various interpretations, ranging from strategies in the rock-paper-scissors game [13] over tree, fire, ash in forest fire models [21] or chemical reactions [22] to different bacterial species [10,11]. In the latter case, a population of poison producing bacteria was brought together with another being resistant to the poison and a third which is not resistant. As the production of poison as well as the resistance against it have some cost, these species show a cyclic dominance: the poison-producing one invades the nonresistant one, which in turn reproduces faster than the resistant one, and the latter finally dominates the poison producing one. In a well-mixed environment, such as a flask in the experiments [10,11], eventually only one species survives. The populations are large but finite, and the dynamics of reproduction and killing events may to a good approximation be viewed as stochastic.

Motivated from these biological experiments, we introduce a stochastic version of the cyclic Lotka-Volterra model. Consider a population of size N which is well mixed, i.e., in the absence of spatial structure. The stochastic dynamics used to describe its evolution, illustrated in Fig. 2, is referred to as the “urn model” [17] and is closely related to the Moran process [23,24]. At every time step, two randomly chosen individuals are selected, which may at certain probability react according to the following scheme:



with reaction rates k_A , k_B , and k_C . We observe the cyclic dominance of the three species. Also, the total number N of individuals is conserved by this dynamics; this will of course play a role in our further analysis.

We now proceed with the analysis of the deterministic version of the system (1). This will prove insightful for building a stochastic description of the model, which is the scope of Sec. III.

B. Deterministic approach

The deterministic rate equations describe the time evolution of the densities $a(t)$, $b(t)$, and $c(t)$ for the species A , B , and C ; they read

$$\begin{aligned} \dot{a} &= a(k_C b - k_B c), \\ \dot{b} &= b(k_A c - k_C a), \\ \dot{c} &= c(k_B a - k_A b), \end{aligned} \quad (2)$$

where the overdot stands for the time derivative. These equations describe a well-mixed system, without any spatial correlations, as naturally implemented in urn models [17] or, equivalently, infinite dimensional lattice systems or complete graphs. In the following, Eqs. (2) are discussed and, from their properties, we gain intuition on the effects of stochasticity.

Already from the basic reactions (1) we have noticed that the total number of individuals is conserved, which is a prop-

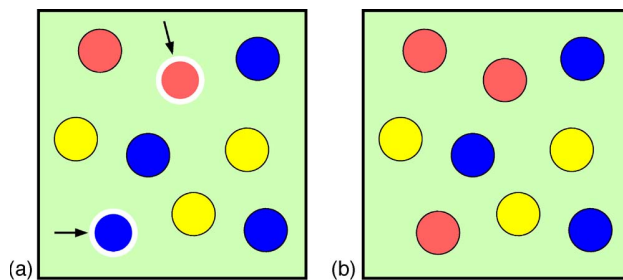


FIG. 2. (Color online) The urn model describes stochastic evolution of well-mixed finite populations. We show three species as yellow or light gray (A), red or medium gray (B), and blue or dark gray (C). At each time step, two random individuals are chosen (indicated by arrows in the top picture) and react (bottom picture).

erty correctly reproduced by the rate equations (2). Setting the total density, meaning the sum of the densities a , b , and c , to unity, we obtain

$$a(t) + b(t) + c(t) = 1 \quad (3)$$

for all times t . Only two out of the three densities are thus independent; we may view the time evolution of the densities in a two-dimensional phase space.

Equations (2) together with Eq. (3) admit three trivial (absorbing) fixed points: $(a_1^*, b_1^*, c_1^*) = (1, 0, 0)$, $(a_2^*, b_2^*, c_2^*) = (0, 1, 0)$, and $(a_3^*, b_3^*, c_3^*) = (0, 0, 1)$. They denote states where only one of the three species survived, the other ones died out. In addition, the rate equations (2) also predict the existence of a fixed point (a^*, b^*, c^*) which corresponds to a reactive steady state, associated with the coexistence of all three species:

$$\begin{aligned} a^* &= \frac{k_A}{k_A + k_B + k_C}, \\ b^* &= \frac{k_B}{k_A + k_B + k_C}, \\ c^* &= \frac{k_C}{k_A + k_B + k_C}. \end{aligned} \quad (4)$$

To determine the nature of this fixed point, we observe that another constant of motion exists for the rate equations (2), namely, the quantity

$$a(t)^{k_A} b(t)^{k_B} c(t)^{k_C} \equiv a(0)^{k_A} b(0)^{k_B} c(0)^{k_C} \quad (5)$$

does not evolve in time. In contrast to the total density (3), this constant of motion is only conserved by the rate equations but does not stem from the reaction scheme (1). Hence, when considering the stochastic version of the cyclic model, the total density remains constant but the expression (5) will no longer be a conserved quantity. The above fixed point (4) and constant of motion (5) have been derived and discussed also within the framework of game theory; see, e.g., Ref. [12].

In Fig. 3, we depict the ternary phase space [25] for the densities a , b , and c : The solutions of the rate equations (2) are shown for different initial conditions and a given set of rates k_A , k_B , and k_C . As the rate equations (2) are nonlinear in the densities, we cannot solve them analytically, but use numerical methods. Due to the constant of motion, the solutions yield cycles around the reactive fixed point (thus corresponding to case 3 in Durrett and Levin's classification [26]). The three trivial steady states, corresponding to saddle points within the linear analysis, are the edges of the simplex. The reactive stationary state, as well as the cycles, are neutrally stable, stemming from the existence of the constant of motion (5). Especially, the reactive fixed point is a center fixed point. The boundary of the simplex denotes states where at least one of the three species died out; as cyclic dominance is lost, states that have reached this boundary will evolve towards one of the edges, making the boundary absorbing.

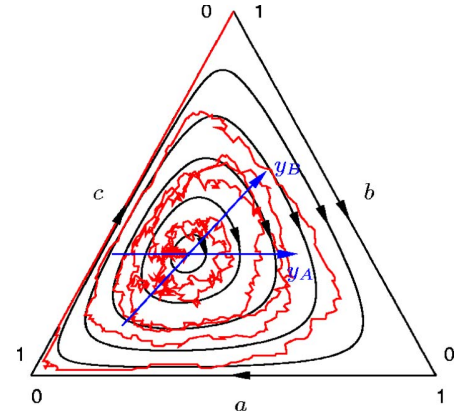


FIG. 3. (Color online) The three-species simplex for reaction rates $k_A=1$, $k_B=1.5$, $k_C=2$. The rate equations predict cycles, which are shown in black. Their linearization around the reactive fixed point is solved in proper coordinates y_A , y_B (blue or dark gray). The red (or light gray) erratic flow denotes a single trajectory in a finite system ($N=200$), obtained from stochastic simulations. It spirals out from the reactive fixed point, eventually reaching an absorbing state.

1. Linear regime

The nonlinearity of Eqs. (2) induces substantial difficulties in the analytical treatment. However, much can already be inferred from the linearization around the reactive fixed point (4), which we will consider in the following. We therefore introduce the deviations from the reactive fixed point, denoted as x_A , x_B , x_C :

$$\begin{aligned} x_A &= a - a^*, \\ x_B &= b - b^*, \\ x_C &= c - c^*. \end{aligned} \quad (6)$$

Using conservation of the total density (3), we can eliminate x_C , and the remaining linearized equations (2) may be put into the form $\dot{\mathbf{x}} = \mathcal{A}\mathbf{x}$, with the vector $\mathbf{x} = (x_A, x_B)$ and the matrix

$$\mathcal{A} = \frac{1}{k_A + k_B + k_C} \begin{pmatrix} k_A k_B & k_A(k_B + k_C) \\ -k_B(k_A + k_C) & -k_A k_B \end{pmatrix}. \quad (7)$$

The reactive fixed point is associated to the eigenvalues $\lambda_{\pm} = \pm i\omega_0$ of \mathcal{A} , where ω_0 is given by

$$\omega_0 = \sqrt{\frac{k_A k_B k_C}{k_A + k_B + k_C}}; \quad (8)$$

oscillations with this frequency arise in its vicinity. In proper coordinates $\mathbf{y} = \mathcal{S}\mathbf{x}$, these oscillations are harmonic, being the solution of $\dot{\mathbf{y}} = \tilde{\mathcal{A}}\mathbf{y}$, with

$$\tilde{\mathcal{A}} = \mathcal{S}\mathcal{A}\mathcal{S}^{-1} = \begin{pmatrix} 0 & \omega_0 \\ -\omega_0 & 0 \end{pmatrix}.$$

For illustration, we have included these coordinates, in which the solutions take the form of circles around the origin, in Fig. 3. The linear transformation $\mathbf{x} \rightarrow \mathbf{y}$ is given by

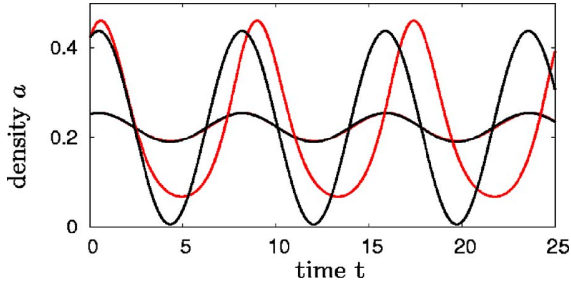


FIG. 4. (Color online) The deterministic time evolution of the density a for small and large amplitudes. The prediction (11), shown in black, is compared to the numerical solution (red or gray) of the rate equations (2). For small amplitudes [$a(0)=a^*+0.03$, $b(0)=b^*$], both coincide. However, for large amplitudes [$a(0)=a^*+0.2$, $b(0)=b^*$], they considerably differ both in amplitude and frequency. We used reaction rates $k_A=1$, $k_B=1.5$, $k_C=2$.

$$S = \frac{\sqrt{3}}{2} \begin{pmatrix} \frac{k_A+k_C}{k_A k_C} \omega_0 & \frac{1}{k_C} \omega_0 \\ 0 & 1 \end{pmatrix}. \quad (9)$$

The equations $\dot{\mathbf{y}} = \tilde{\mathbf{A}}\mathbf{y}$ are easily solved:

$$y_A(t) = y_A(0)\cos(\omega_0 t) + y_B(0)\sin(\omega_0 t),$$

$$y_B(t) = y_B(0)\cos(\omega_0 t) - y_A(0)\sin(\omega_0 t). \quad (10)$$

Eventually, we obtain the solutions for the linearized rate equations

$$a(t) = a^* + [a(0) - a^*]\cos(\omega_0 t) + \omega_0 \left\{ \frac{1}{k_C}[a(0) - a^*] + \frac{k_B + k_C}{k_B k_C}[b(0) - b^*] \right\} \sin(\omega_0 t), \quad (11)$$

where $b(t)$ and $c(t)$ follow by cyclic permutations.

To establish the validity of the linear analysis (7)–(11), we compare the (numerical) solution of the rate equations (2) with the linear approximations (11). As shown in Fig. 4, when $a(0) - a^* \approx 0.03$, $b(0) - b^* = 0$, the agreement between the nonlinear rate equations (2) and the linear approximation (11) is excellent, both curves almost coincide. On the other hand, the nonlinear terms appearing in Eqs. (2) become important already when $a(0) - a^* \approx 0.1$ and are responsible for significant discrepancies both in the amplitudes and frequency from the predictions of Eq. (11).

2. Radius \mathcal{R}

We now aim at introducing a measure of distance \mathcal{R} to the reactive fixed point within the phase portrait. In the next section, this quantity will help quantify effects of stochasticity. As it was recently proved useful in a related context [8], we aim at taking the structure of cycles predicted by the deterministic equations, see Fig. 3, into account by requiring that the distance should not change on a given cycle. Motivated from the constant of motion (5), we introduce

$$\mathcal{R} = \mathcal{N} \sqrt{a^* k_A b^* k_B c^* k_C - a^{k_A} b^{k_B} c^{k_C}}, \quad (12)$$

with the normalization factor (see below)

$$\mathcal{N} = \sqrt{\frac{3}{2} \frac{k_B(k_A + k_C)}{(k_A + k_B + k_C)^3 a^* k_A b^* k_B c^* k_C}}. \quad (13)$$

Being conserved by Eqs. (2), \mathcal{R} remains constant on every deterministic cycle. As it vanishes at the reactive fixed point and monotonically grows when departing from it, \mathcal{R} yields a measure of the distance to the latter.

Expanding the radius \mathcal{R} in small deviations \mathbf{x} from the reactive fixed point results in

$$\mathcal{R}^2 = \frac{\mathcal{N}^2}{2} (k_A + k_B + k_C)^2 a^* k_A b^* k_B c^* k_C \times \left[\left(\frac{1}{k_A} + \frac{1}{k_C} \right) x_A^2 + \left(\frac{1}{k_B} + \frac{1}{k_C} \right) x_B^2 + \frac{2}{k_C} x_A x_B \right] + o(\mathbf{x}^2). \quad (14)$$

In the variables $\mathbf{y} = S\mathbf{x}$, with our choice for \mathcal{N} , it simplifies to

$$\mathcal{R}^2 = y_A^2 + y_B^2 + o(\mathbf{y}^2), \quad (15)$$

corresponding to the radius of the deterministic circles, which emerge in the variables \mathbf{y} .

3. Effects of stochasticity: Qualitative discussion

The fact that the number N of particles is *finite* induces fluctuations that are not accounted for by Eqs. (2). In the following, our goal is to understand the importance of fluctuations and their effects on the deterministic picture (2). We show that, due to the neutrally stable character of the deterministic cycles, fluctuations have drastic consequences. Intuitively, we expect that in the presence of stochasticity, each trajectory performs a random walk in the phase portrait, interpolating between the deterministic cycles (as will be revealed by considering \mathcal{R}), eventually reaching the boundary of the phase space. There, the cyclic dominance is completely lost, as one of the species gets extinct. Of the two remaining ones, one species is defeating the other, such that the latter soon gets extinct as well, leaving the other one as the only survivor (this corresponds to one of the trivial fixed points, the edges of the ternary phase space). We thus observe the boundary to be absorbing, and presume the system to always end up in one of the absorbing states. A first indication of the actual emergence of this scenario can be inferred from the stochastic trajectory shown in Fig. 3.

III. FLUCTUATIONS IN FINITE POPULATIONS: A STOCHASTIC APPROACH

In this section, we set up a stochastic description for the cyclic Lotka-Volterra model in the urn formulation with finite number N of individuals. Starting from the master equation of the stochastic process, we obtain a Fokker-Planck equation for the time evolution of the probability $P(a, b, c, t)$ of finding the system in state a, b, c at time t . It allows us to gain a detailed understanding of the stochastic system. In

particular, we will find that, as anticipated at the end of the last section, after long enough time, the system reaches one of the absorbing states. Our main result is the time dependence of the extinction probability, being the probability that, starting at a situation corresponding to the reactive fixed point, after time t two of the three species have died out. It is obtained through mapping onto a known first-passage problem. We compare our analytical findings to results from stochastic simulations. For the sake of clarity and without loss of generality, throughout this section, the case of equal reaction rates $k_A=k_B=k_C=1$ is considered. Details on the unequal rates situation are relegated to Appendix.

A. Stochastic simulations

We carried out extensive stochastic simulations to support and corroborate our analytical results. An efficient simulation method originally due to Gillespie [27] was implemented for the reactions (1). Time and type of the next reaction taking place are determined by random numbers, using the Poisson nature of the individual reactions. For the extinction probability, to unravel the universal time-scaling, system sizes ranging from $N=100$ to $N=1000$ were considered, with sample averages over 10 000 realizations.

B. From the master to Fokker-Planck equation

Let us start with the master equation of the processes (1). We derive it in the variables x_A, x_B, x_C , which were introduced in Eq. (6) as the deviations of the densities from the reactive fixed point. Using the conservation of the total density, $x_A+x_B+x_C=0$, x_C is eliminated and $\mathbf{x}=(x_A, x_B)$ kept as independent variables. The master equation for the time evolution of the probability $P(\mathbf{x}, t)$ of finding the system in state \mathbf{x} at time t thus reads

$$\partial_t P(\mathbf{x}, t) = \sum_{\delta\mathbf{x}} \{P(\mathbf{x} + \delta\mathbf{x}, t) \mathcal{W}(\mathbf{x} + \delta\mathbf{x} \rightarrow \mathbf{x}) - P(\mathbf{x}, t) \mathcal{W}(\mathbf{x} \rightarrow \mathbf{x} + \delta\mathbf{x})\}, \quad (16)$$

where $\mathcal{W}(\mathbf{x} \rightarrow \mathbf{x} + \delta\mathbf{x})$ denotes the transition probability from state \mathbf{x} to the state $\mathbf{x} + \delta\mathbf{x}$ within one time step; summation extends over all possible changes $\delta\mathbf{x}$. We choose the unit of time so that, on average, every individual reacts once per time step.

According to the Kramers-Moyal expansion of the master equation to second order in $\delta\mathbf{x}$, this results in the Fokker-Planck equation

$$\partial_t P(\mathbf{x}, t) = -\partial_i [\alpha_i(\mathbf{x}) P(\mathbf{x}, t)] + \frac{1}{2} \partial_i \partial_j [\mathcal{B}_{ij}(\mathbf{x}) P(\mathbf{x}, t)]. \quad (17)$$

Here, the indices i, j stand for A and B ; in the above equation, the summation convention implies summation over them. The quantities α_i and \mathcal{B}_{ij} are, according to the Kramers-Moyal expansion

$$\alpha_i(\mathbf{x}) = \sum_{\delta\mathbf{x}} \delta x_i \mathcal{W}(\mathbf{x} \rightarrow \mathbf{x} + \delta\mathbf{x}),$$

$$\mathcal{B}_{ij}(\mathbf{x}) = \sum_{\delta\mathbf{x}} \delta x_i \delta x_j \mathcal{W}(\mathbf{x} \rightarrow \mathbf{x} + \delta\mathbf{x}). \quad (18)$$

Note that \mathcal{B} is symmetric. For the sake of clarity, we outline the calculation of $\alpha_A(\mathbf{x})$: The relevant changes δx_A in the density a result from the basic reactions (1); they are $\delta x_A = 1/N$ in the first reaction, $\delta x_A = 0$ in the second, and $\delta x_A = -1/N$ in the third. The corresponding rates read $\mathcal{W} = Nab$ for the first reaction (the prefactor of N enters due to our choice of time scale, where N reactions occur in one unit of time), and $\mathcal{W} = Nac$ for the third, resulting in $\alpha_A(\mathbf{x}) = ab - ac$. The other quantities are calculated analogously, yielding

$$\alpha_A(\mathbf{x}) = ab - ac,$$

$$\alpha_B(\mathbf{x}) = bc - ab,$$

$$\mathcal{B}_{AA}(\mathbf{x}) = N^{-1}(ab + ac),$$

$$\mathcal{B}_{AB}(\mathbf{x}) = \mathcal{B}_{BA}(\mathbf{x}) = -N^{-1}ab,$$

$$\mathcal{B}_{BB}(\mathbf{x}) = N^{-1}(bc + ab) \quad (19)$$

with $a = a^* + x_A$, $b = b^* + x_B$, $c = c^* - x_A - x_B$.

Van Kampen's linear noise approximation [19] further simplifies these quantities. In this approach, the values $\alpha_i(\mathbf{x})$ are expanded around $\mathbf{x}=0$ to the first order. As they vanish at the reactive fixed point, we obtain

$$\alpha_i(\mathbf{x}) = \mathcal{A}_{ij} x_j, \quad (20)$$

where the matrix elements \mathcal{A}_{ij} are given by

$$\mathcal{A}_{ij} = \left. \frac{\partial \alpha_i}{\partial x_j} \right|_{\mathbf{x}=0}. \quad (21)$$

The matrix \mathcal{A} , already given in Eq. (7), embodies the deterministic evolution, while the stochastic noise is encoded in \mathcal{B} . To take the fluctuations into account within the van Kampen expansion, one approximates \mathcal{B} by its values at the reactive fixed point. Hence, we find

$$\mathcal{A} = \frac{1}{3} \begin{pmatrix} 1 & 2 \\ -2 & -1 \end{pmatrix}, \quad \mathcal{B} = \frac{1}{9N} \begin{pmatrix} 2 & -1 \\ -1 & 2 \end{pmatrix} \quad (22)$$

and the corresponding Fokker-Planck equation reads

$$\partial_t P(\mathbf{x}, t) = -\partial_i [\mathcal{A}_{ij} x_j P(\mathbf{x}, t)] + \frac{1}{2} \mathcal{B}_{ij} \partial_i \partial_j P(\mathbf{x}, t). \quad (23)$$

For further convenience, we now bring Eq. (23) into a more suitable form by exploiting the polar symmetry unveiled by the variables \mathbf{y} . As for the linearization of Eqs. (2), it is useful to rely on the linear mapping $\mathbf{x} \rightarrow \mathbf{y} = \mathcal{S}\mathbf{x}$, with $\mathcal{A} \rightarrow \tilde{\mathcal{A}} = \mathcal{S}\mathcal{A}\mathcal{S}^{-1}$. Interestingly, it turns out that this transformation diagonalizes \mathcal{B} . One indeed finds $\mathcal{B} \rightarrow \tilde{\mathcal{B}} = \mathcal{S}\mathcal{B}\mathcal{S}^T$, with

$$\tilde{\mathcal{B}} = \frac{1}{6N} \begin{pmatrix} 1 & 0 \\ 0 & 1 \end{pmatrix}. \quad (24)$$

In the \mathbf{y} variables, the Fokker-Planck equation (23) takes the simpler form

$$\partial_t P(\mathbf{y}, t) = -\omega_0 [y_A \partial_{y_B} - y_B \partial_{y_A}] P(\mathbf{y}, t) + \frac{1}{12N} [\partial_{y_A}^2 + \partial_{y_B}^2] P(\mathbf{y}, t). \quad (25)$$

To capture the structure of circles predicted by the deterministic approach, we introduce polar coordinates

$$\begin{aligned} y_A &= r \cos \phi, \\ y_B &= r \sin \phi. \end{aligned} \quad (26)$$

Note that in the vicinity of the reactive fixed point, r denotes the distance \mathcal{R} , which is now a random variable $\mathcal{R} = r + o(r)$. The Fokker-Planck equation (25) eventually turns into

$$\begin{aligned} \partial_t P(r, \phi, t) &= -\omega_0 \partial_\phi P(r, \phi, t) \\ &+ \frac{1}{12N} \left[\frac{1}{r^2} \partial_\phi^2 + \frac{1}{r} \partial_r + \partial_r^2 \right] P(r, \phi, t). \end{aligned} \quad (27)$$

The first term on the right-hand side of this equation describes the system's deterministic evolution, being the motion on circles around the origin at frequency ω_0 . Stochastic effects enter through the second term, which corresponds to isotropic diffusion in two dimensions with diffusion constant $D = 1/(12N)$. Note that it vanishes in the limit of infinitely many agents, i.e., when $N \rightarrow \infty$.

If we consider a spherically symmetric probability distribution $P(r, \phi, t_0)$ at time t_0 , i.e., independent of the angle ϕ at t_0 , then this symmetry is conserved by the dynamics according to Eq. (27) and one is left with a radial distribution function $P(r, \phi, t) = P(r, t)$. The Fokker-Planck equation (27) thus further simplifies and reads

$$\partial_t P(r, t) = D \left[\frac{1}{r} \partial_r + \partial_r^2 \right] P(r, t). \quad (28)$$

This is the diffusion equation in two dimensions with diffusion constant $D = 1/(12N)$, expressed in polar coordinates, for a spherically symmetric probability distribution. This is the case on which we specifically focus in the following. Within our approximations around the reactive fixed point, the probability distribution $P(r, t)$ is thus the same as for a system performing a two-dimensional random walk in the \mathbf{y} variables. Intuitively, such behavior is expected and its origin lies in the neutrally stable character of the cycles of the deterministic solution of the rate equations (2). The cycling around the reactive fixed point does not yield additional effects when considering spherically symmetric probability distributions. Furthermore, due to the existence of the constant of motion (5), the neutral stability does not only hold in the vicinity of the reactive fixed point, but in the whole ternary phase space. We thus expect the distance \mathcal{R} from the reactive fixed point, a random variable, to obey a diffusion-like equation in the whole phase space (and not only around the reactive fixed point). Actually, qualitatively identical behavior is also found in the general case of nonequal reaction rates k_A , k_B , and k_C (see the Appendix), as the constant of motion (5) again guarantees the neutral stability of the deterministic cycles.

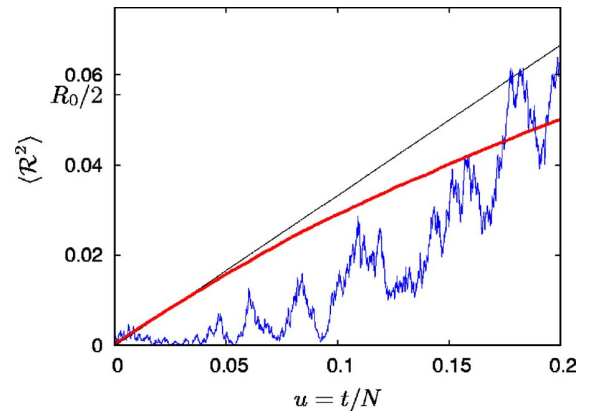


FIG. 5. (Color online) The averaged square radius $\langle \mathcal{R}^2 \rangle$ as a function of the rescaled time $u = t/N$. The blue (or dark gray) curve represents a single trajectory, which is seen to fluctuate widely. The linear black line indicates the analytical prediction (30), the red (or light gray) one corresponds to sample averages over 10^4 realizations in stochastic simulations. Hereby, we used a system size of $N = 1000$.

C. Fluctuations and frequencies around the reactive fixed point

In this subsection, we will use the Fokker-Planck equation (28) to investigate the time dependence of fluctuations around the reactive fixed point. In particular, we are interested in the time evolution of mean deviation from the latter. The average square distance $\langle \mathcal{R}^2(t) \rangle$ will be found to grow linearly in time, rescaled by the number N of individuals, before saturating. The frequency spectrum arising from erratic oscillations around the reactive fixed point is of further interest to characterize the stochastic dynamics: We will show that the frequency (8) predicted by the deterministic approach emerges as a pole in the power spectrum.

1. Fluctuations

Being interested in the vicinity of the reactive fixed point, in this subsection we ignore the fact that the boundary of the ternary phase space is absorbing. Then, the solution to the Fokker-Planck equation (28) with the initial condition $P(r, \phi, t_0 = 0) = \frac{1}{2\pi r} \delta(r)$, where the prefactor $1/(2\pi r)$ ensures normalization, is simply a Gaussian:

$$P(r, t) = \frac{1}{4\pi Dt} \exp\left(-\frac{r^2}{4Dt}\right). \quad (29)$$

This result predicts a broadening of the probability distribution in time, as the average square radius increases linearly with increasing time t :

$$\langle r^2(t) \rangle = \frac{1}{3} \frac{t}{N}. \quad (30)$$

As the time scales linearly with N , increasing the system size results in rescaling the time t , and the broadening of the probability distribution takes longer. To capture these findings, we introduce the rescaled variable $u \equiv t/N$.

In Fig. 5, we compare the time evolution of the squared

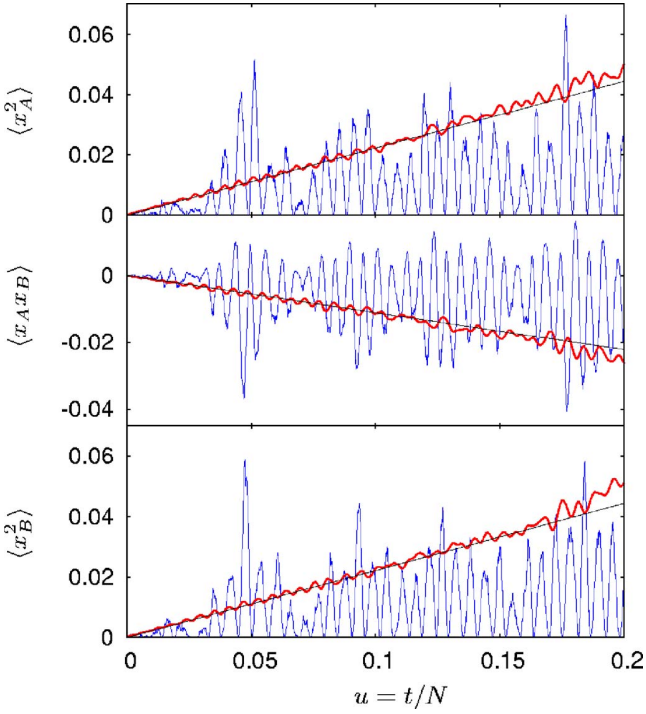


FIG. 6. (Color online) Time evolution of the variances of the densities a and b when starting at the reactive fixed point. The blue (or dark gray) curves correspond to a single realization, while the red (or light gray) ones denote averages over 1000 samples. Our results are obtained from stochastic simulations with a system size of $N=1000$. The black line indicates the analytical predictions.

radius $\langle \mathcal{R}^2(t) \rangle$ obtained from stochastic simulations with the prediction of Eq. (30) and find a good agreement in the linear regime around the reactive fixed point, where $\mathcal{R} = r + o(r)$. In fact, for short times, $\langle \mathcal{R}^2(t) \rangle$ displays a linear time dependence, with systematic deviation from Eq. (30) at longer times. We understand this as being in part due to the linear approximations used to derive Eq. (30), but also, and more importantly, to the fact that so far we ignored the absorbing character of the boundary. We conclude that the latter invalidates the Gaussian probability distribution for longer times. This issue, which requires a specific analysis, is the scope of Sec. III D, where a proper treatment is devised.

From the finding $\langle r^2(t) \rangle = 2u/3$ together with the spherical symmetry of Eq. (29), resulting in $\langle r(t)\phi(t) \rangle = \langle \phi^2(t) \rangle = 0$, we readily obtain the variances of the densities a and b :

$$\begin{aligned} \langle x_A^2(t) \rangle &= \langle x_B^2(t) \rangle = \frac{2}{9}u, \\ \langle x_A(t)x_B(t) \rangle &= -\frac{1}{9}u. \end{aligned} \quad (31)$$

According to these results, the average square deviations of the densities from the reactive fixed point grow linearly in the rescaled time u , thus exhibiting the same behavior as we already found for the average squared radius (30). In Fig. 6, these findings are compared to stochastic simulations for

small times u , where the linear growth is indeed recovered.

We may consider fluctuations of the densities a , b , and c not only around the reactive stationary state, as obtained in Eq. (31), but also as the deviations from the deterministic cycles. We consider the latter in the linear approximation around the fixed point, given by Eq. (11). The fluctuations around them are again described by the Fokker-Planck equation (17) with \mathcal{A} and \mathcal{B} given by Eqs. (19), but now x_A , x_B , and x_C are the deviations from the deterministic cycle $a(t) = a_0(t) + x_A(t)$, $b(t) = b_0(t) + x_B(t)$, and $c(t) = c_0(t) - x_A(t) - x_B(t)$, where a_0 , b_0 , and c_0 obey Eqs. (2) and characterize the deterministic cycles given by Eq. (11). Again performing van Kampen's linear noise approximation, we obtain a Fokker-Planck equation of the type (23), now with the matrices

$$\begin{aligned} \mathcal{A} &= \begin{pmatrix} 2a_0 + 2b_0 - 1 & 2a_0 \\ -2b_0 & -2a_0 - 2b_0 + 1 \end{pmatrix}, \\ \mathcal{B} &= \frac{1}{N} \begin{pmatrix} a_0(1 - a_0) & -a_0b_0 \\ -a_0b_0 & b_0(1 - b_0) \end{pmatrix}. \end{aligned} \quad (32)$$

Note that the entries of the above matrices now depend on time t via $a_0(t)$ and $b_0(t)$. The Fokker-Planck equation (23) yields equations for the time evolution of the fluctuations

$$\partial_t \langle x_i x_j \rangle = \mathcal{A}_{ik} \langle x_k x_j \rangle + \mathcal{A}_{jk} \langle x_k x_i \rangle + \mathcal{B}_{ij}. \quad (33)$$

They may be solved numerically for $\langle x_A^2(t) \rangle$, $\langle x_A(t)x_B(t) \rangle$, and $\langle x_B^2(t) \rangle$, yielding growing oscillations. In Fig. 7 we compare these findings to stochastic simulations. We observe a good agreement for small rescaled times $u = t/N$, while the oscillations of the stochastic results become more irregular at longer times.

2. Frequencies

Recently, it has been shown that the frequency predicted by the deterministic rate equations appears in the stochastic system due to a "resonance mechanism" [28]. Internal noise present in the system covers all frequencies and induces excitations, the largest occurring for the "resonant" frequency predicted by the rate equations. Here, following the same lines, we address the issue of the characteristic frequency in the stochastic cyclic Lotka-Volterra model.

In the vicinity of the reactive fixed point, the deterministic rate equations (2) predict density oscillations with frequency ω_0 given in Eq. (8). For the stochastic model, we now show that a spectrum of frequencies centered around this value ω_0 arises. The most convenient way to compute this power spectrum $P(\omega) \equiv \langle |\tilde{\mathbf{x}}(\omega)|^2 \rangle$ from the Fokker-Planck equation (23) is through the set of equivalent Langevin equations [29]

$$\dot{x}_i = \mathcal{A}_{ij}x_j + \xi_i, \quad (34)$$

with the white noise covariance matrix \mathcal{B} $\langle \xi_i(t)\xi_j(t') \rangle = \mathcal{B}_{ij}\delta(t-t')$. From the Fourier transform of Eq. (34), it follows that

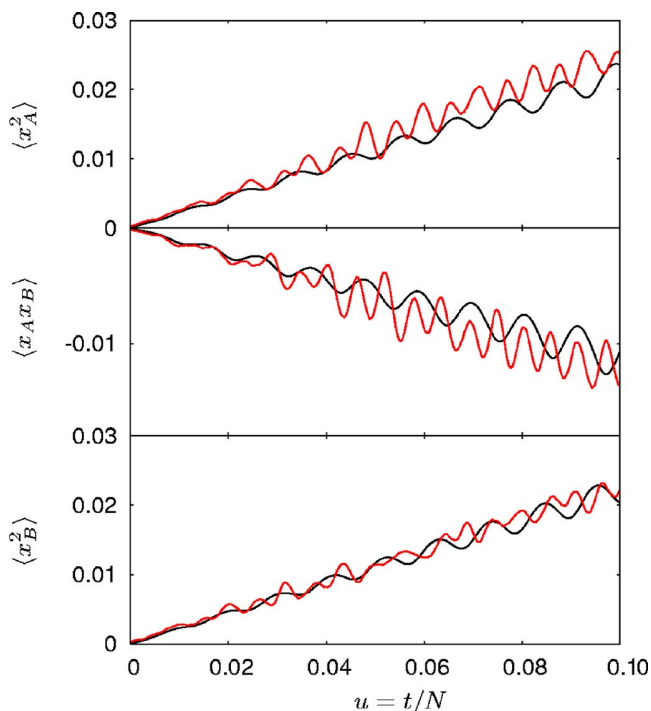


FIG. 7. (Color online) Variances of the densities a and b when starting at a cycle away from the fixed point. The black lines denote our analytical results, while the red (or gray) ones are obtained by stochastic simulations as averages over 1000 realizations. They are seen to agree for small times, while for larger ones the stochasticity of the system induces erratic oscillations. These results were obtained when starting from $a(t_0=0)=0.37$, $b(t_0=0)=1/3$.

$$P(\omega) \equiv \langle |\bar{\mathbf{x}}(\omega)|^2 \rangle = \text{Tr}[(\mathcal{A} + i\omega)^{-1} \mathcal{B} (\mathcal{A} - i\omega)^{-T}]$$

$$= \frac{4}{3N} \frac{1 + 3\omega^2}{(1 - 3\omega^2)^2}. \quad (35)$$

The power spectrum has a pole at the characteristic frequency already predicted from the rate equations (2), $\omega_0 = 1/\sqrt{3}$. For increasing system size N , the power spectrum displays a sharper alignment with this value. In Fig. 8 we compare our results to stochastic simulations and find an excellent agreement, except for the pole, where the power spectrum in finite systems obviously has a finite value. These results were obtained in the vicinity of the reactive fixed point, where the linear analysis (11) applies. As already found in the deterministic description (see Fig. 4), when departing from the center fixed point, nonlinearities will alter the characteristic frequency.

D. The extinction probability

So far, within the stochastic formulation, the fluctuations around the reactive steady state were found to follow a Gaussian distribution, linearly broadening in time. However, when approaching the absorbing boundary, the latter alters this behavior, see Fig. 5. In the following, we will incorporate this effect in our quantitative description. It plays an essential role when discussing the extinction probability, which is the scope of this subsection.

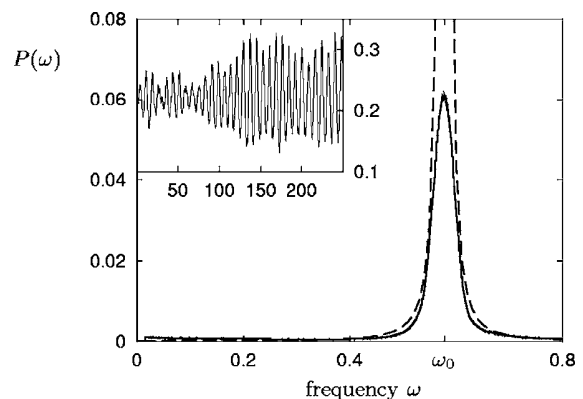


FIG. 8. The power spectrum for densities in the vicinity of the reactive fixed point. The dashed line indicates our analytical result, which has a pole at ω_0 . It agrees with stochastic simulations (solid). The inset shows the erratic oscillations of the density of one of the species for one realization. The system size considered is $N = 10\,000$.

The probability that one or more species die out in the course of time is of special interest within population dynamics from a biological viewpoint. When considering meta-populations formed of local patches, such questions were, e.g., raised in Ref. [30]. Here, we consider the extinction probability $P_{\text{ext}}(t)$ that, starting at the reactive fixed point, after time t two of the three species have died out. In our formulation, this corresponds to the probability that after time t the system has reached the absorbing boundary of the ternary phase space, depicted in Fig. 3. Considering states far from the reactive fixed point, we now have to take into account the absorbing nature of the boundary. This feature is incorporated in our approach by discarding the states having reached the boundary, so that a vanishing density of states occurs there. As the normalization is lost, we do no longer deal with probability distributions: In fact, discarding states at the boundary implies a time decay of the integrated density of states [which, for commodity, we still refer to as $P(r, t)$]. Ignoring the nonlinearities, the problem now takes the form of solving the Fokker-Planck equation (28) for an initial condition $P(r, t_0=0) = \frac{1}{2\pi r} \delta(r)$, and with the requirement that $P(r, t)$ has to vanish at the boundary. Hereby, the triangular shaped absorbing boundary is regarded as the outermost (degenerate) cycle of the deterministic solutions. As the linearization in the y variables around the reactive fixed point maps the cycles onto circles (see above), the triangular boundary is mapped to a sphere as well. Although the linearization scheme on which these mappings rely is inaccurate in the vicinity of the boundary, it is possible to incorporate nonlinear effects in a simple and pragmatic manner, as shown below. However, first let us consider the linearized problem, being a first-passage to a sphere of radius R , which is, e.g., treated in Chap. 6 of Ref. [31]. The solution is known to be a combination of modified Bessel functions of the first and second kind. Actually, the Laplace transform of the density of states reads

$$\begin{aligned}
& \text{LT}\{P(r,t)\} \\
&= \int dt e^{-st} P(r,t) \\
&= \frac{1}{2\pi D} \frac{I_0(R\sqrt{s/D})K_0(r\sqrt{s/D}) - I_0(r\sqrt{s/D})K_0(R\sqrt{s/D})}{I_0(R\sqrt{s/D})},
\end{aligned} \quad (36)$$

where $D=1/(12N)$ is the diffusion constant, I_0 and K_0 denote the Bessel function of the first, respectively, second, kind and of order zero, and R is the radius of the absorbing sphere. It is normalized at the initial time $t_0=0$; however, for later times t , the total number of states $\int_0^R dr \int_0^{2\pi} d\phi r P(r,t)$ will decay in time, as states are absorbed at the boundary.

Equipped with this result, we are now in a position to calculate the extinction probability $P_{\text{ext}}(t)$. It can be found by considering the probability current $J(\tau)$ at the absorbing boundary [31], namely,

$$J(\tau) = D \int_{\text{sphere}} d\Omega \left. \frac{\partial P(r,t)}{\partial r} \right|_{r=R}, \quad (37)$$

whose Laplace transform is given by

$$\text{LT}\{J(\tau)\} = \frac{1}{I_0(R\sqrt{s/D})}. \quad (38)$$

The extinction probability at time t is obtained from $J(\tau)$ by integrating over time τ until time t [31]: $P_{\text{ext}}(t) = \int_0^t d\tau J(\tau)$. Therefore, the Laplace transform of $P_{\text{ext}}(t)$ reads $\text{LT}\{P_{\text{ext}}(t)\} = 1/[sI_0(R\sqrt{s/D})]$. Again, we notice that we can write this equation in a form that depends on the time t only via the rescaled time $u = t/N$:

$$\text{LT}\{P_{\text{ext}}(u)\} = \frac{1}{sI_0(R\sqrt{s/12})}. \quad (39)$$

Hence, for different system sizes N , one obtains the same extinction probability $P_{\text{ext}}(u)$ provided one considers the same value for the scaling variable $t/N = \text{const}$ (see Fig. 9).

We cannot solve the inverse Laplace transform appearing in Eq. (39), but $I_0(z)$ might be expanded according to Ref. [32] as

$$I_0(z) = 1 + \frac{\frac{1}{4}z^2}{(1!)^2} + \frac{(\frac{1}{4}z^2)^2}{(2!)^2} + \frac{(\frac{1}{4}z^2)^3}{(3!)^2} + \dots \quad (40)$$

Considering the first three terms in this expansion, i.e., contributions up to z^4 , yields the approximate result

$$P_{\text{ext}}(t) = 1 - \left(1 + \frac{2}{3} \frac{t}{R^2 N}\right) \exp\left[-\frac{2}{3} \frac{t}{R^2 N}\right]. \quad (41)$$

Numerically, we have included higher terms. The results for contributions up to z^{10} in Eq. (40) are shown in Fig. 9. An estimate of the effective distance R to the absorbing boundary is determined by plugging either $a=0$, or $b=0$, or $c=0$ into Eq. (12), which yields $R_0=1/3$. From Fig. 9, we observe the extinction probability to be overestimated by Eq. (41) with $R=R_0$. This stems from nonlinearities altering the

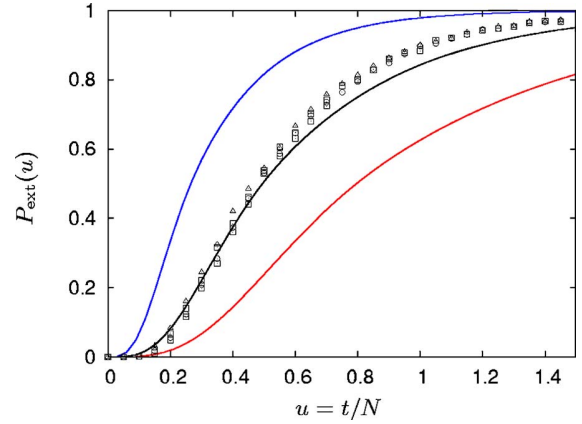


FIG. 9. (Color online) The extinction probability when starting at the reactive fixed point, depending on the rescaled time $u=t/N$. Stochastic simulations for different system sizes ($N=100$: triangles; $N=200$: boxes; $N=500$: circles) are compared to the analytical prediction (39). The left (blue or dark gray) is obtained from $R_0=1/3$, the right one (red or light gray) from $R_1=1/\sqrt{3}$, and the middle (black) corresponds to the average of both $R_2=\frac{1}{2}(R_0+R_1)$.

analysis having led to Eq. (41). However, adjusting R on physical grounds, we are able to capture these effects. Another estimate of P_{ext} is obtained by considering the expression (14), which arises from a linear analysis. As the extinction of two species requires $x_A=x_B=1/3$, in the expression (14) this leads to the estimate $R_1=1/\sqrt{3}$ for R . The comparison with Fig. 9 shows that Eq. (41) together with $R=R_1$ is a lower bound of P_{ext} . A simple attempt to interpolate between the above estimates is to consider the mean value of these radii, $R_2 \equiv \frac{1}{2}(R_0+R_1)$, which happens to yield an excellent agreement with results from stochastic simulations, see Fig. 9. For the latter, we have considered systems of $N=100, 200$, and 500 individuals. Rescaling the time according to t/N , they are seen to collapse on a universal curve. This is well described by Eq. (41) with R_2 as the radius of the absorbing boundary.

To conclude, we consider the mean time t_{abs} that it takes until one species becomes extinct. From Ref. [31] we find for the rescaled mean absorption time

$$u_{\text{abs}} = t_{\text{abs}}/N = 3R^2,$$

which for our best estimate $R=R_2$ yields a value of $u_{\text{abs}} \approx 0.62$.

IV. CONCLUSION

Motivated by recent *in vitro* and *in vivo* experiments aimed at identifying mechanisms responsible for biodiversity in populations of *Escherichia coli* [10,11], we have considered the stochastic version of the ‘‘rock-paper-scissors,’’ or three-species cyclic Lotka-Volterra, system within an urn model formulation. This approach allowed us to quantitatively study the effect of finite-size fluctuations in a system with a large, yet *finite*, number N of agents.

While the classical rate equations of the cyclic Lotka-Volterra model predict the existence of one (neutrally stable)

center fixed point, associated with the coexistence of all the species, this picture is dramatically invalidated by the fluctuations which unavoidably appear in a finite system. The latter were taken into account by a Fokker-Planck equation derived from the underlying master equation through a van Kampen expansion.

Within this scheme, we were able to show that the variances of the densities of individuals grow in time (first linearly) until extinction of two of the species occurs. In this context, we have investigated the probability for such extinction to occur at a given time t . As a main result of this work, we have shown that this extinction probability is a function of the scaling variable t/N . Exploiting polar symmetries displayed by the deterministic trajectories in the phase portrait and using a mapping onto a classical first-passage problem, we were able to provide analytic estimates (upper and lower bounds) of the extinction probability, which have been successfully compared to numerical computation.

From our results, it turns out that the classical rate equation predictions apply to the urn model with a finite number of agents only for short enough time, i.e., in the regime $t \ll N$. As time increases, the probability of extinction grows, asymptotically reaching 1 for $t \gg N$, so that, for finite N , fluctuations are *always* responsible for extinction and thus dramatically jeopardize the possibility of coexistence and biodiversity. Interestingly, these findings are in qualitative agreement with those (both experimental and numerical) reported in Ref. [10], where it was found that in a well-mixed environment (as in the urn model considered here) two species get extinct.

While this work has specifically focused on the stochastic cyclic Lotka-Volterra model, the addressed issues are generic. Indeed, we think that our results and technical approach, here illustrated by considering the case of a paradigmatic model, might actually shed further light on the role of fluctuations and the validity of the rate equations in a whole class of stochastic systems. In fact, while one might believe that fluctuations in an urn model should always vanish in the thermodynamic limit, we have shown that this issue should be dealt with due care: This is true for systems where the rate equations predict the existence of an asymptotically stable fixed point, which is always reached by the stochastic dynamics [28,33]. In contrast, in systems where the deterministic (rate equation) description predicts the existence of (neutrally stable) center fixed points, such as the cyclic Lotka-Volterra model, fluctuations have dramatic consequences and hinder biodiversity by being responsible (at long, yet finite, time) for extinction of species [10]. In this case, instead of a deterministic oscillatory behavior around the linearly (neutrally) stable fixed point, the stochastic dynamics always drives the system toward one of its absorbing states. Thus, the absorbing fixed points, predicted to be linearly unstable within the rate equation theory, actually turn out to be the *only stable fixed points* available at long time.

ACKNOWLEDGMENTS

We would like to thank U. C. Täuber and P. L. Krapivsky for helpful discussions, as well as A. Traulsen and J. C.

Claussen for having made Ref. [9] available to us prior to publication. M.M. gratefully acknowledges the support of the German Alexander von Humboldt Foundation through Grant No. IV-SCZ/1119205 STP.

APPENDIX: UNEQUAL REACTION RATES RECONSIDERED

In Sec. III, when considering the stochastic approach to the cyclic Lotka-Volterra model, for the sake of clarity we have specifically turned to the situation of equal reaction rates $k_A=k_B=k_C=1$. In this appendix, we want to provide some details on the general case with unequal rates. While the mathematical treatment becomes more involved, we will argue that the qualitative general situation still follows along the same lines as the (simpler) case that we have discussed in detail in Sec. III.

The derivation of the Fokker-Planck equation (23) is straightforward, following the lines of Sec. III B. The matrix \mathcal{A} remains unchanged and is given in Eq. (7), for \mathcal{B} we now obtain:

$$\mathcal{B} = \frac{1}{N k_A + k_B + k_C} \begin{pmatrix} \omega_0^2 & 2 & -1 \\ -1 & 2 & \omega_0^2 \end{pmatrix}.$$

The corresponding Fokker-Planck equation reads

$$\partial_t P(\mathbf{x}, t) = -\partial_i [\mathcal{A}_{ij} x_j P(\mathbf{x}, t)] + \frac{1}{2} \mathcal{B}_{ij} \partial_i \partial_j P(\mathbf{x}, t).$$

Again, we aim at benefiting from the cyclic structure of the deterministic solutions, and perform a variable transformation to $\mathbf{y} = \mathcal{S} \mathbf{x}$, with \mathcal{S} given in Eq. (9). As already found in Sec. II B, \mathcal{A} turns into $\tilde{\mathcal{A}} = \begin{pmatrix} 0 & \omega_0 \\ -\omega_0 & 0 \end{pmatrix}$, such that in the \mathbf{y} variables the deterministic solutions correspond to circles around the origin. For the stochastic part, entering via \mathcal{B} , a technical difficulty arises. It is transformed into

$$\tilde{\mathcal{B}} = \frac{3}{2} \frac{1}{N k_A + k_B + k_C} \begin{pmatrix} \frac{k_A^2 + k_A k_C + k_C^2}{k_A^2 k_C^2} \omega_0^2 & \frac{k_A - k_C}{2 k_A k_C} \omega_0 \\ \frac{k_A - k_C}{2 k_A k_C} \omega_0 & 1 \end{pmatrix},$$

being no longer proportional to the unit matrix as in the case of equal reaction rates. We can do slightly better by using an additional rotation $\mathbf{z} = \begin{pmatrix} \cos \theta & \sin \theta \\ -\sin \theta & \cos \theta \end{pmatrix} \mathbf{y}$, with rotation angle

$$\tan(2\theta) = \frac{3(k_C - k_A) \sqrt{k_A k_B k_C (k_A + k_B + k_C)}}{k_A^2 (k_C - k_B) + k_C^2 (k_A - k_B)}.$$

This variable transformation leaves $\tilde{\mathcal{A}}$ invariant, but brings $\tilde{\mathcal{B}}$ to diagonal form, with unequal diagonal elements. The stochastic effects thus correspond to anisotropic diffusion. However, for large system size N , the effects of the anisotropy are washed out: The system's motion on the deterministic cycles, described by \mathcal{A} , occurs on a much faster time scale than the anisotropic diffusion, resulting in an averaging over the different directions.

To calculate the time evolution of the average deviation from the reactive fixed point $\partial_t \langle \mathcal{R}^2(t) \rangle$, we start from the fluctuations in \mathbf{y} , which fulfill the equations

$$\partial_t \langle y_i y_j \rangle = \tilde{A}_{ik} \langle y_k y_j \rangle + \tilde{A}_{jk} \langle y_k y_i \rangle + \tilde{B}_{ij}.$$

Using Eq. (15), we obtain

$$\partial_t \langle \mathcal{R}^2(t) \rangle = \tilde{B}_{AA} + \tilde{B}_{BB}.$$

The dependence on the deterministic part has dropped out, and the solution to the above equation with initial condition $\langle \mathcal{R}^2(t=0) \rangle = 0$ is a linear increase in the rescaled time $u \equiv t/N$:

$$\langle \mathcal{R}^2(t) \rangle = \frac{3}{2} \frac{\omega_0^2}{k_A + k_B + k_C} \left[\frac{k_A^2 + k_A k_C + k_C^2}{k_A^2 k_C} \omega_0^2 + 1 \right] \frac{t}{N},$$

valid around the reactive fixed point. As in the case of equal reaction rates, we have a linear dependence $\langle \mathcal{R}^2(t) \rangle \sim t/N$, corresponding to a two-dimensional random walk.

As a conclusion of the above discussion, the general case of unequal reaction rates qualitatively reproduces the behavior of the before discussed simplest situation of equal rates (confirmed by stochastic simulations). The latter turns out to already provide a comprehensive understanding of the system.

-
- [1] R. M. May, *Stability and Complexity in Model Ecosystems* (Cambridge University Press, Cambridge, 1974).
- [2] H. Haken, *Synergetics*, 3rd ed. (Springer-Verlag, Berlin, 2002).
- [3] D. Neal, *Introduction to Population Biology* (Cambridge University Press, Cambridge, 2004).
- [4] A. J. Lotka, *J. Am. Chem. Soc.* **42**, 1595 (1920).
- [5] V. Volterra, *Atti R. Accad. Naz. Lincei, Mem. Cl. Sci. Fis., Mat. Nat.* **2**, 31 (1926).
- [6] H. H. McAdams and A. Arkin, *Trends Genet.* **15**, 65 (1999).
- [7] E. B. N. V. Shnerb, Y. Louzon, and S. Solomon, *Proc. Natl. Acad. Sci. U.S.A.* **97**, 10322 (2000).
- [8] A. Traulsen, J. C. Claussen, and C. Hauert, *Phys. Rev. Lett.* **95**, 238701 (2005).
- [9] A. Traulsen, J. C. Claussen, and C. Hauert, *Phys. Rev. E* **74**, 011901 (2006).
- [10] B. Kerr, M. A. Riley, M. W. Feldman, and B. J. M. Bohannan, *Nature (London)* **418**, 171 (2002).
- [11] B. C. Kirkup and M. A. Riley, *Nature (London)* **428**, 412 (2004).
- [12] J. Hofbauer and K. Sigmund, *Evolutionary Games and Population Dynamics* (Cambridge University Press, Cambridge, 1998).
- [13] Official “rock-paper-scissors” game, <http://www.worldrps.com>
- [14] L. Frachebourg, P. L. Krapivsky, and E. Ben-Naim, *Phys. Rev. E* **54**, 6186 (1996); *Phys. Rev. Lett.* **77**, 2125 (1996); L. Frachebourg and P. L. Krapivsky, *J. Phys. A* **31**, 287 (1998).
- [15] A. Provata, G. Nicolis, and F. Baras, *J. Chem. Phys.* **110**, 8361 (1999); G. A. Tsekouras and A. Provata, *Phys. Rev. E* **65**, 016204 (2001).
- [16] G. Szabó and T. Czárán, *Phys. Rev. E* **63**, 061904 (2001); G. Szabó and G. A. Sznaider, *ibid.* **69**, 031911 (2004).
- [17] W. Feller, *An Introduction to Probability Theory and Its Application*, 3rd ed. (Wiley, New York, 1968), Vol. 1.
- [18] A. J. McKane and T. J. Newman, *Phys. Rev. E* **70**, 041902 (2004).
- [19] N. van Kampen, *Stochastic Processes in Physics and Chemistry*, 1st ed. (North Holland, Amsterdam, 1981).
- [20] D. W. Jordan and P. Smith, *Nonlinear Ordinary Differential Equations*, 3rd ed. (Oxford University Press, Oxford, 1999).
- [21] S. Clar, B. Drossel, and F. Schwabl, *J. Phys.: Condens. Matter* **8**, 6803 (1996).
- [22] J. D. Murray, *Mathematical Biology* (Springer Verlag, Berlin, 2002).
- [23] P. A. P. Moran, *Proc. Cambridge Philos. Soc.* **54**, 60 (1958).
- [24] E. Liebermann, C. Hauert, and M. A. Nowak, *Nature (London)* **433**, 312 (2005).
- [25] G. W. Rowe, *Theoretical Models in Biology*, 1st ed. (Oxford Science Publications, Oxford, 1994).
- [26] R. Durrett and S. Levin, *Theor. Popul. Biol.* **53**, 30 (1998).
- [27] D. T. Gillespie, *J. Comput. Phys.* **22**, 403 (1976); D. T. Gillespie, *J. Phys. Chem.* **81**, 2340 (1977).
- [28] A. J. McKane and T. J. Newman, *Phys. Rev. Lett.* **94**, 218102 (2005).
- [29] C. W. Gardiner, *Handbook of Stochastic Methods*, 1st ed. (Springer, Berlin, 1983).
- [30] A. M. D. Alonso, *Bull. Math. Biol.* **64**, 913 (2002).
- [31] S. Redner, *A Guide to First-Passage Processes*, 1st ed. (Springer, Berlin, 1983).
- [32] M. Abramowitz and I. A. Stegun, *Handbook of Mathematical Functions*, 9th ed. (Dover, New York, 1972).
- [33] E. Ben-Naim and P. L. Krapivsky, *Phys. Rev. E* **69**, 046113 (2004).

LETTERS

Mobility promotes and jeopardizes biodiversity in rock–paper–scissors games

Tobias Reichenbach¹, Mauro Mobilia¹ & Erwin Frey¹

Biodiversity is essential to the viability of ecological systems. Species diversity in ecosystems is promoted by cyclic, non-hierarchical interactions among competing populations. Central features of such non-transitive relations are represented by the ‘rock–paper–scissors’ game, in which rock crushes scissors, scissors cut paper, and paper wraps rock. In combination with spatial dispersal of static populations, this type of competition results in the stable coexistence of all species and the long-term maintenance of biodiversity^{1–5}. However, population mobility is a central feature of real ecosystems: animals migrate, bacteria run and tumble. Here, we observe a critical influence of mobility on species diversity. When mobility exceeds a certain value, biodiversity is jeopardized and lost. In contrast, below this critical threshold all subpopulations coexist and an entanglement of travelling spiral waves forms in the course of time. We establish that this phenomenon is robust; it does not depend on the details of cyclic competition or spatial environment. These findings have important implications for maintenance and temporal development of ecological systems and are relevant for the formation and propagation of patterns in microbial populations or excitable media.

The remarkable biodiversity present in ecosystems confounds a naive interpretation of darwinian evolution in which interacting species compete for limited resources until only the fitter species survives. As a striking example, consider that a 30 g sample of soil from a Norwegian forest is estimated to contain some 20,000 common bacterial species⁶. Evolutionary game theory^{7–9}, in which the success of one species relies on the behaviour of others, provides a useful framework in which to investigate co-development of populations theoretically. In this context, the rock–paper–scissors game has emerged as a paradigm to describe species diversity^{1–5,10–12}. If three subpopulations interact in this non-hierarchical way, we intuitively expect that diversity may be preserved: Each species dominates another only to be outperformed by the remaining one in an endlessly spinning wheel of species chasing species.

Communities of subpopulations exhibiting such dynamics have been identified in numerous ecosystems, ranging from coral reef invertebrates¹³ to lizards in the inner Coast Range of California¹⁴. In particular, recent experimental studies using microbial laboratory cultures have been devoted to the influence of spatial structure on time development and coexistence of species^{3,15}. Investigating three strains of colicinogenic *Escherichia coli* in different environments, it has been shown that cyclic dominance alone is not sufficient to preserve biodiversity. Only when the interactions between individuals are local (for example, bacteria arranged on a Petri dish) can spatially separated domains dominated by one subpopulation form and lead to stable coexistence^{1,3}.

Here we show that biodiversity is affected drastically by spatial migration of individuals, a ubiquitous feature of real ecosystems.

Migration competes with local interactions such as reproduction and selection, thereby mediating species preservation and biodiversity. For low values of mobility, the temporal development is dominated by interactions among neighbouring individuals, resulting in the long-term maintenance of species diversity. In contrast, when species mobility is high, spatial homogeneity results and biodiversity is lost. Interestingly, a critical value of mobility sharply delineates these two scenarios. We obtain concise predictions for the fate of the ecological system as a function of species mobility, thereby gaining a comprehensive understanding of its biodiversity.

The influence of mobility on species coexistence was previously studied within the framework of coupled habitat patches (“island models”)^{16–19}. In particular, Levin considered an idealized two-patch system and observed a critical mobility for stable coexistence¹⁶. Other models comprising many spatially arranged patches were shown to facilitate pattern formation^{17,18}. Because often in nature spatial degrees of freedom vary continuously (for example, bacteria can visit the entire area of a Petri dish), we relax the simplifying assumption of habitat patches and consider continuous spatial distribution of individuals. Moreover, as an inherent feature of real ecosystems and in contrast to previous deterministic investigations^{16–19}, we explicitly take the stochastic character of the interactions among the populations into account. Such interacting particle systems, where individuals are discrete and space is treated explicitly, have already been considered in ecological contexts^{1,2,4,5,20}. The behaviour of these models often differs from what is inferred from deterministic reaction–diffusion equations, or from interconnected patches²⁰. In the case of cyclic competition, such stochastic spatial systems have been shown to allow for stable coexistence of all species^{1,2,4,5} when individuals are static. Here we explore the novel features emerging from individuals’ mobility.

Consider mobile individuals of three subpopulations (referred to as A, B and C), arranged on a spatial lattice, where they can only interact with nearest neighbours. For the possible interactions, we consider a version of the rock–paper–scissors game, namely a stochastic spatial variant of the model introduced in 1975 by May and Leonard¹⁰ (see Methods). Schematic illustrations of the model’s dynamics are provided in Fig. 1. The basic reactions comprise selection and reproduction processes, which occur at rates σ and μ , respectively. Individuals’ mobility stems from the possibility that two neighbouring individuals will swap their position (at rate ε) and will move to an adjacent empty site: hence, individuals randomly migrate on the lattice. We define the length of the square lattice as the size unit, and denote by N the number of sites. Within this setting, and applying the theory of random walks²¹, the typical area explored by one mobile individual per unit time is proportional to $M = 2\varepsilon N^{-1}$, which we refer to as the mobility. The interplay of the latter with selection and reproduction processes sensitively

¹Arnold Sommerfeld Center for Theoretical Physics (ASC) and Center for NanoScience (CeNS), Department of Physics, Ludwig-Maximilians-Universität München, Theresienstrasse 37, D-80333 München, Germany.

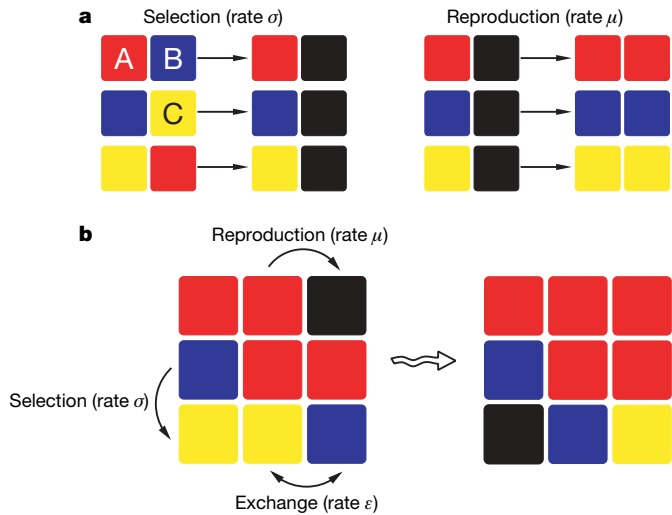


Figure 1 | The rules of the stochastic model. Individuals of three competing species A (red), B (blue), and C (yellow) occupy the sites of a lattice. **a**, They interact with their nearest neighbours through selection or reproduction, both of which reactions occur as Poisson processes at rates σ and μ , respectively. Selection reflects cyclic dominance: A can kill B, yielding an empty site (black). In the same way, B invades C, and C in turn outcompetes A. Reproduction of individuals is only allowed on empty neighbouring sites, to mimic a finite carrying capacity of the system. We also endow individuals with mobility: at exchange rate ε , they are able to swap position with a neighbouring individual or hop onto an empty neighbouring site (exchange). **b**, An example of the three processes, taking place on a 3×3 square lattice.

determines whether species can coexist on the lattice or not, as discussed below.

We performed extensive computer simulations of the stochastic system (see Methods) and typical snapshots of the steady states are reported in Fig. 2. When the mobility of the individuals is low, we find that all species coexist and self-arrange by forming patterns of moving spirals. With increasing mobility M , these structures grow in size, and disappear for large enough M . In the absence of spirals, the system adopts a uniform state where only one species is present, while the others have died out. Which species remains is subject to a random process, all species having equal chances to survive in our model.

We obtain concise predictions on the stability of three-species coexistence by adapting the concept of extensivity from statistical physics (see Supplementary Notes). We consider the typical waiting time T until extinction occurs, and its dependence on the system size N . If $T(N) \propto N$, the stability of coexistence is marginal¹². Conversely, longer (shorter) waiting times scaling with higher (lower) powers of N indicate stable (unstable) coexistence. These three scenarios can be distinguished by computing the probability P_{ext} that two species have gone extinct after a waiting time $t \propto N$. In Fig. 2, we report the dependence of P_{ext} on the mobility M . For illustration, we have considered equal reaction rates for selection and reproduction, and, without loss of generality, set the time-unit by fixing $\sigma = \mu = 1$. With increasing system size N , a sharpened transition emerges at a critical value $M_c = (4.5 \pm 0.5) \times 10^{-4}$ for the fraction of the entire lattice area explored by an individual in one time-unit. Below M_c , the extinction probability P_{ext} tends to zero as the system size increases, and coexistence is stable (implying super-persistent

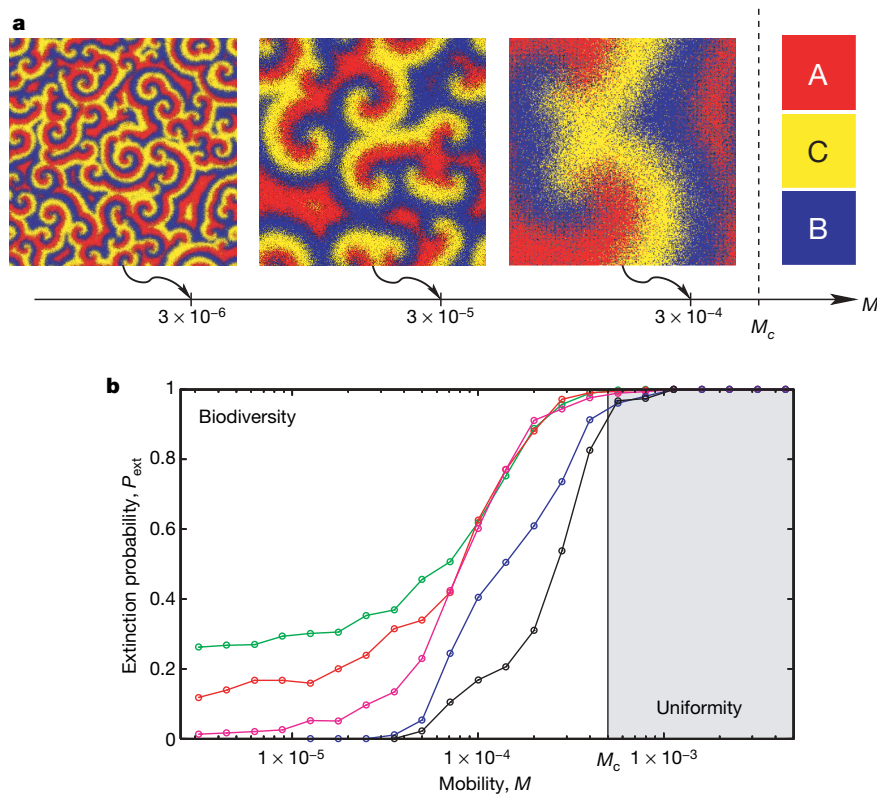


Figure 2 | The critical mobility M_c . Mobility below the value M_c induces biodiversity; while it is lost above that threshold. **a**, We show snapshots obtained from lattice simulations of typical states of the system after long temporal development (that is, at time $t \propto N$) and for different values of M (each colour represents one of the three species and black dots indicate empty spots). With increasing M (from left to right), the spiral structures grow, and outgrow the system size at the critical mobility M_c . Then coexistence of all three species is lost and uniform populations remain

(right). **b**, Quantitatively, we have considered the extinction probability P_{ext} that, starting with randomly distributed individuals on a square lattice, the system has reached an absorbing state after a waiting time $t = N$. We compute P_{ext} as a function of the mobility M (and $\sigma = \mu = 1$), and show results for different system sizes: $N = 20 \times 20$ (green), $N = 30 \times 30$ (red), $N = 40 \times 40$ (purple), $N = 100 \times 100$ (blue), and $N = 200 \times 200$ (black). As the system size increases, the transition from stable coexistence ($P_{\text{ext}} = 0$) to extinction ($P_{\text{ext}} = 1$) sharpens at a critical mobility $M_c = (4.5 \pm 0.5) \times 10^{-4}$.

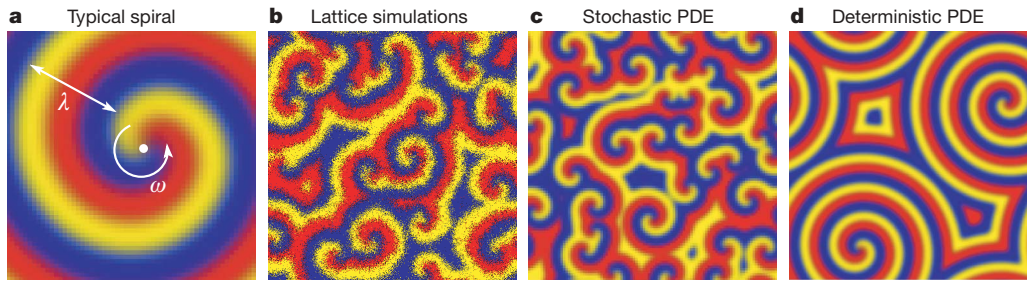


Figure 3 | Spiralling patterns. **a**, Typical spiral (schematic). It rotates around the origin (white dot) at a frequency ω and possesses a wavelength λ . **b**, In our lattice simulations, when the mobility of individuals lies below the critical value, all three species coexist, forming mosaics of entangled, rotating spirals (each colour represents one of the species and black dots indicate empty spots). **c**, We have found that the system's development can aptly be described by stochastic PDE. In the case of lattice simulations and stochastic PDE, internal noise acts as a source of local inhomogeneities and ensures the robustness of the dynamical behaviour: the spatio-temporal

transients²²; see Supplementary Notes). On the other hand, above the critical mobility, the extinction probability approaches 1 for large system size, and coexistence is unstable. One of our central results is that we have identified a mobility threshold for biodiversity:

There exists a critical value M_c such that a low mobility $M < M_c$ guarantees coexistence of all three species, while $M > M_c$ induces extinction of two of them, leaving a uniform state with only one species.

To give a biological illustration of this statement, let us consider colicinogenic strains of *E. coli* growing on a Petri dish³. In this setting, ten bacterial generations have been observed in 24 h, yielding selection and reproduction rates of about ten per day. The typical size of a Petri dish is roughly 10 cm, so we have evaluated the critical mobility to be about $5 \times 10^2 \mu\text{m}^2 \text{s}^{-1}$. Comparing that estimate to the mobility of *E. coli*, we find that it can, by swimming and tumbling in super-soft agar, explore areas of more than $10^3 \mu\text{m}^2 \text{s}^{-1}$ (ref. 23). This value can be considerably lowered by increasing the agar concentration.

When the mobility is low ($M < M_c$), the interacting subpopulations exhibit fascinating patterns, as illustrated by the snapshots of Fig. 2. The emerging reactive states are formed by an entanglement of spiral waves, characterizing the competition among the species which endlessly hunt each other, as illustrated in Supplementary Videos 1 and 2 (see also Supplementary Discussion). Formation of this type of patterns has been observed in microbial populations, such as myxobacteria aggregation²⁴ or multicellular *Dictyostelium* mounds²⁵, as well as in cell signalling and control²⁶. Remarkably, a mathematical description and techniques borrowed from the theory of stochastic processes²⁷ allow us to obtain these complex structures by means of stochastic partial differential equations (PDE), see Fig. 3 and Methods. Furthermore, recasting the dynamics in the form of a complex Ginzburg–Landau equation^{28,29} allows us to obtain analytical expressions for the spirals' wavelength λ and frequency (see Supplementary Notes). These results, up to a constant prefactor, agree with those of numerical computations, and will be published elsewhere (manuscript in preparation).

As shown in Fig. 2, the spirals' wavelength λ rises with the individuals' mobility. Our analysis reveals that the wavelength is proportional to \sqrt{M} (see Supplementary Notes). This relation holds up to the mobility M_c , where a critical wavelength λ_c is reached. For mobilities above the threshold M_c , the spirals' wavelength λ exceeds the critical value λ_c and the patterns outgrow the system size, causing the loss of biodiversity (see Fig. 2). We have found λ_c to be universal, that is, independent on the selection and reproduction rates. This is not the case for M_c , whose value varies with these parameters (see Supplementary Notes). Using lattice simulations, stochastic PDE and the properties of the complex Ginzburg–Landau equation, we have derived the dependence of the critical mobility $M_c(\mu)$ on the

patterns are independent of the initial conditions. **d**, Ignoring the effects of noise, we are left with deterministic PDE that also give rise to spiralling structures. The latter share the same wavelength and frequency with those of the stochastic description but, in the absence of fluctuations, their overall size and number depend on the initial conditions and can deviate significantly from their stochastic counterparts. In **b** and **c**, the system is initially in a homogeneous state, while **d** has been generated by considering an initial local perturbation. Parameters are $\sigma = \mu = 1$ and $M = 1 \times 10^{-5}$.

reproduction rate μ (where the time-unit is set by keeping $\sigma = 1$). This enables us to analytically predict, for all values of parameters, whether biodiversity is maintained or lost. We have summarized these results in a phase diagram, reported in Fig. 4. We identify a uniform phase, in which two species go extinct (when $M > M_c(\mu)$), and a biodiverse phase (when $M < M_c(\mu)$) with coexistence of all species and propagation of spiral waves.

The generic ingredients required for the above scenario to hold are the mobility of the individuals and a cyclic dynamics exhibiting an unstable reactive fixed point. The underlying mathematical description of this class of dynamical systems is derived in terms of complex Ginzburg–Landau equations. Their universality classes reveal the robustness of the phenomena which we have reported above, that is, the existence of a critical mobility and the emergence of spiral waves; they are not restricted to specific details of the model.

Our study has direct implications for experimental research on biodiversity and pattern formation. As an example, one can envisage

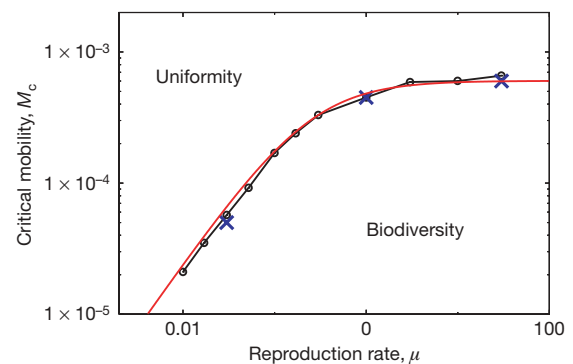


Figure 4 | Phase diagram. The critical mobility M_c as a function of the reproduction rate μ yields a phase diagram with a phase where biodiversity is maintained as well as a uniform one where two species go extinct. The time unit is set by $\sigma = 1$. On the one hand, we have computed M_c from lattice simulations, using different system sizes. The results are shown as blue crosses. On the other hand, we have calculated M_c using the approach of stochastic PDE (black dots, black lines are a guide to the eye) as well as analytically via the complex Ginzburg–Landau equation (red line). When we vary the reproduction rate, two different regimes emerge. If μ is much smaller than the selection rate, that is, $\mu \ll \sigma$, reproduction is the dominant limiter of the temporal development. In this case, there is a linear relation with the critical mobility, that is $M_c \propto \mu$, as follows from dimensional analysis. In the opposite case, if reproduction occurs much faster than selection ($\mu \gg \sigma$), the latter limits the dynamics and M_c depends linearly on σ , so that $M_c \propto \sigma$. Here, as $\sigma = 1$ is kept fixed (time-scale unit), this behaviour is reflected in the fact that M_c approaches a constant value for $\mu \gg \sigma$.

an experiment extending the study³ on colicinogenic *E. coli*. Allowing the bacteria to migrate in soft agar on a Petri dish should, for low mobilities, result in stable coexistence promoted by the formation of spiral patterns. Increasing the mobility (for example, on super-soft agar), the patterns should grow in size and finally outgrow the system at some critical value, corresponding to the threshold M_c discussed above. For even higher values of the mobility, biodiversity should be lost after a short transient time and only one species should cover the entire Petri dish. We think that the regimes of both mobilities, corresponding to the biodiverse and uniform phases, should be experimentally accessible.

We have shown how concepts from game theory combined with methods used to study pattern formation reveal the subtle influence of mobility on the temporal development of coexisting species. Many more questions and applications regarding the seminal interplay between these different fields lie ahead. As an example, it has been shown that cyclic dominance can occur in social dilemmas^{9,30}, which suggests implications of our results for the behavioural sciences.

METHODS SUMMARY

To model cyclic dominance, we use a stochastic lattice version (following work by Durrett and Levin)² of a model proposed by May and Leonard¹⁰ in 1975. As main characteristics, in the absence of spatial structure, their equations possess a deterministically unstable fixed point associated to coexistence of all three species: in the course of time, the system spirals (in the phase space) away from coexistence and moves in turn from a state with nearly only As to another one with nearly only Bs, and then to a state with nearly only Cs.

In our stochastic lattice simulations, we have arranged the three subpopulations on a two-dimensional square lattice with periodic boundary conditions. Every lattice site is occupied by an individual of species A, species B or species C, or left empty. At each simulation step, a random individual is chosen to interact with one of its four nearest neighbours: which one is also randomly determined. Whether selection, reproduction or mobility occurs, as well as the corresponding waiting time, is computed according to the reaction rates using an efficient algorithm due to Gillespie³¹. We set one generation (when every individual has reacted on average once) as the unit of time. To compute the extinction probability, we have used different system sizes, from 20×20 to 200×200 lattice sites, and sampled between 500 and 2,000 realizations. The snapshots shown in Fig. 2 result from system sizes of up to $1,000 \times 1,000$ sites.

Our stochastic PDE consist of a mobility term, nonlinear terms describing the deterministic temporal development of the nonspatial model (May–Leonard equations), and (multiplicative) white noise; see Supplementary Notes.

We have solved the resulting equations with the help of open software from the XMDS project (<http://www.xmds.org>), using the semi-implicit method in the interaction picture (SIIP) as an algorithm, spatial meshes of 200×200 to 500×500 points, and 10,000 points in the time direction.

Received 3 May; accepted 18 July 2007.

1. Durrett, R. & Levin, S. Allelopathy in spatially distributed populations. *J. Theor. Biol.* **185**, 165–171 (1997).
2. Durrett, R. & Levin, S. Spatial aspects of interspecific competition. *Theor. Pop. Biol.* **53**, 30–43 (1998).
3. Kerr, B., Riley, M. A., Feldman, M. W. & Bohannan, B. J. M. Local dispersal promotes biodiversity in a real-life game of rock-paper-scissors. *Nature* **418**, 171–174 (2002).
4. Czárán, T. L., Hoekstra, R. F. & Pagie, L. Chemical warfare between microbes promotes biodiversity. *Proc. Natl Acad. Sci. USA* **99**, 786–790 (2002).
5. Szabó, G. & Fáth, G. Evolutionary games on graphs. *Phys. Rep.* **446**, 97–216 (2007).

6. Dykhuizen, D. E. *Santa rosalia* revisited: Why are there so many species of bacteria? *Antonie Van Leeuwenhoek* **73**, 25–33 (1998).
7. Smith, J. M. *Evolution and the Theory of Games* (Cambridge Univ. Press, Cambridge, 1982).
8. Hofbauer, J. & Sigmund, K. *Evolutionary Games and Population Dynamics* (Cambridge Univ. Press, Cambridge, 1998).
9. Nowak, M. A. *Evolutionary Dynamics* (Belknap Press, Cambridge, Massachusetts, 2006).
10. May, R. M. & Leonard, W. J. Nonlinear aspects of competition between species. *SIAM J. Appl. Math.* **29**, 243–253 (1975).
11. Johnson, C. R. & Seinen, I. Selection for restraint in competitive ability in spatial competition systems. *Proc. R. Soc. Lond. B* **269**, 655–663 (2002).
12. Reichenbach, T., Mobilia, M. & Frey, E. Coexistence versus extinction in the stochastic cyclic Lotka–Volterra model. *Phys. Rev. E* **74**, 051907 (2006).
13. Jäckup, J. B. C. & Buss, L. Allelopathy and spatial competition among coral reef invertebrates. *Proc. Natl Acad. Sci. USA* **72**, 5160–5163 (1975).
14. Sinervo, B. & Lively, C. M. The rock–scissors–paper game and the evolution of alternative male strategies. *Nature* **380**, 240–243 (1996).
15. Kirkup, B. C. & Riley, M. A. Antibiotic-mediated antagonism leads to a bacterial game of rock–paper–scissors *in vivo*. *Nature* **428**, 412–414 (2004).
16. Levin, S. A. Dispersion and population interactions. *Am. Nat.* **108**, 207–228 (1974).
17. Hassell, P. M., Comins, H. N. & May, R. M. Spatial structure and chaos in insect population dynamics. *Nature* **353**, 255–258 (1991).
18. Blasius, B., Huppert, A. & Stone, L. Complex dynamics and phase synchronization in spatially extended ecological systems. *Nature* **399**, 354–359 (1999).
19. King, A. A. & Hastings, A. Spatial mechanism for coexistence of species sharing a common natural enemy. *Theor. Pop. Biol.* **64**, 431–438 (2003).
20. Durrett, R. & Levin, S. The importance of being discrete (and spatial). *Theor. Pop. Biol.* **46**, 363–394 (1994).
21. Redner, S. *A Guide to First-Passage Processes* (Cambridge Univ. Press, Cambridge, 2001).
22. Hastings, A. Transients: the key to long-term ecological understanding? *Trends Ecol. Evol.* **19**, 39–45 (2004).
23. Berg, H. *C. coli in Motion* (Springer, New York, 2003).
24. Igoshin, O. A., Welch, R., Kaiser, D. & Oster, G. Waves and aggregation patterns in myxobacteria. *Proc. Natl Acad. Sci. USA* **101**, 4256–4261 (2004).
25. Siegert, F. & Weijer, C. J. Spiral and concentric waves organize multicellular *Dictyostelium* mounds. *Curr. Biol.* **5**, 937–943 (1995).
26. Thul, R. & Falcke, M. Stability of membrane bound reactions. *Phys. Rev. Lett.* **93**, 188103 (2004).
27. Gardiner, C. W. *Handbook of Stochastic Methods* (Springer, Berlin, 1983).
28. Wiggins, S. *Introduction to Applied Nonlinear Dynamical Systems and Chaos* Ch. 2 and 3 (Springer, New York, 1990).
29. Aranson, I. S. & Kramer, L. The world of the complex Ginzburg–Landau equation. *Rev. Mod. Phys.* **74**, 99–143 (2002).
30. Hauert, C., de Monte, S., Hofbauer, J. & Sigmund, K. Volunteering as red queen mechanism for cooperation in public goods games. *Science* **296**, 1129–1132 (2002).
31. Gillespie, D. T. A general method for numerically simulating the stochastic time evolution of coupled chemical reactions. *J. Comput. Phys.* **22**, 403–434 (1976).

Supplementary Information is linked to the online version of the paper at www.nature.com/nature.

Acknowledgements We thank M. Bathe and M. Leisner for discussions on the manuscript. Financial support of the German Excellence Initiative via the program “Nanosystems Initiative Munich (NIM)” as well as the SFB “Manipulation of Matter at the Nanometer Length Scale” is gratefully acknowledged. M.M. is grateful to the Alexander von Humboldt Foundation for support through a fellowship.

Author Information Reprints and permissions information is available at www.nature.com/reprints. The authors declare no competing financial interests. Correspondence and requests for materials should be addressed to E.F. (frey@lmu.de).

Supplementary Notes

In this Supplementary Notes, we further elaborate our analysis by explaining some technical aspects of the Letter

Below, we first present the concept of extensivity, which allows to precisely discriminate between the regime where biodiversity is stable (i.e. maintained) and the situation where it is unstable and the system settles in one of the uniform (absorbing) states. Then, we present details on the stochastic differential equations as well as the complex Ginzburg-Landau equation used to analyse the system.

We also show how the spirals' wavelength λ is related to the mobility M . We explain that such a relation has allowed to derive the functional dependence $M_c(\mu)$ of the critical mobility on the reproduction rate. Finally, the main findings reported in the Letter are revisited in a supplementary discussion centered on the information conveyed by the movies.

Extensivity

Even if coexistence appears stable, as observed for low mobilities, there is a certain probability that two species go extinct due to possible large yet rare fluctuations. Indeed, the only absorbing states where no reactions (and therefore no fluctuations) occur, are the uniform configurations where only one species survives. For this reason, these are the only stable states in the long run. However, the typical waiting time $T(N)$ until extinction occurs is generally very long when the system size N is large. This suggests to consider the dependence of the waiting time $T(N)$ on N . Quantitatively, we discriminate between stable and unstable coexistence by using the concept of *extensivity*, adapted from statistical physics. If the ratio T/N tends to infinity ($T/N \rightarrow \infty$) in the asymptotic limit of large systems ($N \rightarrow \infty$), the typical waiting time strongly prolongs with N (typically with an exponential dependence). This scenario is called *super-extensive* or stable. On the other hand, if $T/N \rightarrow O(1)$ (i.e. the ratio approaches a finite non-zero value) that is referred to as the *extensive* case, which has been shown to correspond to marginal (or neutral) stability¹². Instability of the coexistence state (towards a uniform one) is encountered when $T/N \rightarrow 0$ (*sub-extensive* scenario), where the waiting time is short as compared to the system size. These definitions of stability and instability (with neutral stability separating the two

cases) in the presence of absorbing states are intimately related to the concept of transients. In fact, Hastings²² suggested to study not only the ultimate fate of a system, but also to consider the behaviour at smaller (and probably ecologically more relevant) time scales. According to the definition introduced above, stable or neutrally stable coexistence implies coevolution of the populations for a very large number of generations. This corresponds to the existence of extremely long-lived persistent transients²² (super-persistent). It is also worth noticing that transients lasting for several generations can occur even in the case of unstable coexistence. This typically happens when the number of individuals N is large. In the situation of Fig. 2, we have considered the extinction probability P_{ext} that, starting from random initial conditions (i.e. spatially homogeneous configurations, with equal concentrations of each species), the system has reached a uniform state after a time t proportional to the system size, i.e. $t \sim N$. In the asymptotic limit $N \rightarrow \infty$, three distinct cases arise. In a first regime, the extinction probability tends to zero with the system size N . In Fig. 2, this occurs when $M < M_c$. This scenario corresponds to the superextensive situation (i.e. $T/N \rightarrow \infty$, with $N \rightarrow \infty$) where the coexistence of all populations is stable. As a second case, the extinction probability approaches a finite value between 0 and 1, i.e. $T/N \rightarrow O(1)$, and we recover neutral stability. In Fig. 2, such a behaviour arises exclusively at the vicinity of the critical mobility M_c . In a third regime, the extinction probability does reach the value 1, which means that $T/N \rightarrow 0$. This is the subextensive scenario where the coexistence is unstable and biodiversity is lost. In Fig. 2, this happens above the critical mobility, i.e. when $M > M_c$.

Stochastic partial differential equations

Within the theory of stochastic processes²⁷, the dynamics of the stochastic lattice system is described by a master equation. In the limit of large systems, using a Kramers-Moyal expansion, the latter allows for the derivation of a proper Fokker-Planck equation, which in turn is equivalent to a set of stochastic partial differential equations. The latter consist of a mobility term, nonlinear terms describing the deterministic dynamics of the nonspatial model (May-Leonard equations), and noise terms. For the noise terms, we have found that contributions stemming from selection and reproduction events scale as $N^{-1/2}$, while fluctuations originating from exchanges (mobility) decay as N^{-1} ; the latter may therefore

be ignored. What remains, is (multiplicative) white noise whose strength scales as $N^{-1/2}$.

Complex Ginzburg-Landau Equation (CGLE)

Ignoring the noise terms in the stochastic differential equations describing the system, the resulting partial differential equations fall into the class of the Poincaré-Andronov-Hopf bifurcation, known from the mathematics literature²⁸. Applying the theory of center manifolds and normal forms developed there, we have been able to cast the deterministic equations into the form of the complex Ginzburg-Landau equation:

$$\partial_t z = M \partial_r^2 z + c_1 z - (1 - ic_3) |z|^2 z, \quad (1)$$

where z is a complex variable and c_1, c_3 are constants depending on the rates σ and μ . This equation leads to the formation of dynamic spirals and allows to derive analytic results for their wavelength and frequency, see e.g. the review by Aranson and Kramer²⁹.

Scaling relation and critical mobility

An important question is to understand what is the mechanism driving the transition from a stable coexistence to extinction at the critical mobility M_c . To address this issue, we first note that varying the mobility induces a scaling effect, as illustrated in Fig. 2. In fact, increasing the mobility rate M results in zooming into the system. As discussed above (see the main text and Methods), the system's dynamics is described by a set of suitable stochastic partial differential equations (SPDE) (T.R., M.M., and E.F., in preparation) whose basic properties help rationalize this scaling relation. In fact, the mobility enters the stochastic equations through a diffusive term $M\Delta$, where Δ is the Laplace operator involving second-order spatial derivatives. Such a term is left invariant when M is multiplied by a factor α while the spatial coordinates are rescaled by $\sqrt{\alpha}$. It follows from this reasoning that varying M into αM translates in a magnification of the system's characteristic size by a factor $\sqrt{\alpha}$ (say $\alpha > 1$). This implies that the spirals' wavelength λ is proportional to \sqrt{M} (i.e. $\lambda \sim \sqrt{M}$) up to the critical M_c .

When the spirals have a critical wavelength λ_c , associated with the mobility M_c , these rotating patterns outgrow the system size which results in the loss of biodiversity (see the

main text). In the “natural units” (length is measured in lattice size units and the time-scale is set by keeping $\sigma = 1$), we have numerically computed $\lambda_c = 0.8 \pm 0.05$. This quantity has been found to be universal, i.e. its value remains constant upon varying the rates σ and μ . However, this is not the case of the critical mobility M_c , which depends on the parameters of the system. Below the critical threshold M_c , the dynamics is characterized by the formation of spirals of wavelength $\lambda(\mu, M) \sim \sqrt{M}$. This relation, together with the universal character of λ_c , leads to the following equation:

$$M_c(\mu) = \left(\frac{\lambda_c}{\lambda(\mu, M)} \right)^2 M, \quad (2)$$

which gives the functional dependence of the critical mobility upon the system’s parameter. To obtain the phase diagram reported in Fig. 4 we have used Eq. (2) together with values of $\lambda(\mu, M)$ obtained from numerical simulations. For computational convenience, we have measured $\lambda(\mu, M)$ by carrying out a careful analysis of the SPDE’s solutions. The results are reported as black dots in Fig. 4. We have also confirmed these results through lattice simulations for systems with different sizes and the results are shown as blue dots in Fig. 2. Finally, we have taken advantage of the analytical expression (up to a constant prefactor, taken into account in Fig. 2) of $\lambda(\mu, M)$ derived from the complex Ginzburg-Landau equation (CGLE) associated with the system’s dynamics (see Methods): with Eq. (2), we have obtained the red curve displayed in Fig. 2. This figure corroborates the validity of the various approaches (SPDE, lattice simulations and CGLE), which all lead to the same phase diagram where the biodiverse and the uniform phases are identified.

Supplementary Video Legend 1

In the first movie, the dynamics of individuals of species A , B and C follows the reactions illustrated in Fig. 1 with rates $\mu = 1$ (reproduction), $\sigma = 1$ (selection) and $\epsilon = 2.4$ (exchange rate). In Movie 1, individuals of each species are indicated in different colours (empty sites are shown as black dots). The dynamics takes place on a square lattice of $N = 400 \times 400$ sites, such that there are up to 1.6×10^5 individuals in the system. This set of parameters corresponds to a mobility rate $M = 2\epsilon/N = 3 \times 10^{-5}$ well below the critical threshold $M_c \approx 4.5 \pm 0.5 \times 10^{-4}$ (see Figs. 2, 4 and text). Initially the system is in a well-mixed configuration with equal density of individuals of each species and empty sites. As time increases and since $M < M_c$, biodiversity is maintained and complex dynamical patterns

form in the course of the temporal development resulting in a rich entanglement of spiral waves.

Supplementary Video Legend 2

In the second movie, the mobility of the individuals has been increased. In fact, the dynamics of individuals of all species still follows the reactions illustrated in Fig. 1 with rates $\mu = 1$ (reproduction) and $\sigma = 1$ (selection), but the exchange rate is now $\epsilon = 6$. In Movie 2, individuals of each species are still indicated in different colours (empty sites are shown as black dots). The dynamics takes place on a square lattice of $N = 200 \times 200$ sites, allowing up to 4×10^4 individuals in the system. This set of parameters corresponds to a mobility rate $M = 3 \times 10^{-4}$ relatively close to the critical threshold $M_c \approx 4.5 \pm 0.5 \times 10^{-4}$ (see Figs. 2, 4 and text). Initially the system is in a well-mixed state with equal density of individuals of each species and empty sites. As time increases and since $M < M_c$, biodiversity is still maintained and patterns form in the course of the time development. However, as compared to the first movie, one notices that the size of the patterns has increased and one now only distinguishes one pair of antirotating spirals.

Supplementary Discussion

The supplementary movies illustrate the system's time development in the coexistence phase, i.e. the emergence of dynamical complex patterns deep in that phase (Movie 1) and close to (yet below) the threshold M_c (Movie 2, see text and Fig. 3).

Starting from initially homogeneous (well-mixed) configurations, after a short transient regime, spiral waves rapidly emerge and characterize the long-time behaviour of the system which settles in a reactive steady state (*super-extensive case*, see text). The wavefronts, merging to form entanglement of spirals, propagate with spreading speed v^* and wavelength λ . In Movies 1 and 2, it appears clearly that by rising the individuals' mobility, one increases the wavefronts propagation velocity and the wavelength of the resulting dynamical patterns, as well as the size of each spiral. From PDE associated with the system's dynamics, we can rationalize this discussion and estimate these quantities for the cases illustrated in Movies 1 and 2. Namely, for the spreading speed, we have obtained $v^* \approx 3.5 \times 10^{-3}$ (lattice-size

units per time-step, Movie 1) and $v^* \approx 1.1 \times 10^{-2}$ (Movie 2). Similarly, the wavelength were found to be $\lambda \approx 0.21$ (lattice-size units, Movie 1) and $\lambda \approx 0.65$ (Movie 2). Here, rising the rate M from 3×10^{-5} (Movie 1) to 3×10^{-4} (Movie 2) results in the enhancement of v^* and λ by a factor $\sqrt{10} \approx 3.16$. In Movie 2, the size of the spirals can also be estimated to have been magnified by the same factor $\sqrt{10} \approx 3.16$ with respect to those of Movie 1. As explained in the text, this scaling property of the system can be understood by considering the stochastic partial differential equation describing the dynamics, which were obtained from the underlying master equation through a system size expansion (see Methods).

By rising the individuals' mobility, one therefore increases the size of the spiralling patterns (whose wavelength is proportional to \sqrt{M}) and for sufficiently large value of the exchange rate (i.e. of M), as in Movie 2, just a few spirals nearly cover the entire lattice. This happens up to the critical value $\lambda_c \approx 0.8$, found to be universal. In fact, when $\lambda \geq \lambda_c$ the whole system is covered with one single ("giant") spiral which cannot fit within the lattice. This effectively results in the extinction of two species and the loss of biodiversity. As explained in the text, by exploiting the fact that $\lambda \propto \sqrt{M}$ and the universal character of λ_c , one can infer the existence of the critical mobility rate $M_c = M_c(\mu)$ [see Eq. (2)], as illustrated in Fig. 4. This allows to discuss the fate of the system (i.e. biodiversity versus extinction) in terms of the reaction and mobility rates μ and M , respectively: For given reaction rates μ and ϵ (without loss of generality σ is set to unity, see text) and system size L , we obtain a critical value $M_c(\mu)$ of the mobility rate. In fact, a reactive steady state is reached (and biodiversity maintained) only if $M < M_c(\mu)$. When the individuals' mobility is too fast, i.e. when $M > M_c(\mu)$, the system can be considered to be *well-mixed* and its dynamics therefore can be aptly described in terms of homogeneous rate equations which predicts the extinction of two species (see Methods).

In the cases illustrated in Movies 1 and 2, $M_c \approx 4.5 \pm 0.5 \times 10^{-4}$ and the wavefronts propagate with $\lambda < \lambda_c$, so that biodiversity is always preserved. However, we notice that the resulting spatio-temporal patterns are quite different: while one finds a rich entanglement of spirals deep in the coexistence phase (i.e. for $M \approx 3 \times 10^{-5} \ll M_c$, Movie 1), only one pair of antirotating spirals fill the system when one approaches the critical value M_c (Movie 2).

Noise and Correlations in a Spatial Population Model with Cyclic Competition

Tobias Reichenbach, Mauro Mobilia,* and Erwin Frey

Arnold Sommerfeld Center for Theoretical Physics (ASC) and Center for NanoScience (CeNS), Department of Physics,
Ludwig-Maximilians-Universität München, Theresienstrasse 37, D-80333 München, Germany

(Received 19 July 2007; published 7 December 2007)

Noise and spatial degrees of freedom characterize most ecosystems. Some aspects of their influence on the coevolution of populations with cyclic interspecies competition have been demonstrated in recent experiments [e.g., B. Kerr *et al.*, *Nature (London)* **418**, 171 (2002)]. To reach a better theoretical understanding of these phenomena, we consider a paradigmatic spatial model where three species exhibit cyclic dominance. Using an individual-based description, as well as stochastic partial differential and deterministic reaction-diffusion equations, we account for stochastic fluctuations and spatial diffusion at different levels and show how fascinating patterns of entangled spirals emerge. We rationalize our analysis by computing the spatiotemporal correlation functions and provide analytical expressions for the front velocity and the wavelength of the propagating spiral waves.

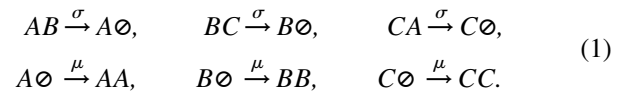
DOI: [10.1103/PhysRevLett.99.238105](https://doi.org/10.1103/PhysRevLett.99.238105)

PACS numbers: 87.23.Cc, 02.50.Ey, 05.10.Gg, 87.18.Hf

Understanding the combined influence of spatial degrees of freedom and noise on biodiversity is an important issue in theoretical biology and ecology. This implies facing the challenging problem of studying complex nonequilibrium structures, which form in the course of nonlinear evolution [1–6]. More generally, self-organized nonequilibrium patterns and traveling waves are ubiquitous in nature and appear, for instance, in chemical reactions, biological systems, as well as in epidemic outbreaks [7]. Among the most studied types of patterns are spiral waves, which are relevant to autocatalytic chemical reactions, aggregating slime-mold cells, and cardiac muscle tissue [8]. In all these *nonequilibrium* and *nonlinear* processes, as well as in population dynamics models [1,3,5], pattern formation is driven by diffusion which, together with internal noise, act as mechanisms allowing for stabilization and coevolution of the reactants. In this work, we consider a paradigmatic spatially extended 3 species population system with cyclic competition, which can be regarded as a simple food-chain model [9]. In fact, such a system is inspired by recent experiments on the coevolution of 3 species of bacteria in cyclic competition [4]. Using methods of statistical physics, we study the influence of spatial degrees of freedom and internal noise on the coevolution of the species and on the emerging spiral patterns. In particular, we compute the correlation functions and provide analytical expressions for the spreading speed and wavelength of the propagating fronts. To underpin the role of internal noise, the results of the stochastic description are compared with those of the deterministic equations.

In this Letter, we investigate a stochastic spatial variant of the *rock-paper-scissors game* [9] (also referred to as cyclic Lotka-Volterra model). These kinds of systems have been studied both from a game-theoretic perspective, see, e.g., [10,11] and references therein, and within the framework of chemical reactions [5,12], revealing rich spatio-temporal behaviors (e.g., emergence of rotating spirals). While our methods have a broad range of applicability,

they are illustrated for a prototypical model introduced by May and Leonard [13] where 3 species, A , B , and C , undergo a cyclic competition (codominance with rate σ) and reproduction (with rate μ), according to the reactions



Hence, an individual of species A will consume one of species B ($AB \rightarrow A\emptyset$) with rate σ and will reproduce with rate μ if an empty spot, denoted \emptyset , is available ($A\emptyset \rightarrow AA$, i.e., there is a *finite* carrying capacity). In addition, to mimic the possibility of migration, it is realistic to endow the individuals with a form of mobility. For the sake of simplicity, we consider a simple exchange process, with rate ϵ , among any *nearest-neighbor* pairs of agents: $XY \xrightarrow{\epsilon} YX$, where $X, Y \in \{A, B, C, \emptyset\}$. If one ignores the spatial structure and assumes the system to be well mixed (with an infinite number of individuals), the population's mobility plays no role and the dynamics is aptly described by the deterministic rate equations (RE) for the densities a , b , c of species A , B , and C , respectively. Introducing $s \equiv (a, b, c)$, the RE read:

$$\partial_t s_i = s_i [\mu(1 - \rho) - \sigma s_{i+2}], \quad i \in \{1, 2, 3\}, \quad (2)$$

where the index i is taken modulo 3 and $\rho = a + b + c$ is the total density. As shown by May and Leonard [13] (see also [14]), these equations possess 4 absorbing fixed points, corresponding to a system filled with only one species and to an empty system. In addition, there is a reactive fixed point $s^* = \frac{\mu}{\sigma+3\mu}(1, 1, 1)$, corresponding to a total density $\rho^* = \frac{3\mu}{\sigma+3\mu}$. A linear stability analysis shows that s^* is *unstable*. The absorbing steady states $(1, 0, 0)$, $(0, 1, 0)$, and $(0, 0, 1)$ are heteroclinic points. The existence of a Lyapunov function $\mathcal{L} = abc/\rho^3$ allows us to prove that, within the realm of the above RE, the phase portrait is characterized by flows spiraling outward from s^* , with

frequency $\omega_0 = \sqrt{3}\mu\sigma/[2(3\mu + 2\sigma)]$ in its vicinity. Approaching the boundaries of the phase portrait, the trajectories form (heteroclinic) cycles indefinitely close to the edges (without ever reaching them), with densities approaching, in turn, the value one. Despite its mathematical elegance, this behavior has been recognized to be unrealistic [13,14]. In fact, for finite populations, fluctuations arise and *always* cause the extinction of two species in finite time (see, e.g., Ref. [15]).

In this work, considering the spatial version of the above model in the presence of internal noise, we show that a robust (and, arguably, more realistic) scenario for the evolution arises. The reaction schemes (2) and the exchange events are considered to occur on a d -dimensional regular lattice of N sites, labeled $\mathbf{r} = (r_1, \dots, r_d)$. Each lattice site has z neighbors at a distance δr (e.g., $z = 2d$ and $N = L^d$ for hypercubic lattices of linear size L) and is either empty or occupied by at most one individual. On the lattice, the binary reactions (1) and exchanges only occur among pairs of *nearest neighbors*. In the situation of large system sizes, the continuum limit reveals that for the exchange process to be an efficient driving mechanism, the rate ϵ has to scale as $\epsilon \propto N^\nu$, with $\nu = 2/d$ and $N \rightarrow \infty$. In fact, if $0 < \nu < 2/d$ the system is dominated by the local reactions (1) among neighboring individuals, while effective diffusion renders locality irrelevant when $\nu > 2/d$. Only when $\nu = 2/d$ is there an effective competition between the stirring process and the local reactions (1). It is therefore useful to introduce the *effective diffusion constant* $D \equiv \frac{z}{2d^2} N^{-2/d} \epsilon$. Because of the discreteness of the number of individuals involved in the reactions, internal fluctuations arise in the system. The latter originate from (i) the interspecies reactions (1) and (ii) the exchange processes. In the continuum limit, where $\delta r = N^{-1/d}$ with $N, \epsilon \rightarrow \infty$ (and finite D), there is a separation of time scales and the pair exchanges occur much faster than the reactions ($\epsilon \propto N^{2/d}$). Actually, the fluctuations associated with (1) and the agents' mobility scale, respectively, as $N^{-1/2}$ and N^{-1} , with the former dominating over the latter and being the only relevant contribution. This result is revealed by a system size, also called Kramers-Moyal (see, e.g., Ref. [16], Chap. 8), expansion (SZE) of the master equation underlying the exchange processes and the reactions (1) [17]. Furthermore, the SZE yields a proper Fokker-Planck equation, which is equivalent to a set of (Ito) stochastic partial differential equations (SPDE) with white noise. The derivation, obtained in the continuum limit from the master equation, is outlined in the supplementary EPAPS document [17] and will be detailed elsewhere [18]. Here, we quote the expression of the SPDE:

$$\partial_t s_i = D \nabla^2 s_i + \mathcal{A}_i(s) + \sum_{j=1}^3 \mathcal{C}_{ij}(s) \xi_j, \quad i \in \{1, 2, 3\}, \quad (3)$$

where ∇^2 is the Laplacian operator; $\langle \xi_i(\mathbf{r}, t) \rangle = 0$,

$\langle \xi_i(\mathbf{r}, t) \xi_j(\mathbf{r}', t') \rangle = \delta_{ij} \delta(\mathbf{r} - \mathbf{r}') \delta(t - t')$, and

$$\mathcal{A}_i(s) = s_i [\mu(1 - \rho) - \sigma s_{i+2}], \quad (4)$$

$$\mathcal{C}_{ij}(s) = \delta_{ij} \sqrt{N^{-1} s_i [\mu(1 - \rho) + \sigma s_{i+2}]}. \quad (5)$$

Again, the indices are taken modulo 3 and now $s_i \equiv s_i(\mathbf{r}, t)$. As explained in [16,18], these SPDE have to be interpreted in the sense of Ito calculus. While Eqs. (3) and our approach are valid in any dimension [17], for specificity, we now analyze the spatiotemporal properties of the system in two dimensions with periodic boundary conditions. On the one hand we have solved numerically the SPDE (3) using the open software from the XMDS project [19]. On the other hand, we have carried out individual-based simulations of the reactions (1) for mobile (exchange process) particles on lattices of size $L \times L$, with $L = 30$ –1000. This allows to carefully study the convergence towards the continuum limit, where the description in terms of (3) is expected to be accurate.

As other spatially extended dynamical systems [5,10–12], the model under consideration displays fascinating nonequilibrium patterns emerging in the course of the evolution. In Fig. 1(a) and 1(b), we report typical long-time snapshots of the system for low (a) and high (b) exchange rates (but keeping D fixed), as obtained from lattice simulations. In both cases we notice that intriguing patterns form. For slow exchange rate, the system displays nongeometrical patches, similarly to what happens in systems with self-organized criticality [20]. When the exchange rate is raised, the patterns display spiral structures. In fact, starting from a spatially homogeneous initial condition, $s(\mathbf{r}, 0) = s^*$, the system is randomly perturbed by the internal noise and the resulting spatial inhomogeneities grow and form wave fronts moving through the system. The emergence of spiral patterns is a feature shared by other *excitable systems* (see, e.g., [7,8]) and corresponds to the ability of the system to sustain the propagation of oscillating waves. For sufficiently large ϵ , one observes a striking resemblance between the size and

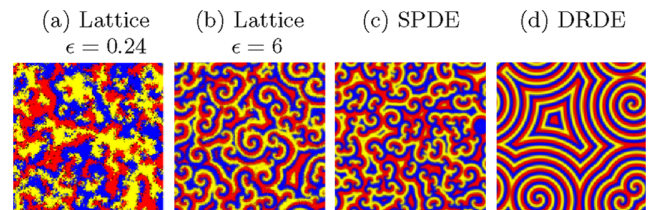


FIG. 1 (color online). Snapshots of reactive steady states for rates $D = 3 \times 10^{-6}$, $\mu = \sigma = 1$. Each color (level of gray) indicates one species (black dots correspond to vacancies). In (a) and (b) results are from lattice simulations for $L = 200$ (a) and $L = 1000$ (b), i.e., different ϵ . Spiral structures emerge for sufficiently large exchange rate (b). Numerical solution of the SPDE (3) and DRDE are shown in (c), respectively (d); see text. In (a)–(c), initially $s(\mathbf{r}, 0) = s^*$.

structure of the patterns obtained from the lattice simulations [Fig. 1(b)] and those from the SPDE (3) [Fig. 1(c)]. To further compare the predictions of the SPDE (3) with the lattice simulations, and to gain additional information on the structure of the emerging patterns, we have computed the correlation functions, $g_{s_i s_j}(\mathbf{r} - \mathbf{r}', t) \equiv \langle s_i(\mathbf{r}, t) s_j(\mathbf{r}', t) \rangle - \langle s_i(\mathbf{r}, t) \rangle \langle s_j(\mathbf{r}', t) \rangle$ in two dimensions. In Fig. 2 (red and blue curves), we report the results for $g_{aa}(\mathbf{r}, t)$ in the steady state and notice an excellent agreement between the results of the lattice simulations and the predictions of the SPDE (3). The inset of Fig. 2 displays the correlation length ℓ_{corr} [21] as a function of ϵ (D is kept fixed, L varies) obtained in the lattice simulations, which is found to coincide with the prediction of the SPDE already for $\epsilon \geq 5$. We have also computed the autocorrelation function $g_{s_i s_j}(0, t)$ and found, both in the lattice simulations and from the solutions of the SPDE, an oscillating behavior with a similar characteristic frequency, markedly different from ω_0 [18]. This confirms that, even for *finite exchange rates*, the solution of the SPDE (3) provides an excellent approximation of the lattice simulations of the system. This is rather surprising since Eqs. (3) have been derived in the continuum limit, where N and $\epsilon \rightarrow \infty$. A comparable influence of finite exchange rate in a predator-prey system has been reported recently [22]. According to the SPDE (3), ℓ_{corr} scales as $D^{1/2}$, so that by raising the diffusion one increases the size of the spirals. As we have shown in Ref. [6], this happens up to a critical value D_c (e.g., $D_c \approx 4.5 \pm 0.5 \times 10^{-4}$ for $\mu = \sigma = 1$): above that threshold, the spiral structures outgrow the system size and only one species survives, corresponding to an absorbing steady state predicted by Eqs. (2).

As the properties of the lattice simulations are well captured by the SPDE (3), where the strength of the noise

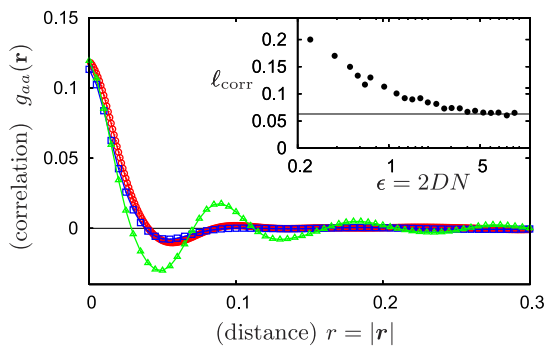


FIG. 2 (color online). Spatial correlation functions in 2D, obtained from lattice simulations (red, circles; $\epsilon = 6$, $L = 1000$), from the solution of the SPDE (3) (dark blue, squares) and of the DRDE (green, triangles), see text. The reaction rates are $\mu = \sigma = 1$ and $D = 3 \times 10^{-6}$. Inset: the correlation length ℓ_{corr} , for $D = 5 \times 10^{-5}$, $\mu = \sigma = 1$, as function of ϵ (i.e., for different lattice sizes) compared to the prediction of the SPDE (black line). The latter is in excellent agreement with lattice simulations already for $\epsilon \geq 5$ (i.e., $L \geq 225$).

scales as $N^{-1/2}$, with $N \rightarrow \infty$, it is natural to investigate the actual influence of this internal noise on the steady state of the system. To address this issue, we have solved numerically (in 2D, with periodic boundary conditions) the deterministic reaction-diffusion equation (DRDE) obtained from (3) by dropping the noise terms, i.e., $\partial_t s_i = D \nabla^2 s_i + \mathcal{A}_i(s)$. Of course, to obtain a nontrivial steady state for the DRDE one has to assume spatially inhomogeneous initial conditions. In Fig. 1(d), we have reported a snapshot of the long-time behavior predicted by the DRDE starting from $s(\mathbf{r}, 0) = s^* + (\frac{1}{100} \cos 2\pi r_1 r_2, 0, 0)$. In this case, the dynamics evolves towards a reactive steady state which also exhibits spiral waves. However, the latter do not form entangled structures, but ordered geometrical patterns. As an example, only four spirals cover the system in Fig. 1(d) [while noise leads to 106 entangled spirals in Fig. 1(c)]. The correlation functions associated with the DRDE therefore exhibit only weakly damped spatial oscillations (see Fig. 2, green triangles). By analyzing typical snapshots like those of Fig. 1(d), we have noted that in the deterministic and stochastic [i.e., lattice simulations with “large” ϵ and solutions of Eqs. (3)] descriptions, the spiral waves share the same propagation velocity, frequency, and wavelength. However, a major difference between these descriptions lies on the crucial dependence of the DRDE on initial conditions, which determine the overall number of spirals and their size. On the contrary, because the internal noise acts a random source of spatial inhomogeneities, the lattice stochastic system and the SPDE display *robust features*. In particular, we have found noise to induce a universal spiral density of about 0.5 per square wavelength.

Analytical expressions for the spreading velocity and the wavelength of the propagating fronts of the DRDE can be obtained by considering the dynamics on the invariant manifold of the RE [23], given by $\mathcal{M}: \{y_C = \frac{\sigma(3\mu+\sigma)}{4\mu(3\mu+2\sigma)} \times (y_A^2 + y_B^2) + O(y^3)\}$, with

$$(y_A, y_B, y_C)^T \equiv \frac{1}{3} \begin{pmatrix} \sqrt{3} & 0 & -\sqrt{3} \\ -1 & 2 & -1 \\ 1 & 1 & 1 \end{pmatrix} (s^T - s^{*T}).$$

On \mathcal{M} , up to 3rd order, the DRDE can be recast in the form of a forced complex Ginzburg-Landau equation (CGLE) [24,25]. By performing the nonlinear transformation $z_A = y_A + \frac{3\mu+\sigma}{28\mu} [\sqrt{3}y_A^2 + 10y_A y_B - \sqrt{3}y_B^2]$ and $z_B = y_B + \frac{3\mu+\sigma}{28\mu} [5y_A^2 + 2\sqrt{3}y_A y_B - 5y_B^2]$, upon ignoring nonlinearities like $(\nabla z_{A,B})^2$, one is left with the following CGLE in the variable $z \equiv z_A + iz_B$ [18]:

$$\partial_t z = D \nabla^2 z + (c_1 - i\omega_0)z - c_2(1 + ic_3)|z|^2 z, \quad (6)$$

with $c_1 \equiv \frac{\mu\sigma}{2(3\mu+\sigma)}$, $c_2 \equiv \frac{\sigma(3\mu+\sigma)(48\mu+11\sigma)}{56\mu(3\mu+2\sigma)}$, and $c_3 \equiv \frac{\sqrt{3}(18\mu+5\sigma)}{(48\mu+11\sigma)}$. The general theory of front propagation [24,25] predicts that Eq. (6) always admits traveling waves as stable solutions (i.e., no Benjamin-Feir or Eckhaus instabilities occur). We have determined such periodic

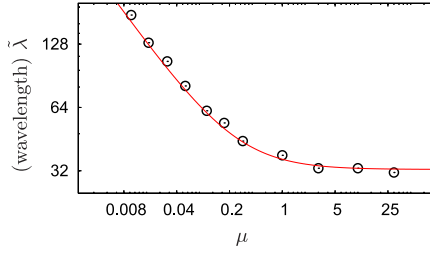


FIG. 3 (color online). Plot of $\tilde{\lambda}$, where $\lambda = \tilde{\lambda}\sqrt{D}$ is the spirals' wavelength of the propagating spiral waves. Analytical results (red curve, rescaled by a factor 1.6; see text) are compared with the solution of the SPDE (3) (black circles).

solutions by computing, from the dispersion relation of (6), the spreading velocity v and the spirals' wavelength λ (details will be given in [18]):

$$v = 2\sqrt{c_1 D}, \quad \lambda = 2\pi c_3 \sqrt{c_1^{-1} D} \left(1 - \sqrt{1 + c_3^2}\right)^{-1}. \quad (7)$$

In the stochastic version of the model, the wavelength and velocity of the wave fronts have been found to agree with those of the deterministic treatment. Hence, the expressions (7) also apply (for large ϵ , with $D < D_c$) to the results of lattice simulations (rescaled by a factor L) and to the solution of the SPDE (3). For instance, on a square grid with $\mu = \sigma = 1$, lattice simulations and Eqs. (3) yield $v \approx 0.63D^{1/2}L$, in good agreement with the prediction of (7): $v = (D/2)^{1/2}L$. For the spirals' wavelength, numerical results (lattice simulations and SPDE) yield $\lambda \propto D^{1/2}$ as predicted by (7). In Fig. 3, the analytical prediction (7) for λ is compared with the values obtained from the SPDE (3), yielding a remarkable agreement for the functional dependence on the parameter μ . Yet, as Eq. (6) does not account for all nonlinearities, the analytical and numerical values differ by a prefactor ≈ 1.6 (considered in Fig. 3) [18]. It can still be noted that (6) and the predictions (7) are valid in all dimensions [17,18].

Motivated by recent experiments [4], we have considered a spatially extended model with three species in cyclic competition and focused on the spatial and stochastic effects. The local character of the reactions and internal noise allow mobile populations to coexist and lead to pattern formation. We have shown that already for finite mobility the lattice model can be described by SPDE. With the latter and lattice simulations, we have studied how entanglement of spirals form and we have obtained expressions for their spreading velocity and wavelength. The size of the patterns crucially depends on the diffusivity: above a certain threshold the system is covered by one species [6]. In the absence of noise, the equations still predict the formation of spiral waves, but their spatial arrangement depends on the initial conditions.

Support of the German Excellence Initiative via the program "Nanosystems Initiative Munich" and of the Grant No. SFB TR 12 are gratefully acknowledged.

M.M. is grateful to the Alexander von Humboldt Foundation for support through the Grant No. IV-SCZ/1119205.

*Current address: Mathematics Institute & Complexity Complex, The University of Warwick, Coventry CV4 7AL, United Kingdom.

- [1] A. M. Turing, *Phil. Trans. R. Soc. B* **237**, 37 (1952).
- [2] R. M. May, *Stability and Complexity in Model Ecosystems* (Cambridge University Press, Cambridge, England, 1974); S. J. Maynard, *Models in Ecology* (Cambridge University Press, Cambridge, England, 1974).
- [3] J. D. Murray, *Mathematical Biology* (Springer-Verlag, Berlin, 2002).
- [4] B. Kerr *et al.*, *Nature (London)* **418**, 171 (2002).
- [5] K. I. Tainaka, *Phys. Rev. Lett.* **63**, 2688 (1989); *Phys. Rev. E* **50**, 3401 (1994).
- [6] T. Reichenbach, M. Mobilia, and E. Frey, *Nature (London)* **448**, 1046 (2007).
- [7] *Chemical Waves and Patterns, Part One*, edited by R. Kapral and K. Showalter (Kluwer Academic Publishers, Dordrecht, 1995); J. Lechleiter *et al.*, *Science* **252**, 123 (1991); B. T. Grenfell, O. N. Bjornstad, and J. Kappey, *Nature (London)* **414**, 716 (2001).
- [8] A. N. Zaikin and A. M. Zhabotinskii, *Nature (London)* **225**, 535 (1970).
- [9] J. Hofbauer and K. Sigmund, *Evolutionary Games and Population Dynamics* (Cambridge University Press, Cambridge, England, 1998).
- [10] C. Hauert and G. Szabó, *Am. J. Phys.* **73**, 405 (2005).
- [11] G. Szabó and G. Fáth, *Phys. Rep.* **446**, 97 (2007).
- [12] L. Frachebourg, P. L. Krapivsky, and E. Ben-Naim, *Phys. Rev. Lett.* **77**, 2125 (1996).
- [13] R. M. May and W. J. Leonard, *SIAM J. Appl. Math.* **29**, 243 (1975).
- [14] R. Durrett and S. Levin, *Theor. Popul. Biol.* **53**, 30 (1998).
- [15] T. Reichenbach, M. Mobilia, and E. Frey, *Phys. Rev. E* **74**, 051907 (2006).
- [16] C. W. Gardiner, *Handbook of Stochastic Methods* (Springer, New York, 1983), 1st ed.
- [17] See EPAPS Document No. E-PRLTAO-99-046747 for two appendices. In Appendix A, we outline the derivation of the stochastic partial differential equations (3) from the underlying master equation. Appendix B is devoted to a brief and general discussion of the properties of the system in arbitrary dimensions. For more information on EPAPS, see <http://www.aip.org/pubservs/epaps.html>.
- [18] T. Reichenbach, M. Mobilia, and E. Frey (to be published).
- [19] <http://www.xmids.org>.
- [20] K. Schenk *et al.*, *Eur. Phys. J. B* **15**, 177 (2000).
- [21] The correlation length denotes the characteristic length at which the spatial correlations decay by a factor $1/e$ from their maximal value.
- [22] M. Mobilia, I. T. Georgiev, and U. C. Täuber, *Phys. Rev. E* **73**, 040903(R) (2006).
- [23] S. Wiggins, *Introduction to Applied Nonlinear Dynamical Systems and Chaos* (Springer, New York, 1990), 1st ed.
- [24] W. Saarloos, *Phys. Rep.* **386**, 29 (2003).
- [25] M. C. Cross and P. C. Hohenberg, *Rev. Mod. Phys.* **65**, 851 (1993).

Self-Organization of Mobile Populations in Cyclic Competition

Tobias Reichenbach¹, Mauro Mobilia^{1,2}, and Erwin Frey¹

¹Arnold Sommerfeld Center for Theoretical Physics and Center for NanoScience, Department of Physics, Ludwig-Maximilians-Universität München, Theresienstrasse 37, D-80333 München, Germany.

²Mathematics Institute and Warwick Centre for Complexity Science, The University of Warwick, Gibbet Hill Road, Coventry CV4 7AL, United Kingdom

Abstract

The formation of out-of-equilibrium patterns is a characteristic feature of spatially-extended, biodiverse, ecological systems. Intriguing examples are provided by cyclic competition of species, as metaphorically described by the ‘rock-paper-scissors’ game. Both experimentally and theoretically, such non-transitive interactions have been found to induce self-organization of static individuals into noisy, irregular clusters. However, a profound understanding and characterization of such patterns is still lacking. Here, we theoretically investigate the influence of individuals’ mobility on the spatial structures emerging in rock-paper-scissors games. We devise a quantitative approach to analyze the spatial patterns self-forming in the course of the stochastic time evolution. For a paradigmatic model originally introduced by May and Leonard, within an interacting particle approach, we demonstrate that the system’s behavior - in the proper continuum limit - is aptly captured by a set of stochastic partial differential equations. The system’s stochastic dynamics is shown to lead to the emergence of entangled rotating spiral waves. While the spirals’ wavelength and spreading velocity is demonstrated to be accurately predicted by a (deterministic) complex Ginzburg-Landau equation, their entanglement results from the inherent stochastic nature of the system. These findings and our methods have important applications for understanding the formation of noisy patterns, e.g., in ecological and evolutionary contexts, and are also of relevance for the kinetics of (bio)-chemical reactions.

1 Introduction

Spatial distribution of individuals, as well as their mobility, are common features of real ecosystems that often come paired [1]. On all scales of living organisms, from bacteria residing in soil or on Petri dishes, to the largest animals living in savannas - like elephants - or in forests, populations’ habitats are spatially extended and individuals interact locally within their neighborhood. Field studies as well as experimental and theoretical investigations have shown that the locality of the interactions leads to the self-formation of complex spatial patterns [1, 2, 3, 4, 5, 6, 7, 8, 9, 10, 11, 12, 13, 14, 15]. Another important property of most individuals is mobility. For example, bacteria swim and tumble, and animals migrate. As motile individuals are capable of enlarging their district of residence, mobility may be viewed as a mixing, or stirring mechanism which “counteracts” the locality of spatial interactions.

The combined influence of these effects, i.e. the competition between mobility and spatial separation, on the spatio-temporal development of populations is one of the most interesting and complex problems in theoretical ecology [1, 2, 3, 6, 9, 16, 17]. If mobility is low, locally interacting populations can exhibit involved spatio-temporal patterns, like traveling waves [18], and for example lead to the self-organization of individuals into spirals in myxobacteria aggregation [18] and insect host-parasitoid populations [5], or more fractal-like structures in competing strains of *E.coli*

[8]. On the other hand, high mobility results in well-mixed systems where the spatial distribution of the populations is irrelevant [19, 20]. In this situation, spatial patterns do no longer form: The system adopts a spatially uniform state, which therefore drastically differs from the low-mobility scenario.

An intriguing motif of the complex competitions in a population, promoting species diversity, is constituted by three subpopulations exhibiting cyclic dominance. This basic motif is metaphorically described by the rock-paper-scissors game, where rock crushes scissors, scissors cut paper, and paper wraps rock. Such non-hierarchical, cyclic competitions, where each species outperforms another, but is also itself outperformed by a remaining one, have been identified in different ecosystems like coral reef invertebrates [21], rodents in the high-Arctic tundra in Greenland [22], lizards in the inner Coast Range of California [23] and microbial populations of colicinogenic *E. coli* [8, 24]. In the latter situation, it has been shown that spatial arrangement of quasi-immobile bacteria (because of ‘hard’ nutrient or substrate) on a Petri-dish leads to the stable coexistence of all three competing bacterial strains, with the formation of irregular patterns. In stark contrast, when the system is well-mixed, there is spatial homogeneity resulting in the take over of one subpopulation and the extinction of the others after a short transient.

It is worth noting that the emergence of noisy patterns, as those studied here, is a feature shared across disciplines

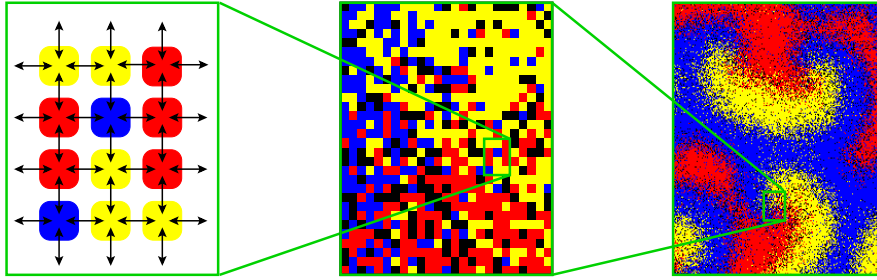


Figure 1: The stochastic spatial system at different scales. Here, each of the colors yellow, red, and blue (level of gray) represents one species, and black dots identify empty spots. Left: Individuals are arranged on a spatial lattice and randomly interact with their nearest neighbors. Middle: At the scale of about 1,000 individuals, stochastic effects dominate the system’s appearance, although domains dominated by different subpopulations can already be detected. Right: About 50,000 mobile interacting individuals self-organize into surprisingly regular spiral waves.

by many complex systems characterized by their out-of-equilibrium nature and nonlinear interactions. Examples range from the celebrated Belousov-Zhabotinsky reaction [25] (spiralling patterns) and many other chemical reactions [26], to epidemic outbreaks (traveling waves) [27, 28], excitable media [29, 26], and calcium signalling within single cells [30, 31, 32]. Moreover, cyclic dynamics as described by the rock-paper-scissors game occur not only in population dynamics but have, e.g., been observed in social dilemmas relevant in behavioral sciences [33, 34]. Therefore, we would like to emphasize that the methods presented in this work are not limited to theoretical ecology and biology, but have a broad range of multidisciplinary applications and notably include the above fields.

Pioneering work on the role of mobility in ecosystems was performed in Ref. [35], where the dynamics of a population residing in two coupled patches was investigated: Within a deterministic description, Levin identified a critical value for the individuals’ mobility between the patches. Below the critical threshold, all subpopulations coexisted, while only one remained above that value. Later, more realistic models of many patches, partly spatially arranged, were also studied, see Refs. [5, 6, 7, 36] as well as references therein. These works shed light on the formation of patterns, in particular traveling waves and spirals. However, patch models have been criticized for treating the space in an “implicit” manner (i.e. in the form of coupled habitats without internal structure) [37]. In addition, the above investigations were often restricted to deterministic dynamics and thus did not address the spatio-temporal influence of noise. To overcome these limitations, Durrett and Levin [38] proposed to consider interacting particle systems, i.e. stochastic spatial models with populations of discrete individuals distributed on lattices. In this realm, studies have mainly focused on numerical simulations and on (often heuristic) deterministic reaction-diffusion equations, or coupled maps [39, 38, 37, 9, 40, 41, 42, 43, 13].

Here, we demonstrate how a - spatially explicit - stochastic model of cyclically interacting subpopulations exhibits self-formation of spatial structures which, in the presence of

individuals’ mobility, turn into surprisingly regular, geometric spiral waves. The latter become visible on the scale of a large number of interacting individuals, see Fig. 1 (right). In contrast, stochastic effects solely dominate on the scale of a few individuals, see Fig. 1 (left), which interact locally with their nearest neighbors. Spatial separation of subpopulations starts to form on an intermediate scale, Fig. 1 (middle), where mobility leads to fuzzy domain boundaries, with major contributions of noise. On a larger scale, Fig. 1 (right), these fuzzy patterns adopt regular geometric shapes. As shown below, the latter are jointly determined by the deterministic dynamics and intrinsic stochastic effects. In the following, we elucidate this subtle interplay by mapping - in the continuum limit - the stochastic spatial dynamics onto a set of stochastic partial differential equations (SPDE) and, using tools of dynamical systems (such as normal forms and invariant manifolds), by recasting the underlying deterministic kinetics in the form of a complex Ginzburg-Landau equation (CGLE). The CGLE allows us to make analytical predictions for the spreading velocity and wavelength of the emerging spirals waves. Below, we provide a detailed description of these methods and convey a thorough discussion of the spatio-temporal properties of the system with an emphasis on the role of spatial degrees of freedom, mobility and internal noise.

2 Simulations and Results

We study a stochastic spatially-extended version of a three species model originally investigated (on rate equations level) by May and Leonard [44]. In Ref. [17] we have already considered such a model to demonstrate the existence of a critical value of the populations’ mobility separating a biodiverse regime, where all subpopulations coexist, from a uniform regime, where only one subpopulation survives. A brief account of the analysis of the spatio-temporal properties of the coexistence phase has recently been given in Ref. [45].

Consider three subpopulations A , B and C which cycli-

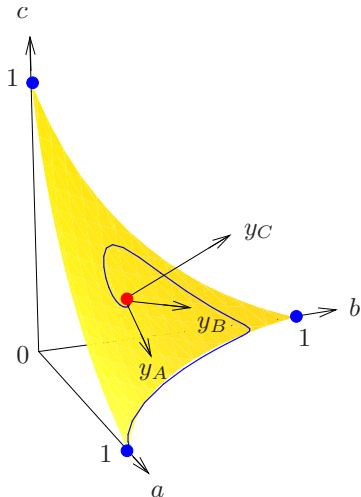
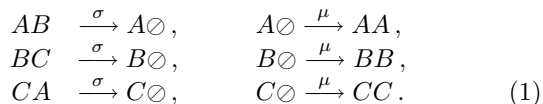


Figure 2: The phase space of the non-spatial system. It is spanned by the densities a, b , and c of species A, B , and C . On an invariant manifold (in yellow/light gray, see text), the flows obtained as solutions of the rate equations (4) (an example is shown in blue/dark gray) initially in the vicinity of the reactive fixed point (red/gray, see text) spiral outwards, approaching the heteroclinic cycle which connects three trivial fixed points (blue/dark gray). In Subsection 3.2, we introduce the appropriate coordinates (y_A, y_B, y_C) which reveal the mathematical structure of the manifold and reflect the cyclic symmetry of the system.

ally dominate each other. An individual of subpopulation A outperforms a B individual through “killing” (or “consuming”), symbolized by the reaction equation $AB \rightarrow A\emptyset$, where \emptyset denotes an available empty space. In the same way, B outperforms C , and C beats A in turn, closing the cycle. We refer to these processes as selection and denote the corresponding rate by σ . To mimic a finite carrying capacity, we allow each subpopulation to reproduce only if an empty space is available, as described by the reaction $A\emptyset \rightarrow AA$ and analogously for B and C . For all subpopulations, these reproduction events occur with rate μ , such that the three subpopulations equally compete for empty space. To summarize, the reactions that define the model (selection and reproduction) read



In the absence of spatial degrees of freedom, the kinetics of these reactions are embodied by rate equations for the temporal evolution of the mean densities $a(t), b(t), c(t)$ of the subpopulations A, B and C , respectively, given by Eqs. (4) in Subsection 3.1. These equations provide a deterministic description which is well suited to describe well-mixed systems with a large number of individuals, such as Moran processes [46, 47, 48] or urn models [49, 50]. For the system under consideration, the rate equations are given and care-

fully investigated in Subsection 3.1. As main features, they possess three absorbing fixed points corresponding to survival of only one subpopulation (the solution corresponding to an empty system is also an absorbing state, but is irrelevant for our purpose and will be ignored thereafter), as well as a reactive fixed point where all three subpopulations coexist, see Fig. 2. The coexistence fixed point is unstable, and trajectories starting in its vicinity spiral outwards. They lie on an invariant manifold, and approach a heteroclinic cycle which connects the three absorbing fixed points. The approaching trajectories spend longer and longer periods of time in a neighborhood of each (absorbing) fixed points, before departing to the next one. This means that the system alternates between states where nearly only one of the three species is present, with rapidly increasing time period. However, this picture is idealized as it crucially (and tacitly) assumes the presence of an infinite population. In fact, fluctuations, e.g. stemming from a finite number of individuals, lead to reach one of the absorbing states where only one subpopulation takes over the whole system. Which of the absorbing states is reached depends on the initial conditions as well as on random fluctuations. Due to the symmetry of the reactions (1), when averaging over all possible initial conditions as well as fluctuations, all species have an equal chance to survive.

In the spatially-extended stochastic version of the model, we adopt an interacting particle description where individuals of all subpopulations are arranged on a lattice. In this approach, each site of the grid is either occupied by one individual or empty, meaning that the system has a finite carrying capacity, and the reactions (1) are then only allowed between *nearest neighbors*. In addition, we endow the individuals with a certain form of mobility. Namely, at rate ϵ all individuals can exchange their position with a nearest neighbor. With that same rate, any individual can hop on a neighboring empty site. These exchange processes lead to an effective diffusion of the individuals. Denote L the linear size of the d -dimensional hypercubic lattice (i.e. the number of sites along one edge), such that the total number of sites reads $N = L^d$. Choosing the linear dimension of the lattice as the basic length unit, the macroscopic diffusion constant D of individuals stemming from exchange processes reads

$$D = \epsilon d^{-1} N^{-2/d}; \quad (2)$$

the derivation of this relation is detailed in Subsection 3.4.

How do individual’s mobility and internal noise, in addition to nonlinearity, affect the system’s behavior? Insight into this ecologically important issue can be gained from a continuum limit where the diffusion constant D is *finite*. Namely, we investigate the limit of infinite system size, $N \rightarrow \infty$, where the diffusion D is kept constant (implying that the local exchange rate tends to infinity, $\epsilon \rightarrow \infty$). In Subsections 3.4 and 3.5, we show how, in this limit, a description of the stochastic lattice system through stochastic partial differential equations (SPDE) becomes feasible. These SPDE describe the time evolution of the (spatially

dependent) densities $a(\mathbf{r}, t), b(\mathbf{r}, t), c(\mathbf{r}, t)$ of the subpopulations A, B , and C , respectively. The expression of the SPDE, Eqs. (30), is given in Subsection 3.5 along with their detailed derivation. The latter relies on a system-size expansion in the continuum limit which allows to obtain the noise terms of the SPDE. Noise stems from the stochasticity of the reactions (1) as well as the discreteness and the finite number of the individuals.

To investigate the behavior of the interacting particle system and to compare it with the predictions of the SPDE (30), we have carried out stochastic simulations of the model on a square lattice with periodic boundary conditions and of size ranging from $L = 50$ up to $L = 1000$ sites. In the following, we always consider the system in two spatial dimensions, $d = 2$. At each simulation step, a randomly chosen individual interacts with one of its four nearest neighbors, being also randomly determined. In a straightforward algorithm, at each Monte Carlo (MC) step, one determines (via a random number) which reaction (exchange, selection, or reproduction) occurs next. Reproduction happens with probability $\mu/(\mu + \sigma + \epsilon)$, selection with $\sigma/(\mu + \sigma + \epsilon)$, and exchange events occur with probability $\epsilon/(\mu + \sigma + \epsilon)$. Then, a random pair of nearest neighbors is selected and the chosen type of interaction (reproduction, selection or exchange) is performed, if the move is allowed. In our situation, a more efficient algorithm inspired by Gillespie [51, 52] can be implemented. Namely, in the continuum limit $N \rightarrow \infty$, the exchange rate ϵ becomes large compared to the selection and reproduction rates, μ and σ . Thus, a large number of exchange events occurs between two reactions (1). Indeed, the probability P of having E exchanges between two subsequent May-Leonard reactions reads

$$P(E) = \left(\frac{\epsilon}{\mu + \sigma + \epsilon} \right)^E \left(\frac{\mu + \sigma}{\mu + \sigma + \epsilon} \right). \quad (3)$$

Hereby, the first factor on the right hand side denotes the probability of subsequently drawing E exchange events, and the second factor is the probability that the next event is either a selection or reproduction process. To efficiently take this high number of exchanges occurring between selection/reproduction processes into account, at each MC step, we draw the number of such exchange events from the probability distribution (3). This number of random exchanges is performed, and then followed by one of the May-Leonard reactions (1).

All results we present from lattice simulations were obtained starting from a random initial distribution of individuals and vacancies: the probability for each site to be in one of the four possible states (i.e. A, B, C or \emptyset) has been chosen to coincide with the value of the (unstable) internal fixed point of the rate equations (4). Thereafter, without loss of generality, we often consider equal selection and reproduction rates, which we set to one (thereby defining the time scale), i.e. $\mu = \sigma = 1$. In this case, all four states initially occur with equal probability $1/4$. Generally, after a short transient, a reactive steady state emerges. Concerning its stability, note that the states where only one

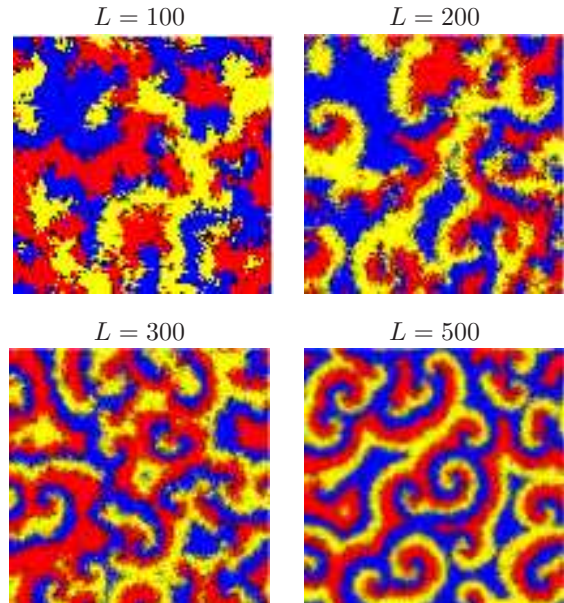


Figure 3: Approach of the continuum limit. We show snapshots of the reactive steady state of the stochastic system, for $D = 1 \times 10^{-5}$, $\mu = \sigma = 1$, and different system sizes. Each color (level of gray) represent a different species (black dots denote empty spots). The lattice sizes are $L = 100$ ($\epsilon = 0.2$) in the top left panel, $L = 200$ ($\epsilon = 0.8$, top right), $L = 300$ ($\epsilon = 1.8$, bottom left), and $L = 500$ ($\epsilon = 5$, bottom right). Increasing the system size (D is kept fixed), the continuum limit is approached. Random patterns appear for small systems ($L = 100$), while entangled spiral waves emerge when L is raised and clearly emerge in large systems ($L = 500$).

subpopulation uniformly covers the system are absorbing, while the reactive state is not. The latter is therefore not stable in a strict sense. Indeed, eventually, the system will end up in one of the absorbing uniform states. However, the typical waiting time until extinction of two subpopulations occurs is extremely long for large systems and it diverges with increasing system size [17], implying the existence of super-persistent transients [53]. Therefore, on ecologically reasonable time scales, the reactive state is stable [17].

In the continuum limit, the system is described in terms of the SPDE (30). To compare this approach with the results of the lattice system, we have numerically solved Eqs. (30) using open software from the XMDS project [54, 55]. For specificity, we have used spatial meshes of 200×200 to 500×500 points, and 10,000 steps in the time-direction. Initially, we started with homogeneous densities, corresponding to the values of the unstable internal fixed point of the RE (4), as in the lattice simulations.

2.1 Spiral structures in the continuum limit

To study the system's behavior in the approach of the continuum limit, we have kept the diffusion fixed at a value

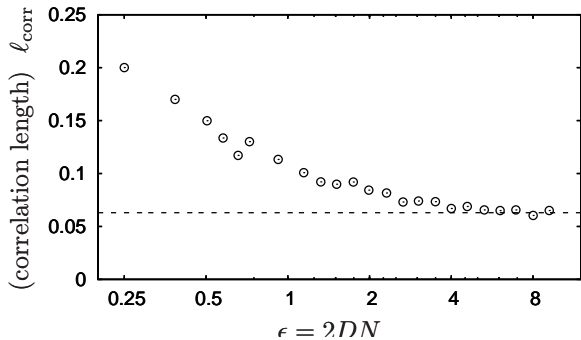


Figure 4: The typical size of the patterns, as described by the correlation length ℓ_{corr} . We show its dependence on the exchange rate ϵ , for fixed $D = 5 \times 10^{-5}$, $\mu = \sigma = 1$, and different system sizes N . For large N , i.e. large ϵ , we expect the system to be well described by SPDE, the correlation length of the latter is depicted as a dashed line. Surprisingly, the correlation length already agrees excellently with this continuum model for $\epsilon \geq 5$.

$D = 1 \times 10^{-5}$, and systematically varied the system size (and henceforth the exchange rate ϵ). In Fig. 3, we report typical long-time snapshots of the reactive steady states for various values of the exchange rate and different system sizes. In small lattices, e.g. $L = 100$, we observe that all subpopulations coexist and form clustering patterns of characteristic size. The spatio-temporal properties of the latter do not admit simple description and appear to be essentially dominated by stochastic fluctuations. When the size of the lattice is large, e.g. $L = 300 - 500$, the three populations also coexist in a reactive steady state. However, in stark contrast from the above scenario, we now find that individuals self-organize in entanglement of rotating spiral waves. The properties of these spirals, such as their wavelength, their frequency and the spreading velocity, are remarkably regular and will be studied below.

The asymptotic approach towards the continuum limit, as illustrated in the snapshots of Fig. 3, can be rationalized by considering the typical size of the patterns. The latter are obtained from the computation of spatial correlation functions (see next Subsection for the definition of correlation functions) and the ensuing correlation length ℓ_{corr} (denoting the length at which the correlations decay by a factor $1/e$ from their maximal value). This quantity gives the average spatial extension of the patterns. In Fig. 4, we report ℓ_{corr} as obtained for systems of different sizes, i.e. for various values of ϵ . For small systems (low exchange rate ϵ), the pattern size is considerably larger than in the continuum limit (dashed line obtained from SPDE, see below). Increasing the system size (larger values of ϵ), the continuum limit is approached. Remarkably, there is a striking agreement between the results from the lattice simulations and the SPDE already for $\epsilon \geq 5$. Hereby, $\mu = \sigma = 1$, such that the continuum limit is already closely approached when ϵ is of the same order as the rates for the selection and reproduction events, yet larger. This result is also ap-

parent in Fig. 3, where for $L = 500$ and $\epsilon = 5$, the system already exhibits regular spiral waves. It follows from this discussion that the results obtained in the continuum limit (derived assuming $\epsilon \rightarrow \infty$), actually have a broader range of validity and allow to aptly describe the interacting particle system already for ϵ finite and of the same order of (yet larger than) μ and σ . A comparable influence of short-range mixing has also been reported recently for a predator-prey - or host-pathogen - model, where a short-range exchange process with finite rate has been shown to crucially affect the fate of the system (absorbing or coexistence state) through a (first-order) phase transition [42].

In Fig. 5, we report snapshots of the reactive steady state obtained from the stochastic simulation (left column) and as predicted by the SPDE (right column) for different values of the diffusion constant D . In Fig. 5, panels in the same row have been obtained for the same parameters (for lattices of size $L = 300, 500$ and 1000). We observe an excellent qualitative and quantitative agreement between both descriptions, which yield the formation of rotating spiral waves whose typical sizes and wavelengths manifestly coincide (see below). When the diffusion constant D is increased, the size of the spirals increases, too. With help of the underlying SPDE (30), this observation can be rationalized by noting that the size of the spatial structures is proportional to \sqrt{D} . This scaling relation stems from the fact that spatial degrees of freedom only enter the Eqs. (30) through the diffusion term $D\Delta$, where the Laplacian operator Δ involves second-order spatial derivatives. Therefore, rescaling the spatial coordinates by a factor $1/\sqrt{D}$ makes the diffusive contribution independent of D , with the ensuing scaling relation. As we have shown in Ref. [17], the three subpopulations can coexist only up to a critical value of the diffusion rate. Above that threshold, the spirals outgrow the system and there is extinction of two populations: only one subpopulation (at random) survives and covers the entire lattice.

2.2 Correlations

The comparison of snapshots obtained from lattice simulations with the numerical solutions of the SPDE reveals a remarkable coincidence of both approaches (see Fig. 5). Of course, due to the inherent stochastic nature of the interacting particle system, the snapshots do not match exactly for each realization. To reach a quantitative assessment on the validity of the SPDE (30) to describe the spatio-temporal properties of the system in the continuum limit, we have computed various correlation functions.

We first consider equal-time correlation functions, which yield information about the size of the emerging spirals. As an example, we focus on the correlation $g_{AA}(|\mathbf{r} - \mathbf{r}'|)$ at \mathbf{r} and \mathbf{r}' of the subpopulation A , $g_{AA}(|\mathbf{r} - \mathbf{r}'|) = \langle a(\mathbf{r}, t)a(\mathbf{r}', t) \rangle - \langle a(\mathbf{r}, t) \rangle \langle a(\mathbf{r}', t) \rangle$. Here, the brackets $\langle \dots \rangle$ stand for an average over all histories. In the steady state, the time dependence drops out and, because of translational and rotational invariance, the latter depends only on the

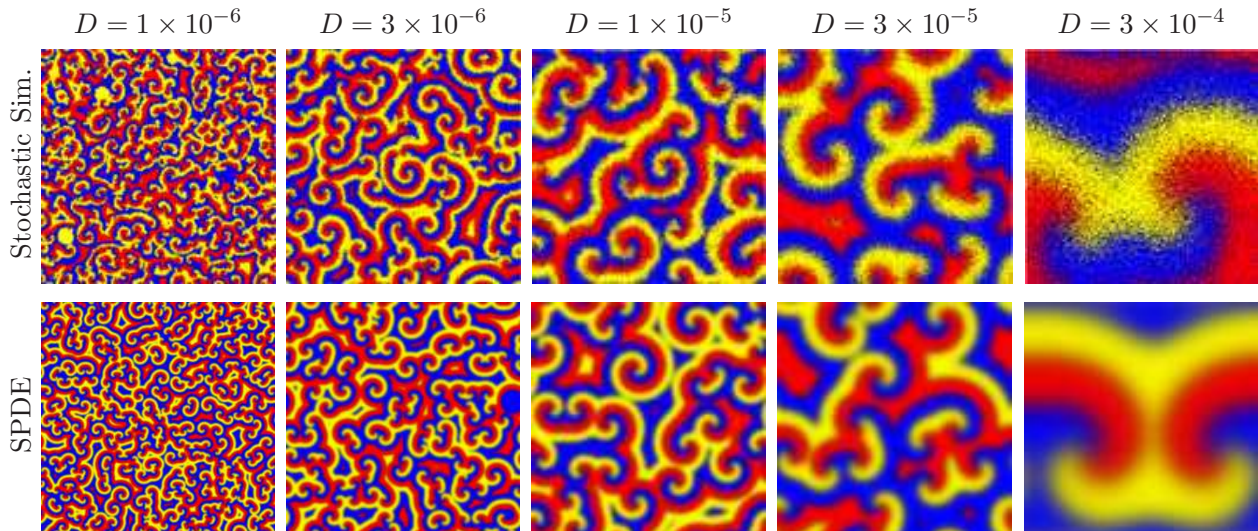


Figure 5: The reactive steady states. We show snapshots emerging in simulations of the interacting particle system (1) (top row) and obtained by solving the SPDE (30) (bottom row). Each color (level of gray) represent a different species (black dots denote empty spots). From left to right, the diffusion constant is increased from $D = 1 \times 10^{-6}$ to $D = 3 \times 10^{-4}$. The latter value is slightly below the critical threshold above which the spiral structures can no longer fit within the system [17]; see text. The system sizes used in the stochastic simulations are $L = 1000$ in the upper two panels, $L = 300$ for that at bottom, and $L = 500$ for the other two (middle). The selection and reproduction rates are chosen as $\sigma = \mu = 1$.

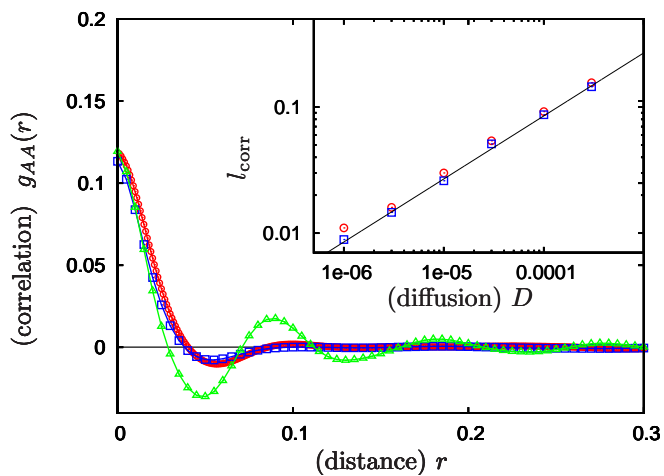


Figure 6: Correlation functions. The spatial correlation $g_{AA}(r)$ as function of r in the reactive steady state is shown. We report results obtained from stochastic simulations (red circles, for a lattice of linear size $L = 1000$) and numerical solutions of the SPDE (30), blue squares, and notice an excellent agreement. In both cases, results have been obtained for a value $D = 3 \times 10^{-6}$ and $\mu = \sigma = 1$. The typical correlation length ℓ_{corr} as a function of the diffusion constant D is shown in the inset (on a double logarithmic scale). The scaling relation $\ell_{\text{corr}} \sim \sqrt{D}$, indicated by a black line, is clearly confirmed. We have also reported the results for the static correlation function $g_{AA}(r)$ of the patterns predicted by the deterministic PDE (green triangles); see text. The latter are found to be markedly less damped than those arising in the stochastic descriptions of the system.

separating distance $|\mathbf{r} - \mathbf{r}'|$. In Fig. 6, we report results for g_{AA} obtained from lattice simulations (red circles) and from numerical solutions of the SPDE (30) (blue squares), finding an excellent agreement between them. When the separating distance vanishes, the autocorrelation reaches its maximal value and then decreases, exhibiting (damped) spatial oscillations. The latter reflect the underlying spiralling spatial structures, where the three subpopulations alternate in turn. Damping results from the averaging over many small spirals. As described in the previous subsection, the correlation functions are characterized by their correlation length ℓ_{corr} , which conveys information on the typical size of the spirals. In the inset of Fig. 6, we show the dependence of the correlation length on the diffusion rate D in a double logarithmic plot. The scaling relation $\ell_{\text{corr}} \sim \sqrt{D}$, inferred from general considerations is confirmed.

We now consider the time dependence of the correlation functions and study the autocorrelation $g_{AA}(|t - t'|)$ of subpopulation A at times t and t' , for a fixed spatial position. This quantity is given by $g_{AA}(|t - t'|) = \langle a(\mathbf{r}, t)a(\mathbf{r}, t') \rangle - \langle a(\mathbf{r}, t) \rangle \langle a(\mathbf{r}, t') \rangle$ and only depends on the time difference $|t - t'|$. Both lattice simulations and SPDE (30) yield oscillating correlation functions, as shown in Fig. 7. This periodic behavior, with a frequency numerically found to be $\Omega^{\text{num}} \approx 0.103$ (for $\sigma = \mu = 1$), stems from the rotational nature of the spiral waves and is independent of the diffusion constant D . Below, this value is compared with an analytical prediction inferred from a deterministic description of the spatial system. As the oscillations reported in Fig. 7 are undamped, the rotation of the spirals is stable in the steady state. This means that noise does not cause any

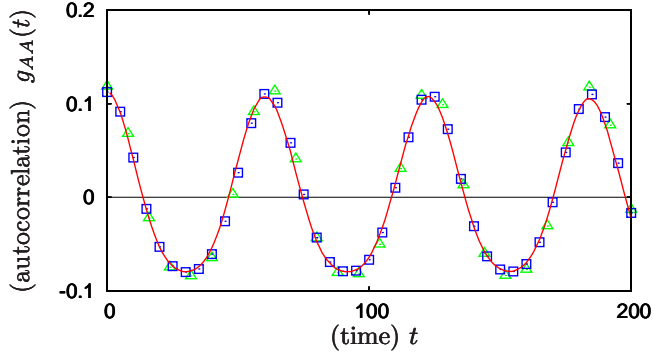


Figure 7: Autocorrelation. We show the correlation $g_{AA}(t)$ as a function of time t . Results from stochastic simulations (red/gray line) are compared with those obtained from the numerical solutions of the SPDE (blue squares), as well as with those computed from the deterministic PDE (green triangles). All results are in excellent agreement with each other and are characterized by oscillations at frequency $\Omega^{\text{num}} \approx 0.103$ (for $\mu = \sigma = 1$); the latter is independent from the value of the diffusion D . These oscillations reflect the rotation of the spiral waves. The results from the SPDE and deterministic PDE have been obtained using $D = 10^{-5}$, while stochastic simulations have been performed on a lattice of length $L = 300$ with $D = 10^{-4}$.

drift or break up of these patterns. Nonetheless, stochastic fluctuations do significantly influence the steady state of the system, as discussed below.

2.3 The role of stochasticity

So far, we have considered stochastic descriptions, relying on lattice simulations and stochastic partial differential equations (30). In the latter, the noise terms are proportional to $1/\sqrt{N}$, i.e. vanishing in the limit of $N \rightarrow \infty$. It is therefore legitimate to ask whether it is possible to simply neglect noise and describe the system in terms of deterministic partial differential equations (PDE) (23) given in Subsection 3.4. To address this question and to reach a better understanding of the effects of internal noise, we have numerically solved the deterministic PDE (23) for various initial conditions. Of course, the latter have always to be spatially inhomogeneous, otherwise spatial patterns cannot form. Starting from a spatially inhomogeneous distribution of the populations, the deterministic equations are found to evolve towards a reactive steady state also characterized by the emergence of spirals. We have numerically checked that these spirals' wavelengths λ are the same as those obtained in the stochastic lattice simulations and for the solutions of the SPDE (30).

However, there are major differences between the deterministic and the stochastic descriptions of the spatially extended system. Concerning the SPDE, when the initial densities are the ones corresponding to the unstable internal fixed point of the rate equations (4), even without initial inhomogeneities and only due to noise, an entanglement of

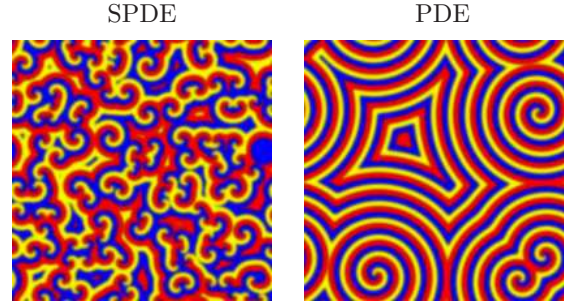


Figure 8: The role of noise. Left: numerical solution of the SPDE (30), starting from an homogeneous initial state (all sub-populations have an initial density $1/4$). Each color (level of gray) represent a different species (black dots denote empty spots). Right: if we ignore the noise terms of the SPDE (30) and study the resulting deterministic PDE (23), the steady state depends on the initial configuration. Here, this is illustrated by a snapshot of the steady state evolving from the initial condition: $a(0) = a^* + \cos(2\pi xy)/100$, $b(0) = b^*$, $c(0) = c^*$, see text. In both panels, the diffusion constant is $D = 3 \times 10^{-6}$ and $\sigma = \mu = 1$.

spiral waves arises in the course of time evolution. We have numerically found that the latter is characterized by a universal vortex density of about 0.5 per square wave length. For the deterministic PDE, spatially homogeneous initial conditions do not yield spiralling patterns. When starting with initial spatial inhomogeneities, the density of the latter sensitively determines the density of spirals, which can be much lower than in the stochastic situation. As an illustration, in Fig. 8 we compare snapshots of the steady state of the SPDE and of the PDE. For the latter, we have chosen the initial condition $a(t=0) = a^* + \cos(2\pi xy)/100$, $b(0) = b^*$, $c(0) = c^*$, just adding a small local perturbation to the value of the homogeneous fixed point (a^*, b^*, c^*) . A large number of spirals cover the system in the stochastic case (Fig. 8 left) while only four spirals appear in the deterministic situation; Fig. 8 right. This difference is also manifest when one considers the spatial dependence of the correlation functions, as shown in Fig. 6. These quantities share the same maxima and minima for the stochastic and deterministic descriptions, which can be traced back to the fact that spirals have the same wavelengths, not affected by the noise. However, the correlations obtained from lattice simulations and from the SPDE are much more strongly damped than in the case of a deterministic PDE. This stems from the fact that stochasticity effectively acts as an internal source of spatial inhomogeneities (randomly distributed), resulting in a larger number of spirals (of small size). The agreement between the temporal dependence of the correlation functions in the deterministic and stochastic descriptions (see Fig. 7) is another consequence of the fact that the spirals' frequency is not affected by the noise.

We can now ask what happens if one solves the SPDE (30) with inhomogeneous initial conditions. To answer this ques-

tion, we have systematically studied the emerging steady state upon varying the noise level and the degree of spatial inhomogeneity of the initial configuration. When these effects are of comparable intensity (i.e. the system is as noisy as initially inhomogeneous), the steady state is still driven by noise and gives rise to an entanglement of small spirals. In this situation, the universal density of 0.5 spiral vortices per square wavelength arises. On the other hand, if the degree of inhomogeneity of the initial state is significantly higher than the noise level, the former dominates the systems' behavior and the density of spirals is determined by the spatial structure of the initial configuration, as in Fig. 8 (right). Therefore, if no initial inhomogeneities are present, stochasticity acts as a random source of inhomogeneities leading to the emergence of an entanglement of stable spiral vortices. The latter are stable against stochastic effects, as reflected by the undamped temporal oscillations of the autocorrelation function of Fig. 7. On the other hand, if initial inhomogeneities exceed the noise level, they are responsible for the formation of vortices before noise can influence the system.

From the above discussion, we infer that the range of initial conditions where noise influences the system's fate and leads to the universal density of about 0.5 spiral vortices per square wavelength is rather small. It contains initial densities that lie around the values of the unstable reactive fixed point of the rate equations (4), with spatial variations whose amplitude does not exceed the noise level. Other initial conditions, with more strongly pronounced spatial inhomogeneities, lead to spiral vortices that are determined by the initial inhomogeneities, and not stochastic effects. The latter behavior is remarkable, as it corresponds to a *memory* of the system: The information about the initial state, i.e. its spatial inhomogeneities, is preserved in the reactive steady state where it manifests itself in the position of the spirals' vortices. The latter are stable during the temporal evolution: noise does not change their location. This feature is intimately connected to the nonequilibrium nature of the system. Indeed, in noisy equilibrium systems, the steady state does not convey information about the initial conditions. Only a genuine nonequilibrium steady state can display memory of the initial state.

Finally, let us comment on the nature of the noise encountered in our analysis. In the SPDE (30), the noise is multiplicative because its strength depends on the densities of the subpopulations. Approximating the latter by additive white noise [e.g., substituting (a, b, c) by the values (a^*, b^*, c^*) in the expressions of the noise contributions], we obtain the same results as with multiplicative noise. We understand this behavior as stemming from the fact that the main influence of noise is to spatially and randomly perturb the system's initial state. Hence, as long its intensity scales like $N^{-1/2}$ (weak noise), the fact that noise is either multiplicative or additive has no significant impact on the system's fate.

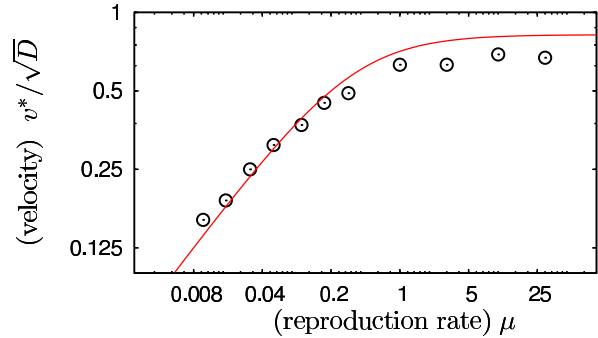


Figure 9: Spreading velocity. We report the dependence of front velocity v^* (rescaled by a factor \sqrt{D}) on the reproduction rate μ . The time scale is set by keeping $\sigma = 1$. In red (full line), we report the analytical predictions (37) obtained from the CGLE, which are compared with numerical results (black dots). The latter are obtained from the numerical solutions of the SPDE (30).

2.4 The spirals' velocities, wavelengths, and frequencies

Above, we have found that characteristic properties of the emerging spiral waves, like their wavelength and frequency, are unaffected by noise. To compute these quantities analytically, it is therefore not necessary to take noise into account, and we may focus on the study of the deterministic PDE (23). In Subsection 3.6, we show how the dynamics of the latter is essentially captured by an appropriate complex Ginzburg-Landau equation (CGLE), given by Eq. (32) for the case under consideration here. The CGLE (32) allows to derive analytical results for the emergence of spiral waves, their stability and their spreading velocity, as well as their wavelength and frequency. We detail these findings in Subsections 3.7 and 3.8. Here, we assess the accuracy and validity of these analytical predictions by comparing them with values obtained from the numerical solutions of the SPDE (30).

Let us first consider the spreading velocity v^* of the emerging wave fronts. The analytical value, inferred from the CGLE (32) and derived in Subsection 3.7 [see Eq. (37)], reads $v^* = 2\sqrt{c_1 D}$, where $c_1 = \mu\sigma/[2(3\mu + \sigma)]$ is a coefficient appearing in the CGLE (32). In numerical computations, the front velocity is obtained from the wavelength λ and the frequency Ω of the emerging spirals. Namely, the wavelength λ^{num} can be inferred from snapshots (as in Fig. 5), and the frequency Ω^{num} is computed from the oscillations of the autocorrelation (as in Fig. 7). The velocity then follows via $v^{\text{num}} = \lambda^{\text{num}}\Omega^{\text{num}}/2\pi$. As the wavelength is proportional to \sqrt{D} and the frequency does not depend on the diffusion constant, one can easily check that the relation $v^{\text{num}} = \lambda^{\text{num}}\Omega^{\text{num}}/2\pi$ confirms that $v^{\text{num}} \sim \sqrt{D}$, as in Eq. (37). In Fig. 9, we compare the analytical prediction (37) for v^* with results obtained from the numerical solution of the SPDE (30), as function of the reproduction rate

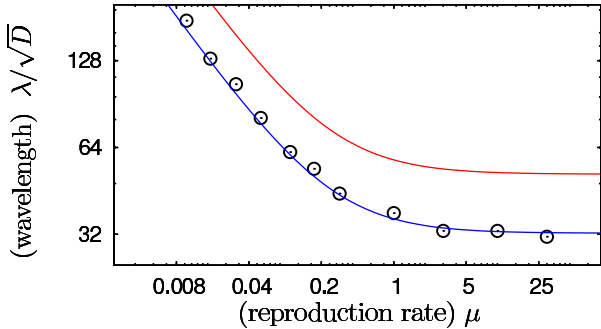


Figure 10: The spirals' wavelength. We show the functional dependence of the wavelength λ on the rate μ (with $\sigma = 1$), and compare numerical results (black circles), obtained from the numerical solutions of the SPDE (30), to analytical predictions (red line). The latter stem from the CGLE and are given by Eq. (42). They differ from the numerics by a factor of 1.6, see text. Adjusting this factor, c.f. the blue line, the functional dependence is seen to agree very well with numerical results.

μ (setting $\sigma = 1$, we fix the time scale), and find a good agreement. On the one hand, for small values of μ (much lower than the selection rate, $\mu \ll 1$), reproduction is the dominant limiter of the spatio-temporal evolution. In the limit $\mu \rightarrow 0$, the front velocity therefore only depends on μ . From dimensional analysis, it follows $v^* \sim \sqrt{\mu}$, as also confirmed by the analytical solution Eq. (37). On the other hand, if reproduction is much faster than selection, $\mu \gg 1$, the latter limits the dynamics, and we recover $v^* \sim \sqrt{\sigma}$. In Fig. 9, as $\sigma = 1$, this behavior translates into v^* being independent of μ in this limit. While the numerical and analytical results coincide remarkably for low reproduction rates (i.e. $\mu \leq 0.3$), systematic deviations ($\approx 10\%$) appear at higher values. As an example, when selection and reproduction rates are equal, $\sigma = \mu = 1$ (as was considered throughout the last section), we have numerically found a velocity $v^{\text{num}} \approx 0.63\sqrt{D}$, while Eq. (37) yields the analytical result $v^* = \sqrt{D/2} \approx 0.71\sqrt{D}$.

Concerning the spirals' wavelengths and frequencies, in Subsection 3.8, we analytically infer predictions from the CGLE (32) given by Eqs. (41) and (42). We have checked these results against numerical computations. In Fig. 10, the analytical estimates for the wavelength λ are compared with those obtained from the numerical solution of the SPDE (30) for different values of the reproduction rate μ . We notice that there is an excellent agreement between analytical and numerical results for the functional dependence of λ on μ . For low reproduction rates ($\mu \ll 1$) we have $\lambda \sim 1/\sqrt{\mu}$, while when reproduction occurs much faster than selection ($\mu \gg 1$), the dynamics is independent of μ and $\lambda \sim 1/\sqrt{\sigma}$. We have also found that the analytical result predicts an amplitude of λ which exceeds that obtained from numerical computations by a constant factor ≈ 1.6 , taken into account in Fig. 10. We attribute this deviation to the fact that the CGLE (32) (stemming from

the normal form (13)) describes a dynamics exhibiting a limit cycle, while the full May-Leonard rate equations (4) are characterized by heteroclinic orbits. The correct functional dependence of the wavelength λ on the reproduction rate μ is therefore especially remarkable. Elsewhere [56], it will be shown that in the presence of mutations, inducing a limit-cycle behavior, the description of the emerging spiral waves in terms of CGLE (32) becomes fully accurate.

For the spirals' frequency, we analytically obtain $\Omega = \Omega(q^{\text{sel}}) = \omega + 2(c_1/c_3) \left(1 - \sqrt{1 + c_3^2}\right)$, see Subsection 3.8. As already inferred from numerical simulations (Sec. III.B), Ω does not depend on the diffusion D . Quantitatively, and as an example for $\mu = \sigma = 1$, we obtain the analytical prediction $\Omega \approx 0.14$, which differs by a factor ≈ 1.4 from the numerical value $\Omega^{\text{num}} \approx 0.103$ found in Fig. 7. As for the wavelength, this difference stems from the fact that the May-Leonard rate equations (4) predict heteroclinic orbits approaching the boundaries of the phase space, while the dynamics underlying the CGLE is characterized by limit cycles (usually distant from the edges of the phase space) resulting from a (supercritical) Hopf bifurcation.

3 Theory

In the following, we present and evaluate an analytical approach building on stochastic partial differential equations (SPDE) arisen in the proper continuum limit of large systems with mobile individuals. Applying the theory of invariant manifolds and normal forms to the nonlinear parts of these equations, we show that the SPDE fall into the universality class of a complex Ginzburg-Landau equation (CGLE). We derive the latter and employ it for a quantitative determination of properties of the spiral waves.

3.1 Rate equations

The deterministic rate equations (RE) describe the temporal evolution of the stochastic lattice system, defined by the reactions (1), in a mean-field manner, i.e. they neglect all spatial correlations. They may be seen as a deterministic description (for example emerging in the limit of large system sizes) of systems without spatial structure, such as Moran processes [46, 47, 48] or urn models [49, 50]. The study of the RE is the ground on which the analysis of the stochastic spatial system is built. In particular, the properties of the RE are extremely useful for the derivation of the system's SPDE (30) and CGLE (32).

Let a , b , c denote the densities of subpopulations A , B , and C , respectively. The overall density ρ then reads $\rho = a + b + c$. As every lattice site is at most occupied by one individual, the overall density (as well as densities of each subpopulation) varies between 0 and 1, i.e. $0 \leq \rho \leq 1$. With these notations, the RE for the reaction (1) are given by

$$\begin{aligned} \partial_t a &= a[\mu(1 - \rho) - \sigma c], \\ \partial_t b &= b[\mu(1 - \rho) - \sigma a], \end{aligned}$$

$$\partial_t c = c[\mu(1 - \rho) - \sigma b]. \quad (4)$$

They imply the following temporal evolution of the total density:

$$\partial_t \rho = \mu\rho(1 - \rho) - \sigma(ab + bc + ac). \quad (5)$$

These equations have been introduced and investigated by May and Leonard [44]. In the following, we review some of their properties.

Equations (4) possess four absorbing fixed points. One of these (unstable) is associated with the extinction of all subpopulations, $(a_1^*, b_1^*, c_1^*) = (0, 0, 0)$. The others are heteroclinic points (i.e. saddle points underlying the heteroclinic orbits) and correspond to the survival of only one subpopulation, $(a_2^*, b_2^*, c_2^*) = (1, 0, 0)$, $(a_3^*, b_3^*, c_3^*) = (0, 1, 0)$ and $(a_4^*, b_4^*, c_4^*) = (1, 0, 0)$, shown in blue (dark gray) in Fig. 2. In addition, there exists a fixed point, indicated in red (gray) in Fig. 2, where all three subpopulations coexist (at equal densities), namely $(a^*, b^*, c^*) = \frac{\mu}{3\mu + \sigma}(1, 1, 1)$. For a non-vanishing selection rate, $\sigma > 0$, May and Leonard [44] showed that the reactive fixed point is unstable, and the system asymptotically approaches the boundary of the phase space (given by the planes $a = 0$, $b = 0$, and $c = 0$). There, they observed *heteroclinic orbits*: the system oscillates between states where nearly only one subpopulation is present, with rapidly increasing cycle duration. While mathematically fascinating, this behavior was recognized to be unrealistic [44]. For instance, in a biological setting, the system will, due to finite-size fluctuations, always reach one of the absorbing fixed points in the vicinity of the heteroclinic orbit, and then only one population survives.

Linearization of the RE (4) around the reactive fixed point leads to $\partial_t \mathbf{x} = \mathcal{A}\mathbf{x}$ with the vector $\mathbf{x} = (a - a^*, b - b^*, c - c^*)^T$ and the Jacobian matrix

$$\mathcal{A} = -\frac{\mu}{3\mu + \sigma} \begin{pmatrix} \mu & \mu & \mu + \sigma \\ \mu + \sigma & \mu & \mu \\ \mu & \mu + \sigma & \mu \end{pmatrix}. \quad (6)$$

As this matrix is circulant, its eigenvalues can be obtained from a particularly simple general formula (see e.g. [20]); they read:

$$\begin{aligned} \lambda_0 &= -\mu, \\ \lambda_1 &= \frac{1}{2} \frac{\mu\sigma}{3\mu + \sigma} [1 + \sqrt{3}i], \\ \lambda_2 &= \frac{1}{2} \frac{\mu\sigma}{3\mu + \sigma} [1 - \sqrt{3}i]. \end{aligned} \quad (7)$$

This shows that the reactive fixed point is stable along the eigendirection of the first eigenvalue λ_0 . As elaborated below, there exists an invariant manifold [57] (including the reactive fixed point), that the system quickly approaches. To first order such a manifold is the plane normal to the eigendirection of λ_0 . On this invariant manifold, flows spiral away from the reactive fixed point, which is an unstable focus, as sketched in Fig. 2 (blue trajectory).

The linear stability analysis only reveals the local stability of the fixed points. The global instability of the reactive fixed point is proven by the existence of a Lyapunov function L [20, 44]:

$$L = \frac{abc}{\rho^3}. \quad (8)$$

In fact, using Eqs. (4) and (5), the time derivative of L is found to be always non-positive,

$$\partial_t L = -\frac{1}{2} \sigma \rho^{-4} abc [(a - b)^2 + (b - c)^2 + (c - a)^2] \leq 0. \quad (9)$$

We note that $\partial_t L$ vanishes only at the boundaries ($a = 0$, $b = 0$ or $c = 0$) and along the line of equal densities, $a = b = c$. The latter coincides with the eigendirection of λ_0 , along which the system approaches the reactive fixed point. However, on the invariant manifold we recover $\partial_t L < 0$, corresponding to a globally unstable reactive fixed point, as exemplified by the trajectory shown in Fig. 2.

As the RE (4) have one real eigenvalue smaller than zero and a pair of complex conjugate eigenvalues, they fall into the class of the Poincaré-Andronov-Hopf bifurcation, well known in the mathematical literature [57]. The theory of invariant and center manifolds allows us to recast these equations into a normal form. The latter will turn out to be extremely useful in the derivation of the CGLE. In the following, we derive the invariant manifold to second order as well as the normal form of the RE.

3.2 Invariant manifold

An invariant manifold is a subspace, embedded in the phase space, which is left invariant by the RE (4), i.e. by the deterministic dynamics. In the phase space, this means that flows starting on an invariant manifold always lie and evolve on it. Here, we consider a two-dimensional invariant manifold associated with the reactive fixed point of the RE (4) onto which all trajectories (initially away from the invariant manifold) decay exponentially quickly (see below). Upon restricting the dynamics to that appropriate invariant manifold, the system's degrees of freedom are reduced from three to two, which greatly simplifies the mathematical analysis.

To determine this invariant manifold, we notice that the eigenvector of the eigenvalue $\lambda_0 < 0$ at the reactive fixed point is a stable (attractive) direction. Therefore, to lowest order around the reactive fixed point, the invariant manifold is simply the plane normal to the eigendirection of λ_0 . As well known in the theory of dynamical systems, beyond first order, nonlinearities affect the invariant manifold, which is therefore only tangent to this plane. To include nonlinearities, it is useful to introduce suitable coordinates (y_A, y_B, y_C) originating in the reactive fixed point. We choose the y_C -axis to coincide with the eigenvector of λ_0 , such that the plane $y_C = 0$ is the invariant manifold to linear order, onto which the flows of (4) relax quickly. The coordinates y_A and y_B are chosen to span the plane normal to the axis y_C , forming an orthogonal set. Such coordinates $\mathbf{y} = (y_A, y_B, y_C)$ are, e.g., obtained by the linear

transformation $\mathbf{y} = \mathcal{S}\mathbf{x}$, with the matrix \mathcal{S} given by

$$\mathcal{S} = \frac{1}{3} \begin{pmatrix} \sqrt{3} & 0 & -\sqrt{3} \\ -1 & 2 & -1 \\ 1 & 1 & 1 \end{pmatrix}, \quad (10)$$

where $\mathbf{x} = (a - a^*, b - b^*, c - c^*)^T$ denotes the deviation of the densities from the reactive fixed point. The coordinates (y_A, y_B, y_C) are shown in Fig. 2 and their equations of motion are given in Appendix A.

The May-Leonard model is symmetric under cyclic permutations of A, B , and C . In the \mathbf{y} -coordinates, each of these permutations translates into a rotation of $2\pi/3$ around the y_C axis. The equations of motion reflect this symmetry of the system, as can be checked explicitly in the Eqs. (44) in Appendix A.

To parameterize the invariant manifold sketched in Fig. 2, we seek a function $G(y_A, y_B)$, with $y_C = G(y_A, y_B)$. If all nonlinearities of the RE are taken into account, this is a very complicated problem. However, for our purpose it is sufficient to expand G to second order in y_A, y_B . As the invariant manifold is left invariant by the RE, by definition, G must obey

$$\partial_t G(y_A(t), y_B(t)) = \frac{\partial G}{\partial y_A} \partial_t y_A + \frac{\partial G}{\partial y_B} \partial_t y_B = \partial_t y_C \Big|_{y_C=G}. \quad (11)$$

To linear order in y_A and y_B , we simply have $G = 0$ and recover $y_C = 0$, corresponding to the plane normal to the y_C -direction. We have anticipated this result above: to first order, the invariant manifold coincides with this plane, and is tangential to it when higher orders are included. To second order, only linear terms of $\partial_t y_A, \partial_t y_B$ contribute to Eq. (11). The latter are invariant under rotations in the (y_A, y_B) -plane, and G must obey the same symmetry. It is therefore proportional to $y_A^2 + y_B^2$. After some calculations, detailed in Appendix B, one obtains:

$$y_C = G(y_A, y_B) = \frac{\sigma}{4\mu} \frac{3\mu + \sigma}{3\mu + 2\sigma} (y_A^2 + y_B^2) + o(\mathbf{y}^2). \quad (12)$$

The comparison of this expression for the invariant manifold, valid to second order, with the numerical solutions of the RE (4) (which should, up to an initial transient, lie on the invariant manifold) confirms that (12) is an accurate approximation, with only minor deviations occurring near the boundaries of the phase space.

3.3 Normal form

Nonlinear systems are notably characterized by the bifurcations that they exhibit [57]. Normal forms are defined as the simplest differential equations that capture the essential features of a system near a bifurcation point, and therefore provide insight into the system's universal behavior. Here, we derive the normal form associated with the RE (4) of the May-Leonard model and show that they belong to the universality class of the Hopf bifurcation [57]. Below, we

demonstrate that this property allows to describe the system in terms of a well-defined complex Ginzburg-Landau equation.

Restricting the (deterministic) dynamics onto the invariant manifold, given by Eq. (12), the system's behavior can be analyzed in terms of two variables. Here, we choose to express y_C as function of y_A and y_B , with the resulting rate equations (up to cubic order) given in Appendix A. The latter can be cast into a normal form (see [57] Chapter 2.2) by performing a nonlinear variable transformation $\mathbf{y} \rightarrow \mathbf{z}$ which eliminates the quadratic terms and preserves the linear ones (i.e. to linear order \mathbf{y} and \mathbf{z} coincide). As an ansatz for such a transformation, we choose the most general quadratic expression in \mathbf{y} for the new variable \mathbf{z} . Details of the calculation can be found in Appendix C. Here we quote the result for the normal form of the RE in the new variables:

$$\begin{aligned} \partial_t z_A &= c_1 z_A + \omega z_B - c_2 (z_A + c_3 z_B) (z_A^2 + z_B^2) + o(\mathbf{z}^3), \\ \partial_t z_B &= c_1 z_B - \omega z_A - c_2 (z_B - c_3 z_A) (z_A^2 + z_B^2) + o(\mathbf{z}^3). \end{aligned} \quad (13)$$

In these equations,

$$\omega = \frac{\sqrt{3}}{2} \frac{\mu\sigma}{3\mu + \sigma}, \quad (14)$$

is the (linear) frequency of oscillations around the reactive fixed point. The constant

$$c_1 = \frac{1}{2} \frac{\mu\sigma}{3\mu + \sigma}, \quad (15)$$

gives the intensity of the linear drift away from the fixed point, while

$$c_2 = \frac{\sigma(3\mu + \sigma)(48\mu + 11\sigma)}{56\mu(3\mu + 2\sigma)}, \quad (16)$$

$$c_3 = \frac{\sqrt{3}(18\mu + 5\sigma)}{48\mu + 11\sigma}, \quad (17)$$

are the coefficients of the cubic corrections.

To gain some insight into the dynamics in the normal form, it is useful to rewrite (13) in polar coordinates (r, ϕ) , where $z_A = r \cos \phi, z_B = r \sin \phi$. This leads to

$$\begin{aligned} \partial_t r &= r[c_1 - c_2 r^2], \\ \partial_t \theta &= -\omega + c_2 c_3 r^2. \end{aligned} \quad (18)$$

These equations only have a radial dependence, which clearly reveals a polar symmetry. They predict the emergence of a limit cycle of radius $r = \sqrt{c_1/c_2}$ and therefore fall into the universality class of the (supercritical) Hopf bifurcation. However, when all nonlinearities are taken into account, the RE (4) give rise to heteroclinic orbits instead of limit cycles. The latter rapidly approach the boundaries of the phase space, and thus are in general well separated from the limit cycles predicted by (18). When comparing results

inferred from the CGLE and stochastic lattice simulations in the results section, we have shown how this causes some quantitative mismatch, stemming from the differences between the solutions of (4) and (18). However, we have also seen that most features of the system are actually aptly captured by the normal form (13). Elsewhere, it will be shown that mutations between subpopulations lead to limit cycles resulting from a Hopf bifurcation [56].

3.4 Spatial structure and the continuum limit

The system under consideration possesses spatial degrees of freedom, which are neither taken into account in the RE (4) nor in the normal form (13). Here, within a proper continuum limit, we show how spatial arrangements of mobile individuals may be included into the analytical description by supplementing the RE (4) with spatially dependent densities and diffusive terms (23). When one additionally accounts for stochastic effects (internal noise, see below), the system is aptly described by a set of stochastic partial differential equations (SPDE) (30).

The reactions (1) and the exchange processes take place on a d -dimensional hypercubic lattice (with periodic boundary conditions) of linear size L and comprising $N = L^d$ sites. The coordination number $z = 2d$ gives the number of nearest neighbors of each lattice site. We set the length of the lattice to unity, such that the distance between two nearest neighbors is $\delta r = N^{-1/d}$. The density of subpopulations A , B and C at time t and site $\mathbf{r} = (r_1, \dots, r_d)$ is denoted $a(\mathbf{r}, t)$, $b(\mathbf{r}, t)$, and $c(\mathbf{r}, t)$, respectively. According to the ‘‘bimolecular’’ reactions (1), the equations of motion of these quantities only involve neighbors located at $\mathbf{r} \pm \delta r \cdot \mathbf{e}_i$, where $\{\mathbf{e}_i\}_{i=1\dots d}$ is the basis of the lattice. Here, we first ignore all forms of correlation and fluctuations of the local density. While noise will be taken into account below, due to diffusion, correlations between neighboring sites vanish in the continuum limit of large systems (see below). We obtain the following equation for the time evolution of its mean (average) value $a(\mathbf{r}, t)$:

$$\begin{aligned} \partial_t a(\mathbf{r}, t) = & \frac{1}{z} \sum_{\pm, i=1}^d \left\{ 2\epsilon [a(\mathbf{r} \pm \delta r \cdot \mathbf{e}_i, t) - a(\mathbf{r}, t)] \right. \\ & + \mu a(\mathbf{r} \pm \delta r \cdot \mathbf{e}_i, t) [1 - a(\mathbf{r}, t) - b(\mathbf{r}, t) - c(\mathbf{r}, t)] \\ & \left. - \sigma c(\mathbf{r} \pm \delta r \cdot \mathbf{e}_i, t) a(\mathbf{r}, t) \right\}. \end{aligned} \quad (19)$$

For an analytical description of the lattice model, fruitful insights are gained by considering a continuum limit with $N \rightarrow \infty$. As the lattice size is kept fixed to 1, in this limit the distance δr between two neighboring sites approaches zero, i.e. $\delta r = N^{-1/d} \rightarrow 0$. This allows to treat \mathbf{r} as a continuous variable and the following expansion is justified:

$$\begin{aligned} a(\mathbf{r} \pm \delta r \cdot \mathbf{e}_i, t) = & a(\mathbf{r}, t) \pm \delta r \partial_i a(\mathbf{r}, t) \\ & + \frac{1}{2} \delta r^2 \partial_i^2 a(\mathbf{r}, t) + o(\delta r^2). \end{aligned} \quad (20)$$

With this expression, the first term on the right-hand-side (RHS) of Eq. (19) becomes (up to second order)

$$(2\epsilon/z) \sum_{\pm} [a(\mathbf{r} \pm \delta r \cdot \mathbf{e}_i, t) - a(\mathbf{r}, t)] = (\epsilon/d) \delta r^2 \partial_i^2 a(\mathbf{r}, t).$$

If we rescale the exchange rate ϵ with the system size N according to

$$\epsilon = DdN^{2/d}, \quad (21)$$

with a fixed (diffusion) constant D , we note that $\epsilon \delta r^2 = Dd$. For the other terms on RHS of Eq. (19), only the zeroth-order contributions in the expansion of $a(\mathbf{r} \pm \delta r \cdot \mathbf{e}_i, t)$ do not vanish when $N \rightarrow \infty$ (i.e. $\delta r \rightarrow 0$). In this continuum limit, Eq. (19) thus turns into

$$\partial_t a(\mathbf{r}, t) = D\Delta a(\mathbf{r}, t) + \mu a(\mathbf{r}, t) [1 - \rho(\mathbf{r}, t)] - \sigma a(\mathbf{r}, t) c(\mathbf{r}, t), \quad (22)$$

with the local density $\rho(\mathbf{r}, t) = a(\mathbf{r}, t) + b(\mathbf{r}, t) + c(\mathbf{r}, t)$. The equations of motion for $b(\mathbf{r}, t)$ and $c(\mathbf{r}, t)$ are obtained similarly. We therefore obtain the following set of partial differential equations (PDE):

$$\begin{aligned} \partial_t a(\mathbf{r}, t) = & D\Delta a(\mathbf{r}, t) + \mu a(\mathbf{r}, t) [1 - \rho(\mathbf{r}, t)] - \sigma a(\mathbf{r}, t) c(\mathbf{r}, t), \\ \partial_t b(\mathbf{r}, t) = & D\Delta b(\mathbf{r}, t) + \mu b(\mathbf{r}, t) [1 - \rho(\mathbf{r}, t)] - \sigma b(\mathbf{r}, t) a(\mathbf{r}, t), \\ \partial_t c(\mathbf{r}, t) = & D\Delta c(\mathbf{r}, t) + \mu c(\mathbf{r}, t) [1 - \rho(\mathbf{r}, t)] - \sigma b(\mathbf{r}, t) c(\mathbf{r}, t). \end{aligned} \quad (23)$$

The difference to the rate equations (4) lies in the spatial dependence through diffusive terms, proportional to the diffusion constant D .

3.5 Noise

The discrete character of the individuals involved in the May-Leonard reactions (1) and the exchange processes are responsible for intrinsic stochasticity arising in the system. For the treatment of this internal noise, we note a time-scale separation between the reactions (1) and the exchange events. Namely, in the continuum limit $N \rightarrow \infty$, according to (2) one has $\epsilon \rightarrow \infty$. This means that exchanges occur on a much faster time-scale than the reactions (1). Consequently, a large number of exchange events occurs between two reactions and can be treated deterministically. As shown below, the fluctuations associated with the exchange processes vanish as $1/N$ (for $N \rightarrow \infty$), while those stemming from (1) scale as $1/\sqrt{N}$. The latter are therefore the dominating source of noise, while the former can be neglected in the continuum limit. To establish these results, we consider the limit of large systems ($N \rightarrow \infty$) where a stochastic description in terms of Fokker-Planck equations is generally appropriate [58, 59]. The latter can be obtained from Kramers-Moyal expansion (i.e. a system-size expansion) of the underlying master equation [60], see Appendix D. In Fokker-Planck equations, fluctuations are encoded in a noise matrix denoted \mathcal{B} . Equivalently, a set of Ito stochastic (partial) differential equations (often referred to as Langevin

equations) can be systematically derived. For these SPDE, the noise, often white, is encoded in the “square root” of the matrix \mathcal{B} . Namely, in this framework, the strength of fluctuations and the correlations are given by a matrix \mathcal{C} , defined as $\mathcal{C}\mathcal{C}^T = \mathcal{B}$. Below, we derive the relevant contributions to the noise matrices \mathcal{B} and \mathcal{C} , which leads to the appropriate stochastic partial differential equations (SPDE) of the system.

Following [59] (Chapter 8.5), we first show that fluctuations stemming from pair exchanges scale as $1/N$. Consider two nearest neighboring lattice sites \mathbf{r} and \mathbf{r}' . The rate for an individual A to hop from \mathbf{r} to \mathbf{r}' is given by $\epsilon z^{-1}a(\mathbf{r})[1 - a(\mathbf{r}')]$ (for simplicity, we drop the time-dependence). Together with the reverse process, i.e. hopping from site \mathbf{r}' to \mathbf{r} , this yields the non-diagonal part of $\mathcal{B}(\mathbf{r}, \mathbf{r}')$ (see e.g. [60]):

$$\mathcal{B}(\mathbf{r}, \mathbf{r}' \neq \mathbf{r}) = -\frac{\epsilon}{Nz} \{a(\mathbf{r})[1 - a(\mathbf{r}')] + a(\mathbf{r}')[1 - a(\mathbf{r})]\}. \quad (24)$$

Similarly, the diagonal entries of \mathcal{B} read

$$\mathcal{B}(\mathbf{r}, \mathbf{r}) = \frac{\epsilon}{Nz} \sum_{\text{n.n.}\mathbf{r}''} \{a(\mathbf{r})[1 - a(\mathbf{r}'')] + a(\mathbf{r}'')[1 - a(\mathbf{r})]\}, \quad (25)$$

where the sum runs over all nearest neighbors (n.n.) \mathbf{r}'' of the site \mathbf{r} . It follows from these expressions that

$$\begin{aligned} \mathcal{B}(\mathbf{r}, \mathbf{r}') &= \frac{\epsilon}{Nz} \sum_{\text{n.n.}\mathbf{r}''} (\delta_{\mathbf{r}, \mathbf{r}'} - \delta_{\mathbf{r}', \mathbf{r}''}) \\ &\times \{a(\mathbf{r})[1 - a(\mathbf{r}'')] + a(\mathbf{r}'')[1 - a(\mathbf{r})]\}. \end{aligned} \quad (26)$$

In the continuum limit, with $\delta r \rightarrow 0$, we use the fact that $\delta_{\mathbf{r}, \mathbf{r}'} \rightarrow \delta r^d \delta(\mathbf{r} - \mathbf{r}')$ and obtain

$$\begin{aligned} \mathcal{B}(\mathbf{r}, \mathbf{r}') &= \frac{\epsilon}{Nz} \delta r^d \sum_{\pm, i=1}^d [\delta(\mathbf{r} - \mathbf{r}') - \delta(\mathbf{r} \pm \delta r \mathbf{e}_i - \mathbf{r}')] \\ &\times \{a(\mathbf{r})[1 - a(\mathbf{r} \pm \delta r \mathbf{e}_i)] + a(\mathbf{r} \pm \delta r \mathbf{e}_i)[1 - a(\mathbf{r})]\}. \end{aligned} \quad (27)$$

As in Eq. (20), we expand $\delta(\mathbf{r} \pm \delta r \mathbf{e}_i - \mathbf{r}')$ and $a(\mathbf{r} \pm \delta r \mathbf{e}_i)$ to second order and observe that only quadratic terms in δr do not cancel. With $\epsilon = DdN^{2/d}$ and $\delta r = N^{-1/d}$, we thus find:

$$\mathcal{B}(\mathbf{r}, \mathbf{r}') = \frac{D}{N^2} \partial_{\mathbf{r}} \partial_{\mathbf{r}'} [\delta(\mathbf{r} - \mathbf{r}') a(\mathbf{r})(1 - a(\mathbf{r}))]. \quad (28)$$

The noise matrix \mathcal{B} of the Fokker-Planck equation associated with the exchange processes therefore scales as N^{-2} . In the corresponding SPDE, the contribution to noise of the exchange processes scales like N^{-1} .

We now consider the fluctuations stemming from May-Leonard reactions (1). A detailed discussion of the treatment of fluctuations arising from discrete reactions in lattice systems can be found in Chapter 8 of Ref. [59]. Following the derivation therein, one recovers noise terms of the same

form as in the corresponding non-spatial model, although the densities now have spatial dependencies. Thus, they may be found via a straightforward Kramers-Moyal expansion of the master equation describing the well-mixed system, see e.g. [47, 48, 50]. Here, we report the results and relegate details of the derivation to Appendix D. As the reactions (1) decouple birth from death processes, the noise matrices \mathcal{B} and \mathcal{C} are diagonal. In particular, the diagonal parts of \mathcal{C} read

$$\begin{aligned} \mathcal{C}_A &= \frac{1}{\sqrt{N}} \sqrt{a(\mathbf{r}, t) [\mu(1 - \rho(\mathbf{r}, t)) + \sigma c(\mathbf{r}, t)]}, \\ \mathcal{C}_B &= \frac{1}{\sqrt{N}} \sqrt{b(\mathbf{r}, t) [\mu(1 - \rho(\mathbf{r}, t)) + \sigma a(\mathbf{r}, t)]}, \\ \mathcal{C}_C &= \frac{1}{\sqrt{N}} \sqrt{c(\mathbf{r}, t) [\mu(1 - \rho(\mathbf{r}, t)) + \sigma b(\mathbf{r}, t)]}. \end{aligned} \quad (29)$$

The SPDE for the densities $a(\mathbf{r}, t), b(\mathbf{r}, t), c(\mathbf{r}, t)$ are thus given by the partial differential equations (23) supplemented by the corresponding noise terms, which leads to:

$$\begin{aligned} \partial_t a(\mathbf{r}, t) &= D\Delta a(\mathbf{r}, t) + \mu a(\mathbf{r}, t)[1 - \rho(\mathbf{r}, t)] \\ &\quad - \sigma a(\mathbf{r}, t)c(\mathbf{r}, t) + \mathcal{C}_A \xi_A, \\ \partial_t b(\mathbf{r}, t) &= D\Delta b(\mathbf{r}, t) + \mu b(\mathbf{r}, t)[1 - \rho(\mathbf{r}, t)] \\ &\quad - \sigma b(\mathbf{r}, t)a(\mathbf{r}, t) + \mathcal{C}_B \xi_B, \\ \partial_t c(\mathbf{r}, t) &= D\Delta c(\mathbf{r}, t) + \mu c(\mathbf{r}, t)[1 - \rho(\mathbf{r}, t)] \\ &\quad - \sigma b(\mathbf{r}, t)c(\mathbf{r}, t) + \mathcal{C}_C \xi_C, \end{aligned} \quad (30)$$

where Δ denotes the Laplacian operator, and the Gaussian white noise terms $\xi_i(\mathbf{r}, t)$ have a spatio-temporal dependence, with the correlations

$$\langle \xi_i(\mathbf{r}, t) \xi_j(\mathbf{r}', t') \rangle = \delta_{ij} \delta(\mathbf{r} - \mathbf{r}') \delta(t - t'). \quad (31)$$

3.6 Complex Ginzburg-Landau Equation (CGLE)

The reaction terms appearing in the SPDE (30) coincide with those of the rate equations (4). Above, we have recast the latter in the normal form (13). Applying the same transformations to the SPDE (30) yields reaction terms as in (13). However, owed to the nonlinearity of the transformation, additional nonlinear diffusive terms appear in the spatially-extended version of (13). In the following, the latter will be ignored. Furthermore, when discussing the spatio-temporal properties of the system, we have encountered rotating spiral waves, whose velocity, wavelength and frequency have turned out to be unaffected by noise (in the continuum limit). An important consequence of this finding is that it is not necessary to take noise into account to compute such quantities. This greatly simplifies the problem and, omitting any noise contributions, we focus on two coupled partial differential equations which are conveniently rewritten as a complex PDE in terms of the complex variable $z = z_A + iz_B$ (see Appendix C):

$$\begin{aligned} \partial_t z(\mathbf{r}, t) &= D\Delta z(\mathbf{r}, t) + (c_1 - i\omega)z(\mathbf{r}, t) \\ &\quad - c_2(1 - ic_3)|z(\mathbf{r}, t)|^2 z(\mathbf{r}, t). \end{aligned} \quad (32)$$

Here, we recognize the celebrated complex Ginzburg-Landau equation (CGLE), whose properties have been extensively studied [61, 62]. In particular, it is known that in two dimensions the latter gives rise to a broad range of coherent structures, including spiral waves whose velocity, wavelength and frequency can be computed analytically.

For the system under consideration, we can check that the CGLE (32) predicts the emergence of spiral waves which are stable against frequency modulation: no Benjamin-Feir or Eckhaus instabilities occur. As a consequence, one expects no intermittencies or spatio-temporal chaos, but only rotating spirals [62]. In our discussion, we have verified the validity of this prediction for various sets of the parameters, both for stochastic lattice simulations and for the solutions of the SPDE (30).

In the following, we describe how characteristic properties of the spiral waves, such as the spreading velocity, the selected frequency and wavelength can be inferred from the above CGLE (32).

3.7 The linear spreading velocity

We have found [see, e.g., snapshots (Fig. 5)] that in the long-time regime the system exhibits traveling waves. Namely, in the steady state, regions with nearly only A individuals are invaded by a front of C individuals, which is taken over by B in turn, and so on. The theory of front propagation into unstable states (see, e.g., [63] and references therein) is useful to study analytically the related dynamics. Indeed, to determine the spreading velocity of the propagating fronts one linearizes the CGLE (32) around the coexistence state $z = 0$ [i.e. the reactive fixed point of (4)], which yields

$$\partial_t z(\mathbf{r}, t) = D\Delta z(\mathbf{r}, t) + (c_1 - i\omega)z(\mathbf{r}, t) + o(z^2). \quad (33)$$

It is then useful to perform a Fourier transformation:

$$\tilde{z}(\mathbf{k}, \Omega) = \int_{-\infty}^{\infty} d\mathbf{r} dt z(\mathbf{r}, t) e^{-i\mathbf{k}\mathbf{r} - i\Omega t}, \quad (34)$$

which, together with (33), gives the following dispersion relation:

$$\Omega(k) = \omega + i(c_1 - Dk^2), \quad (35)$$

where $k = |\mathbf{k}|$. As $\text{Im}\Omega(k) > 0$ for $k^2 < c_1/D$, the state $z = 0$ is linearly unstable in this range of wavevectors k . This confirms the analysis of the spatially homogeneous RE (4), where we already found that the coexistence fixed point is unstable. As for other systems characterized by fronts propagating into unstable states [63], from Eq. (33) one can now compute the linear spreading velocity, i.e. the speed v^* at which fronts (e.g. generated by local perturbations around $z = 0$) propagate. Following a classic treatment, whose general derivation can, e.g., be found in [63], the spreading velocity is obtained by determining a wavevector k_* according to

$$\left. \frac{d\Omega(k)}{dk} \right|_{k_*} = \frac{\text{Im}\Omega(k_*)}{\text{Im}k_*} \equiv v^*. \quad (36)$$

The first equality singles out k_* and the second defines the linear spreading velocity v^* . Here, we find:

$$\text{Re}k_* = 0, \quad \text{Im}k_* = \sqrt{c_1/D}, \quad v^* = 2\sqrt{c_1 D}. \quad (37)$$

The comparison of this analytical prediction with numerical results has revealed a good agreement, as illustrated in Fig. 9 and discussed in the corresponding previous section.

3.8 Wavelength and frequency

To determine analytically the wavelength λ and the frequency Ω of the spiral waves, the (cubic) nonlinear terms of the CGLE (32) have to be taken into account. From the understanding gained in the previous sections, we make a traveling-wave ansatz $z(\mathbf{r}, t) = Ze^{-i\Omega t - i\mathbf{q}\cdot\mathbf{r}}$ leading to the following dispersion relation

$$\Omega(\mathbf{q}) = \omega + i(c_1 - Dq^2) - c_2(i + c_3)Z^2. \quad (38)$$

Separating real and imaginary parts, we can solve for Z , resulting in $Z^2 = (c_1 - Dq^2)/c_2$. As already found above, the range of wavevectors that yield traveling wave solutions is therefore given by $q \equiv |\mathbf{q}| < \sqrt{c_1/D}$. The dispersion relation can, upon eliminating Z , be rewritten as

$$\Omega(q) = \omega + c_3(Dq^2 - c_1). \quad (39)$$

As manifests on the RHS of (39), Ω comprises two contributions. On the one hand there is ω , acting as a “background frequency”, which stems from the nonlinear nature of the dynamics and is already accounted by (4) when the system is spatially homogeneous. On the other hand, the second contribution on the RHS of (39) is due to the spatially-extended character of the model and to the fact that traveling fronts propagate with velocity v^* , therefore generating oscillations with a frequency of v^*q . Both contributions superpose and, to sustain a velocity v^* , the dynamics selects a wavenumber q^{sel} according to the relation $\Omega(q^{\text{sel}}) = \omega + v^*q^{\text{sel}}$ [63]. Solving this equation for q^{sel} under the restriction $q^{\text{sel}} < \sqrt{c_1/D}$ yields

$$q^{\text{sel}} = \frac{\sqrt{c_1}}{c_3\sqrt{D}} \left(1 - \sqrt{1 + c_3^2} \right). \quad (40)$$

Analytical expressions of the frequency $\Omega(q^{\text{sel}})$ and of the wavelength of the spirals, $\lambda = 2\pi/q^{\text{sel}}$, can be obtained immediately from (39) and (40). In fact, the frequency reads

$$\Omega = \Omega(q^{\text{sel}}) = \omega + \frac{2c_1}{c_3} \left(1 - \sqrt{1 + c_3^2} \right), \quad (41)$$

and the wavelength is given by

$$\lambda = \frac{2\pi c_3 \sqrt{D}}{\sqrt{c_1} (1 - \sqrt{1 + c_3^2})}. \quad (42)$$

These expressions have been derived by considering a traveling wave ansatz as described above. The latter hold in arbitrary dimensions. However, while traveling waves

appear in one dimensions, in higher dimensions, the generic emerging structures are somewhat different. E.g. rotating spirals arise in two dimensions, as described in this article, while scroll waves are robust solutions of the CGLE (32) in three spatial dimensions [62]. However, the characteristic properties of these patterns, such as wavelength and frequency, still agree with those of traveling waves. Indeed, concerning the dynamical system investigated in this article, we have shown how the self-forming spirals are well characterized by the expressions (41) and (42). The same system studied in three dimensions is therefore expected to exhibit an entanglement of scroll waves, whose wavelengths and frequencies are again given by Eqs. (41) and (42).

4 Discussion

Individuals' mobility as well as intrinsic noise have crucial influence on the self-formation of spatial patterns. We have quantified their influence by investigating a stochastic spatial model of mobile individuals experiencing cyclic dominance via interactions of 'rock-paper-scissors' type. We have demonstrated that individuals' mobility has drastic effects on the emergence of spatio-temporal patterns. Low exchange rate between neighboring individuals leads to the formation of small and irregular patterns. In this case coexistence of all subpopulations is preserved and the ensuing patterns are mainly determined by stochastic effects. On the other hand, in two dimensions, larger exchange rates (yet of same order as the reaction rates) yield the formation of (relatively) regular spiral waves whose rotational nature is reminiscent of the cyclic and out-of-equilibrium ensuing kinetics. In fact, the three subpopulations endlessly, and in turn, hunt each other. The location and density of the spirals' vortices is either determined by initial spatial inhomogeneities, if these are large enough, or by stochasticity. In the latter case, internal noise leads to an entanglement of many small spirals and a universal vortex density of about 0.5 per square wavelength. Increasing the diffusion rate (i.e. individuals' mobility), the typical size of the spiral waves rises, up to a critical value. When that threshold is reached, the spiral patterns outgrow the two-dimensional system and there is only one surviving subpopulation covering uniformly the system [17].

The language of interacting particles enabled us to devise a proper treatment of the stochastic spatially-extended system and to reach a comprehensive understanding of the resulting out-of-equilibrium and nonlinear phenomena. In particular, we have shown how spatio-temporal properties of the system can be aptly described in terms of stochastic partial differential equations (SPDE) and confirmed our findings with lattice simulations. We have paid special attention to analyze the wavelength and frequency of the spiral waves, as well as the velocity of the propagating fronts. Numerical solutions of the SPDE have been shown to share (statistically) the same steady states as the lattice simulations, with the emerging spiral waves having in both cases

the same wavelength, overall sizes and frequency. We have also studied the influence of stochasticity on the properties of the coexistence state and its spatio-temporal structure. Namely, we have compared the results obtained from the SPDE with those of the deterministic PDE (obtained by dropping the noise contributions in the SPDE), which still yield spiralling structures. This allowed us to shed light on the fact that, in the presence of (sufficient) mobility, the wavelength and frequency of the spirals are not affected by internal noise. However, there are major differences between the stochastic and deterministic descriptions of the system. One of the most important is the influence of the initial conditions. On the one hand, if initial spatial inhomogeneities are larger than the noise level, or if noise is absent as in the deterministic descriptions, these initial spatial structures determine the position of the spirals' vortices. In this situation, the system "memorizes" its initial state, and the latter crucially influences the overall size of the emerging spiral waves. On the other hand, for rather homogeneous initial densities (at values of the unstable reactive fixed point), the patterns emerging from the stochastic descriptions (lattice simulations and SPDE) are caused by noise and characterized by a universal density of 0.5 spiral vortices per square wavelength. While we have provided qualitative explanations of these findings, a profound understanding is still desirable and could motivate further investigations.

We have also shown that analytical expressions for the spirals' wavelength and frequency can be determined by means of a complex Ginzburg-Landau equation (CGLE) obtained by recasting the PDE of the system, restricted onto an invariant manifold, in a normal form. There is good agreement between analytical predictions stemming from the system's CGLE and numerical results (obtained from stochastic lattice simulations as well as the numerical solution of the SPDE). This can be traced back to the fact that May-Leonard rate equations are characterized by heteroclinic orbits very much reminiscent of limit cycles resulting from a Hopf bifurcation. The fact that the dynamics can be recast in the form of a CGLE, known to give rise to the emergence of coherent structures, reveals the generality of the phenomena discussed in this work and greatly facilitates their quantitative analysis. In particular, the emergence of an entanglement of spiral waves in the coexistence state, the dependence of spirals' size on the diffusion rate, and the existence of a critical value of the diffusion above which coexistence is lost are robust phenomena. This means that they do not depend on the details of the underlying spatial structure: While, for specificity, we have (mostly) considered square lattices, other two-dimensional topologies (e.g. hexagonal or other lattices) will lead to the same phenomena, too. Also the details of the cyclic competition have no qualitative influence, as long as the underlying rate equations exhibit an unstable coexistence fixed point and can be recast in the universality class of Hopf bifurcations. We still note that instead of defining the model in terms of chemical reactions, as done here (1), we can equivalently choose a

formulation in terms of payoff matrices [19, 20].

We have investigated the system's behavior in two spatial dimensions. However, our approach, using a continuum limit to derive the SPDE (30) as well as the CGLE (32), is equally valid in other dimensions and expected to describe the formation of spatial patterns, as long as the mobility is below a certain threshold value [17]. As examples, in one dimension, the CGLE yields traveling waves, while "scroll waves", i.e. vortex filaments, result in three dimensions [62].

In this article, we have mainly focused on the situation where the exchange rate between individuals is sufficiently high, which leads to the emergence of regular spirals in two dimensions. However, when the exchange rate is low (or vanishes), we have seen that stochasticity strongly affects the structure of the ensuing spatial patterns. In this case, the (continuum) description in terms of SPDE breaks down. In this situation, the quantitative analysis of the spatio-temporal properties of interacting particle systems requires the development of other analytical methods, e.g. relying on field theoretic techniques [43]. Investigations along these lines represent a major future challenge in the multidisciplinary field of complexity science.

Acknowledgments

Financial support of the German Excellence Initiative via the program "Nanosystems Initiative Munich" and the German Research Foundation via the SFB TR12 "Symmetries and Universalities in Mesoscopic Systems" is gratefully acknowledged. M. M. is grateful to the Alexander von Humboldt Foundation and to the Swiss National Science Foundation for support through the grants IV-SCZ/1119205 and PA002-119487, respectively.

Appendix A. Equations for the y -variables

In this Appendix, as well as the two following, some further details on the derivation of the normal form (13) of the May-Leonard RE (4) are given. Namely, we derive the time evolution of the y -variables introduced in Subsection 3.2, and use the invariant manifold to eliminate the stable degree of freedom. The derivation of the invariant manifold is presented in the next section, while the transformation from y - to z -variables yielding the normal form is detailed in a third appendix.

In Subsection 3.2, we have introduced proper coordinates (y_A, y_B, y_C) by $\mathbf{y} = \mathcal{S}\mathbf{x}$ with the matrix \mathcal{S} given by

$$\mathcal{S} = \frac{1}{3} \begin{pmatrix} \sqrt{3} & 0 & -\sqrt{3} \\ -1 & 2 & -1 \\ 1 & 1 & 1 \end{pmatrix}. \quad (43)$$

Hereby, the vector $\mathbf{x} = (a - a^*, b - b^*, c - c^*)^T$ encodes the deviation of the densities from the reactive fixed point. Of

course, the time evolution of \mathbf{x} is just given by the time evolution of the densities, Eqs. (4): $\partial_t \mathbf{x} = (\partial_t a, \partial_t b, \partial_t c)^T$. For the temporal evolution of the \mathbf{y} -variables, we have to apply the transformation given by \mathcal{S} : $\partial_t \mathbf{y} = \mathcal{S} \partial_t \mathbf{x}$. Expressing them in terms of \mathbf{y} -variables, we eventually obtain

$$\begin{aligned} \partial_t y_A &= \frac{\mu\sigma}{2(3\mu + \sigma)} [y_A + \sqrt{3}y_B] + \frac{\sqrt{3}}{4}\sigma [y_A^2 - y_B^2] \\ &\quad - \frac{\sigma}{2}y_A y_B - \frac{1}{2}y_C [(6\mu + \sigma)y_A - \sqrt{3}\sigma y_B], \\ \partial_t y_B &= \frac{\mu\sigma}{2(3\mu + \sigma)} [y_B - \sqrt{3}y_A] - \frac{\sigma}{4}[y_A^2 - y_B^2] \\ &\quad - \frac{\sqrt{3}}{2}\sigma y_A y_B - \frac{1}{2}y_C [\sqrt{3}\sigma y_A + (6\mu + \sigma)y_B], \\ \partial_t y_C &= -\mu y_C - (3\mu + \sigma)y_C^2 + \frac{\sigma}{4}[y_A^2 + y_B^2]. \end{aligned} \quad (44)$$

Using the invariant manifold, Eq. (12), we eliminate y_C from the above and are left with equations for y_A, y_B alone. According to Eq. (12) y_C has been determined to second order in y_A, y_B , and as y_C contributes to the time-evolution of y_A, y_B through quadratic terms, we obtain $\partial_t y_A, \partial_t y_B$ up to third order:

$$\begin{aligned} \partial_t y_A &= \frac{\mu\sigma}{2(3\mu + \sigma)} [y_A + \sqrt{3}y_B] + \frac{\sqrt{3}}{4}\sigma [y_A^2 - y_B^2] - \frac{\sigma}{2}y_A y_B \\ &\quad - \frac{\sigma(3\mu + \sigma)}{8\mu(3\mu + 2\sigma)} (y_A^2 + y_B^2) [(6\mu + \sigma)y_A - \sqrt{3}\sigma y_B] + o(y^3), \\ \partial_t y_B &= \frac{\mu\sigma}{2(3\mu + \sigma)} [y_B - \sqrt{3}y_A] - \frac{\sigma}{4}[y_A^2 - y_B^2] - \frac{\sqrt{3}}{2}\sigma y_A y_B \\ &\quad - \frac{\sigma(3\mu + \sigma)}{8\mu(3\mu + 2\sigma)} (y_A^2 + y_B^2) [\sqrt{3}\sigma y_A + (6\mu + \sigma)y_B] + o(y^3). \end{aligned} \quad (45)$$

These equations describe the system's temporal evolution on the invariant manifold.

Appendix B. The invariant manifold

We provide further details concerning the derivation (to second order) of the invariant manifold of the RE (4) given by Eq. (12).

To determine the invariant manifold parametrized by $y_C = G(y_A, y_B)$ up to second order in y_A, y_B , we make the ansatz $G(y_A, y_B) = K(y_A^2 + y_B^2) + o(y^2)$, and calculate K . The condition (11) turns into

$$2Ky_A \partial_t y_A + 2Ky_B \partial_t y_B = \partial_t y_C \Big|_{y_C=G}. \quad (46)$$

Using Eqs. (44), we obtain (to second order in y_A, y_B)

$$K \frac{\mu\sigma}{3\mu + \sigma} (y_A^2 + y_B^2) = \left(-\mu K + \frac{\sigma}{4} \right) (y_A^2 + y_B^2), \quad (47)$$

which is satisfied for

$$K = \frac{\sigma}{4\mu} \frac{3\mu + \sigma}{3\mu + 2\sigma}. \quad (48)$$

Appendix C. Normal Form: the nonlinear transformation $\mathbf{y} \rightarrow \mathbf{z}$

The normal form (13) of the May-Leonard RE (4) follows from the time-evolution equations in the y -variables, given by (45), through an additional nonlinear variable transformation. Here, we present the latter.

The equations of motion (45) comprise quadratic and cubic terms. To recast Eqs. (45) in their normal form, we seek a transformation allowing to eliminate the quadratic terms. We make the ansatz of a quadratic transformation $\mathbf{y} \rightarrow \mathbf{z}$ and determine the coefficients by cancelling the quadratic contributions to the RE in the \mathbf{z} variables, this leads to

$$\begin{aligned} z_A &= y_A + \frac{3\mu + \sigma}{28\mu} [\sqrt{3}y_A^2 + 10y_A y_B - \sqrt{3}y_B^2], \\ z_B &= y_B + \frac{3\mu + \sigma}{28\mu} [5y_A^2 - 2\sqrt{3}y_A y_B - 5y_B^2]. \end{aligned} \quad (49)$$

To second order, this nonlinear transformation can be inverted:

$$\begin{aligned} y_A &= z_A - \frac{3\mu + \sigma}{28\mu} [\sqrt{3}z_A^2 + 10z_A z_B - \sqrt{3}z_B^2] \\ &\quad + \frac{(3\mu + \sigma)^2}{14\mu^2} [z_A^3 + z_A z_B^2] + o(z^3), \\ y_B &= z_B - \frac{3\mu + \sigma}{28\mu} [5z_A^2 - 2\sqrt{3}z_A z_B - 5z_B^2] \\ &\quad + \frac{(3\mu + \sigma)^2}{14\mu^2} [z_A^2 z_B + z_B^3] + o(z^3). \end{aligned} \quad (50)$$

With these expressions, one can check that equations of motion (45) are recast in the normal form (13).

Appendix D. Kramers-Moyal expansion of the master equation

For a large number N of interacting individuals, the master equation describing the stochastic system may be expanded in the system size N , often referred to as Kramers-Moyal expansion [58, 59, 60]. As a result, one obtains a Fokker-Planck equation which is equivalent to a set of Ito stochastic differential equations (with white noise). In Subsection 3.5, we have shown that for the present stochastic spatial system, only noise terms stemming from the reactions (1) contribute. The latter may be derived considering the stochastic non-spatial system. Here, we follow this approach. Starting from the master equation for the stochastic well-mixed system, we detail the system size expansion, and derive the Fokker-Planck equation as well as the corresponding Ito stochastic differential equations.

Denote $\mathbf{s} = (a, b, c)$ the frequencies of the three subpopulations A , B , and C . The Master equation for the time-evolution of the probability $P(\mathbf{s}, t)$ of finding the system in

state \mathbf{s} at time t reads

$$\begin{aligned} \partial_t P(\mathbf{s}, t) &= \sum_{\delta\mathbf{s}} \{ P(\mathbf{s} + \delta\mathbf{s}, t) \mathcal{W}(\mathbf{s} + \delta\mathbf{s} \rightarrow \mathbf{s}) \\ &\quad - P(\mathbf{s}, t) \mathcal{W}(\mathbf{s} \rightarrow \mathbf{s} + \delta\mathbf{s}) \}. \end{aligned} \quad (51)$$

Hereby, $\mathcal{W}(\mathbf{s} \rightarrow \mathbf{s} + \delta\mathbf{s})$ denotes the transition probability from state \mathbf{s} to the state $\mathbf{s} + \delta\mathbf{s}$ within one time step; summation extends over all possible changes $\delta\mathbf{s}$. The relevant changes $\delta\mathbf{s}$ in the densities result from the basic reactions (1); as an example, concerning the change in the density of the subpopulation A , it reads $\delta s_A = 1/N$ in the reaction $A\emptyset \xrightarrow{\mu} AA$, $\delta s_A = -1/N$ in the reaction $CA \xrightarrow{\sigma} C\emptyset$, and zero in the remaining ones. Concerning the rates for these reactions, we choose the unit of time such that, on average, every individual reacts once per time step. The transition rates resulting from the reactions (1) then read $\mathcal{W} = N\sigma ac$ for the reaction $CA \xrightarrow{\sigma} C\emptyset$ and $\mathcal{W} = N\mu a(1 - a - b - c)$ for $A\emptyset \xrightarrow{\mu} AA$. Transition probabilities associated with all other reactions (1) follow analogously.

The Kramers-Moyal expansion [60] of the Master equation is an expansion in the increment $\delta\mathbf{s}$, which is proportional to N^{-1} . Therefore, it may be understood as an expansion in the inverse system size N^{-1} . To second order in $\delta\mathbf{s}$, it yields the (generic) Fokker-Planck equation [60]:

$$\partial_t P(\mathbf{s}, t) = -\partial_i [\alpha_i(\mathbf{s}) P(\mathbf{s}, t)] + \frac{1}{2} \partial_i \partial_j [\mathcal{B}_{ij}(\mathbf{s}) P(\mathbf{s}, t)]. \quad (52)$$

Hereby, the summation convention implies sums carried over the indices $i, j \in \{A, B, C\}$. According to the Kramers-Moyal expansion, the quantities α_i and \mathcal{B}_{ij} read [60]

$$\begin{aligned} \alpha_i(\mathbf{s}) &= \sum_{\delta\mathbf{s}} \delta s_i \mathcal{W}(\mathbf{s} \rightarrow \mathbf{s} + \delta\mathbf{s}), \\ \mathcal{B}_{ij}(\mathbf{s}) &= \sum_{\delta\mathbf{s}} \delta s_i \delta s_j \mathcal{W}(\mathbf{s} \rightarrow \mathbf{s} + \delta\mathbf{s}). \end{aligned} \quad (53)$$

Note that \mathcal{B} is symmetric. As an example, we now present the calculation of $\alpha_A(\mathbf{s})$. The relevant changes $\delta s_A = \delta a$ result from the reactions $A\emptyset \xrightarrow{\mu} AA$ and $CA \xrightarrow{\sigma} C\emptyset$. The corresponding rates as well as the changes in the density of subpopulation A have been given above; together, we obtain $\alpha_A(\mathbf{s}) = \mu a(1 - a - b - c) - \sigma ac$. The other quantities are computed analogously; eventually, one finds

$$\begin{aligned} \alpha_A(\mathbf{s}) &= \mu a(1 - a - b - c) - \sigma ac, \\ \alpha_B(\mathbf{s}) &= \mu b(1 - a - b - c) - \sigma ab, \\ \alpha_C(\mathbf{s}) &= \mu c(1 - a - b - c) - \sigma bc, \end{aligned} \quad (54)$$

and

$$\begin{aligned} \mathcal{B}_{AA}(\mathbf{s}) &= N^{-1} [\mu a(1 - a - b - c) + \sigma ac], \\ \mathcal{B}_{BB}(\mathbf{s}) &= N^{-1} [\mu b(1 - a - b - c) + \sigma ab], \\ \mathcal{B}_{CC}(\mathbf{s}) &= N^{-1} [\mu c(1 - a - b - c) + \sigma bc]. \end{aligned} \quad (55)$$

The well-known correspondence between Fokker-Planck equations and Ito calculus [59] implies that (52) is equivalent to the following set of Ito stochastic differential equations:

$$\begin{aligned}\partial_t a &= \alpha_A + C_{AA}\xi_A, \\ \partial_t b &= \alpha_B + C_{BB}\xi_B, \\ \partial_t c &= \alpha_C + C_{CC}\xi_C.\end{aligned}\tag{56}$$

Hereby, the ξ_i denotes (uncorrelated) Gaussian white noise terms. The matrix C is defined from B via the relation $CC^T = B$ [59]. As B is diagonal, we may choose C diagonal as well, with the square roots of the corresponding diagonal entries of B on the diagonal. We obtain the expressions (29).

References

- [1] R. M. May. *Stability and Complexity in Model Ecosystems*. Cambridge University Press, 1974.
- [2] J. D. Murray. *Mathematical Biology*. Springer Verlag, third edition, 2002.
- [3] A. M. Turing. The chemical basis of morphogenesis. *Phil. Trans. Roy. Soc. London B*, 237:37–72, 1952.
- [4] M. A. Nowak and R. M. May. Evolutionary games and spatial chaos. *Nature*, 359:826–829, 1992.
- [5] M. P. Hassell, H. N. Comins, and R. M. May. Spatial structure and chaos in insect population dynamics. *Nature*, 353:255–258, 1991.
- [6] M. P. Hassell, H. N. Comins, and R. M. May. Species coexistence and self-organizing spatial dynamics. *Nature*, 370:290–292, 1994.
- [7] B. Blasius, A. Huppert, and L. Stone. Complex dynamics and phase synchronization in spatially extended ecological systems. *Nature*, 399:354–359, 1999.
- [8] B. Kerr, M. A. Riley, M. W. Feldman, and B. J. M. Bohannan. Local dispersal promotes biodiversity in a real-life game of rock-paper-scissors. *Nature*, 418:171–174, 2002.
- [9] A. A. King and A. Hastings. Spatial mechanism for coexistence of species sharing a common natural enemy. *Theor. Pop. Biol.*, 64:431–438, 2003.
- [10] C. Hauert and M. Doebeli. Spatial structure often inhibits the evolution of cooperation in the snowdrift game. *Nature*, 428:643–646, 2004.
- [11] T. M. Scanlon, K. K. Caylor, and I. Rodriguez-Iturbe. Positive feedbacks promote power-law clustering of Kalahari vegetation. *Nature*, 449:09–212, 2007.
- [12] S. Kefi, M. Rietkerk, C. L. Alados, Y. Pueyo, V. P. Papanastasis, A. ElAich, and P. C. de Ruiter. Spatial vegetation patterns and imminent desertification in mediterranean arid ecosystems. *Nature*, 449:213–217, 2007.
- [13] G. Szabó and G. Fath. Evolutionary games on graphs. *Phys. Rep.*, 446:97–216, 2007.
- [14] M. Perc, A. Szolnoki, and G. Szabó. Cyclical interactions with alliance-specific heterogeneous invasion rates. *Phys. Rev. E*, 75:052102, 2007.
- [15] M. A. Nowak. *Evolutionary Dynamics*. Belknap Press, first edition, 2006.
- [16] H. Janssen. Directed percolation with colors and flavors. *J. Stat. Phys.*, 103:801–839, 2001.
- [17] T. Reichenbach, M. Mobilia, and E. Frey. Mobility promotes and jeopardizes biodiversity in rock-paper-scissors games. *Nature*, 448:1046–1049, 2007.
- [18] O. A. Igoshin, R. Welch, D. Kaiser, and G. Oster. Waves and aggregation patterns in myxobacteria. *Proc. Natl. Acad. Sci. U.S.A.*, 101:4256–4261, 2004.
- [19] J. Maynard Smith. *Evolution and the Theory of Games*. Cambridge University Press, 1982.
- [20] J. Hofbauer and K. Sigmund. *Evolutionary Games and Population Dynamics*. Cambridge University Press, 1998.
- [21] J. B. C. Jackson and L. Buss. Allelopathy and spatial competition among coral reef invertebrates. *Proc. Natl. Acad. Sci. U.S.A.*, 72:5160–5163, 1975.
- [22] O. Gilg, I. Hanski, and B. Sittler. Cyclic dynamics in a simple vertebrate predator-prey-community. *Science*, 302:866–868, 2001.
- [23] B. Sinervo and C. M. Lively. The rock-scissors-paper game and the evolution of alternative male strategies. *Nature*, 380:240–243, 1996.
- [24] B. C. Kirkup and M. A. Riley. Antibiotic-mediated antagonism leads to a bacterial game of rock-paper-scissors *in vivo*. *Nature*, 428:412–414, 2004.
- [25] A. N. Zaikin and A. M. Zhabotinsky. Concentration wave propagation in two-dimensional liquid-phase self-oscillating system. *Nature*, 225:535, 1970.
- [26] In R. Kapral and K. Showalter, editors, *Chemical Waves and Patterns, Part One*. Kluwer Academic Publishers, Dordrecht, 1995.
- [27] B. T. Grenfell, O. N. Bjornstad, and J. Kappey. Travelling waves and spatial hierarchies in measles epidemics. *Nature*, 414:716–723, 2001.
- [28] D. A. T. Cummings, R. A. Irizarry, N. E. Huang, T. P. Endy, A. Nisalak, K. Ungchusak, and D. S. Burke. Travelling waves in the occurrence of dengue haemorrhagic fever in thailand. *Nature*, 427:344–347, 2004.
- [29] C. B. Muratov, E. Vanden-Eijnden, and W. E. Noise can play an organizing role for the recurrent dynamics in excitable media. *Proc. Natl. Acad. Sci. U.S.A.*, 104:702–707, 2007.
- [30] J. Lechleiter, S. Girard, E. Peralta, and D. Clapham. Spiral calcium wave propagation and annihilation in *Xenopus laevis* oocytes. *Science*, 252:123–126, 1991.
- [31] M. Falcke. Reading the patterns in living cells - the physics of Ca^{2+} signaling. *Adv. Phys.*, 53:255–440, 2004.
- [32] M. D. Bootmann, D. R. Higazi, S. Coombes, and H. L. Rodgerick. Calcium signalling during excitation-contraction coupling in mammalian atrial myocytes. *J. Cell Sci.*, 119:3915–3925, 2006.
- [33] K. Sigmund, C. Hauert, and M. A. Nowak. Reward and punishment. *Proc. Natl. Acad. Sci. U.S.A.*, 98:10757–10762, 2001.
- [34] C. Hauert, S. de Monte, J. Hofbauer, and K. Sigmund. Volunteering as red queen mechanism for cooperation in public goods games. *Science*, 296:1129–1132, 2002.

- [35] S. A. Levin. Dispersion and population interactions. *Am. Nat.*, 108:207–228, 1974.
- [36] A. McKane D. Alonso. Extinction dynamics in mainland-island metapopulations: An n -patch stochastic model. *Bull. Math. Biol.*, 64:913–958, 2002.
- [37] R. Durrett and S. Levin. Spatial aspects of interspecific competition. *Theor. Pop. Biol.*, 53:30–43, 1998.
- [38] R. Durrett and S. Levin. Allelopathy in spatially distributed populations. *J. Theor. Biol.*, 185:165–171, 1997.
- [39] R. Durrett and S. Levin. The importance of being discrete (and spatial). *Theor. Pop. Biol.*, 46:363–394, 1994.
- [40] T. L. Czárán, R. F. Hoekstra, and L. Pagie. Chemical warfare between microbes promotes biodiversity. *Proc. Natl. Acad. Sci. U.S.A.*, 99:786–790, 2002.
- [41] E. Liebermann, C. Hauert, and M. A. Nowak. Evolutionary dynamics on graphs. *Nature*, 433:312, 2005.
- [42] M. Mobilia, I. T. Georgiev, and U. C. Täuber. Fluctuations and correlations in lattice models for predator-prey interaction. *Phys. Rev. E*, 73:040903(R), 2006.
- [43] M. Mobilia, I. T. Georgiev, and U. C. Täuber. Phase transitions and spatio-temporal fluctuations in stochastic lattice Lotka-Volterra models. *J. Stat. Phys.*, 128:447, 2007.
- [44] R. M. May and W. J. Leonard. Nonlinear aspects of competition between species. *SIAM J. Appl. Math.*, 29:243–253, 1975.
- [45] T. Reichenbach, M. Mobilia, and E. Frey. Noise and correlations in a spatial population model with cyclic competition. *Phys. Rev. Lett.*, 99:238105, 2007.
- [46] P. A .P. Moran. Random processes in genetics. *Proc. Camb. Phil. Soc.*, 54:60–71, 1958.
- [47] A. Traulsen, J. C. Claussen, and C. Hauert. Coevolutionary dynamics: From finite to infinite populations. *Phys. Rev. Lett.*, 95:238701, 2005.
- [48] A. Traulsen, J. C. Claussen, and C. Hauert. Coevolutionary dynamics in large, but finite populations. *Phys. Rev. E*, 74:011901, 2006.
- [49] W. Feller. *An Introduction to Probability Theory and its Application*, volume 1. Wiley, third edition, 1968.
- [50] T. Reichenbach, M. Mobilia, and E. Frey. Coexistence versus extinction in the stochastic cyclic Lotka-Volterra model. *Phys. Rev. E*, 74:051907, 2006.
- [51] D. T. Gillespie. A general method for numerically simulating the stochastic time evolution of coupled chemical reactions. *J. Comp. Phys.*, 22:403–434, 1976.
- [52] D. T. Gillespie. Exact simulations of coupled chemical reactions. *J. Phys. Chem.*, 81:2340–2361, 1977.
- [53] A. Hastings. Transients: the key to long-term ecological understanding? *Trends Ecol. Evol.*, 19:39–45, 2004.
- [54] G. R. Colletcutt and P. D. Drummond. Xmds: eXtensible multi-dimensional simulator. *Comput. Phys. Commun.*, 142:219, 2001.
- [55] XmdS, <http://www.xmds.org>.
- [56] J. Cremer, T. Reichenbach, and E. Frey, 2008. Manuscript in preparation.
- [57] S. Wiggins. *Introduction to Applied Nonlinear Dynamical Systems and Chaos*. Springer, first edition, 1990.
- [58] N. G. van Kampen. *Stochastic processes in physics and chemistry*. North Holland Publishing Company, first edition, 1981.
- [59] C. W. Gardiner. *Handbook of Stochastic Methods*. Springer, first edition, 1983.
- [60] U. C. Täuber. Critical Dynamics, Lecture notes, <http://www.phys.vt.edu/~tauber/>, year = 2007.
- [61] M. C. Cross and P. C. Hohenberg. Pattern formation outside of equilibrium. *Rev. Mod. Phys.*, 65:851–1112, 1993.
- [62] I. S. Aranson and L. Kramer. The world of the complex Ginzburg-Landau equation. *Rev. Mod. Phys.*, 74:99, 2002.
- [63] W. v. Saarloos. Front propagation into unstable states. *Phys. Rep.*, 386:29, 2003.

Bibliography

- [1] Bruce Alberts, Dennis Bray, Julian Lewis, Martin Raff, Keith Roberts, and James D. Watson. *Molecular Biology of the Cell*. Garland Publishing, fourth edition, 2002.
- [2] William Thomson. On the age of the sun's heat. *Macmillan's Mag.*, 5:288–293, 1962.
- [3] Sean B. Carroll. *Endless Forms Most Beautiful. The New Science of Evo Devo*. W. W. Norton & Company, first edition, 2004.
- [4] Fred Wolf and Theo Geisel. Spontaneous pinwheel annihilation during visual development. *Nature*, 395:73–78, 1998.
- [5] Meg Schnabel, Matthias Kaschube, Siegrid Löwel, and Fred Wolf. Symmetries and defect generation in the visual cortex. *Eur. Phys. J. - Spec. Top.*, 145:137–157, 2007.
- [6] Anna Levina, J. Michael Herrmann, and Theo Geisel. Dynamical synapses causing self-organized criticality in neural networks. *Nat. Phys.*, 3:857–860, 2007.
- [7] Dante R. Chialvo, Robert F. Gilmour, and Jose Jalife. Low dimensional chaos in cardiac tissue. *Nature*, 343:653 – 657, 1990.
- [8] Jeffrey J. Fox, Mark L. Riccio, Fei Hua, Eberhard Bodenschatz, and Robert F. Gilmour. Spatiotemporal transition to conduction block in canine ventricle. *Circ. Res.*, 90:289–296, 2002.
- [9] James D. Murray. How the leopard gets its spots. *Sci. Am.*, 258:80–87, 1988.
- [10] James D. Murray. *Mathematical Biology*. Springer Verlag, third edition, 2002.
- [11] Hauke Hirsch, Roger Kouyos, and Erwin Frey. In Andreas Schadschneider, Thorsten Pöschel, Reinhart Kühne, Michael Schreckenberg, and Dietrich E. Wolf, editors, *Traffic and Granular Flow '05*. Springer, 2006.
- [12] Katsuhiko Nishinari, Yasushi Okada, Andreas Schadschneider, and Debashish Chowdhury. Intracellular Transport of Single-Headed Molecular Motors KIF1A. *Phys. Rev. Lett.*, 95:118101, 2005.

-
- [13] Francesco Pampaloni, Gianluca Lattanzi, Alexandr Jonás, Thomas Surrey, Erwin Frey, and Ernst-Ludwig Florin. Thermal fluctuations of grafted microtubules provide evidence of a length-dependent persistence length. *Proc. Natl. Acad. Sci. U.S.A.*, 103:10248–10253, 2006.
- [14] Stefan Klumpp and Reinhard Lipowsky. Traffic of molecular motors through tube-like compartments. *J. Stat. Phys.*, 113:233, 2003.
- [15] Andrea Parmeggiani, Thomas Franosch, and Erwin Frey. Phase coexistence in driven one dimensional transport. *Phys. Rev. Lett.*, 90:086601, 2003.
- [16] Andrea Parmeggiani, Thomas Franosch, and Erwin Frey. The totally asymmetric simple exclusion process with Langmuir kinetics. *Phys. Rev. E*, 70:046101, 2004.
- [17] Paolo Pierobon, Thomas Franosch, and Erwin Frey. Driven lattice gas of dimers coupled to a bulk reservoir. *Phys. Rev. E*, 74:031920, 2006.
- [18] Tobias Reichenbach, Thomas Franosch, and Erwin Frey. Exclusion processes with internal states. *Phys. Rev. Lett.*, 97:050603, 2006.
- [19] Tobias Reichenbach, Erwin Frey, and Thomas Franosch. Traffic jams induced by rare switching events in two-lane transport. *New J. Phys.*, 9:159, 2007.
- [20] <http://en.wikipedia.org/wiki/Image:Kinetochore.jpg>.
- [21] François Nédélec, Thomas Surrey, Anthony C. Maggs, and Stanislas Leibler. Self-organization of microtubules and motors. *Nature*, 389:305–308, 1997.
- [22] Philip Greulich, Ashok Garai, Katsuhiko Nishinari, Andreas Schadschneider, and Debashish Chowdhury. Intracellular transport by single-headed kinesin KIF1A: Effects of single-motor mechanochemistry and steric interactions. *Phys. Rev. E*, 75:041905, 2007.
- [23] Raul Urrutia, Mark A. McNiven, Joseph P. Albanesi, Douglas B. Murphy, and Bechara Kachar. Modelling microtubule patterns. *Proc. Natl. Acad. Sci. U.S.A.*, 88:6701–6705, 1991.
- [24] Thomas Surrey, François Nédélec, Stanislas Leibler, and Eric Karsenti. Physical properties determining self-organization of motors and microtubules. *Science*, 292:1167 – 1171, 2001.
- [25] Sumithra Sankararaman and Gautam I. Menon. Self-organized pattern formation in motor-microtubule mixtures. *Phys. Rev. E*, 70:031905, 2004.
- [26] Eric Karsenti, François Nédélec, and Thomas Surrey. Modelling microtubule patterns. *Nat. Cell Biol.*, 8:1204 – 1211, 2006.

- [27] Roland Wedlich-Söldner, Steve Altschuler, Lani Wu, and Rong Li. Spontaneous cell polarization through actomyosin-based delivery of the Cdc42 GTPase. *Science*, 299:1231–1235, 2003.
- [28] Lawrence Rothfield, Aziz Taghbalout, and Yu-Ling Shih. Spatial control of bacterial division-site placement. *Nat. Rev. Microbiol.*, 3:959–968, 2005.
- [29] David M. Raskin and Piet A. J. de Boer. Rapid pole-to-pole oscillation of a protein required for directing division to the middle of *Escherichia coli*. *Proc. Natl. Acad. Sci. U.S.A.*, 96:4971–4976, 1999.
- [30] Martin Howard and Karsten Kruse. Cellular organization by self-organization: mechanisms and models for Min protein dynamics. *J. Cell Biol.*, 168:533–536, 2005.
- [31] Donald A. Drew, Mary J. Osborn, and Lawrence I. Rothfield. A polymerization-depolymerization model that accurately generates the self-sustained oscillatory system involved in bacterial division site placement. *Proc. Natl. Acad. Sci. U.S.A.*, 102:6114–6118, 2005.
- [32] Giovanni Meacci. Physical aspects of Min oscillations in *Escherichia coli*, 2006. PhD Thesis, Technical University Dresden.
- [33] Giovanni Meacci, Jonas Ries, Elisabeth Fischer-Friedrich, Nicoletta Kahya, Petra Schwille, and Karsten Kruse. Mobility of Min-proteins in *Escherichia coli* measured by fluorescence correlation spectroscopy. *Phys. Biol.*, 3:255–263, 2006.
- [34] Elisabeth Fischer-Friedrich, Romain Nguyen van Yen, and Karsten Kruse. Surface waves of Min-proteins. *Phys. Biol.*, 4:38–47, 2007.
- [35] Florian Siegert and Cornelis J. Weijer. Spiral and concentric waves organize multicellular *Dictyostelium* mounds. *Curr. Biol.*, 5:937–943, 1995.
- [36] Owen M. Gilbert, Kevin R. Foster, Natasha J. Mehdiabadi, Joan E. Strassmann, and David C. Quelle. High relatedness maintains multicellular cooperation in a social amoeba by controlling cheater mutants. *Proc. Natl. Acad. Sci. U.S.A.*, 104:4256–4261, 2007.
- [37] John B.S. Haldane. Population genetics. *New Biol.*, 18:34–51, 1955.
- [38] William D. Hamilton. The evolution of altruistic behavior. *Am. Nat.*, 97:354–356, 1963.
- [39] Garrett J. Hardin. The competitive exclusion principle. *Science*, 131:1292–1297, 1960.
- [40] Georgii F. Gause. *The Struggle for Existence*. Baltimore MD: Williams & Wilkins, 1934.

- [41] G. Evelyn Hutchinson. The paradox of the plankton. *Am. Nat.*, 95:137–145, 1961.
- [42] Tatsuo Miyazaki, Kei-ichi Tainaka, Tatsuya Togashi, Takanori Suzuki, and Jin Yoshimura. Spatial coexistence of phytoplankton species in ecological timescale. *Popul. Ecol.*, 48:107–112, 2006.
- [43] Benjamin Kerr, Margaret A. Riley, Marcus W. Feldman, and Brendan J. M. Bohannan. Local dispersal promotes biodiversity in a real-life game of rock-paper-scissors. *Nature*, 418:171–174, 2002.
- [44] Barry Sinervo and Curtis M. Lively. The rock-scissors-paper game and the evolution of alternative male strategies. *Nature*, 380:240–243, 1996.
- [45] Barry Sinervo. Lizard land. <http://bio.research.ucsc.edu/barrylab/>.
- [46] Todd M. Scanlon, Kelly K. Caylor, and Ignacio Rodriguez-Iturbe. Positive feedbacks promote power-law clustering of Kalahari vegetation. *Nature*, 449:09–212, 2007.
- [47] Mercedes Pascual and Frédéric Guichard. Criticality and disturbance in spatial ecological system. *Trends Ecol. Evol.*, 20:88–95, 2005.
- [48] Joe Howard. *Mechanics of Motor Proteins and the Cytoskeleton*. Sinauer Press, Sunderland, Massachusetts, 2001.
- [49] Igor Žutić, Jaroslav Fabian, and S. Das Sarma. Spintronics: Fundamentals and applications. *Rev. Mod. Phys.*, 76:323, 2004.
- [50] Debashish Chowdhury, Ludger Santen, and Andreas Schadschneider. Statistical physics of vehicular traffic and some related systems. *Phys. Rep.*, 329:199, 2000.
- [51] Dirk Helbing. Traffic and related self-driven many-particle systems. *Rev. Mod. Phys.*, 73:1067, 2001.
- [52] R. John Ellis. Macromolecular crowding: an important but neglected aspect of the intracellular environment. *Curr. Opin. Struct. Biol.*, 11:114–119, 2001.
- [53] Matthias Weiss, Markus Elsner, Fredrik Kartberg, and Tommy Nilsson. Anomalous subdiffusion is a measure for cytoplasmic crowding in living cells. *Biophys. J.*, 87:3518–3524, 2004.
- [54] Felix Höfling, Thomas Franosch, and Erwin Frey. Localization transition of the three-dimensional Lorentz model and continuum percolation. *Phys. Rev. Lett.*, 96:165901, 2006.
- [55] Erwin Frey, Andrea Parmeggiani, and Thomas Franosch. Collective phenomena in intracellular processes. *Genome Informatics*, 15:46–55, 2004.

- [56] Nobutaka Hirokawa. Kinesin and dynein superfamily proteins and the mechanism of organelle transport. *Science*, 279:519–526, 1998.
- [57] Ahmet Yildiz, Michio Tomishige, Ronald D. Vale, and Paul R. Selvin. Kinesin walks hand-over-hand. *Science*, 303:676 – 678, 2004.
- [58] Peter Reimann. Brownian motors: noisy transport far from equilibrium. *Phys. Rep.*, 361:57, 2002.
- [59] Katsuyuki Shiroguchi and Kazuhiko Kinoshita. Myosin V walks by lever action and Brownian motion. *Science*, 316:1208–1212, 2007.
- [60] Teppei Mori, Ronald D. Vale, and Michio Tomishig. How kinesin waits between steps. *Nature*, 450:750–754, 2007.
- [61] Mark F. Bear, Barry W. Connors, and Michael A. Paradiso. *Neuroscience. Exploring the Brain*. Lippincott Williams&Wilkins, 2001.
- [62] Anthony Brown. Opinion: Slow axonal transport: stop and go traffic in the axon. *Nat. Rev. Mol. Cell Biol.*, 1:153–156, 2000.
- [63] Anthony Brown. Axonal transport of membranous and nonmembranous cargos: a unified perspective. *J. Cell Biol.*, 160:817–821, 2003.
- [64] Tom Chou. Ribosome recycling, diffusion, and mRNA loop formation in translational regulation. *Biophys. J.*, 85:755–773, 2003.
- [65] Tom Chou and Greg Lakatos. Clustered bottlenecks in mRNA translation and protein synthesis. *Phys. Rev. Lett.*, 93:198101, 2004.
- [66] Beate Schmittmann and Royce K. P. Zia. In Cyril Domb and Joel L. Lebowitz, editors, *Phase Transitions and Critical Phenomena*, volume 17. Academic Press, London, 1995.
- [67] Carolyn T. MacDonald, Julian H. Gibbs, and Allen C. Pipkin. Kinetics of biopolymerization on nucleic acid templates. *Biopolymers*, 6:1, 1968.
- [68] Bernard Derrida, Eytan Domany, and David Mukamel. An exact solution of a one-dimensional asymmetric exclusion model with open boundaries. *J. Stat. Phys.*, 69:667, 1992.
- [69] Bernard Derrida, M.R. Evans, V. Hakim, and V. Pasquier. Exact solution of a 1D asymmetric exclusion model using a matrix formulation. *J. Phys. A: Math. Gen.*, 26:1493, 1993.
- [70] Bernard Derrida and Joel L. Lebowitz. Exact large deviation function in the asymmetric exclusion process. *Phys. Rev. Lett.*, 80:209–213, 1998.

- [71] Bernard Derrida. An exactly soluble non-equilibrium system: The asymmetric simple exclusion process. *Phys. Rep.*, 301:65–83, 1998.
- [72] Joachim Krug. Boundary-induced phase transitions in driven diffusive systems. *Phys. Rev. Lett.*, 67:1882, 1991.
- [73] M. R. Evans, D. P. Foster, C. Godrèche, and D. Mukamel. Spontaneous symmetry breaking in a one dimensional driven diffusive system. *Phys. Rev. Lett.*, 74:208, 1995.
- [74] Vladislav Popkov and Ingo Peschel. Symmetry breaking and phase coexistence in a driven diffusive two-channel system. *Phys. Rev. E*, 64:026126.
- [75] Vladislav Popkov, Attila Rákos, Richard D. Willmann, Anatoly B. Kolomeisky, and Gunter M. Schütz. Localization of shocks in driven diffusive systems without particle number conservation. *Phys. Rev. E*, 67:066117, 2003.
- [76] Ivan T. Georgiev, Beate Schmittmann, and Royce K. P. Zia. Anomalous nucleation far from equilibrium. *Phys. Rev. Lett.*, 94:115701.
- [77] Ivan T. Georgiev, Beate Schmittmann, and Royce K. P. Zia. Cluster growth and dynamic scaling in a two-lane driven diffusive system. *J. Phys. A: Math. Gen.*, 39(14):3495–3509.
- [78] Tobias Reichenbach, Thomas Franosch, and Erwin Frey. Domain wall delocalization, dynamics and fluctuations in an exclusion process with two internal states, 2008. Manuscript submitted, cond-mat.stat-mech/0801.4394.
- [79] Wolfgang Knospe, Ludger Santen, Andreas Schadschneider, and Michael Schreckenberg. A realistic two-lane traffic model for highway traffic. *J. Phys. A: Math. Gen.*, 35:3369–3388, 2002.
- [80] Beate Schmittmann, Justin Krometis, and Royce K. P. Zia. Will jams get worse when slow cars move over? *Europhys. Lett.*, 70:299–305, 2005.
- [81] Dirk Helbing and Andreas Greiner. Modeling and simulation of multilane traffic flow. *Phys. Rev. E*, 55:5498–5508, 1997.
- [82] Boris S. Kerner. Empirical macroscopic features of spatial-temporal traffic patterns at highway bottlenecks. *Phys. Rev. E*, 65:046138, 2002.
- [83] Ekaterina Pronina and Anatoly B. Kolomeisky. Two-channel totally asymmetric simple exclusion processes. *J. Phys. A: Math. Gen.*, 37:9907, 2004.
- [84] Vladislav Popkov and Gunter M. Schütz. Shocks and excitation dynamics in a driven diffusive two-channel system. *J. Stat. Phys.*, 112:523, 2003.
- [85] Anna Melbinger. Classical spin transport far away from equilibrium, 2007. Diploma Thesis at the Ludwigs-Maximilians-University Munich.

- [86] Anna Melbinger, Tobias Reichenbach, Thomas Franosch, and Erwin Frey. Manuscript in preparation.
- [87] Ekaterina Pronina and Anatoly B. Kolomeisky. Asymmetric coupling in two-channel simple exclusion processes. *Phys. A*, 372:12–21, 2006.
- [88] Tetsuya Mitsudo and Hisao Hayakawa. Synchronisation of kinks in the two-lane totally asymmetric simple exclusion process with open boundary conditions. *J. Phys. A: Math. Gen.*, 38:3087–3096, 2005.
- [89] Robert Juhasz. Weakly coupled, antiparallel, totally asymmetric simple exclusion processes. *Phys. Rev. E*, 76:021117, 2007.
- [90] Wilfred G. van der Wiel, Silvano De Franceschi, Jeroen M. Elzerman, Toshimasa Fujisawa, Seigo Tarucha, and Leo P. Kouwenhoven. Electron transport through double quantum dots. *Rev. Mod. Phys.*, 75:1–22, 2002.
- [91] Daniel S. Saraga and Daniel Loss. Spin-entangled currents created by a triple quantum dot. *Phys. Rev. Lett.*, 90:166803, 2003.
- [92] Yoram Alhassid. The statistical theory of quantum dots. *Rev. Mod. Phys.*, 72:895–968, 2000.
- [93] Sara M. Cronenwett, Tjerk H. Oosterkamp, and Leo P. Kouwenhoven. A tunable Kondo effect in quantum dots. *Science*, 281:540–544, 1998.
- [94] G. Binasch, Peter Grünberg, F. Saurenbach, and W. Zinn. Enhanced magnetoresistance in layered magnetic structures with antiferromagnetic interlayer exchange. *Phys. Rev. B*, 39:4828–4830, 1989.
- [95] M. N. Baibich, J. M. Broto, Albert Fert, F. Nguyen Van Dau, F. Petroff, P. Eitenne, G. Creuzet, A. Friederich, and J. Chazelas. Giant magnetoresistance of (001)Fe/(001)Cr magnetic superlattices. *Phys. Rev. Lett.*, 61:2472–2475, 1988.
- [96] Fabian H. L. Essler, Holger Frahm, Frank Göhmann, Andreas Klümper, and Vladimir E. Korepin. *The One-Dimensional Hubbard Model*. Cambridge University Press, first edition, 2005.
- [97] Debashish Chowdhury, Andreas Schadschneider, and Katsuhiko Nishinari. Physics of transport and traffic phenomena in biology: from molecular motors and cells to organisms. *Phys. Life Rev.*, 2:318–352, 2005.
- [98] Iain D. Couzin and Nigel R. Franks. Self-organized lane formation and optimized traffic flow in army ants. *Proc. Roy. Soc. London B*, 20:139–146, 2003.
- [99] Rick Durrett and Simon Levin. Spatial aspects of interspecific competition. *Theor. Pop. Biol.*, 53:30–43, 1998.

- [100] Michael P. Hassell, Hugh N. Comins, and Robert M. May. Spatial structure and chaos in insect population dynamics. *Nature*, 353:255–258, 1991.
- [101] György Szabó and Gabor Fath. Evolutionary games on graphs. *Phys. Rep.*, 446:97–216, 2007.
- [102] Vigdis Torsvik, Jostein Goksøyr, and Frida L. Daae. High diversity in DNA of soil bacteria. *Appl. Environ. Microbiol.*, 56:782–787, 1990.
- [103] Daniel E. Dykhuizen. Santa rosalia revisited: Why are there so many species of bacteria? *Antonie Leeuwenhoek*, 73:25–33, 1998.
- [104] Klaus Rohde. Latitude gradients in species-diversity - the search for the primary cause. *Oikos*, 65:514–527, 1992.
- [105] John R. G. Turner. Explaining the global biodiversity gradient: energy, area, history and natural selection. *Bas. Appl. Ecol.*, 5:435–448, 2004.
- [106] W. Wayt Thomas. Conservation and monographic research on the flora of Tropical America. *Biodivers. Cons.*, 8:1007–1015, 1999.
- [107] Carlos Jaramillo, Milton J. Rueda, and Germán Mora. Cenozoic plant diversity in the neotropics. *Science*, 311:1893–1896, 2006.
- [108] Purificación López-García, Francisco Rodríguez-Valera, Carlós Pedrós-Alió, and David Moreira. Unexpected diversity of small eukaryotes in deep-sea antarctic plankton. *Nature*, 409:603–607, 2001.
- [109] Angelika Brandt, Andrew J. Gooday, and Simone N. Brandão et al. First insights into the biodiversity and biogeography of the southern ocean deep sea. *Nature*, 447:307–311, 2007.
- [110] Douglas B. Rusch, Aaron L. Halpern, Granger Sutton, and Karla B. Heidelberg et al. The *Sorcerer II* global ocean sampling expedition: Northwest atlantic through eastern tropical pacific. *PLoS Biol.*, 5:e77, 2007.
- [111] Natarajan Kannan, Susan S. Taylor, Yufeng Zhai, J. Craig Venter, and Gerard Manning. Structural and functional diversity of the microbial kinome. *PLoS Biol.*, 5:e17, 2007.
- [112] Michel Loreau, Shahid Naeem, and Pablo Inchausti et al. Biodiversity and ecosystem functioning: Current knowledge and future challenges. *Science*, 294:804–808, 2001.
- [113] Anthony R. Ives and Stephen C. Carpenter. Stability and diversity of ecosystems. *Science*, 317:58–62, 2007.
- [114] Motoo Kimura. *The Neutral Theory of Molecular Evolution*. Cambridge University Press, 1983.

- [115] Sewall Wright. *Evolution and the Genetics of Populations*. Chicago University Press, 1969.
- [116] J. Maynard Smith. *Evolution and the Theory of Games*. Cambridge University Press, 1982.
- [117] J. Hofbauer and K. Sigmund. *Evolutionary Games and Population Dynamics*. Cambridge University Press, 1998.
- [118] Martin A. Nowak. *Evolutionary Dynamics*. Belknap Press, first edition, 2006.
- [119] Martin A. Nowak and Karl Sigmund. Evolutionary dynamics of biological games. *Science*, 303:793–799, 2004.
- [120] Alfred J. Lotka. Undamped oscillations derived from the law of mass action. *J. Amer. Chem. Soc.*, 42:1595–1599, 1920.
- [121] Vito Volterra. Variazioni e fluttuazioni del numero d’individui in specie animali conviventi. *Mem. Accad. Lincei*, 2:31, 1926.
- [122] Steven H. Strogatz. *Nonlinear dynamics and chaos*. Westview, 1994.
- [123] Stephen Wiggins. *Introduction to Applied Nonlinear Dynamical Systems and Chaos*. Springer, first edition, 1990.
- [124] Stuart L. Pimm, John H. Lawton, and Joel E. Cohen. Food web patterns and their consequences. *Nature*, 350:669 – 674, 1991.
- [125] Uri Alon. *An Introduction to Systems Biology*. Chapman & Hall/CRC, 2006.
- [126] Ron Milo, Shai Shen-Orr, Shalev Itzkovitz, Nadav Kashtan, Dmitri Chklovskii, and Uri Alon. Network motifs: Simple building blocks of complex networks. *Science*, 298:824–827, 2002.
- [127] Uri Alon. Network motifs: theory and experimental approaches. *Nat. Rev. Genet.*, 8:450–461, 2007.
- [128] Leland H. Hartwell, John J. Hopfield, Stanislas Leibler, and Andrew W. Murray. From molecular to modular cell biology. *Nature*, 402:C47–C52, 1999.
- [129] Amos B. Oppenheim, Oren Kobiler, Joel Stavans, Donald L. Court, and Sankar Adhya. Switches in bacteriophage lambda development. *Ann. Rev. Genet.*, 39.
- [130] Morten Ernebjerg and Roy Kishony. Private communication.
- [131] Barry Sinervo, Benoit Heulin, Yann Surget-Groba, and Jean et al. Clobert. Models of density-dependent genic selection and a new rock-paper-scissors social system. *Am. Nat.*, 170:663–680, 2007.

- [132] J. B. C. Jackson and Leo Buss. Allelopathy and spatial competition among coral reef invertebrates. *Proc. Natl. Acad. Sci. U.S.A.*, 72:5160–5163, 1975.
- [133] Oliver Gilg, Ilkka Hanski, and Benoit Sittler. Cyclic dynamics in a simple vertebrate predator-prey-community. *Science*, 302:866–868, 2001.
- [134] Crispin W. Gardiner. *Handbook of Stochastic Methods*. Springer, first edition, 1983.
- [135] N.G. van Kampen. *Stochastic processes in physics and chemistry*. North Holland Publishing Company, first edition, 1981.
- [136] Uwe C. Täuber. Graduate textbook (work in progress): Critical Dynamics (2008) <http://www.phys.vt.edu/~tauber>.
- [137] Arne Traulsen, Jens Christian Claussen, and Christoph Hauert. Coevolutionary dynamics: From finite to infinite populations. *Phys. Rev. Lett.*, 95:238701, 2005.
- [138] Arne Traulsen, Jens Christian Claussen, and Christoph Hauert. Coevolutionary dynamics in large, but finite populations. *Phys. Rev. E*, 74:011901, 2006.
- [139] Tobias Reichenbach, Mauro Mobilia, and Erwin Frey. Coexistence versus extinction in the stochastic cyclic Lotka-Volterra model. *Phys. Rev. E*, 74:051907, 2006.
- [140] Maximilian Berr. Survival probabilities in a stochastic evolutionary game of rock, paper, and scissors, 2008. Diploma Thesis at the Ludwigs-Maximilians-University Munich.
- [141] Maximilian Berr, Tobias Reichenbach, Erwin Frey, and Martin Schottenloher, 2008. Manuscript in preparation.
- [142] Sidney Redner. *A guide to first-passage processes*. Cambridge University Press, 1983.
- [143] Tibor Antal and Istvan Scheuring. Fixation of strategies for an evolutionary game in finite populations. *Bull. Math. Biol.*, 68:1923, 2006.
- [144] Jonas Cremer. Evolutionary dynamics of finite populations, 2007. Diploma Thesis at the Ludwigs-Maximilians-University Munich.
- [145] Jonas Cremer, Tobias Reichenbach, and Erwin Frey. Anomalous finite-size effects in the Battle of the Sexes, 2007. *Eur. Phys. J. B* (2008) Online first, doi: 10.1140/epjb/e2008-00036-x.
- [146] Jonas Cremer, Tobias Reichenbach, and Erwin Frey, 2008. Manuscript in preparation.
- [147] Alan Hastings. Transients: the key to long-term ecological understanding? *Trends Ecol. Evol.*, 19:39–45, 2004.

- [148] Alan Hastings. Transient dynamics and persistence of ecological systems. *Ecol. Lett.*, 4:215–220, 2001.
- [149] Sonia Kefi, Max Rietkerk, Concepcion L. Alados, Yolanda Pueyo, Vasilios P. Papanastasis, Ahmed ElAich, and Peter C. de Ruiter. Spatial vegetation patterns and imminent desertification in mediterranean arid ecosystems. *Nature*, 449:213–217, 2007.
- [150] Simon A. Levin. Dispersion and population interactions. *Am. Nat.*, 108:207–228, 1974.
- [151] Michael P. Hassell, Hugh N. Comins, and Robert M. May. Species coexistence and self-organizing spatial dynamics. *Nature*, 370:290–292, 1994.
- [152] Rick Durrett and Simon Levin. The importance of being discrete (and spatial). *Theor. Pop. Biol.*, 46:363–394, 1994.
- [153] Rick Durrett and Simon Levin. Allelopathy in spatially distributed populations. *J. Theor. Biol.*, 185:165–171, 1997.
- [154] Aaron A. King and Alan Hastings. Spatial mechanism for coexistence of species sharing a common natural enemy. *Theor. Pop. Biol.*, 64:431–438, 2003.
- [155] Robert M. May and Warren J. Leonard. Nonlinear aspects of competition between species. *SIAM J. Appl. Math.*, 29:243–253, 1975.
- [156] Tobias Reichenbach, Mauro Mobilia, and Erwin Frey. Mobility promotes and jeopardizes biodiversity in rock-paper-scissors games. *Nature*, 448:1046–1049, 2007.
- [157] Michael C. Cross and Pierre C. Hohenberg. Pattern formation outside of equilibrium. *Rev. Mod. Phys.*, 65:851–1112, 1993.
- [158] Igor S. Aranson and Lorenz Kramer. The world of the complex Ginzburg-Landau equation. *Rev. Mod. Phys.*, 74:99, 2002.
- [159] Wim van Saarloos. Front propagation into unstable states. *Phys. Rep.*, 386:29, 2003.
- [160] Boris P. Belousov. A periodic reaction and its mechanism. *Comp. Abstr. Rad. Med.*, 147:145, 1959.
- [161] Anatol M. Zhabotinsky. Periodic processes of malonic acid oxidation in a liquid phase. *Biofizika*, 9:306–311, 1964.
- [162] A. N. Zaikin and Anatol M. Zhabotinsky. Concentration wave propagation in two-dimensional liquid-phase self-oscillating system. *Nature*, 225:535, 1970.

- [163] James Lechleiter, Steven Girard, Ernest Peralta, and David Clapham. Spiral calcium wave propagation and annihilation in *Xenopus laevis* oocytes. *Science*, 252:123–126, 1991.
- [164] Rüdiger Thul and Martin Falcke. Stability of membrane bound reactions. *Phys. Rev. Lett.*, 93:188103, 2004.
- [165] Martin Falcke. Reading the patterns in living cells - the physics of Ca^{2+} signaling. *Adv. Phys.*, 53:255–440, 2004.
- [166] Jorge M. Davidenko, Arcady V. Pertsov, Remy Salomonsz, William Baxter, and Jos Jalife. Stationary and drifting spiral waves of excitation in isolated cardiac muscle. *Nature*, 355:349, 1992.
- [167] Richard Gray and Nipon Chattipakorn. Termination of spiral waves during cardiac fibrillation via shock-induced phase resetting. *Proc. Natl. Acad. Sci. U.S.A.*, 102:4672, 2005.
- [168] Catelijne van Oss, Alexandre V. Panfilov, Pauline Hogeweg, Florian Siegert, and Cornelis J. Weijer. Spatial pattern formation during aggregation of the slime mould *Dictyostelium discoideum*. *J. Theor. Biol.*, 181:203–213, 1996.
- [169] Oleg A. Igoshin, Roy Welch, Dale Kaiser, and George Oster. Waves and aggregation patterns in myxobacteria. *Proc. Natl. Acad. Sci. U.S.A.*, 101:4256–4261, 2004.
- [170] Laurent Frachebourg, Paul L. Krapivsky, and Eli Ben-Naim. Spatial organization in cyclic Lotka-Volterra systems. *Phys. Rev. E*, 54:6186–6200, 1996.
- [171] George A. Tsekouras and Astero Provata. Fractal properties of the lattice Lotka-Volterra model. *Phys. Rev. E*, 65:016204, 2001.
- [172] György Szabó and Attila Szolnoki. A three-state cyclic voter model extended with potts energy. *Phys. Rev. E*, 65:036115.
- [173] Attila Szolnoki, György Szabó, and Maria Ravasz. Three-state potts model in combination with the rock-scissors-paper game. *Phys. Rev. E*, 71:027102.
- [174] Tobias Reichenbach, Mauro Mobilia, and Erwin Frey. Noise and correlations in a spatial population model with cyclic competition. *Phys. Rev. Lett.*, 99:238105, 2007.
- [175] Tobias Reichenbach, Mauro Mobilia, and Erwin Frey. Self-organization of mobile populations in cyclic competition, 2008. Manuscript submitted, q-bio.PE/0801.1798.
- [176] Tobias Reichenbach and Erwin Frey, 2008. Manuscript in preparation.
- [177] Alan M. Turing. The chemical basis of morphogenesis. *Phil. Trans. Roy. Soc. London B*, 237:37–72, 1952.

- [178] Anton A. Winkler. Renormalization arguments on species coexistence far from equilibrium, 2007. Diploma Thesis at the Ludwigs-Maximilians-University Munich.
- [179] Anton A. Winkler, Tobias Reichenbach, and Erwin Frey, 2008. Manuscript in preparation.
- [180] Robert Axelrod. *The Evolution of Cooperation*. Perseus Books Group, revised edition, 2006.
- [181] Edited by John H. Kagel & Alvin E. Roth. *The Handbook of Experimental Economics*. Princeton University Press, 1995.
- [182] Martin A. Nowak and Robert M. May. Evolutionary games and spatial chaos. *Nature*, 359:826–829, 1992.
- [183] Karl Sigmund, Christoph Hauert, and Martin A. Nowak. Reward and punishment. *Proc. Natl. Acad. Sci. U.S.A.*, 98:10757–10762, 2001.
- [184] Christoph Hauert, Arne Traulsen, Hannelore Brandt, Martin A. Nowak, and Karl Sigmund. Via freedom to coercion: The emergence of costly punishment. *Science*, 316:1905–1907, 2007.
- [185] Oskar Hallatschek, Pascal Hersen, Sharad Ramanathan, and David R. Nelson. Genetic drift at expanding frontiers promotes gene segregation. *Proc. Natl. Acad. Sci.*, 104:19926–19930, 2007.

Danksagung

An erster Stelle möchte ich mich bei Prof. Erwin Frey für die interessanten Thematiken der Doktorarbeit, die Betreuung und vielfältige Unterstützung bedanken. Unsere Diskussionen waren immer von einer offenen und konstruktiven Atmosphäre geprägt, in denen Ideen entstanden und entwickelt werden konnten. Seine Hochschätzung des kreativen und schöpferischen Aspekts der Wissenschaft sowie seine motivierende Art hat mir sehr gut getan. Weiterhin hat mich Erwin schon früh auf Konferenzen und Tagungen mitgenommen oder mir die Teilnahme ermöglicht. Die Diskussionen dort wie auch mit den vielen Gästen, die regelmässig an den Lehrstuhl eingeladen werden, waren spannend und haben meinen wissenschaftlichen Horizont beträchtlich erweitert.

Die Arbeiten zu Stauphänomenen in Transportprozessen sind in Zusammenarbeit mit Prof. Thomas Franosch entstanden. Thomas' kritischer Geist war dabei von grossem Wert, und ich habe durch die Arbeit mit ihm viel gelernt, wofür ich mich bei ihm an dieser Stelle bedanken möchte.

Dr. Mauro Mobilia war ein wichtiger Partner in der Arbeit über ökologische Systeme, Mobilität und Musterbildung. Seiner Expertise und seinem freimütigen Umgang verdanke ich viel. Ausserdem erinnere ich mich gern an lange Diskussionen mit ihm und Paolo Pierobon über die kleinen und großen Geheimnisse des Wissenschaftsbetriebs.

Für das Korrekturlesen der Arbeit danke ich Karen Alim, Jonas Cremer, Anna Melbinger und Anton Winkler.

Während des vergangenen Jahres konnte ich an der Betreuung von Diplomanden am Lehrstuhl mitwirken, was mir viel Spass gemacht hat. Anna Melbinger hat eine Arbeit zu Transportprozessen geschrieben, Jonas Cremer, Anton Winkler, und Heiko Hotz beschäftigen sich mit Spieltheorie. Unsere Diskussionen waren engagiert und angeregt, wofür ich mich herzlich bedanken möchte. Bei unseren Skatabenden, oft zusammen mit Karen und Murad, konnten wir uns davon wieder gut erholen!

Experimente zur Koexistenz von Bakterienstämmen sind derzeit am Lehrstuhl von Prof. Rädler geplant. Ihm sowie vor allem auch Madeleine Leisner, die sich sehr engagiert darum kümmert, bin ich dafür sehr dankbar, und schon gespannt, was dabei herauskommen wird.

Den Oktober 2007 habe ich am Program for Evolutionary Dynamics in Harvard verbracht, und danke Prof. Christoph Hauert und Prof. Martin A. Nowak sowie der ganzen Gruppe herzlich für ihre Gastfreundschaft. Es war eine sowohl schöne als auch fruchtbare und wichtige Zeit, in der ich viele Leute kennengelernt habe.

Schließlich möchte ich mich bei allen Leuten am Lehrstuhl, insbesondere meiner Bürokollegin Marta, sehr für eine angenehme Atmosphäre und ein gutes Miteinander bedanken!

Curriculum Vitae

Address

Arnold Sommerfeld Center for Theoretical Physics (ASC) and
Center for NanoScience (CeNS),
Department of Physics,
Ludwig-Maximilians-Universität München,
Theresienstrasse 37,
D-80333 München, Germany
Phone: +49 (0)89 2180 4560
Email: tobias.reichenbach@physik.lmu.de

Personal Data

Date of birth: 26th of February, 1981
Place of birth: Berlin
Nationality: German

Education

10/1999 - 09/2001	Undergraduate studies in physics, Leipzig University
09/2001	Prediploma in physics, Grade 1.0 "Very Good"
10/2001 - 11/2004	Graduate studies in physics, Leipzig University
09/2002 - 03/2003	Exchange student at Chalmers University, Göteborg, Sweden
07/2003 - 08/2003	Internship at the European Organization for Nuclear Research (CERN), Geneva, Switzerland
11/2004	Diploma in physics, Grade 1.0 "Excellent" Thesis advisor: Prof. Klaus Sibold Thesis title: Quantized Equations of Motion and Currents in Noncommutative Theories
02/2005 - 04/2008	PhD student at the Ludwigs-Maximilians-University München Thesis advisor: Prof. Erwin Frey Thesis title: Dynamic Patterns of Biological Systems
10/2007	Visiting scientist in the group of Prof. Martin A. Nowak, Program for Evolutionary Dynamics, Harvard University